

DISSERTATION

ELASTIC FREE-STANDING RTIL COMPOSITE MEMBRANES FOR CO₂/N₂
SEPARATION BASED ON SPHERE-FORMING TRIBLOCK/DIBLOCK COPOLYMER
BLENDS

Submitted by

Dilanji B. Wijayasekara

Department of Chemical and Biological Engineering

In partial fulfillment of the requirements

For the Degree of Doctor of Philosophy

Colorado State University

Fort Collins, Colorado

Fall 2016

Doctoral Committee:

Advisor: Travis S. Bailey

John D. Fisk

Matthew Kipper

Susan James

Copyright by Dilanji Wijayasekara 2016

All rights reserved

ABSTRACT

ELASTIC FREE-STANDING RTIL COMPOSITE MEMBRANES FOR CO₂/N₂ SEPARATION BASED ON SPHERE-FORMING TRIBLOCK/DIBLOCK COPOLYMER BLENDS

The main focus of this dissertation was the development of a robust polymeric membrane material for separating CO₂ from a gas mixture of CO₂ and N₂. Flu gas, which is mainly a mixture CO₂ and N₂, is the single largest form of anthropogenic CO₂ emissions to the atmosphere. Capturing CO₂ from flu gas is considered as a measure of controlling anthropogenic CO₂ emissions. Existing CO₂ capturing technologies for flu gas suffer from low efficiency and the low cost effectiveness. Adoption of membrane technology is comparatively the best route towards the economical separations. Challenges faced by existing CO₂ separation membrane materials are the lack of high mechanical robustness and the processability required for fabrication of membrane units while maximizing their gas separation properties. We were able to form a novel membrane material that addresses each of these challenges. These novel membranes are based on highly swollen, self-standing films produced using sphere-forming PS-PEO diblock and PS-PEO-PS triblock copolymer blends. The intricate connectivity among spherical domains produced during melt-state assembly (prior to swelling), provides a framework that remains elastically tough even in the presence of large quantities of 1-ethyl-3-methylimidazolium bis(trifluoromethylsulfonyl)imide (EMIMTf₂N) - a room temperature ionic liquid (RTIL) that has high selectivity for CO₂ over N₂.

Further investigations on improving the robustness of these membranes and the gas separation properties were carried out based on two scenarios. First, potential of improving the thermal stability of these membranes by replacing the thermoplastic polystyrene with a thermoset moiety such as a chemically cross-linked polyisoprene (PI) was researched. Cross-linking chemistry utilized required a post-polymerization modification of PI and it was found that this oxidation modification of olefins on PI caused the decoupling of triblock copolymer in the blend and also substantially hindered melt-state self assembly. The membranes formed with this modification turned out to have inferior mechanical properties compared to the polystyrene based ones, most likely due to the above mentioned complications. Due to the time restrictions, this study was limited to just the identification of the existing challenges in the proposed strategy. Recommendations for addressing the challenges identified are also presented later in the dissertation.

The second scenario for improving the performance of these membranes was to increase their productivity by improving both the CO₂ permeability and maximizing the trans-membrane pressure differentials possible during operation. To accomplish this we focused on the development of an alternative matrix material (alternative for PEO) enriched with ionic groups. The goal was to increase matrix solubility in the RTIL (improved CO₂ permeability) while simultaneously strengthening matrix-RTIL interactions for reduced leaching under higher pressure differentials. Synthetic routes to achieve this task involved a sequential polymerization of isoprene and ethoxy ethyl glycidyl ether (EEGE) monomers. Polymerization of EEGE to yield high molecular weight linear blocks proved to be extremely challenging due to the undesirable chain transfer reaction tendency of EEGE monomer. A great deal of research effort was spent characterizing various anionic reaction conditions and developing measures aimed at suppressing

chain transfer. While ultimately unsuccessful, the results of these studies provide significant insight into the challenges of forming high molecular weight linear polyglycidols and will hopefully provide inspiration for the development of future synthetically successful strategies. A series of proof of concept experiments for transforming alcohol functionalities on this polymer system to imidazolium was also completed successfully.

The dissertation concludes with a final project completed outside the main objective of the dissertation - a morphological characterization of a series of thermoplastic elastomers with unique molecular architectures. This work is reported separately in the appendix I.

TABLE OF CONTENT

ABSTRACT.....	ii
CHAPTER 1	1
PERSPECTIVE OF THE DISSERTATION	1
CHAPTER 2	4
INTRODUCTION TO THE THESIS.....	4
2.1 MOTIVATION.....	4
2.2 BACKGROUND	9
2.2.1 The basic membrane structure	9
2.2.2 The origins of the spherical morphology in block copolymers.	11
2.3 FUNDAMENTALS OF GAS SEPARATION MEMBRANES.....	12
REFERENCES	15
CHAPTER 3	18
ELASTIC FREE-STANDING RTIL COMPOSITE MEMBRANES FOR CO ₂ /N ₂ SEPARATION BASED ON SPHERE-FORMING TRIBLOCK/DIBLOCK COPOLYMER BLENDS.....	18
3.1 INTRODUCTION	18
3.2 EXPERIMENTAL.....	23
3.2.1 Materials	23
3.2.2 Membrane fabrication and characterization.....	24
3.2.2.1 Fabrication	24
3.2.2.2 Characterization	25
3.2.3 Single-gas permeation testing on membranes.....	25
3.2.4 Mechanical testing.....	27
3.2.4.1 Uniaxial tensile strength testing.....	27
3.2.4.2 Unconfined compression testing.....	28
3.3 RESULTS AND DISCUSSION	28
3.3.1 Material synthesis and membrane fabrication	28
3.3.2 Gas Separation Performance.....	32
3.3.2.1 CO ₂ /N ₂ Permeation and Separation Performance.....	32
3.3.3 Mechanical Performance	35
3.3.4 Additional Operational Considerations.....	40
3.3.4.1 Effect of Transmembrane Pressure on CO ₂ /N ₂ Separation Performance	40
3.3.4.2 Performance Longevity.....	42
3.4 Conclusions.....	44
3.5 Author Information	45
REFERENCES	46
CHAPTER 4	51
FEASIBILITY STUDY OF PHOTO CROSS-LINKED POLYISOPRENE AS A REPLACEMENT FOR POLYSTYRENE IN SO/SOS MEMBRANES	51

4.1 INTRODUCTION	51
4.2 EXPERIMENTAL.....	53
4.2.1 Materials and Methods.....	53
4.2.2 Physical and Analytical Measurements	54
4.2.3 Dynamic Mechanical Spectroscopy.....	55
4.2.4 Small Angle X-Ray Scattering (SAXS).....	55
4.2.5 ω -hydroxy-polyisoprene (PIOH)	56
4.2.6 ω -hydroxy-polyisoprene-b-poly(ethylene oxide)(PI-PEO)	56
4.2.7 ω -hydroxy-polyisoprene-b-poly(ethylene oxide)- ω -hydroxy- polyisoprene (PI-PEO-PI).....	57
4.2.8 Standard procedure for epoxidized polyisoprene-b-poly(ethylene oxide)-polyisoprene.....	57
4.2.9 General procedure for preparing samples for photocuring.....	58
4.3 RESULTS AND DISCUSSION.....	58
4.3.1 Block copolymer blend synthesis and characterization.....	58
4.3.2 Epoxidation of block copolymer blends and characterization.....	65
4.3.3 Photo cross-linking and swelling studies on each block copolymer blend.....	71
4.3.3.1 IOI25	71
4.3.3.2 PIOH	76
4.3.3.3 IOI22.....	80
4.3.3.3 IOI46.....	84
4.4 CONCLUSIONS.....	87
REFERENCES	90
CHAPTER 5	92
INVESTIGATION OF ALTERNATIVE MATERIALS FOR	92
CO ₂ /N ₂ SEPARATION MEMBRANES	92
5.1 INTRODUCTION	92
5.2 BCP SYSTEM 1 – P(NBe)-P(NBC ₆ MIM)/ P(NBe)-P(NBC ₆ MIM)-P(NBe).....	96
5.2.1 Experimental Procedures	99
5.2.1.1 Materials and General Procedures	99
5.2.1.2 Synthesis of (1R, 4R)-oxiran-2-ylmethyl bicyclo[2,2,1]hept-5-ene-2-carboxylate (monomer 1).....	99
5.2.1.3 Polymerization of (1R, 4R)-oxiran-2-ylmethyl bicyclo[2,2,1]hept-5-ene-2-carboxylate (monomer 1).....	100
5.2.1.4 Molecular characterization of synthesized products.....	100
5.2.2 Material Characterization and discussion	101
5.2.3. Summary of progress on the investigation of BCP system 1.....	105
5.3 BCP SYSTEM 2 – (ePI)-P(EOemim) / (ePI)-P(EOemim)- (ePI)	105
5.3.1 Experimental Section.....	111
5.3.1.1 Materials and Methods.....	111
5.3.1.2 Physical and Analytical Measurements	112
5.3.1.3 EEGE monomer synthesis and purification.....	113
5.3.1.4 Standard anionic polymerization procedure for EEGE with PIOH as macro-initiator.....	113
5.3.1.5 De-protection of poly(EEGE) to yield Polyglycidol (PG).....	114

5.3.1.6 De-protection of poly(EEGE) on PI- <i>b</i> -P(EO- <i>stat</i> -EEGE) to yield PI- <i>b</i> -P(EO- <i>stat</i> -G)	114
5.3.1.7. Summary of polymerizations attempted to yield the high molecular weight linear polyglycidols block copolymers	116
5.3.1.8 Modification of terminal hydroxyl group on PIOH with imidazolium.....	119
5.3.1.8.1 Mesylation of PIOH.....	119
5.3.1.8.2 Imidazole modifications of mesylated PI.....	119
5.3.2 Results and Discussion	120
5.3.2.1 Investigation of synthetic strategies for integrating pendant hydroxyl functionality to SOS and IOI polymer systems.	120
5.3.2.2 Deprotection of the PEEGE to yield PG.....	147
5.3.2.3 Functionalization of PIOH with imidazolium.....	149
5.4 CONCLUSIONS AND RECOMMENDATIONS FOR RELEVANT FUTURE WORK	150
REFERENCES	152
CHAPTER 6	155
SUMMARY OF THE DISSERTATION AND FUTURE DIRECTIONS	155
6.1 MAJOR RESULTS AND RECOMMENDATIONS FOR FUTURE STUDIES.....	155
APPENDIX I	159
THE ROLE OF ARCHITECTURE IN THE MELT-STATE SELF ASSEMBLY OF (POLYSTYRENE) _{star} - <i>b</i> -P(ISOPRENE) _{linear} - <i>b</i> -(POLYSTYRENE) _{star} POM-POM TRIBLOCK COPOLYMERS.....	159
A.1 Introduction.....	159
A.2 Experimental	162
A.3 Results and Discussion.....	167
A.4 Conclusions.....	191
REFERENCES	193
SUPPORTING INFORMATION I.....	198
REFERENCES	210
ADDENDUM I.....	211
ADDENDUM II.....	222
ADDENDUM III	225
SUPPORTING INFORMATION II	228
REFERENCES	236
COMMON ABBREVIATIONS AND CHEMICAL STRUCTURES USED WITHIN DISSERTATION	237

CHAPTER 1

PERSPECTIVE OF THE DISSERTATION¹

The purpose of this introductory chapter is to provide context and perspective for the research involved in completing this dissertation. There are four main projects described within: 1) Development of mechanically robust and efficient membranes and membrane materials for separating CO₂ from CO₂ and N₂ mixtures based on polystyrene (PS, or S) and polyethylene oxide (PEO, or O) block copolymer (BCP) systems (Chapter 3), 2) Feasibility study of photo cross-linked polyisoprene as a replacement for polystyrene in SO/SOS membranes (Chapter 4), 3) Alternative matrix materials for enhancing the overall performance of the separation membranes (Chapter 5), 4) Morphological characterization of PS(star)-*b*-PI(linear)-*b*-PS(star) thermoplastic BCP system (Appendix I).

The primary objective of the dissertation was the development of mechanically robust and efficient membranes and membrane materials for separating CO₂ from CO₂ and N₂ mixtures. The importance and relevance of this research focus to the present time, the deficiencies of existing solutions, and an overview of the current state of the art in this area are discussed in Chapter 2. A conceptual background describing the proposed membrane materials and the main theories used to evaluate the gas separation performance of these membranes are also discussed in Chapter 2.

¹ The contents of this dissertation chapter were written by Dilanji B. Wijayasekara.

Chapter 3 contains a manuscript published in *Journal of Membrane Science* on novel membranes developed using a polystyrene based block copolymer system). Chapter 3 followed with supporting information and an addendum (I), which documents the detailed experimental protocols used for evaluating the gas separation performance of the membranes.

Chapter 4 describes efforts to improve the thermal and chemical stability of the CO₂ separation membranes developed in Chapter 3, through replacement of the thermoplastic, glassy PS component with chemically cross-linked PI blocks. Ultimately, the epoxidation chemistry explored as a crosslinking strategy created new challenges that made retaining the mechanical integrity of the membrane difficult. However, the findings from these studies suggest a number of promising alternative routes that support future studies in this area.

Chapter 5 consists of two parts, both focused on determining the synthetic feasibility of new BCP systems intended to be used as SO/SOS membrane replacement materials. The first BCP system investigated was based on ring opening metathesis polymerization (ROMP) of norbornene monomer derivatives. Ultimately, the very poor yields after monomer purification and the challenges encountered in product characterization led to a decision to discontinue this project at an early stage. A second BCP system explored was based on anionically polymerized linear polyglycidols. The preliminary findings from these studies (described in detail) document the difficulties in obtaining high molecular weight materials. However, there appears to be considerable promise in these new systems with a small amount of future development.

Finally, the dissertation also contains a manuscript submitted to *Macromolecules* on a study of morphological characterization of thermoplastic elastomers with uniquely architected macromolecules. The research focus of this study was independent from the main objective of the dissertation and has been included as Appendix (I).

Some of the work in this dissertation was collaborative. Delineation of all research within this dissertation can be found at the beginning of each chapter.

CHAPTER 2

INTRODUCTION TO THE THESIS²

2.1 MOTIVATION

With the increase in conventional energy consumption in the past century^[1], the emission of anthropogenic CO₂ to the atmosphere has risen dramatically. Using Arctic ice core data^[2] it has been discovered that the atmospheric CO₂ concentration only changed slightly over the millennium prior to the 20th century, from 228 ppmv (parts per million by volume) in 1000 to 295 ppmv in 1900, However, the levels have since increased to 315 ppmv in 1958 and further to 337 ppmv in 2004 based on recent atmospheric analysis in Hawaii^[3]. This data indicates the rate of increase of CO₂ concentration in atmosphere in past century has been five times that experienced over the previous millennium. As a consequence, there is serious concern over associated irreversible global climate change including global warming ^[4, 5]. Efficient CO₂ capture and sequestration is now considered mandatory if the impacts to our environment are to be minimized. In addition to environmentally motivated CO₂ separations solutions, cost effective methods of CO₂ separation from light gas mixtures is of great industrial interest due to its commercial importance in a number of applications, including enhanced oil recovery (EOR) and firefighting ^[6].

² The contents of this dissertation chapter were written by Dilanji B. Wijayasekara.

In a global context, among all the industries emitting CO₂, fossil-fueled power plants are by far the largest producer, accounting for an estimated 33 - 40 percent of the total^[7] through the emission of flu gas (CO₂/N₂ gas mixture) as the combustion waste product^[8, 9]. The conventional industrial scale technology widely developed for separating CO₂ from flue gas is aqueous amino scrubbing. This technique produces the high purity levels of the processed gases required but at costs^[8-11] and energy requirements that are prohibitive for its wide-spread implementation. Cryogenic distillation, physical solvent absorption, pressure swing adsorption and membrane-based processes are other technologies being considered for separating CO₂ from light gas mixtures^[8-11]. Among these, membrane technology is currently being investigated at the pilot plant scale as a promising alternate solution for separating CO₂ from flue gas. Membrane technology offers advantages in terms of lower operating energies, modular scalability, a small physical footprint, and the elimination of a dependence on volatile chemicals^[9]. However, the biggest challenge for advancing membrane technology as a solution is the absence of membrane materials that possess the CO₂ separation performance (permeability and selectivity) in combination with the mechanical strength to meet demands of high volume industrial processing.

Current research on membrane technologies for CO₂ separation has focused on four types of membranes: 1) solid polymer membranes including polymerized room temperature ionic liquids^[12-14]; 2) supported liquid membranes (SLM)^[8, 15]; 3) composite membranes that have a selective layer and a supportive layer^[16, 17] and 4) gelled membranes^[18, 19]. In the past decade, room temperature ionic liquids (RTILs) have become the key component in all four types of membranes. The popularity of RTILs in CO₂ separation applications over other volatile organic solvents^[20] is a product of their intrinsically negligible vapor pressure, low flammability, and thermal and chemical stability. However, the most prominent characteristic of RTILs driving

their application as key ingredients in membrane-based CO₂ separations, is their outstanding separation performance when compared with existing materials. Such comparisons are most convincingly presented using the so-called Robeson plot, named for Lloyd Robeson who developed the plot to demonstrate the clear flux-selectivity tradeoff intrinsic to gas separation materials. The Robeson plot, for a selected gas pair, juxtaposes on a single plot the permselectivity vs. the permeability for different membrane materials. An example of a typical Robeson style plot is shown in Figure 2.1. As shown in the plot, RTILs generically fall in the right most region of the plot, with excellent permeabilities (expected for liquids) coupled with excellent permselectivity.

The attractiveness in RTILs as a class of liquids is the wide range of cation and anion choices available for tuning the material properties exhibited. The most studied RTILs for CO₂ separation are ionic liquids with imidazolium-based cations, and these have exhibited excellent CO₂ permeabilities in the 800-1000 barrer range and selectivities for CO₂/N₂ anywhere from 20 to as high as 90^[8, 21]. Common counter ions used with imidazolium based cations are triflate (OTf), dicyanamide (dca), tetrafluoroborate (BF₄), hexafluorophosphate (PF₆) and bis(trifluoromethane)-sulfonimide (Tf₂Nor TFSI)^[8, 12, 22, 23]. Figure 2.1 shows a Robeson plot used to compare the CO₂/N₂ separation performance of several membrane materials^[19], highlighting several RTIL-based materials proposed in the last decade. According to Figure 2.1, neat RTIL (generically speaking) has the highest perm-selectivity and CO₂ permeability pairing suggesting it may be the best candidate for CO₂ separation from N₂. However, the problem lies in its inability to be cast as a mechanically robust membrane introducible into traditional membrane modules. SLMs are the most common configuration proposed for introducing free RTIL into a membrane configuration; i.e., by simply wetting an existing solid porous membrane

support with RTIL. Even though this arrangement allows RTIL to perform as a liquid in which its selectivity and permeability are largely maximized, such supported membranes cannot withstand typical operating transmembrane pressure differentials without suffering from RTIL “blowout” or leakage placing considerable doubt on their viability for industrial implementation. In recognition of such limitations, strategies to generate solid-phase membranes from polymerizable RTIL-based monomers have been pursued, in an attempt to retain the RTIL selectivity while imparting mechanical strength to the system. However, the performance of such poly(RTIL) membranes so far has been plagued by a drastic loss in permeability, and in some cases, the CO₂ selectivity, relative to the neat RTIL (Figure 2.1).

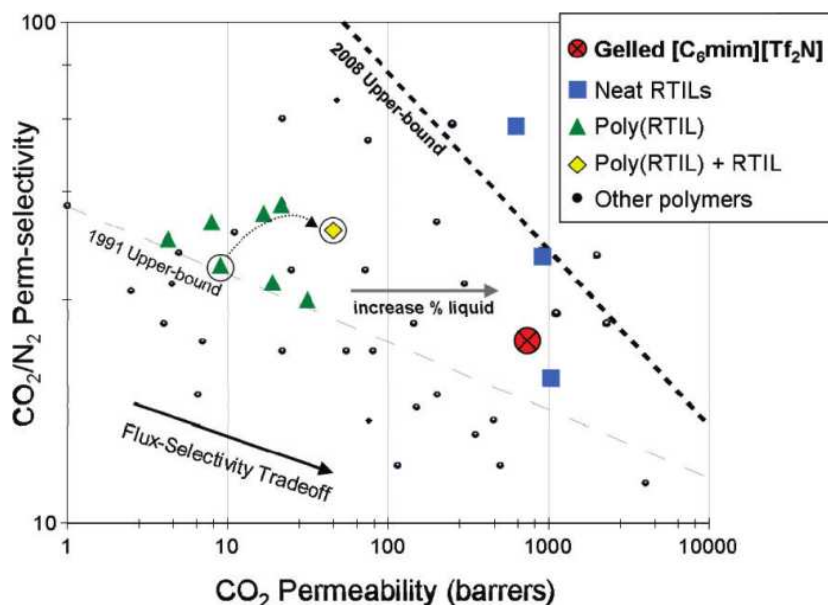


Figure 2.1 A Robeson style plot comparing CO₂ and N₂ transport properties of various dense membrane materials. Notably, the poly(RTIL)-RTIL and gelled RTIL composites, discussed in the text, sit below the empirical upper bound for dense materials.^[19]

Ultimately, such approaches may still be successful if the poly(RTILs) produced can be synthetically designed to possess high chain mobilities, like those intrinsic to polysiloxane based

membrane materials. So far this has not proven possible. The obvious compromise are Poly(RTIL)-RTIL composite membranes, in which researchers try to combine the desired mechanical strength of solid-phase poly(RTIL)s, with the liquid-like transport properties of neat RTIL, in chemical configurations that can be developed into a traditional membrane units. Two examples of composite membranes recently developed are one that incorporates a neat RTIL component within a polymer matrix formed using photo-cross-linkable gemini RTILs (GRTIL)^[23], and one that was constructed via gelation of a neat RTIL with a small molecule gelator (hydroxystearic acid)^[19]. Both approaches produce composite membranes showing a promising improvement in overall performance compared to poly(RTIL) membranes alone^[22]. However, the performance still places these materials below the 2008 upper bound suggested by Robeson as the benchmark for new materials (Figure 2.1). Ultimately, despite increased separation factors compared to SILMs and improved mechanical strength, these materials continued to show compromised permeability associated with the reduced mobility of the RTIL matrix. Considering each of these results, it seems realistic to conclude that the primary factor challenging the emergence of CO₂ separation membranes as a viable large-scale separations technology is the common issue of simultaneously combining the necessary separation performance (as defined by proximity to the Robeson upper bound) with the necessary mechanical strength required for industrial implementation.

In specific terms, the “ideal” CO₂ separation membrane material would be economically manufacturable as a mechanically robust membrane compatible with current membrane module technologies. It would possess high CO₂ selectivity (> 30) over other light gases of concern, combined with permeabilities approaching if not exceeding 1000 barrer^[9]. It would have high thermal and chemical tolerance, exhibit resistance to physical aging or CO₂ plasticization^[9, 10]

and have an extended operating lifetime. The overriding objective of this thesis was to explore the strategic synthesis of novel membrane materials designed to achieve many of these idealized constraints.

2.2 BACKGROUND

2.2.1 The basic membrane structure

The premise of this thesis project is based on the hypothesis that a membrane structure based on a three-dimensionally periodic, tethered-micelle network designed to absorb large quantities of neat RTIL would also provide the necessary mechanical framework to required to achieve efficient CO₂ separation when cast as a thin membrane film. Ideally the network proposed was to be designed such that neat RTIL would comprise more than 90% of the membrane volume at swelling equilibrium. Figure 2.2 summarizes the proposed membrane structure previously developed in our group for hydrogel applications, in which aqueous media was used to swell the network. The basic structure is formed by preserving a melt state self-assembled nanostructure of sphere-forming AB diblock and ABA triblock copolymer blend, followed by swelling. In the proposed variation, the swelling was to be performed using CO₂ selective RTILs instead of water.

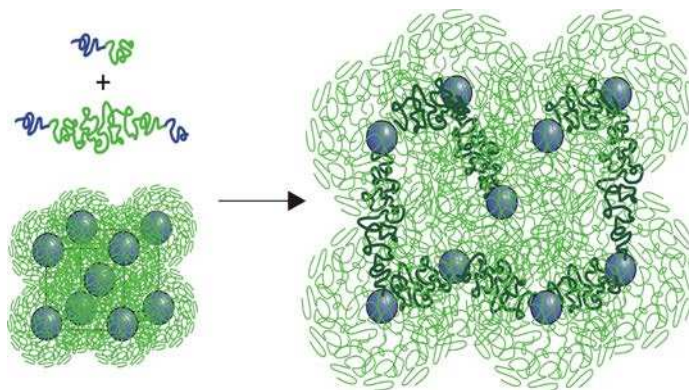


Figure 2.2 Schematic of proposed membrane structure; right side shows the swollen structure still holding the original shape^[24]

The schematic diagram of Figure 2.2 shows two populations of block copolymers key to formation of the network: an AB diblock copolymer and an ABA triblock copolymer. Here, the blue chains represent A blocks that by synthetic design (controlling block volume fraction) form into spherical aggregates when the blend of block copolymers is heated to the melt-state (without solvent). The green chains represent B blocks that by necessity form coronal brush layers emanating radially from the spherical domains. The B blocks associated with the ABA triblock copolymer population are a part of the coronal brush layer, but can act to bridge adjacent spherical domains. In the system proposed for these studies, the A blocks were chosen to be polystyrene (PS), such that the spherical domains would vitrify upon cooling from the melt. The B blocks were chosen to be PEO, which has been shown to be soluble in a number of RTIL solvents. Introduction of the RTIL selectively swells the coronal matrix surrounding the vitrified (and non-soluble) PS spheres, producing the expanded structure shown in the right of Figure 2.2. In that image, the bridging B blocks are highlighted in dark bold to emphasize the connections between spheres produced in the final swollen material. One of the caveats of this strategy for network formation is the inability to keep the ABA triblock copolymer from looping back into the same spherical domain. However, it has been predicted that bridging to looping ratios in

spherical block copolymer morphologies are typically at least 3:1. Ultimately, the fraction of ABA triblock copolymer in the blend determines the mechanical connectivity across the entire material. Typical sizes of the spherical domains in this work are around 20 nm in diameter, with each spherical aggregate comprised of approximately 200 - 220 polymer chains (A blocks). While these numbers and domain sizes are dependent on the overall molecular weights chosen for the block copolymers, attempts to vary those parameters were not investigated in this work.

2.2.2 The origins of the spherical morphology in block copolymers.

The basic membrane structure discussed in the previous section is based on exploiting the ability of specifically designed block copolymer (BCP) systems to adopt the spherical morphology described in Section 2.2.1 and Figure 2.2. BCP systems inherit the ability to self-assemble into a range of defined, periodic morphologies from the covalently forced juxtaposition of two polymer chains that possess an intrinsic thermodynamic incompatibility. This covalent bond restricts phase separation to length scales that mimic the spatial dimensions of polymer chain, resulting in a range of microphase separated structures with periodic compositional heterogeneities on the nanometer length scale^[25]. The competitive balance between interfacial segment-segment contact and the chain-stretching dictate the self-selection of the lowest free energy ordered state morphology. Figure 2.3 shows pictorial examples of the four unique morphologies formed, along with the theoretical phase diagram of morphologies predicted using self-consistent field calculations for a generalized AB BCP system^[26]. The four equilibrium structures (Figure 2.3a) that have been observed in AB/ABA BCP melt systems are the lamellar structure (L), hexagonally packed cylinders (Hex), a complex bicontinuous gyroid network (G),

and body-centered-cubic spheres (BCC)^[26]. The free energy landscape governing that balance produces morphologies in ordered AB/ABA BCP systems that primarily depends on the relative volume fraction of each block in the block copolymer (f), such that most of the phase boundaries shown in Figure 2.3 are vertical. The determination of whether a particular system phase separates or not, often described as the degree of segregation between the A and B segments, has been shown to be dependent on the volume fraction, in combination with the product of the degree of polymerization (N) and the effective interaction parameter per segment (χ)^[27].

The sphere morphology targeted in this work (BCC) requires compositionally asymmetric molecules with the volume fractions of the minority component (f_{ps}) in the 0.09 - 0.13 range^[25]. Practically speaking, the BCC lattice depicted in Figure 2.3 is difficult to achieve in high molecular weight systems, because of the kinetic limitations associated with inter-sphere chain diffusion and chain entanglements. As such, essentially all the systems studied in this work adopt the spherical domain structure but fail to organize the spheres into the BCC lattice. Instead, the spheres adopt a structure often described as liquid-like packing (LLP), which has been characterized in detail using numerical fits to SAXS data. Importantly, the LLP of spheres has no impact on the ability of triblock copolymer to bridge between spherical domains, and network connectivity is unaffected by this minor degree of system disorder.

2.3 FUNDAMENTALS OF GAS SEPARATION MEMBRANES

For purposes of this thesis, a membrane is simply defined as a discrete thin interface that moderates the permeation of chemical species in contact with it. There are mainly two types of

membranes, isotropic and anisotropic. Isotropic membranes have homogeneous structure across the thickness and the anisotropic membranes do not. These two types of membranes can be further categorized into two groups: porous and non-porous. Isotropic porous membranes, as the names implies have interconnected pores of same size throughout its thickness. On the other hand, anisotropic porous membranes have pore size distributions varying along the thickness. Non-porous membranes, just as the name implies do not have pores, and have a different permeation mechanism than the porous membranes, which we will discuss later in this thesis (Chapter 3). These nonporous membranes are also called “dense” membranes, are typically made of polymeric materials, and can be recognized as isotropic^[28].

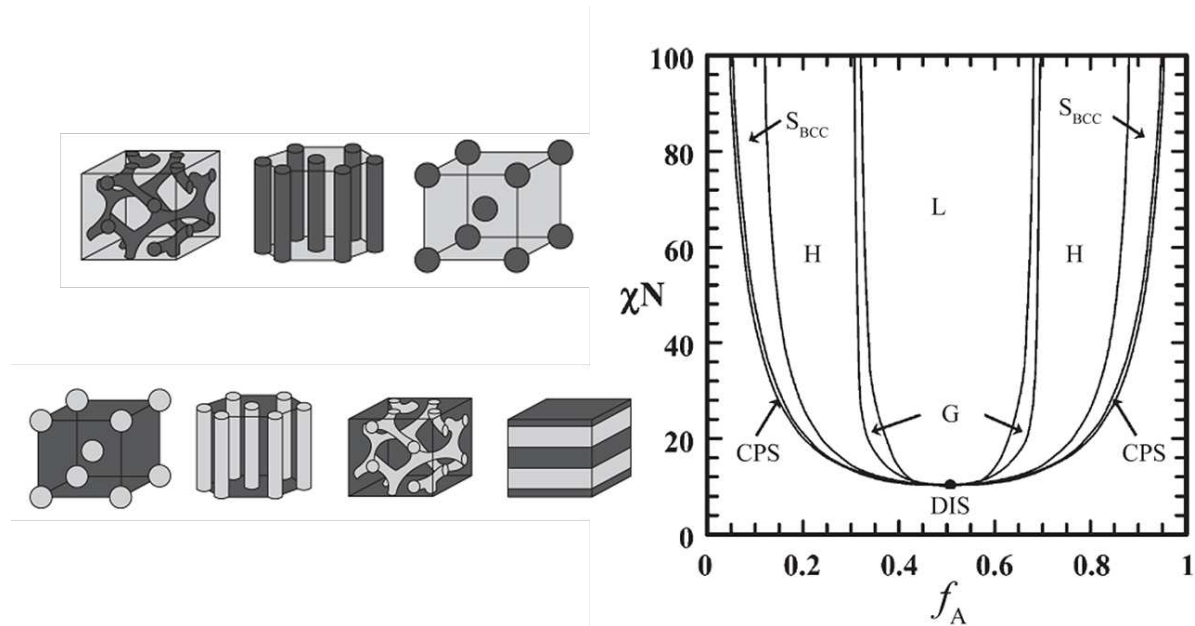


Figure 2.3 (left) Schematic diagrams of AB diblock copolymer that self-assembled structures corresponding to the equilibrium phases shown in the phase diagram to the right.^[26] (right) Calculated self-consistency field theory (SCFT) phase diagram for a linear AB diblock copolymer. Reproduced from reference^[26]

Depending on the type of the membrane, porous or non-porous, different models of permeate transport are used for calculation of species permeability through a membrane.

Transport of permeate through a porous membrane is typically assumed to follow the *pore-flow model*^[29], in which permeants are transported by pressure-driven convective flow through the interconnected pores. Porous gas separation membranes separate species mainly by two mechanisms. First is known as molecular sieving. If the pores of the membrane are of the order of molecular size for some of the components in the feed mixture, the diffusion of those components will be hindered, resulting in enhanced separation. Molecules of size larger than the pores will be prevented altogether from diffusing through the pores. The second mechanism is called *Knudson diffusion*. This is a special case in gas diffusion, where the pore size and/or pressure is such that the mean free path (defined as the average distance traversed by gas molecules between collisions) of the molecules is greater than the pore diameter. This difference creates a size based diffusion rate dependence that can create opportunities for preferential transport of one of the gases.

Transport of permeates through non-porous (dense) gas separations membranes follows the *solution-diffusion* model, in which permeants dissolve in the membrane material and then diffuse through the membrane down a concentration gradient. The permeants are separated because of the differences in the solubilities of the species in the membrane and the differences in the rates at which the species diffuse through the membrane. Light gas separation membranes discussed in this project are categorized as non-porous, isotropic dense membranes. Hence, calculation of the permeability and selectivity of a particular species for the proposed membranes is determined using solution diffusion model. The details of these types of calculations are included in Chapter 3.

REFERENCES

- [1] C. Song, Global challenges and strategies for control, conversion and utilization of CO₂ for sustainable development involving energy, catalysis, adsorption and chemical processing, *Catalysis Today*, 115 (2006) 2-32.
- [2] C.D. Keeling, T.P. Whorf, Atmospheric CO₂ records from sites in the SiO air sampling network in trends :A Compendium of Data on Global Change. , in: *Carbon Dioxide Information Analysis Center, Oak Ridge National Laboratory, U. S. Department of Energy, Oak Ridge, TN, USA, 2005.*
- [3] D.M.S. Etheridge, L.P.; Langenfelds, R. L.; Francey, R.J.; Barnola, J. M; Morgan, V. I.; , Historical CO₂ record from the Law Dome DE08, DE08-2, and DSS ice cores (atmospheric CO₂ concentrations, Antarctic ice cores). in: *A Compendium of Data on Global Change, on line at the Carbon Dioxide Information Analysis Center, June 1998.*
- [4] C.M.S. White, B. R.; Granite, E. J.; Hoffman, J. S.; Pennline, H. W. , Separation and capture of CO₂ from large stationary sources and sequestration in geological formations--coalbeds and deep saline aquifers., *J. Air Waste Manage. Assoc. , 53 (2003) 645-715.*
- [5] H.D. Herzog, E. , CO₂ Capture, Reuse and Storage Technologies for Mitigating Global Climate Change., in, *Pittsburgh, PA, 1999.*
- [6] X.S. Xu, C.; Wincek, R.; J Andresen, J. M.; Miller, B. G.; Scaroni, A. W.; Separation of CO₂ from power plant flue gas using a novel CO₂ “molecular basket” adsorbent. , *Fuel Chemistry Division Preprints, 48 (2003) 163.*
- [7] E.S. Rubin, C. Chen, A.B. Rao, Cost and performance of fossil fuel power plants with CO₂ capture and storage, *Energy Policy, 35 (2007) 4444-4454.*
- [8] J.E. Bara, T.K. Carlisle, C.J. Gabriel, D. Camper, A. Finotello, D.L. Gin, R.D. Noble, Guide to CO₂ Separations in Imidazolium-Based Room-Temperature Ionic Liquids, *Industrial & Engineering Chemistry Research, 48 (2009) 2739-2751.*
- [9] C.W. Jones, CO₂ Capture from Dilute Gases as a Component of Modern Global Carbon Management, *Annual Review of Chemical and Biomolecular Engineering, 2 (2011) 31-52.*
- [10] A. Brunetti, F. Scura, G. Barbieri, E. Drioli, Membrane technologies for CO₂ separation, *Journal of Membrane Science, 359 (2010) 115-125.*
- [11] M. Radosz, X. Hu, K. Krutkramelis, Y. Shen, Flue-Gas Carbon Capture on Carbonaceous Sorbents: Toward a Low-Cost Multifunctional Carbon Filter for “Green” Energy Producers†, *Industrial & Engineering Chemistry Research, 47 (2008) 3783-3794.*

- [12] J. Tang, Y. Shen, M. Radosz, W. Sun, Isothermal Carbon Dioxide Sorption in Poly(ionic liquid)s, *Industrial & Engineering Chemistry Research*, 48 (2009) 9113-9118.
- [13] J.E. Bara, C.J. Gabriel, S. Lessmann, T.K. Carlisle, A. Finotello, D.L. Gin, R.D. Noble, Enhanced CO₂ Separation Selectivity in Oligo(ethylene glycol) Functionalized Room-Temperature Ionic Liquids, *Industrial & Engineering Chemistry Research*, 46 (2007) 5380-5386.
- [14] J.T. Tang, H.; Sun, W.; Radosz, M.; Shen, Y. , Poly(ionic liquid)s as new materials for CO₂ absorption, *Journal of Polymer Science Part A: Polymer Chemistry*, 43 (2005) 5477-5489.
- [15] J. Ilconich, C. Myers, H. Pennline, D. Luebke, Experimental investigation of the permeability and selectivity of supported ionic liquid membranes for CO₂/He separation at temperatures up to 125°C , *Journal of Membrane Science*, 298 (2007) 41-47.
- [16] T.K. Carlisle, E.F. Wiesenauer, G.D. Nicodemus, D.L. Gin, R.D. Noble, Ideal CO₂/Light Gas Separation Performance of Poly(vinylimidazolium) Membranes and Poly(vinylimidazolium)-Ionic Liquid Composite Films, *Industrial & Engineering Chemistry Research*, 52 (2013) 1023-1032.
- [17] P.T. Nguyen, E.F. Wiesenauer, D.L. Gin, R.D. Noble, Effect of composition and nanostructure on CO₂/N₂ transport properties of supported alkyl-imidazolium block copolymer membranes, *Journal of Membrane Science*, 430 (2013) 312-320.
- [18] T.K. Carlisle, G.D. Nicodemus, D.L. Gin, R.D. Noble, CO₂/light gas separation performance of cross-linked poly(vinylimidazolium) gel membranes as a function of ionic liquid loading and cross-linker content, *Journal of Membrane Science*, 397–398 (2012) 24-37.
- [19] B.A. Voss, J.E. Bara, D.L. Gin, R.D. Noble, Physically Gelled Ionic Liquids: Solid Membrane Materials with Liquidlike CO₂ Gas Transport, *Chemistry of Materials*, 21 (2009) 3027-3029.
- [20] M.N. Koel, *Ionic liquids in chemical analysis*, CRC press, Boca Raton, 2009.
- [21] D. Camper, J. Bara, C. Koval, R. Noble, Bulk-Fluid Solubility and Membrane Feasibility of Rmim-Based Room-Temperature Ionic Liquids, *Industrial & Engineering Chemistry Research*, 45 (2006) 6279-6283.
- [22] D. Camper, J.E. Bara, D.L. Gin, R.D. Noble, Room-Temperature Ionic Liquid–Amine Solutions: Tunable Solvents for Efficient and Reversible Capture of CO₂, *Industrial & Engineering Chemistry Research*, 47 (2008) 8496-8498.
- [23] J.E. Bara, E.S. Hatakeyama, D.L. Gin, R.D. Noble, Improving CO₂ permeability in polymerized room-temperature ionic liquid gas separation membranes through the formation of a solid composite with a room-temperature ionic liquid, *Polymers for Advanced Technologies*, 19 (2008) 1099-1581.

- [24] C. Guo, T.S. Bailey, Highly distensible nanostructured elastic hydrogels from AB diblock and ABA triblock copolymer melt blends, *Soft Matter*, 6 (2010) 4807-4818.
- [25] F.S.F. Bates, Block Copolymers—Designer Soft Materials, *Phys. Today*, (1999) 32.
- [26] E.W. Cochran, C.J. Garcia-Cervera, G.H. Fredrickson, Stability of the Gyroid Phase in Diblock Copolymers at Strong Segregation, *Macromolecules*, 39 (2006) 2449-2451.
- [27] N.A. Lynd, M.A. Hillmyer, Influence of Polydispersity on the Self-Assembly of Diblock Copolymers, *Macromolecules*, 38 (2005) 8803-8810.
- [28] A. Sengupta, K.K. Sirkar, Chapter 11 Analysis and design of membrane permeators for gas separation, in: D.N. Richard, S.A. Stern (Eds.) *Membrane Science and Technology*, Elsevier, 1995, pp. 499-552.
- [29] W.S. Ho, K.K. Sirkar, *Membrane Handbook*, 1992 ed., Springer, New York, 1992.

CHAPTER 3

ELASTIC FREE-STANDING RTIL COMPOSITE MEMBRANES FOR CO₂/N₂ SEPARATION BASED ON SPHERE-FORMING TRIBLOCK/DIBLOCK COPOLYMER BLENDS³

3.1 INTRODUCTION

Anthropogenic CO₂ emissions have been linked to climate change and ocean acidification, phenomena which have been predicted to have significant adverse global consequences in both the short- and long-term^[1]. Significant reduction, sequestration, or recycling of these anthropogenic CO₂ emissions will help to mitigate or delay such consequences. One of the most realistic strategies for reducing worldwide CO₂ emissions is to capture and sequester CO₂ from large point sources such as coal-fired electric power plants^[2-5]. CO₂ is emitted from coal-fired power plants as part of a mixture called ‘flue gas’ which contains 10-15% CO₂ along with N₂ (70-80%), H₂O, O₂, and other trace gases. In order to efficiently sequester or recycle CO₂, it must first be separated from the flue gas mixture.

³ The contents of this dissertation chapter have been adapted from the publication published in Journal of Membrane Science in 2016. The development, fabrication and mechanical testing of the membranes were performed by Dilanji Wijayasekara. The synthesis of membrane materials was performed by Dilanji Wijayasekara and Jackson Lewis. The synthesis of ionic liquid and gas permeation testing was performed by Matthew G. Cowan (University of Colorado, Boulder). The manuscript and adapted dissertation chapter was written by Dilanji Wijayasekara with collaborative editing of authors Matthew G. Cowan, Douglas L. Gin, Richard D. Noble (University of Colorado, Boulder) and Travis S. Bailey.

Existing technologies for the separation of CO₂ from flue gas include aqueous amine scrubbing, pressure swing absorption, and cryogenic distillation^[6]. The implementation of these technologies currently requires approximately 30% of the energy produced by the power plant, making them economically unsustainable^[7]. Membrane-based alternatives are currently being investigated at the pilot plant scale as a superior solution for separating CO₂ from flue gas^[8]. Successful membrane technologies offer several advantages over traditional methods in terms of lower operating energies, modular scalability, a reduced physical footprint, and elimination of volatile chemicals^[9].

For successful application to flue gas separations, membranes must have high CO₂ permeance and reasonable CO₂/N₂ selectivities (≥ 20), be processable into defect-free thin films, have long operating lifetimes, and have reasonable production costs^[10-12]. As a starting point, new membrane materials are often screened by measuring single-gas permeability and selectivity, which are then compared with performance values of existing materials using comprehensive Robeson plots^[12, 13]. However, many of the other critical properties such as mechanical stability over time, processability into free-standing or stable thin films, and compatibility with current module configurations are often not addressed^[12].

Recently, composite membranes containing room-temperature ionic liquids (RTILs) have gained attention due to their high CO₂/N₂ selectivity, high CO₂ permeability, low volatility, and promising thermal and chemical stability^[14]. Examples of RTIL-based membrane materials include supported ionic liquid membranes (SILMs)^[15], ion gels^[16, 17], poly(ionic liquid) (poly(IL))/IL composites^[5, 18-20] and block copolymer/RTIL blends^[21-23]. Recent advances in polymerizing RTIL-containing monomers have also permitted direct incorporation of the ionic species into block copolymer architectures. While these systems offer an intrinsic ability to

produce distinct ionic and non-ionic domains through predictable phase separation on the nanometer length scale^[24-29], the dense polymer materials have significantly lower CO₂ permeability than composite materials that contain free RTIL^[28, 29].

Of the few examples of membranes based on block copolymer/RTIL blends reported to date^[21-23, 28, 29], all involve a shared fabrication strategy dependent on solvent-casting of a co-solution of block copolymer and RTIL into a porous support material. Gu et al.^[21, 22] and Rabiee et al.^[23] report CO₂/N₂ separation performances of their membranes to be slightly above the 2008 Robeson plot upper bound, showing the potential of block-copolymer-based materials to be used as efficient CO₂/N₂ separation membrane materials. However, the common disadvantage shared by these systems is the apparent compromise of mechanical integrity with increased RTIL loadings, a strategy used to improve the liquid-like character of the membrane and thus CO₂ permeabilities. In the case of Gu et al.^[21, 22], RTIL loadings approaching 85 wt% were handled by direct integration into a commercially available porous support (e.g., PVDF). In a subsequent publication, the mechanical properties of the composite were improved through chemical cross-linking of the polystyrene (PS) domains. However, no new gas measurements were included for these mechanically improved materials^[30].

Previously, we reported the ability to achieve highly swollen, yet highly elastic, mechanically robust hydrogels exploiting a *melt-assembled* (solvent-free) tethered micelle structure in a series of polystyrene-*b*-poly(ethylene oxide) diblock copolymer/polystyrene-*b*-poly(ethylene oxide)-*b*-polystyrene triblock copolymer (SO/SOS) blends^[31, 32]. Such melt-assembled, tethered micelle systems, once vitrified, have shown an ability to incorporate very high loadings of water (up to 97 wt%) while maintaining the mechanical properties of an elastic solid. Importantly, the ability of these sphere-forming AB/ABA block copolymer blends to

mechanically out-perform solution assembled ABA systems (such as those described by Gu et al.^[21, 22]) is a direct result of an improved micelle core integrity provided by the melt-assembly process, in combination with the ability of the dynamic entanglements in the dangling *diblock copolymer chain ends*^[32] to absorb stress reversibly throughout the network. An important advantage of this system is its ability to be formed into membrane sheets using traditional (thermoplastic) melt processing or coating techniques prior to the introduction of added free RTIL. Processibility as a thermoplastic is critical for low cost, high volume production consistent with large-scale implementation as an industrially viable separation material^[20].

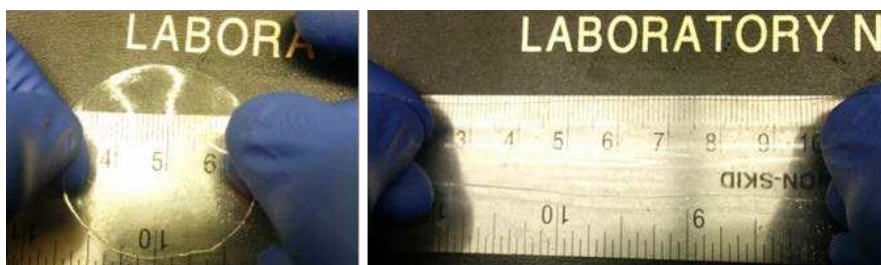


Figure 3.1 SO/SOS RTIL composite membranes containing ca. 95 wt% [EMIM][TFSI] (left). Membranes produced are highly elastic, with an ability to accommodate strains to nearly 300% without plastic deformation (right).

Herein, we describe an adapted preparation in which similarly formed tethered micelle networks based on SO/SOS blends were fabricated into free-standing thin films containing up to 95 wt% RTIL ([EMIM][TFSI]) (Figure 3.1). The selection of [EMIM][TFSI] was predicated on several important factors, including its ease of synthesis and purification in large quantities, considerable stability, and established performance in CO₂/N₂ separations^[14]. However, most critical to this application was the ability of [EMIM][TFSI] to be a very good solvent for PEO and a non-solvent for the vitrified PS cores, to promote swelling without loss of mechanical stability. Notably, this important characteristic happened to be a general feature of most

imidazolium-based RTILs, with selective swelling of the PEO matrix possible with a variety of alkyl (ethyl, hexyl) and diol substituted MIM cations and associated anions (TFSI, dicyanamide (DCA), tetrafluoroborate (BF₄))^[14, 33].

The CO₂/N₂ separation performance of these new composite RTIL-based membranes, measured as a function of transmembrane pressure differentials exceeding 400 kPa, exhibited figures of merit pushing the limits of the 2008 Robeson plot upper bound, while maintaining exceptional mechanical integrity as a free-standing film even in its swollen state. Included is an evaluation of the unique tensile and compressive properties of these RTIL composite membranes under cyclic loading conditions, as well as the extended CO₂/N₂ separation performance of these membranes over a period of 28 days. To our knowledge, there have been no prior reports of free-standing RTIL-based composite membranes prepared from melt-state processing of sphere-forming *diblock*/triblock copolymer blends swollen with RTIL that have been subsequently employed for light gas separations. Importantly, we believe the utilization of melt-state processing and self-assembly, in combination with the use of diblock copolymer as a significant blend component, dramatically enhances the future ability of RTIL-based composite membranes to mechanically compete as truly viable CO₂/light gas separation technologies.

3.2 EXPERIMENTAL

3.2.1 Materials

Ultra-high purity CO₂, N₂, and CH₄ gases (99.99%) used for membrane testing were purchased from Air Gas. The RTIL [EMIM][TFSI] was synthesized by adapting a previously reported procedure^[34]. Materials specific its synthesis can be found there. The SO diblock and SOS triblock copolymer blends (SOS22 and SOS46) were also synthesized according to previously reported procedures^[31, 32]. Reagents associated with these syntheses and their purification protocols can be found in the ESI. In brief, synthesis of the SO diblock copolymer (Mn = 107,000 g mol⁻¹, PDI = 1.07, f_{PS} = 0.085 (volume fraction PS)) was accomplished through sequential, step-wise anionic polymerization of styrene followed by ethylene oxide, exploiting a hydroxyl-functionalized polystyrene intermediate (Mn = 8370 g mol⁻¹, PDI = 1.03) as a macroinitiator^[31, 35]. The SOS22 and SOS46 blends were then formed through partial coupling of the SO diblock copolymer using dibromoxylene as a coupling agent, to generate blends containing 22 mol% and 46 mol% SOS triblock copolymer, respectively.

¹H NMR spectra (Figures S1 and S2, ESI) were collected at room temperature in CDCl₃ on a Varian Inova 400 MHz Spectrometer (n = 32, delay = 30 s). Size exclusion chromatography (SEC) (Figures S3 and S4, ESI) was performed on a Viscotek GPC-Max chromatography system fitted with three 7.5 × 340 mm PolyporeTM (Polymer Laboratories) columns in series, an Alltech external column oven, and a Viscotek differential refractive index (RI) detector. Measurements were performed using a DMF (55 °C) mobile phase (1 mL/min) with PS standards

(Polymer Laboratories). Final SO/SOS compositions were confirmed via relative peak integrations in the SEC chromatograms of these blends (Figure S4, ESI).

3.2.2 Membrane fabrication and characterization

3.2.2.1 Fabrication

Membranes were fabricated by sandwiching 0.05 g of the desired diblock/triblock copolymer blend between two Kapton sheets and pressed in a Carver, Inc. manual heating press at 10000 lbs force and 125 °C for 10 min. The Kapton-sandwiched membrane was then placed in a vacuum bag and re-pressed at the same pressure and temperature (22–24 °C) conditions for another 15 min under vacuum of 5 torr. The membrane was then allowed to cool to room temperature (15 min). This procedure was repeated three times for each membrane, during which the pressure was increased by 5000 lbs force in each successive press. After three vacuum-press cycles, defect-free polymer films ranging from 55–190 μm in thickness were obtained. These dry films were then swollen in an excess of [EMIM][TFSI] (vacuum-dried) for 20 h under vacuum at room temperature. The resulting RTIL-containing composite membranes were allowed to reach equilibrium swelling dimensions (about 20 h swelling time) before being removed from the RTIL and lightly patted dry with Kimwipes[®] to remove excess [EMIM][TFSI]. Membranes were then cut to 47-m- diameter discs using a punch prior to mounting in a Millipore[™] membrane testing fixture as part of our house-built time-lag permeability apparatus^[36].

3.2.2.2 Characterization

Thicknesses of the resulting dry and swollen RTIL composite membranes were measured using an ZeScope optical profilometer (Zygo, Middlefield, CT). ATR-IR measurements were performed using a Nicolet iS50 FTIR (16 scans, 2 cm⁻¹ resolution). Small angle X-ray scattering (SAXS) was used to characterize the melt-state morphology of the SOS22 and SOS46 blends. SAXS data were collected on a Rigaku S-Max 3000 High Brilliance 3 Pinhole SAXS system outfitted with a MicroMax-007HFM Rotating Anode (Cu K_α), Confocal Max-Flux™ Optic, Gabriel Multiwire Area Detector and a Linkham thermal stage. Pressed membrane samples were mounted on the thermal stage and heated to 170 °C, then cooled to 120 °C prior data collection. Three hour exposure times were used to maximize signal to noise for Percus-Yevick data fits.

3.2.3 Single-gas permeation testing on membranes

Single-gas CO₂ and N₂ permeability measurements were performed using a time-lag apparatus similar to those reported previously^[17, 36, 37]. Experiments were performed across a range of pressures on three SOS22 and four SOS46 membrane samples. Experiments were performed at room temperature (22–24 °C). Between experiments the apparatus and membrane were evacuated for at least 6 h using an Edwards RV8 vacuum pump. Data from the steady-state region was used to calculate the flux (J), permeability (P), and gas diffusivity (D_i) from Equations 1, 2, and 3^[38, 39].

$$J_i = \left(\frac{\Delta p_i}{\Delta t} - \frac{\Delta p_{leak}}{\Delta t} \right) \cdot \frac{V}{A \cdot T} \cdot \frac{273.15}{14.504} = \frac{\Delta V_i(stp)}{A \cdot \Delta t} \quad (1)$$

Equation 1. Determination of steady-state flux (J_i) (cm^3 (STP)· cm^{-2} · s^{-1}). Where Δp_i is the change in permeate pressure (psi); Δt is the change in time (s); Δp_{leak} is the change in the permeate pressure when system is evacuated then sealed (psi), i.e. the ‘leak rate’; V is the permeate volume (cm^3); A is the membrane area (cm^2); T is the temperature (K); ΔV_i is the volume of gas accumulated in the permeate volume at standard temperature and pressure.

$$P_i = \frac{J_i}{\Delta P_i} \cdot l \quad (2)$$

Equation 2. Determination of the permeability (P_i) (barrers). J_i is the flux (cm^3 (STP)· cm^{-2} · s^{-1}); l is the membrane thickness (cm); and ΔP_i is the trans-membrane pressure difference (cm Hg).

$$D_i = \frac{l^2}{6\theta} \quad (3)$$

Equation 3. Determination of the diffusion coefficient (D_i) (cm^2 · s^{-1}). l is the membrane thickness (cm); and θ is the time-lag (s). The time lag (θ) is determined from the x-axis intercept from a plot of the steady-state flow rate (V_i (STP)) against time (t).

The solution-diffusion model was used to extract the permeability, diffusivity, and solubility from the raw experimental data (flux) using Equations 1, 2, 3, and 4 [40]. The ideal selectivity ($\alpha_{i/j}$) between the two gases (i and j) was calculated using Equation 4. Results for all membranes tested are included in the Electronic Supporting Information (ESI). The membranes reported herein are free-standing, dense films, so no tortuosity and porosity corrections were applied.

$$P_i = D_i \cdot S_i \quad (4)$$

Equation 4. P_i is the permeability of gas i (barrers); D_i is the diffusion coefficient of gas i (cm^2/s); S_i is the solubility coefficient of gas i (cm^3 of i at STP $\cdot \text{cm}^{-3}$ of polymer $\cdot \text{atm}^{-1}$).

$$\alpha_{i/j} = \frac{P_i}{P_j} \quad (5)$$

Equation 5. α_{ij} is the ideal selectivity (unitless); P_i is the permeability of the faster gas ‘ i ’ (barrers); P_j is the permeability of the slower gas ‘ j ’ (barrers).

3.2.4 Mechanical testing

3.2.4.1 Uniaxial tensile strength testing

A TA Instruments ARES rheometer with rectangular geometry test fixtures was used to perform tensile testing on ion gel samples of rectangular shape. Dimensions of the samples were ca. 6 mm in width and 0.2–0.3 mm thick. All tensile tests were run at room temperature using the normal force transducer. The surfaces of the transducer grips were modified with 600 grit sand paper to eliminate the slip on the sample. An initial force of 1 g was applied to the sample and strain rate of $2\% \text{ s}^{-1}$ from the initial length was applied until mid-sample failure occurred. Stress was calculated as the force normalized by the initial cross sectional area of each sample (engineering stress). Strain at failure (λ_f) was used for calculating the cyclic loading intervals for the cyclic load testing. A strain rate of $2\% \text{ s}^{-1}$ from the initial length was maintained for loading cycles.

3.2.4.2 Unconfined compression testing

Multiple extension mode strain controlled transient compression tests were performed on a TA instrument ARES rheometer with parallel plate fixtures using the integrated normal force transducer. An upper plate (25 mm in diameter) was used with an infinite diameter lower plate (63 mm). The sample diameter was 20 mm in diameter and 2.2 mm in thickness. Sample was placed in the center of the lower plate stage and initial normal force of 10 g was applied. A strain rate of $10\% \text{ s}^{-1}$ from the initial thickness per second was applied on the sample up to 40% strain. Multiple cycles of normal compressive force loading and unloading were measured.

3.3 RESULTS AND DISCUSSION

3.3.1 Material synthesis and membrane fabrication

All membranes were formed using two distinct compositions of pre-blended SO diblock and SOS triblock copolymer as described in Table 1 and Figure 2. The naming convention used is based on designating the mol% triblock copolymer in the sample following the SOS label. For example, the SOS22 membrane is made of a blend that has 22 mol% SOS triblock copolymer and 78 mol% SO diblock copolymer *prior* to RTIL loading (Figure 3.2-A.2).

The desired nanostructure of the SO/SOS blends was achieved by designing the volume fraction of PS ($f_{\text{PS}} = 0.085$) to fall into the sphere-forming regime of the typical AB diblock

copolymer phase diagram^[41, 42]. Simultaneously, the ultimate mechanical performance of the SO/SOS blends was achieved by maintaining a PS molecular weight (8370 g·mol⁻¹) capable of vitrification (a glass transition) above the PEO crystallization temperature of 65 °C. The latter requirement was necessary to ensure trapping of the spherical domain structure prior to (PEO) crystallization and guarantee the mechanical integrity of those domains (and thus the network) even at elevated temperatures. Importantly, the use of melt state self-assembly facilitates the formation of a homogeneous periodic domain structure as suggested by Figure 3.2B.

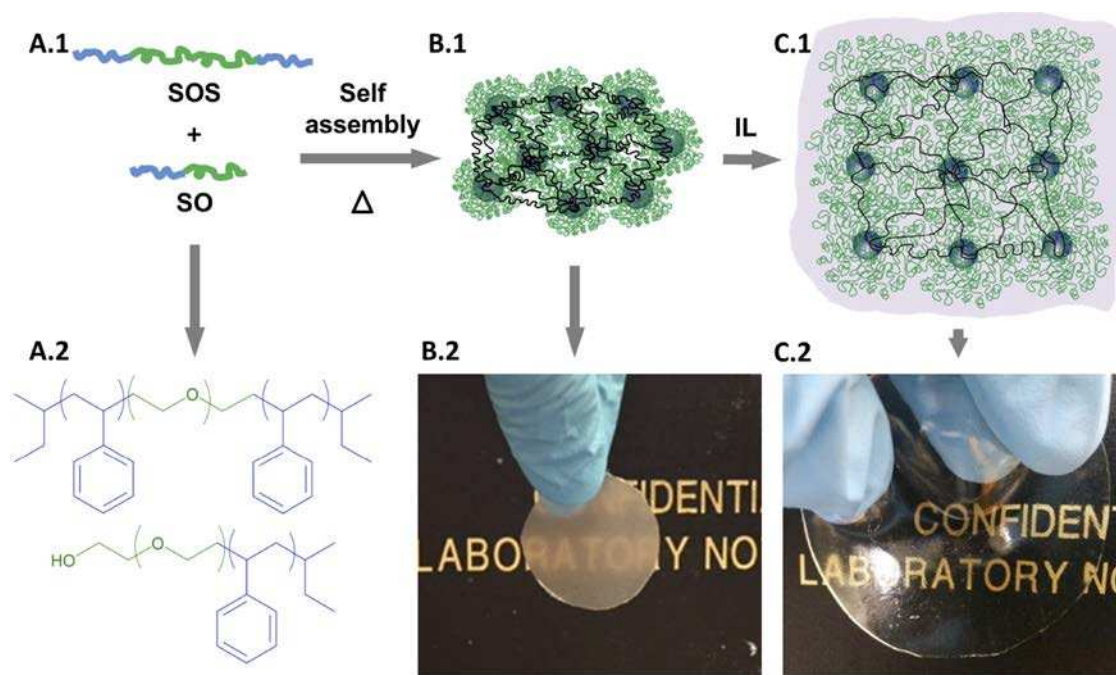


Figure 3.2 Membrane fabrication: **A.1)** Cartoon representation of polystyrene-*b*-poly(ethylene oxide)-polystyrene triblock (SOS) and polystyrene-*b*-poly(ethylene oxide) diblock (SO). **A.2)** Chemical structure of SOS and SO **B.1)** Melt state self-assembly of SO/SOS blend with heat; polystyrene blocks in spherical domains with poly(ethylene oxide) coronas and tethers (highlighted in bold) **B.2)** Melt-pressed film prior to RTIL loading. **C.1)** Swelling of self-assembled film in RTIL with preservation of tethered spherical morphology. **C.2)** Example of an elastic free-standing membrane of SOS46 loaded with 94 wt% RTIL.

Small angle X-ray scattering (SAXS) was able to confirm the targeted spherical morphology and coincident principal domain spacings of 32 nm for both the dry SOS22 and

SOS46 melt blends (Figure S1.7, SI). In addition, key structural characteristics of the pre-swollen networks could be extracted from SOS46 data fits using a modified Percus-Yevick hard sphere model^[43] as described previously by our group^[31, 32] and others^[44-48]. These fits confirmed a liquid-like packing of the spherical domains, an aggregation number of approximately 338 chains per sphere, and PS core radii of 10.5 nm (Figure S1.7 and Table S1.8, SI). This corresponds to trillions of spherical domains per milligram of dry polymer blend, which when tethered together by SOS triblock copolymer produces a network that is extremely efficient at distributing stress across the sample. When the polymer film is loaded with free RTIL, the dense PEO matrix formed by the coronal layers surrounding each sphere are selectively swollen, forming a continuous RTIL/PEO domain structure that traverses the entire expanse of the membrane. Analysis of swelling in analogous tethered sphere systems^[49] by our group (involving photo-cross-linkable polydiene cores^[50], a PEO matrix, and water as the swelling medium) showed the increase in average spacing between spherical domains measured by SAXS is identical to that predicted by simply considering the macroscopic expansion in membrane dimensions upon swelling. Importantly, this continuous domain structure provides a capability to easily absorb both tensile and compressive strains, while providing excellent gas transport through the membrane. Importantly, the vitrified PS cores remain impervious to the RTIL and provide solid multifunctional junction points anchoring the tethered network in-place. Even with RTIL loadings approaching 95 wt%, this framework grants the membrane solid-like mechanical properties. Based on previous studies of this structure in water, the PS molecular weight of 8370 g mol⁻¹ guarantees the cores remain vitrified at temperatures up to 80 °C^[31].

A single melt-processing step (molding under a hot press) was used to self-assemble the SO/SOS blends into the desired nanostructured free-standing film (Figure 3.2B). The thickness

of each film was then reduced by repeating the melt-pressing process under vacuum while applying step increases in the applied pressure. Typical dry film thicknesses ranged from 55 μm up to 190 μm . SO/SOS films containing two different SO/SOS ratios were then swollen with excess [EMIM][TFSI] to produce the desired composite membranes (Figure 3.2C and Table 3.1). The equilibrium swelling ratios (Q) were calculated based on gravimetric analysis of the membranes before and after swelling with RTIL, producing final membrane thicknesses falling between 135 and up to 430 μm . The thickness of each membrane was measured using an optical profilometer.

In our previous studies with SO/SOS systems of similar molecular weights, we discovered the concentration of SOS triblock copolymer in the blend dramatically influenced the swelling ratio and mechanical properties when water was used as the swelling medium (ca. $Q_{\text{H}_2\text{O}, 22 \text{ mol}\%} = 14.2$, $Q_{\text{H}_2\text{O}, 46 \text{ mol}\%} = 7.1$). Thus, the choice of SOS concentrations in this study were selected in an attempt to produce membranes with two very different RTIL compositions under equilibrium swelling, based on the hypothesis that higher RTIL loadings would produce greater CO_2 permeability. Unexpectedly, the selected SOS concentrations of 22 and 46 mol% produced much smaller differences in RTIL swelling ratios (18.4 vs. 16.5), with mass concentrations of RTIL both reaching or exceeding 94 wt%. Clearly, the RTIL is a better solvent for PEO than water, with a much higher swelling capacity regardless of SOS content. The exceptional compatibility of [EMIM][TFSI] with the PEO matrix may involve coordination of the polyether backbone with the cationic imidazolium, and potential hydrogen bonding of the oxygen species in the PEO backbone with the C(2)-H of the imidazolium heterocycle. We attempted to use FT-IR spectroscopy to confirm the latter, through detection of a shift in the C(2)-H stretch ($\nu_{\text{CH}} \sim 3425 \text{ cm}^{-1}$) to lower wavenumbers as also attempted by Arduengo et al.^[51] As with that study, the

data (Figure S1.6, SI) proved inconclusive, as we were unable to discern a conclusive peak shift from the superimposed SOS absorption and surrounding baseline regions. As discussed in greater detail below, the similarity in final RTIL content between membranes produced relatively minor differences in CO₂ permeability, consistent with such high RTIL loadings. In contrast, the impact of differing SOS content on the resultant mechanical properties remained significant.

Table 3.1 Characterization of membrane composition and mechanical properties.

Blend	SOS Loading (mol%^a)	RTIL Loading (wt%^b)	Q^c	λ_f^d	UTS (kPa)^e	Compressive Modulus (kPa)^f
SOS22	22	94.8	18.4	3.8	80	71
SOS46	46	94.0	16.5	3.8	250	348

^a Composition of un-swollen BCP membranes; ^bRTIL weight percent in a swollen membrane; ^c Equilibrium swelling ratio of the membranes defined as the grams of liquid/gram of polymer; ^d Extension ratio at break (failure) under tensile loading; ^e Ultimate tensile strength; ^f Compressive modulus at 40% strain.

3.3.2 Gas Separation Performance

3.3.2.1 CO₂/N₂ Permeation and Separation Performance

The CO₂/N₂ selectivity and CO₂ permeation performance of multiple SOS46 and SOS22 membranes were measured and assessed against the 2008 Robeson plot upper bound, as presented in Figure 3.3. This collection of measured values represents a total of three different SOS22 and three different SOS46 membranes measured over a range of transmembrane pressures from 26 to 413 kPa (see ESI Tables S1, S2, S4, and S5). Data included in Figure 3.3 represent only composite values for which both the CO₂/N₂ permi-selectivity and the CO₂

permeability were recorded at matched transmembrane pressures (within 5%). Additional CO₂ permeability data collected during a 28-day membrane longevity experiment is also included in the SI (Table S7). As shown by the collection of measured values, both SOS22 and SOS46 membranes performed similarly, producing measured CO₂ permeabilities from 567 to 996 barrers, coupled with CO₂/N₂ selectivities ranging from 21.3 to 59.8. Notably, this collection of measured values traverses the 2008 Robeson plot upper bound, and importantly, is on par with similar style membranes previously reported by Gu et al.^[21, 22] and Rabiee et. al.^[23], which also show significant increases in CO₂/N₂ selectivity while experiencing relatively small losses in CO₂ permeability (compared to supported ionic liquid membranes of neat [EMIM][TFSI]). As we show in detail below, the highly elastic and yet distensible nature of these membranes at such high loadings differentiates them from this group. Additionally, we show that this elasticity and intrinsic ability to accommodate tensile loading without plastic deformation gives these membranes an inherent ability to withstand transmembrane pressures over significant time durations (*vide infra*).

The origin of measurement-to-measurement and membrane-to-membrane differences in performance produced within the same SOS blend types remains under investigation. Variations in film thickness uniformity, surface morphology, and stress states across the membrane surface are likely contributors, as well as intrinsic uncertainties associated with gas permeability measurements (sample mounting, leak rates, etc.) However, correlations between performance and these specific film characteristics remain unaddressed at this time. Importantly, the data collected represents that from a range of measured membrane thicknesses (135 to 430 μm), for which no discernable trend in separation performance was observed.

Interestingly, both membrane systems examined here, as well as the ion-gel block polymer-based membranes reported by Gu et al.^[21, 22] and Rabiee et al.^[23], display CO₂/N₂ selectivities higher than neat [EMIM][TFSI]. Gu et al. proposed that this effect was due to the influence of gas permeation through the block copolymer phase. And while it has been shown that the nanostructure of block copolymers has a significant effect on light-gas permeation and selectivity properties^[28], it is not clear that glassy polystyrene domains (comprising only 0.5 wt% of the membrane mass) can be responsible in this case. On the other hand, it has also been shown that confinement of ionic liquids inside the nanostructure of porous materials can significantly affect CO₂ diffusivity and solubility properties^[52, 53]. In our case, there is no definable pore space like that present in the previously cited reports involving inorganic supports; however, the idea that the local environment can disrupt the bulk RTIL liquid structure (producing increased free volume and differences in RTIL mobility) should not be dismissed. The active matrix in SOS membranes in this work is comprised of dense high molecular weight PEO brushes saturated with RTIL solvent. It is conceivable that the local interaction between the PEO chains and the RTIL (a good solvent for PEO) acts to ultimately decrease resistance to CO₂ transport. Likewise, one must also consider the interaction between quadrupolar CO₂ and the PEO chains themselves as an influential contributor to this increase^[54]. Figure 3.3 includes the combined CO₂ permselectivities and permeabilities of semi-crystalline PEO at 790 kPa and three different temperatures (25, 35 and 45°C) for comparison with neat [EMIM][TFSI] and the SOS membranes. Notably, PEO has exceptional CO₂/N₂ selectivity at room temperature (140), although its permeability is typical of most polymeric solids (8.1 barrers). At temperatures closer to the PEO melt temperature (65°C), permeability is improved moderately, presumably as the amorphous chains (not involved in crystalline lamellae) gain mobility. Some of the exceptional

selectivity sacrificed, of course. Regardless, it seems reasonable that the "doping" of the [EMIM][TFSI] with the PEO chains of the block copolymer is consistent with the improved selectivity measured (over the neat RTIL) in the SOS membranes.

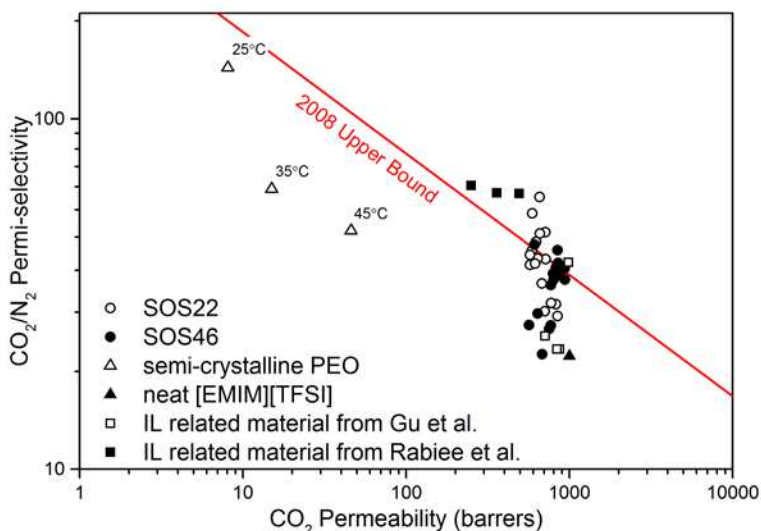


Figure 3.3 Robeson plot showing the single-gas CO₂/N₂ separation performance of SOS22 and SOS46 saturated with [EMIM][TFSI]. SOS data were collected at 22-24 °C and at range of transmembrane pressures 26-413 kPa. Individual testing conditions for all membranes are documented in the ESI. Separation performance data from similar RTIL-block copolymer membrane materials produced by Gu et al. (at room temperature and transmembrane pressure of 202 kPa)[21, 22] and Raibee et al. (at 25 °C and transmembrane pressure of 400 kPa) [23] are also included, along with that for neat [EMIM][TFSI] (at 25 °C) [21, 22] and semi-crystalline PEO (at 790 kPa and 25, 35 and 45 °C) [54]. The 2008 Robeson upper bound was adopted from reference [55].

3.3.3 Mechanical Performance

The elastic behavior of these RTIL composite membranes stands in stark contrast to the many solid, gel-like, and liquid phase RTIL-containing membranes reported to date. Such elasticity can be demonstrated qualitatively in simple stretching experiments, such as those shown in Figure 3.1. As a free-standing membrane placed upon a porous support, it must be able to withstand both a normal compressive force associated with the transmembrane pressure

differential, as well as a significant tensile force, generated (by a Laplace pressure) where the membrane spans (like a diaphragm) the pore openings of the support.

To evaluate the mechanical performance of the SO/SOS RTIL composite membranes, the stress-strain behavior under both uniaxial tension and unconfined compression was evaluated (Figure 3.4). Figure 3.4a shows representative stress-strain data from typical tensile loading experiment in which the samples were pulled at $10\% \text{ s}^{-1}$ to failure. In the plot, the normal engineering stress (kPa) is plotted against the extension ratio ($\lambda \equiv$ ratio of the length under tension to the original sample length). Both RTIL loaded samples of SOS46 and SOS22 failed at a λ value of approximately 3.8 (a strain of nearly 300%). However, the ultimate tensile strength (UTS), defined as the highest normal stress prior to failure, was just greater than three times higher for SOS46 than for SOS22 (250 and 80 kPa, respectively), underscoring the importance of triblock copolymer concentration in dictating the mechanical response of the swollen composite.

Similar differences in behavior were observed when subjected to unconfined compression. Using a strain rate of $10\% \text{ s}^{-1}$, unconfined compression was performed to 40% strain (Figure 3.4b). Beyond 40% strain, the RTIL composite samples underwent a rapid increase in compressive stress that was beyond our transducer capabilities, and thus behavior under more extreme compressive conditions was not investigated. As in the tensile experiment, the compressive modulus of the RTIL swollen SOS46 up to 40% strain was about five times higher than that of SOS22 (348 kPa vs. 71 kPa, respectively).

The mechanical property dependence on triblock copolymer composition found in the RTIL-swollen composites mimics what we have found in similarly designed hydrogel systems, where the UTS and compressive modulus also increased with increasing triblock content^[31]. It is believed that a greater number of topologically fixed entanglements among the tethers adjoining

spherical domains are ultimately responsible for the higher UTS and Young' moduli exhibited by the SOS46 membranes. Higher numbers of topological entanglements among triblock copolymers act to restrict swelling in the system, which enforces greater overlap between the coronal layers (dense brushes of PEO chains surrounding each PS core) of adjacent spheres. Increased coronal overlap has been found to have a significant influence on the overall mechanical response of these types of swollen network materials [32].

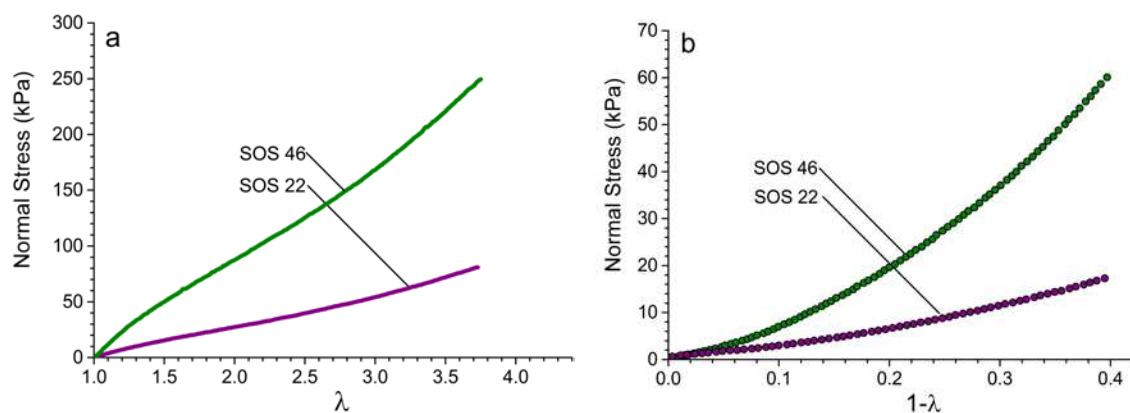


Figure 3.4 Mechanical response of SOS22 and SOS46 swollen to equilibrium dimensions in [EMIM][TFSI]. All data collected at 20 °C. **a)** Stress-strain behavior of under uniaxial tension applied with a strain rate of 2% s⁻¹. **b)** Stress-strain behavior under unconfined compression applied at a strain rate = 10% s⁻¹.

Importantly, one can conclude that the ability to tune the mechanical properties of the composite membrane through simple shifts in SOS content provide a facile and convenient strategy for optimizing the mechanical behavior in these systems. More specifically, the 24 mol% increase in SOS (from 22 mol% to 46 mol%) resulted in a three- to four-fold increase in mechanical strength, at the cost of a mere 10% drop in RTIL swelling ratio. The latter appears to be related to the high PEO solubility in [EMIM][TFSI], which produces CO₂ gas permeability and separation properties in SOS46 and SOS22 membranes that are quite similar. Notably, there

appears to be an opportunity to increase triblock copolymer in these membranes even further, without significant loss in CO₂/N₂ separation performance^[56].

Ultimately, the ability of the tethered-sphere nanostructure to withstand significant transmembrane pressure differentials requires that its intrinsic distensibility as a biphasic elastomer composite be reversible, without undergoing plastic deformation under a sustained (or changing) load. Consequently, we also examined the ability of these membranes to be cycled reversibly under both tensile and compressive loading.

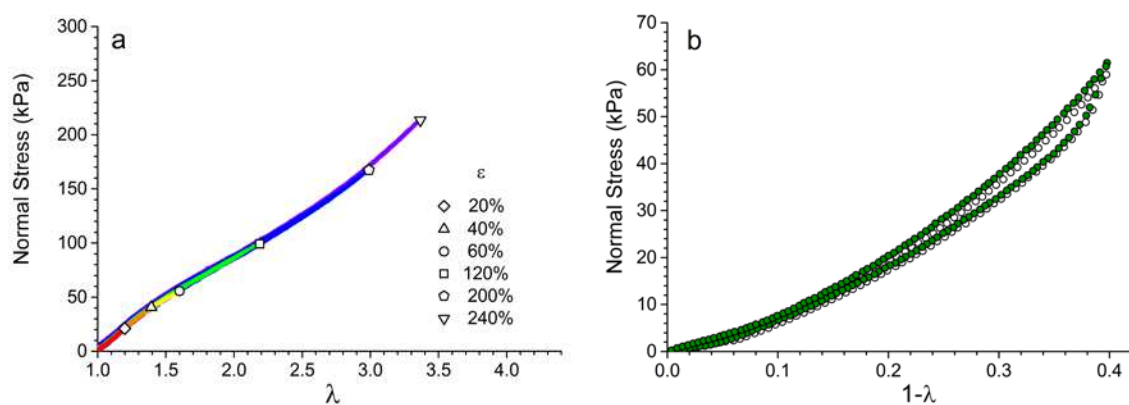


Figure 3.5 **a)** Cyclic tensile loading performed on a single sample of RTIL swollen on SOS46 membrane at 20 °C. Tensile loading was cycled through progressively increasing strains. Loading and unloading was performed with a strain rate of 2% s⁻¹. **b)** Unconfined compression–decompression cycles performed on a single sample of RTIL swollen SOS46 membrane at 20 °C. Both compression and release were performed at a strain rate of 10% s⁻¹. Cycles two (open circles) and ten (filled circles) are shown. Data for all cycles provided in the ESI.

Figure 3.5a shows the results of a progressive tensile loading experiment in which a single coupon of the membrane is subjected to loading and unloading to progressively higher strains. Using a strain rate of 2% s⁻¹ (Figure 3.5a), the swollen RTIL composites displayed no degradation in modulus with each additional cycle, (until failure) and exhibited no detectable

hysteresis during the release of the tensile force. From these observations, two important conclusions can be drawn: First, the tethered-sphere network has an ability to absorb the stress elastically and reversibly without breaking bonds or disrupting the network structure over a significant range of stresses. We attribute this to the ability of the network to absorb stress through relaxation of dynamic chain entanglements in the diblock copolymer population, in combination with traditional mechanisms of energy dissipation associated with chain stretching and chain slip in the tethering triblock copolymer population. The connectivity among the individual spheres, which is highly redundant at 46 mol% triblock copolymer, produces an mechanical connectivity that is extremely efficient at distributing stress across the sample. Second, the lack of any significant hysteresis upon the release of the tensile force confirms the observation (during separations testing) that strain produces RTIL movement internal to the membrane only, with no detectable RTIL leakage occurring under load conditions. The lack of hysteresis indicates the elastic restoring force in the tethered-sphere network is such that RTIL redistribution is promoted at a rate slower than that used in the experiment ($2\% \text{ s}^{-1}$). Notably, we have found no other membranes based on BCP and RTILs^[21-23, 29, 57] that have been reported to have these unique material properties.

Cyclic loading under unconfined compression confirms the conclusions drawn about the elastic reversibility of the membranes that provides them with such a unique mechanical advantage. Ten unconfined compression-decompression cycles at a constant strain rate of $10\% \text{ s}^{-1}$ (Figure 3.5b) were also performed on the swollen SOS46 samples. Importantly there is superb agreement between the first and tenth cycles, again showing the absence of property degradation during mechanical loading and unloading. In the case of compression, however, intra-cycle hysteresis was observed during the release of the compressive load. Coincidence with

the compression data is eventually achieved prior to reaching zero applied force, implying redistribution of RTIL molecules is occurring on a relatively fast time scale. This type of behavior confirms that the hysteresis in the observed under cyclic compression is related to the differences between the strain rate and the RTIL mass-transfer rates in the membrane. Regardless, the full recovery and excellent reproducibility of successive cycles indicates, that very little, if any, liquid is being exuded from the membrane under compressive strains up to 40%.

3.3.4 Additional Operational Considerations

3.3.4.1 Effect of Transmembrane Pressure on CO₂/N₂ Separation Performance

Industrial processes for separating light gases can operate over a wide range of pressure differentials. With that in mind, we began the process of assessing the impact of different transmembrane pressures on the separation performance of these RTIL composite membranes. As shown in Figure 3.6, CO₂/N₂ selectivity and CO₂ permeability were measured as a function of increasing transmembrane pressure differentials including pressures just exceeding 400 kPa in both the SOS22 and SOS46 systems. In some cases, data were collected at a given pressure differential using multiple membranes. In those cases, the data are presented as mean values with calculated standard deviations. And while the relationship between membrane thickness and burst pressure remains to be quantified in these systems, these initial measurements are quite encouraging.

For the membranes of a given triblock copolymer blend ratio, the effect of increasing transmembrane pressure on CO₂/N₂ separation performance appears to be minor over the range of pressures examined, with the highest pressure being a possible exception. In the case of the SOS46 membrane run just above 400 kPa, a slight decline in both CO₂ permeability and CO₂/N₂ selectivity was observed. Notably, the thickness of this membrane was 430 microns, which is approximately twice the thickness of the other three SOS46 membranes tested. If the observed drop in the CO₂ permeability and the CO₂/N₂ selectivity for that particular membrane is representative of true mean behavior, the underlying reason is not outwardly apparent. Further studies in replicate, beyond the scope of this initial report, will be needed to evaluate its authenticity.

Interestingly, the SOS22 membranes examined appear to exhibit a slightly higher average CO₂/N₂ selectivity when compared to the SOS46 composites when the behavior across all transmembrane pressures is considered. In contrast, the CO₂ permeability exhibits the inverse trend. While the inverse relationship itself, being consistent with the Robeson flux-selectivity tradeoff, is not entirely unexpected, that the membrane system containing the higher RTIL content (SOS22) should exhibit the lower permeability (but the higher selectivity) is not entirely obvious. As proposed earlier, it seems possible the role of RTIL mobility and liquid structure as a function of the PEO chain concentration throughout active layer may be playing an important role in the determination of ultimate gas separation performance.

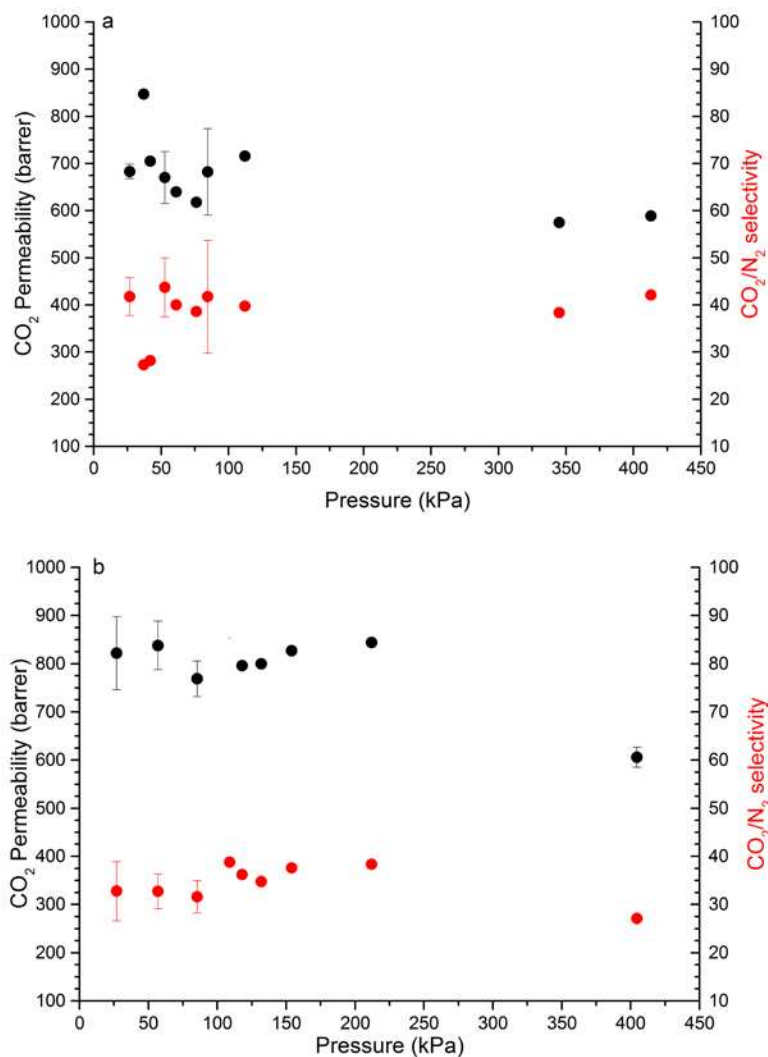


Figure 3.6 Single-gas CO₂/N₂ permselectivity data as a function of increasing feed pressure for the RTIL composite membranes fabricated from SOS22 (top) and SOS46 (bottom). All data was collected at 23 °C. In cases where multiple membranes were tested, mean values and standard errors are indicated.

3.3.4.2 Performance Longevity

To examine the potential long-term stability of the SO/SOS RTIL composite membranes under gas separation conditions, we mounted a single SOS46 membrane saturated with [EMIM][TFSI] and measured CO₂ permeation 16 times over the course of 28 days (Figure 3.7). Between tests the membrane was kept under dynamic vacuum. All tests were performed with a

CO₂ feed pressure of approximately 230 kPa. Initially, variations in CO₂ permeability of ca. 50 barrers were observed. However, between days 8 and 28 the CO₂ permeability of this membrane stabilized, giving consistent readings of $9.7 \pm 0.1 \times 10^2$ barrers. Importantly, these results show that membranes of the SO/SOS based RTIL composite membranes maintain their permeation performance over a reasonable timescale while sustaining cycled transmembrane pressures between applied vacuum and 230 kPa. Perhaps most importantly, they did not appear to leak any of the physically entrained RTIL over the 28-day time period.

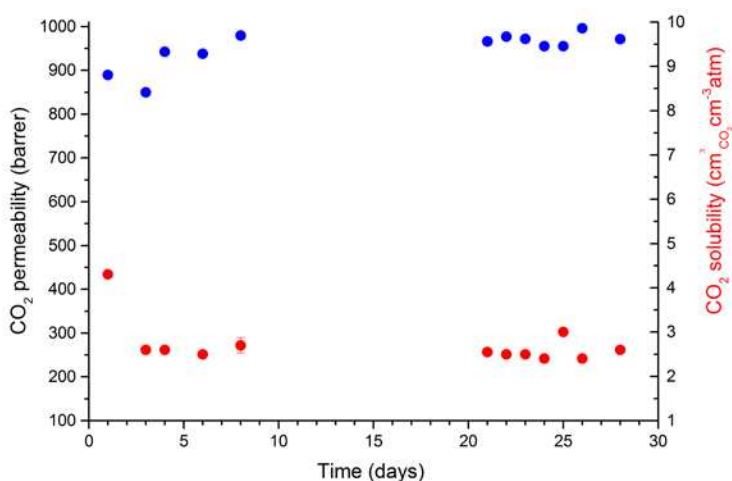


Figure 3.7 CO₂ permeability and CO₂ solubility over a 28-day time period for a SOS46 membrane saturated with [EMIM][TFSI]. Data was collected at 23 °C with a fixed feed pressure of approximately 230 kPa for each measurement. Data reported for days 3,8 and 21 are averaged values. Standard errors in some cases are small enough to be obscured by the data point marker.

The longevity test also suggests the ability of the PS core domains to remain glassy, confirming that exposure to the RTIL solvating the PEO chains, or the dissolved CO₂ during measurement does not negatively impact the mechanical integrity of these membranes through plasticization. In addition, given the ability of the SOS membranes to exhibit exceptional mechanical performance when swollen in aqueous media for extended periods^[31, 32], we do not anticipate the presence of water in the feed gas to adversely affect the system mechanical

properties. However, the influence on the stability of the RTIL itself, and the extended gas separation performance of the membrane in the presence of humidified feed gas will need to be established. Notably, our recent studies separating humidified CO₂/N₂ mixed-gas streams with [EMIM][TFSI] saturated epoxy-amine ion gel membranes did not reveal any acute stability issues^[58]. And while additional species in the feed gas such as oxygen or other oxide contaminants have also yet to be evaluated, the ability of the PS to impart the mechanical stability to remain a free-standing membrane, before, during, and after use in these extended single gas experiments is promising. While use of alternate RTILs and increased operating temperatures may eventually require more permanent fixation of the core material, the ability to use simple vitrification following melt-assembly may be one of the most attractive features of this system.

3.4 CONCLUSIONS

We have examined a new series of RTIL-based composite membranes that were fabricated by exploiting the melt-state self-assembly of vitrified sphere-forming diblock and triblock copolymer blends swollen with free RTIL. The SO/SOS system used proved to be an exceptional absorber of the RTIL, [EMIM][TFSI], which resulted in elastic free-standing membranes containing 94–94.8 wt% free RTIL. As a consequence of the RTIL loading, these membranes exhibited combined CO₂ permeabilities and CO₂/N₂ selectivities traversing the 2008 Robeson plot upper bound. Tensile and compression testing confirmed the ability of these composite membranes to withstand cyclic loading in both compression and tension with no RTIL

loss under mechanical loading. The membranes tested exhibited complete recovery of modulus in successive cycling, and showed only transient, rapidly recovered hysteresis in compression. Transmembrane pressure differentials ≥ 400 kPa could be successfully applied, and membrane performance over a 28-day period was used to demonstrate mechanical and CO₂ permeability stability ($9.7 \pm 0.1 \times 10^2$ barrers over days 8 – 28). Such stability over time reveals the impressive ability of the PS cores, vitrified from the melt-state through standard melt-processing techniques, to resist plasticization or mechanical failure in the presence of large quantities of RTIL or recurring mechanical loads.

3.5 AUTHOR INFORMATION

(T.S.B)* Corresponding author at: Department of Chemical and Biological Engineering, Colorado State University, Fort Collins, CO 80523, United States. Tel.: +1 970 491 4648. E-mail address: travis.bailey@colostate.edu

(D.L.G)* Corresponding author at: Department of Chemical and Biological Engineering, and Department of Chemistry and Biochemistry, University of Colorado, University of Colorado, CO 80309, United States. Tel.: +1 303 735 5448. E-mail address: douglas.gin@colorado.edu

(R.D.N)* Corresponding author at: Department of Chemical and Biological Engineering, University of Colorado, University of Colorado, CO 80309, United States. Tel.: +1 303 492 6100. E-mail address: nobler@colorado.edu

REFERENCES

- [1] R.K. Pachauri, L.A. Meyer, Climate change 2014: Synthesis report, in: Contribution of Working Groups I, II and III to the Fifth Assessment Report of the Intergovernmental Panel on Climate Change, IPCC, Geneva, Switzerland, 2014, pp. 151.
- [2] C.W. Jones, CO₂ capture from dilute gases as a component of modern global carbon management, *Annu Rev Chem Biomol Eng*, 2 (2011) 31-52.
- [3] C.S. Song, Global challenges and strategies for control, conversion and utilization of CO₂ for sustainable development involving energy, catalysis, adsorption and chemical processing, *Catal. Today*, 115 (2006) 2-32.
- [4] D.P. Schrag, Preparing to capture carbon, *Science*, 315 (2007) 812-813.
- [5] P. Li, K.P. Pramoda, T.S. Chung, CO₂ Separation from Flue Gas Using Polyvinyl-(Room Temperature Ionic Liquid)-Room Temperature Ionic Liquid Composite Membranes, *Ind. Eng. Chem. Res.*, 50 (2011) 9344-9353.
- [6] R. Ducroux, P. Jean-Baptiste, Technologies, methods and modelling for CO₂ capture, in: E.S. Wilson, D.W. Rubin, C.F. Keith, M. Gilboy, T. Thambimuthu, J. Morris, K. Gale (Eds.) *Greenhouse Gas Control Technologies 7*, Elsevier Science Ltd, Oxford, 2005, pp. 1835-1839.
- [7] E.S. Rubin, C. Chen, A.B. Rao, Cost and performance of fossil fuel power plants with CO₂ capture and storage, *Energy Policy*, 35 (2007) 4444-4454.
- [8] W.R. Baker, *Membrane Technology and Applications*, 3rd ed., John Wiley & Sons, 2012.
- [9] Y. Huang, T.C. Merkel, R.W. Baker, Pressure ratio and its impact on membrane gas separation processes, *J. Membr. Sci.*, 463 (2014) 33-40.
- [10] R.W. Baker, Future directions of membrane gas separation technology, *Ind. Eng. Chem. Res.*, 41 (2002) 1393-1411.
- [11] T.C. Merkel, H.Q. Lin, X.T. Wei, R. Baker, Power plant post-combustion carbon dioxide capture: An opportunity for membranes, *J. Membr. Sci.*, 359 (2010) 126-139.
- [12] R.W. Baker, B.T. Low, Gas Separation Membrane Materials: A Perspective, *Macromolecules*, 47 (2014) 6999-7013.
- [13] Z.D. Dai, R.D. Noble, D.L. Gin, X.P. Zhang, L.Y. Deng, Combination of ionic liquids with membrane technology: A new approach for CO₂ separation, *J. Membr. Sci.*, 497 (2016) 1-20.

- [14] J.E. Bara, T.K. Carlisle, C.J. Gabriel, D. Camper, A. Finotello, D.L. Gin, R.D. Noble, Guide to CO₂ Separations in Imidazolium-Based Room-Temperature Ionic Liquids, *Ind. Eng. Chem. Res.*, 48 (2009) 2739-2751.
- [15] S. Paul, E.V. Ann, H.D. James, D.R. Robin, A.K. Carl, L.D. Dan, D.N. Richard, Supported Ionic Liquid Membranes and Facilitated Ionic Liquid Membranes, in: *Ionic Liquids*, American Chemical Society, 2002, pp. 69-87.
- [16] B.A. Voss, J.E. Bara, D.L. Gin, R.D. Noble, Physically Gelled Ionic Liquids: Solid Membrane Materials with Liquidlike CO₂ Gas Transport, *Chem. Mater.*, 21 (2009) 3027-3029.
- [17] W.M. McDanel, M.G. Cowan, T.K. Carlisle, A.K. Swanson, R.D. Noble, D.L. Gin, Cross-linked ionic resins and gels from epoxide-functionalized imidazolium ionic liquid monomers, *Polymer*, 55 (2014) 3305-3313.
- [18] T.K. Carlisle, W.M. McDanel, M.G. Cowan, R.D. Noble, D.L. Gin, Vinyl-Functionalized Poly(imidazolium)s: A Curable Polymer Platform for Cross-Linked Ionic Liquid Gel Synthesis, *Chem. Mater.*, 26 (2014) 1294-1296.
- [19] T.K. Carlisle, E.F. Wiesenauer, G.D. Nicodemus, D.L. Gin, R.D. Noble, Ideal CO₂/Light Gas Separation Performance of Poly(vinylimidazolium) Membranes and Poly(vinylimidazolium)-Ionic Liquid Composite Films, *Ind. Eng. Chem. Res.*, 52 (2013) 1023-1032.
- [20] J. Zhou, M.M. Mok, M.G. Cowan, W.M. McDanel, T.K. Carlisle, D.L. Gin, R.D. Noble, High-Permeance Room-Temperature Ionic-Liquid-Based Membranes for CO₂/N₂ Separation, *Ind. Eng. Chem. Res.*, 53 (2014) 20064-20067.
- [21] Y.Y. Gu, E.L. Cussler, T.P. Lodge, ABA-triblock copolymer ion gels for CO₂ separation applications, *J. Membr. Sci.*, 423 (2012) 20-26.
- [22] Y.Y. Gu, T.P. Lodge, Synthesis and Gas Separation Performance of Triblock Copolymer Ion Gels with a Polymerized Ionic Liquid Mid-Block, *Macromolecules*, 44 (2011) 1732-1736.
- [23] H. Rabiee, A. Ghadimi, T. Mohammadi, Gas transport properties of reverse-selective poly(ether-*b*-amide6)/[Emim][BF₄] gel membranes for CO₂/light gases separation, *J. Membr. Sci.*, 476 (2015) 286-302.
- [24] E.F. Wiesenauer, J.P. Edwards, V.F. Scalfani, T.S. Bailey, D.L. Gin, Synthesis and Ordered Phase Separation of Imidazolium-Based Alkyl-Ionic Diblock Copolymers Made via ROMP, *Macromolecules*, 44 (2011) 5075-5078.
- [25] V.F. Scalfani, E.F. Wiesenauer, J.R. Ekblad, J.P. Edwards, D.L. Gin, T.S. Bailey, Morphological Phase Behavior of Poly(RTIL)-Containing Diblock Copolymer Melts, *Macromolecules*, 45 (2012) 4262-4276.

- [26] E.F. Wiesenauer, P.T. Nguyen, B.S. Newell, T.S. Bailey, R.D. Noble, D.L. Gin, Imidazolium-containing, hydrophobic-ionic-hydrophilic ABC triblock copolymers: synthesis, ordered phase-separation, and supported membrane fabrication, *Soft Matter*, 9 (2013) 7923-7927.
- [27] Z. Shi, B.S. Newell, T.S. Bailey, D.L. Gin, Ordered, microphase-separated, noncharged-charged diblock copolymers via the sequential ATRP of styrene and styrenic imidazolium monomers, *Polymer*, 55 (2014) 6664-6671.
- [28] P.T. Nguyen, E.F. Wiesenauer, D.L. Gin, R.D. Noble, Effect of composition and nanostructure on CO₂/N₂ transport properties of supported alkyl-imidazolium block copolymer membranes, *J. Membr. Sci.*, 430 (2013) 312-320.
- [29] I.N. Yoon, S. Yoo, S.J. Park, J. Won, CO₂ separation membranes using ion gels by self-assembly of a triblock copolymer in ionic liquids, *Chem. Eng. J.*, 172 (2011) 237-242.
- [30] Y. Gu, S. Zhang, L. Martinetti, K.H. Lee, L.D. McIntosh, C.D. Frisbie, T.P. Lodge, High toughness, high conductivity ion gels by sequential triblock copolymer self-assembly and chemical cross-linking, *JACS*, 135 (2013) 9652-9655.
- [31] C. Guo, T.S. Bailey, Highly distensible nanostructured elastic hydrogels from AB diblock and ABA triblock copolymer melt blends, *Soft Matter*, 6 (2010) 4807-4818.
- [32] C. Guo, T.S. Bailey, Tailoring mechanical response through coronal layer overlap in tethered micelle hydrogel networks, *Soft Matter*, 11 (2015) 7345-7355.
- [33] A.L. LaFrata, J.E. Bara, D.L. Gin, R.D. Noble, Diol-Functionalized Imidazolium-Based Room-Temperature Ionic Liquids with Bis(trifluoromethanesulfonimide) Anions that Exhibit Variable Water Miscibility, *Ind. Eng. Chem. Res.*, 48 (2009) 8757-8759.
- [34] J.E. Bara, C.J. Gabriel, S. Lessmann, T.K. Carlisle, A. Finotello, D.L. Gin, R.D. Noble, Enhanced CO₂ separation selectivity in oligo(ethylene glycol) functionalized room-temperature ionic liquids, *Ind. Eng. Chem. Res.*, 46 (2007) 5380-5386.
- [35] T.S. Bailey, Morphological behavior spanning the symmetric AB and ABC block copolymer states, in, University of Minnesota, Minneapolis, Minnesota, 2001.
- [36] J.E. Bara, S. Lessmann, C.J. Gabriel, E.S. Hatakeyama, R.D. Noble, D.L. Gin, Synthesis and performance of polymerizable room-temperature ionic liquids as gas separation membranes, *Ind. Eng. Chem. Res.*, 46 (2007) 5397-5404.
- [37] A. Voleno, M.C. Romano, D.M. Turi, P. Chiesa, M.T. Ho, D.E. Wiley, Post-combustion CO₂ capture from natural gas combined cycles by solvent supported membranes, 12th International Conference on Greenhouse Gas Control Technologies, Ghgt-12, 63 (2014) 7389-7397.

- [38] R.C.L. Jenkins, P.M. Nelson, L. Spirer, Calculation of the Transient Diffusion of a Gas through a Solid Membrane into a Finite Outflow Volume, *Trans. Faraday. Soc.*, 66 (1970) 1391-1401.
- [39] D. Morgan, L. Ferguson, P. Scovazzo, Diffusivities of gases in room-temperature ionic liquids: Data and correlations obtained using a lag-time technique, *Ind. Eng. Chem. Res.*, 44 (2005) 4815-4823.
- [40] W.S. Ho, K.K. Sirkar, *Membrane Handbook*, 1992 ed., Springer, New York, 1992.
- [41] T.G. Fox, P.J. Flory, The Glass Temperature and Related Properties of Polystyrene - Influence of Molecular Weight, *J. Polym. Sci.*, 14 (1954) 315-319.
- [42] P.G. Santangelo, C.M. Roland, Molecular weight dependence of fragility in polystyrene, *Macromolecules*, 31 (1998) 4581-4585.
- [43] J.K. Percus, G.J. Yevick, Analysis of Classical Statistical Mechanics by Means of Collective Coordinates, *Phys. Rev.*, 110 (1958) 1-13.
- [44] E.E. Dormidontova, T.P. Lodge, The order-disorder transition and the disordered micelle regime in sphere-forming block copolymer melts, *Macromolecules*, 34 (2001) 9143-9155.
- [45] D.J. Kinning, E.L. Thomas, Hard-Sphere Interactions between Spherical Domains in Diblock Copolymers, *Macromolecules*, 17 (1984) 1712-1718.
- [46] M. Schwab, B. Stuhn, Thermotropic transition from a state of liquid order to a macrolattice in asymmetric diblock copolymers, *Phys. Rev. Lett.*, 76 (1996) 924-927.
- [47] M. Schwab, B. Stuhn, Asymmetric diblock copolymers - Phase behaviour and kinetics of structure formation, *Colloid. Polym. Sci.*, 275 (1997) 341-351.
- [48] X. Wang, E.E. Dormidontova, T.P. Lodge, The Order-Disorder Transition and the Disordered Micelle Regime for Poly(ethylenepropylene-*b*-dimethylsiloxane) Spheres, *Macromolecules*, 35 (2002) 9687-9697.
- [49] V.F. Scalfani, T.S. Bailey, Access to Nanostructured Hydrogel Networks through Photocured Body-Centered Cubic Block Copolymer Melts, *Macromolecules*, 44 (2011) 6557-6567.
- [50] V.F. Scalfani, T.S. Bailey, Thermally Stable Photocuring Chemistry for Selective Morphological Trapping in Block Copolymer Melt Systems, *Chem. Mater.*, 22 (2010) 5992-6000.
- [51] A.J. Arduengo, S.F. Gamper, M. Tamm, J.C. Calabrese, F. Davidson, H.A. Craig, A Bis(Carbene) Proton Complex - Structure of a C-H-C Hydrogen-Bond, *JACS*, 117 (1995) 572-573.

- [52] J. Albo, T. Tsuru, Thin Ionic Liquid Membranes Based on Inorganic Supports with Different Pore Sizes, *Ind. Eng. Chem. Res.*, 53 (2014) 8045-8056.
- [53] L.A. Banu, D. Wang, R.E. Baltus, Effect of Ionic Liquid Confinement on Gas Separation Characteristics, *Energy & Fuels*, 27 (2013) 4161-4166.
- [54] H. Lin, B.D. Freeman, Gas solubility, diffusivity and permeability in poly(ethylene oxide), *J. Membr. Sci.*, 239 (2004) 105-117.
- [55] L.M. Robeson, The upper bound revisited, *J. Membr. Sci.*, 320 (2008) 390-400.
- [56] We believe there is an upper limit in the amount of triblock copolymer that is desirable in these systems. We have observed that the addition of diblock copolymer can greatly enhance the (kinetic) ability of the material to develop a well-ordered, phase-separated state, and suspect that the number of bridging tethers (compared with looping tethers) may find a maximum at less than 100% triblock copolymer. This has yet to be evaluated.
- [57] P. Bernardo, J.C. Jansen, F. Bazzarelli, F. Tasselli, A. Fuoco, K. Friess, P. Izák, V. Jarmarová, M. Kačírková, G. Clarizia, Gas transport properties of Pebax®/room temperature ionic liquid gel membranes, *Sep. Purif. Technol.*, 97 (2012) 73-82.
- [58] W.M. McDanel, M.G. Cowan, N.O. Chisholm, D.L. Gin, R.D. Noble, Fixed-site-carrier facilitated transport of carbon dioxide through ionic-liquid-based epoxy-amine ion gel membranes, *J. Membr. Sci.*, 492 (2015) 303-311.

CHAPTER 4

FEASIBILITY STUDY OF PHOTO CROSS-LINKED POLYISOPRENE AS A REPLACEMENT FOR POLYSTYRENE IN SO/SOS MEMBRANES⁴

4.1 INTRODUCTION

The uniqueness of the CO₂/N₂ separation membrane materials discussed in Chapter 3 originates from their nanostructure, which was based on an elastically tethered network of spheres made from AB/ABA block copolymer blends. The spherical domains (A), which function as the anchoring junction points for the whole network, were composed of polystyrene chains (~ 8000 g mol⁻¹) that stay vitrified below their glass transition temperature (T_g ~ 80 °C). These glassy polystyrene cores played a central role in the mechanical properties exhibited by the membrane. However, at temperature approaching the T_g, these cores began to soften, causing mechanical failure of the membrane. The focus of this chapter is to study the feasibility of replacing these thermoplastic PS cores (A blocks) with a cross-linked thermoset, simultaneously improving the thermal and chemical (solvent) tolerance of these membranes. An improved solvent tolerance of the spherical domains becomes beneficial if these membranes are to be utilized with a host of developed RTILs with varying cation and anion combinations. For

⁴ The contents of this dissertation chapter were written by Dilanji Wijayasekara. Special acknowledgements are dedicated to Patricia Ribeiro, visiting undergraduate student, for active participation in many of the photo-curing experiments.

example, [C₆mim][Tf₂N]^[1], is known to have a higher CO₂ affinity than [emim][Tf₂N] but tends to plasticize (soften) the PS domains, rendering the current SO/SOS type membranes mechanically vulnerable.

Our group has previously researched low molecular weight BCP systems with cross-linked polybutadiene (PB) as the sphere forming component, and PEO as the coronal layer. This system has shown the ability to produce hydrogels with reasonably high swelling ratios but the mechanical properties at room temperature proved inferior to the SO/SOS system^[2]. The diminished mechanical properties were attributed to the much smaller PB-PEO molecular weights used, in comparison to the SO/SOS systems studied previously. The smaller overall molecular weight drastically reduces the number of coronal layer entanglements present in the swollen hydrogels, which have been shown previously by our group to play a significant role in mechanical property determination^[3]. Our goal was to revisit the use of a crosslinked polydiene spherical core in higher molecular weight systems as a possible route to improved solvent and thermal tolerance.

In this case, polyisoprene (PI) was chosen as an alternative to polybutadiene (PB) used previously in hydrogel formation. Isoprene monomer is safer to handle compared to explosive butadiene monomer. Furthermore, our group has experience with preserving the melt state morphologies (cylinders and gyroid) of low molecular weight PI-*b*-PEO systems by selectively photocrosslinking lightly epoxidized PI domains^[4] in those systems. The work in this chapter can be considered as an important unification of many previous concepts developed by our group. A major distinction between current work and the previous work is the magnitude of the molecular weight of the diblock and triblock copolymers proposed. The higher molecular weight BCP system was anticipated to be advantageous not only for the improved mechanical properties

expected for the system, but for its ability to simultaneously accommodate more ionic liquid than the a lower molecular analogs.

This chapter describes a series of proof of concept experiments exploring the viability of using epoxidized PI as a suitable material for producing crosslinked spherical cores. The chapter starts with the successful synthesis of a high molecular weight PI-PEO/PI-PEO-PI system that melt assembles into a liquid like packing of PI spheres. What follows is a series of attempts to use selective photo crosslinking of the PI spheres using photoactivated cationic polymerization of epoxidized versions of the above system. There are well established methods for chemical crosslinking PI^[5-9], however routes for selectively crosslinking PI without disturbing the existing morphology when it is a part of a phase-separated structure are rare. In this work, we have adapted the chemistry developed specifically for this purpose by our group and validated in low molecular weight systems to this new system of much higher molecular weight.

4.2 EXPERIMENTAL

4.2.1 Materials and Methods

Isoprene (99%, 100 ppm *p*-tert-butylcatechol inhibitor, Aldrich) was purified by successive static vacuum (15-30 mTorr) distillations with *n*-butyllithium (1.6M in hexanes, Aldrich). Ethylene oxide (99.5+%, compressed gas, Aldrich) was purified by successive distillations with di-*n*-butylmagnesium (1.0M in heptane, Aldrich). *sec*-butyllithium (1.3M in cyclohexane/hexane, Fisher) was used as received. 3-chloroperoxybenzoic acid (MCPBA, 70-75%, Acros Organics)

was dissolved in t-BuOH and dried twice over anhydrous sodium sulfate. Naphthalene (Fisher) was recrystallized once from diethyl ether. Potassium metal (98%, Fisher) was cut into pieces under light mineral oil and fresh non-oxidized metal surfaces were obtained by washing in a pentane for 30s. Potassium naphthalenide solution was prepared by dissolving excess (1.1x) recrystallized naphthalene and freshly cut potassium in tetrahydrofuran (THF) under argon. The dark green solution was allowed to stir overnight with a glass spinbar before use. (4-iodophenyl) diphenylsulfonium triflate (IPDPST) photo initiator was purchased from Aldrich and used as received. α,α' -Dibromo-p-xylene (98%, GC Purum Fluka) was vacuum dried for a hour. All other common chemicals were used as received unless otherwise stated. THF was degassed by sparging with argon (10 psi) for a period of 45 minutes and then purified over two molecular sieve columns of neutral alumina (Glass Contour, Inc.) Cyclohexane (CHX) was degassed with argon and purified through a column of neutral alumina followed by a column of Q5 copper(II)oxide catalyst (Glass Contour, Inc.). Ultra high purity argon (99.998% Airgas) was passed through a column of 5Å molecular sieves with drierite (Agilent) and an oxygen absorbing purifier column (Matheson Tri-gas). All glassware and polymerization reactors were flamed under vacuum and backfilled with argon (3x).

4.2.2 Physical and Analytical Measurements

^1H NMR spectra were recorded on a Varian Inova 400 MHz spectrometer with a pulse delay of 25s to ensure complete relaxation of end groups. The spectra were referenced to the residual protio solvent (CHCl_3). Gel permeation chromatography (GPC, also referred to as size exclusion chromatography, SEC) was performed on a Viscotek GPC-Max chromatography

system outfitted with three 7.5 x 340 mm Polypore (Polymer Laboratories) columns in series. The columns were maintained at 40°C or 55°C in an Alltech column oven depending on the mobile phase. The GPC system was attached to a Viscotek differential refractive index (RI) detector. All polymer samples were run in THF or DMF (mobile phase, 1 ml min⁻¹).

4.2.3 Dynamic Mechanical Spectroscopy

Rheological experiments were run on a TA Instruments ARES rheometer. Samples were formed as discs (8mm) and put between two parallel plates. In UV photo curing experiments, the upper plate was a 20 mm quartz parallel plate attachment with a 45° reflecting mirror (used to direct the light from the source to the sample) and the lower plate was a peltier attachment. The gap between two plates was adjusted to ensure even distribution of the sample. Typical gaps were 0.2 - 0.5 mm. A Hamamatsu Lightning Cure LC8 UV spot cure system was utilized with a 200W mercury xenon lamp, synthetic silica light guide, and short focal point condenser lens. Dynamic temperature ramp tests were performed while heating and cooling at 1°C min⁻¹ at angular frequency of 1 rad s⁻¹ and a strain of 0.5 - 2.0% (depending on the linear viscoelastic regime).

4.2.4 Small Angle X-Ray Scattering (SAXS)

Scattering data was collected on a Rigaku S-Max 3000 High Brilliance three pinhole SAXS system outfitted with a MicroMax-007HFM rotating anode (CuK α), Confocal Max-Flux Optics, Gabriel multiwire area detector, and a Linkam thermal stage. Polymer samples were

sandwiched between Kapton discs. Exposure times for uncured samples were typically on the order of 1200–3600 s. Cured sample exposure times varied between 3600–10800s.

4.2.5 ω -hydroxy-polyisoprene (PIOH)

Anionic polymerization of isoprene (30.8 g, 12 hrs) was initiated with sec-butyllithium (3.03 mL, 1.28 M) in 1L of cyclohexane at 40°C under a positive argon pressure of 5 psi. Ethylene oxide (1.7g, 20 hrs) was added as an end-capping agent. The terminal alkoxide was quenched with methanol (25 mL), and the cyclohexane polymer solution was reduced to 500 mL on a roto-evaporator. The product was precipitated from 4:1 MeOH:EtOH solution (2.5L). The polymeric alcohol was redissolved in THF and freeze-dried in vacuo (25°C, 7 days). The recovered product was a sticky clear viscous liquid, 30.2 g (98%). SEC (Polystyrene standards): $M_w/M_n = 1.06$. M_n (calc. From ^1H NMR integrations) = 8450 g mol⁻¹.

4.2.6 ω -hydroxy-polyisoprene-*b*-poly(ethylene oxide)(PI-PEO)

PIOH (4.80g) was dissolved in 500 mL dry THF. The solution was titrated with potassium naphthalenide until a light green color remained for at least 5 min at 40°C. Ethylene oxide (46.2g, 20hrs) was added to the reactor under a slight positive pressure of argon (1 psi), the solution immediately went from light green to clear. The terminal alkoxide was quenched with 25mL of methanol. Then the polymer solution was reduced to 200 mL on a roto-evaporator. The block copolymer alcohol product was precipitated from pentane (2L). Filtration and drying in

vacuo (25°C, 24 hrs) resulted in a white elastic solid as the product. Yield= 46.4 g (91%). SEC (Polystyrene standards): Mw/Mn = 1.08.

4.2.7 ω -hydroxy-polyisoprene-*b*-poly(ethylene oxide)- ω -hydroxy- polyisoprene (PI-PEO-PI)

PI-PEO (7.0g) was dissolved in 750mL of THF and titrated to a light green color with potassium naphthalenide under argon. α,α -Dibromo-*p*-xylene was dissolved in THF (2.08 mL, 0.024 M, 1:0.5 eq PI-PEO: α,α -Dibromo-*p*-xylene), and was added at a rate of 0.1 mL h⁻¹ with a Chemu Fusion 200 syringe pump to the titrated PI-PEO flask. The copolymer mixture was precipitated from pentane (1.5L, -20°C). After filtration and drying in vacuo (25°C, 48 hrs), the copolymer was an off-white elastic solid. Yield = 5.7g (82 %). The copolymer mixture was 22 mole % triblock (calculated from SEC peak integrations).

4.2.8 Standard procedure for epoxidized polyisoprene-*b*-poly(ethylene oxide)- polyisoprene (*e*PI-PEO-*e*PI)

A PI-*b*-PEO-*b*-PI triblock and PI-*b*-PEO diblock blend was dissolved in a 20:1 t-BuOH:CH₂Cl₂ mixture. For a targeted epoxidation of 80% of the olefins on PI, an equal number of moles of MCPBA was used. The calculated amount of MCPBA, dissolved in t-BuOH and dried twice with anhydrous Na₂SO₄, was added to the polymer solution and stirred for 20 hrs at 50°C. The reaction mixture was then filtered with a 0.22 micron filter. Filtrate was washed with Na₂CO₃ (2x), followed with DI water (3x), and then dried with anhydrous Na₂SO₄. The product was then precipitated in an excess of pentane. The precipitated product was isolated and dried in vacuo

(25°C, 48 h). This reaction yielded the epoxidized blockcopolymer blend as an off-white solid. Yield: 20 - 40% (highly epoxidized products become more and more miscible with water). The product was characterized with ^1H NMR and SEC chromatography.

4.2.9 General procedure for preparing samples for photocuring

Epoxidized diblock and triblock copolymer blend samples were co-dissolved with 1 mol% (relative to modified and unmodified PI repeat units) IPDPST in a 5:1 benzene:chloroform mixture and freeze-dried overnight. The resulting blend was then melt pressed into discs (8mm diameter, ~0.2 mm thickness) at 100°C for 15mins. The sample disc was placed (centered) on a TA instruments rheometer outfitted with a peltier and a quartz parallel plate attachment. The sample was heated to 95°C prior to cure and held at the same temperature during the curing. All experiments were conducted under argon. The intensity at the cure site was 90 - 100 mWcm^{-2} (measured in the range of 230-410nm with a Con-Trol- Cure Silver Line UV-radiometer).

4.3 RESULTS AND DISCUSSION

4.3.1 Block copolymer blend synthesis and characterization

A single ω -hydroxy-polyisoprene(PIOH) was used as the basis for all studies in this chapter. The PIOH parent molecule was synthesized by anionic polymerization of isoprene

monomer, initiated with *sec*-butyl lithium, end capped with single ethylene oxide unit and terminated with methanol to give the terminal hydroxyl functionality. The procedures used were identical to those documented in a previous publication from our group^[4]. ¹H NMR and the SEC chromatography allowed the efficient characterization of the product. A molecular weight of 8450g/mol (DP = 125) was calculated using end group analysis of ¹H NMR, and the SEC chromatogram calibrated using PS standards verified a narrow poly-dispersity index (PDI) of 1.06. (Figure 4.1)

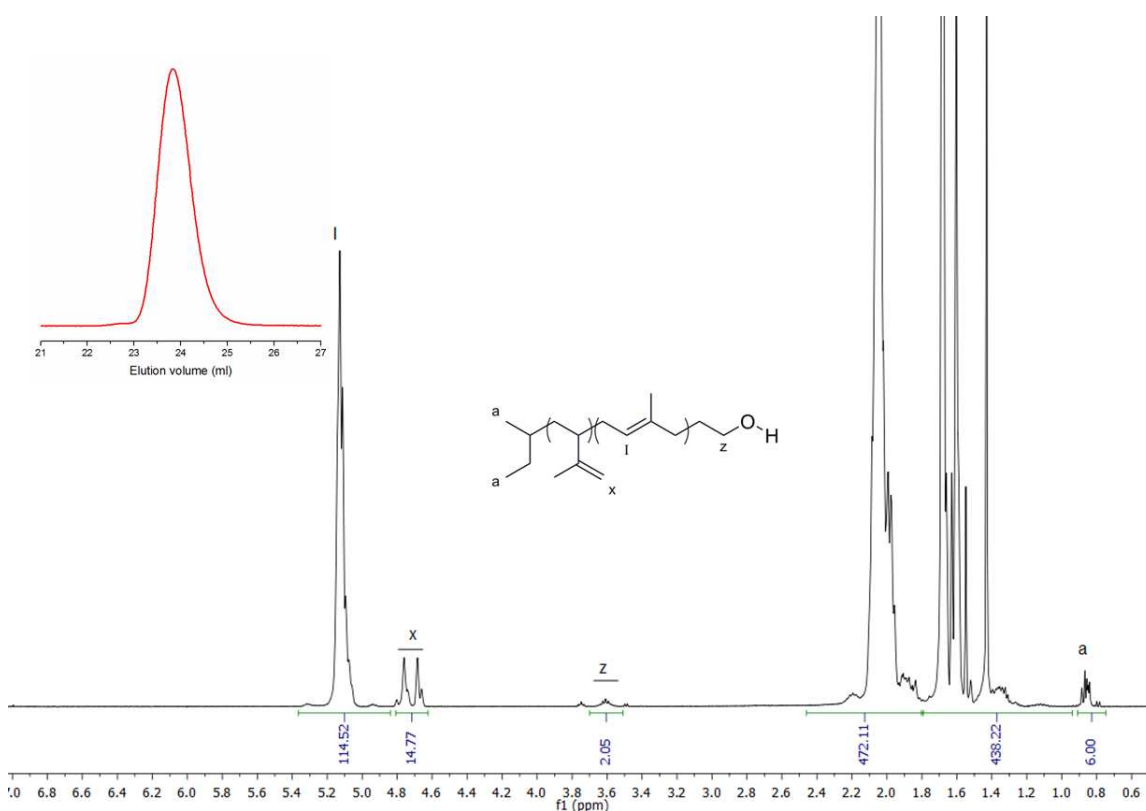


Figure 4.1 ¹H NMR and SEC data for anionically polymerized isoprene capped with single EO unit. The molecular weight of the resulting PIOH parent molecule was calculated utilizing end group analysis (utilizing normalized peak integral ratios of **x** and **I**, relative to the normalized peak integral of the initiator fragment, **a**).

The PI-*b*-PEO (referred as IO hereafter) diblock copolymer used was synthesized by anionic ring opening polymerization of ethylene oxide utilizing the parent PI-OH as a

macroinitiator. The PIOH could be activated for anionic polymerization through facile deprotonation of the terminal hydroxyl using quantitative titration with potassium naphthalenide to generate the initiating system. A final molecular weight of 92350g/mol was calculated by analyzing the ^1H NMR spectra of the product, and the narrow PDI of 1.08 was derived from the SEC chromatogram of the product (Figure AII.1, Addendum II). The targeted volume fraction of PEO ($f_{\text{PEO}}=0.89$) was confirmed by ^1H NMR spectroscopy. Small angle x-ray scattering was used to characterize the morphology of this diblock copolymer (Figure 4.2).

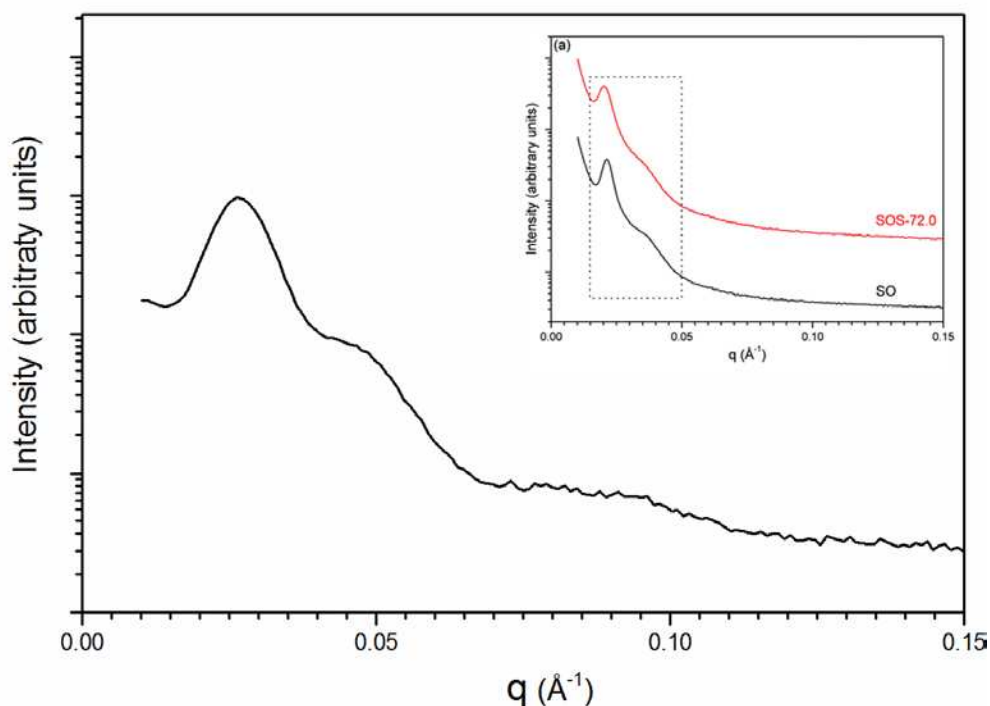


Figure 4.2 SAXS data for IO showing a scattering pattern consistent with liquid-like packing (LLP) of spheres. For comparison, the inset depicts SAXS data of an analogous SO system of similar molecular weight and composition determined to also adopt a LLP of spheres, described previously by Guo et al.^[17]

The existence of the prominent (Bragg) scattering peak at a low q (at 0.0263 \AA^{-1}) is indicative of some lattice-like (i.e., bcc-like, given the very asymmetric volume fraction and known phase diagram for AB diblock copolymer systems) character on the local scale, but the

prominent shoulder (and lack of higher order Bragg reflections) at the same time indicates significant disorder, or liquid-like packing, when longer-range organization is considered. This liquid-like packing of spheres is here after denoted by S_{LLP} . For large molecular weight block copolymer systems liquid like packing is quintessential^[10-13]. Larger molecular weight systems in general and sphere-forming systems in particular, often kinetically hindered from forming phase-separated structures with long-range periodic order^[14-16].

The inset of Figure 4.2 is adapted from a previous publication by Guo et al.^[17] and depicts the SAXS data collected for a PS-*b*-PEO (SO) diblock copolymer with similar molecular weight and block composition to the PI-*b*-PEO (IO) considered here. That data has been closely fitted to the Percus-Yevik (PY) model^[18] of polydisperse solid spheres, through which key dimensional characteristics of the structure could be extracted. A similar analysis on SAXS data of IO would provide similar structural details, but was not performed for this sample due to the extensive data collection and analysis required. However, Guo et al. showed that a rough estimation of the dimensions of these spherical PI domains is possible by simply assuming the localized bcc lattice structure is representative of the sample. In such a case, the principal scattering wave vector is taken to be the first allowed reflection of the Im3m (bcc) space group (q_{110}). Calculations based on this assumption were used to analyze the IO sample and are presented later in this chapter.

The next step was development of a PI-*b*-PEO-*b*-PI (referred to as IOI hereafter) triblock copolymer with lattice-matched symmetry to the IO diblock copolymer. A good approximation for matching the lattice dimensions adopted during self-assembly between AB diblock and ABA triblock copolymer is to simply couple the diblock copolymer. While there is some computational evidence that the phase diagrams do not entirely overlay for such systems, the

distinctions are quite minor. Thus, a coupling reaction of IO diblock copolymer was used to form IOI triblock copolymer. In general, these types of coupling reactions with high molecular weight polymer systems are never quantitative, resulting in a mixture of (uncoupled) diblock and (coupled) triblock copolymers. Several reactions were carried out. The diblock and triblock copolymer blends that resulted were named as IOI_{xx} where xx indicates the triblock copolymer mole percent in the blend. Diblock and triblock copolymer mole percentages in the product were calculated using SEC peak integrations. The SEC data is shown in Figure 4.3.

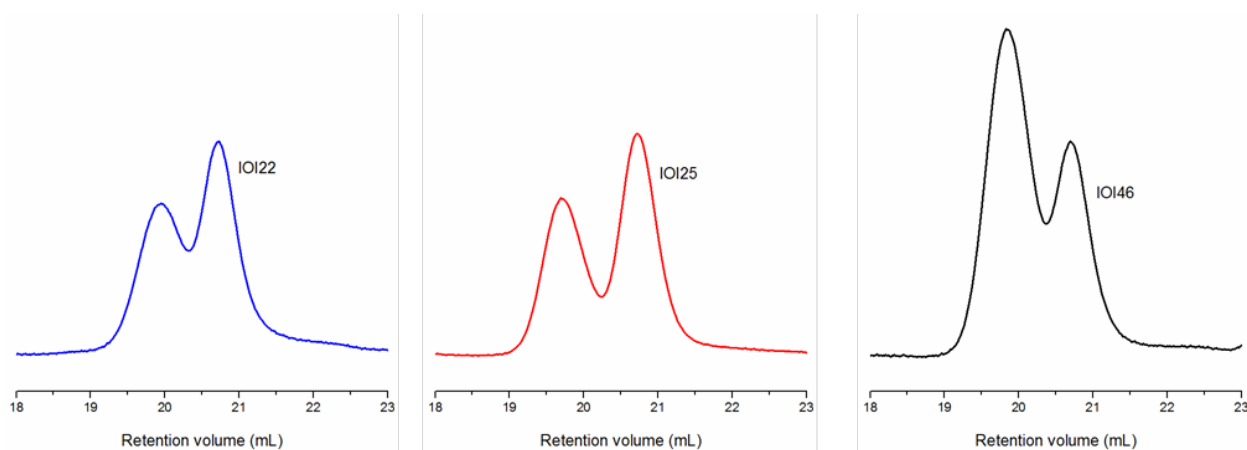


Figure 4.3 SEC chromatographs of the three BCP blends; IOI₂₂, IOI₂₅ and IOI₄₆. SEC traces are normalized to the height of the diblock peak for the ease of comparison. All the samples were run in THF as the mobile phase at 40°C.

Three coupling reactions were run at three different times. The degree of coupling for each run was different even though the same reaction conditions were used for all three experiments. The efficiency of coupling reactions applied to macromolecule chain ends is highly susceptible to the adventitious concentration of impurities present in the system. This is the probable cause of differences in the coupling efficiencies obtained in the three independent coupling reactions carried out.

The morphology of the resulting IOIxx blends was then characterized using SAXS (Figure 4.4 -data in green). All three blends show a well-developed, prominent principal scattering peak at low q , and a slight shoulder at higher q , but no higher order scattering peaks can be distinguished. As discussed previously, the form of the scattering profile is characteristic of the classical liquid-like packing of spheres (S_{LLP}) so prominent in this region of the phase diagram (very asymmetric volume fractions ($f_{PS} < 0.14$)). Given the S_{LLP} behavior exhibited by the IO diblock copolymer, a similar morphology and scattering is anticipated for the IOIxx blends. Notably, the addition of the triblock copolymer does reduce the definition in the LLP structure factor when compared with the analogous neat diblock copolymer samples. It is reasonable to assign this change in the structure factor with the loss in kinetic mobility expected in the system with the addition of a significant fraction of even higher molecular weight IOI chains (2x the molecular weight of the IO).

Figure 4.5 shows the melt-state rheological properties, in this case given by a dynamic temperature ramp test (DTRT), for the IOI25 blend. The dynamic temperature ramp test is performed by performing oscillatory shear on a polymer sample in the melt state using a fixed strain (here, 2%) and frequency of oscillation (1 rad s^{-1}), and allowing the temperature to be ramped at a constant rate (1°C min^{-1}). The IOI25 blend exhibited elastic moduli in the 10^5 Pa range (typical of ordered block copolymer melts up to 150°C). The transition visible at 65°C corresponds to the PEO crystal melt transition^[2]. The largely plateau behavior in both elastic and loss modulus is prototypical for an ordered spherical morphology. According to the data this material (IOI25) shows no observable phase transitions below 300°C . An order to disorder transition (ODT) was observed around 310°C , although this is beyond what is typically considered an experimentally viable temperature range for these measurements. That is, above

about 250°C, sample degradation can influence observed behaviors and so transitions above this temperature must be considered cautiously. It is evident that the polyisoprene based BCP system has improved flow resistance over the polystyrene based system, as indicated by a significantly higher ODT temperature (310 °C versus 225°C). This is consistent with the larger Flory-like interaction parameter (χ) between PI and PEO, as compared with that between PS and PEO in the previously studied system.

Once synthesis and morphological characterization of all blends was complete, the next step was to determine the feasibility of selectively cross-linking PI domains. First, incorporation of a cross-linkable epoxide moiety into the PI domains was attempted, and the effect of that modification on the molecular weight distribution and subsequent melt-state self-assembly of the blends was systematically studied using SEC chromatography and SAXS analysis.

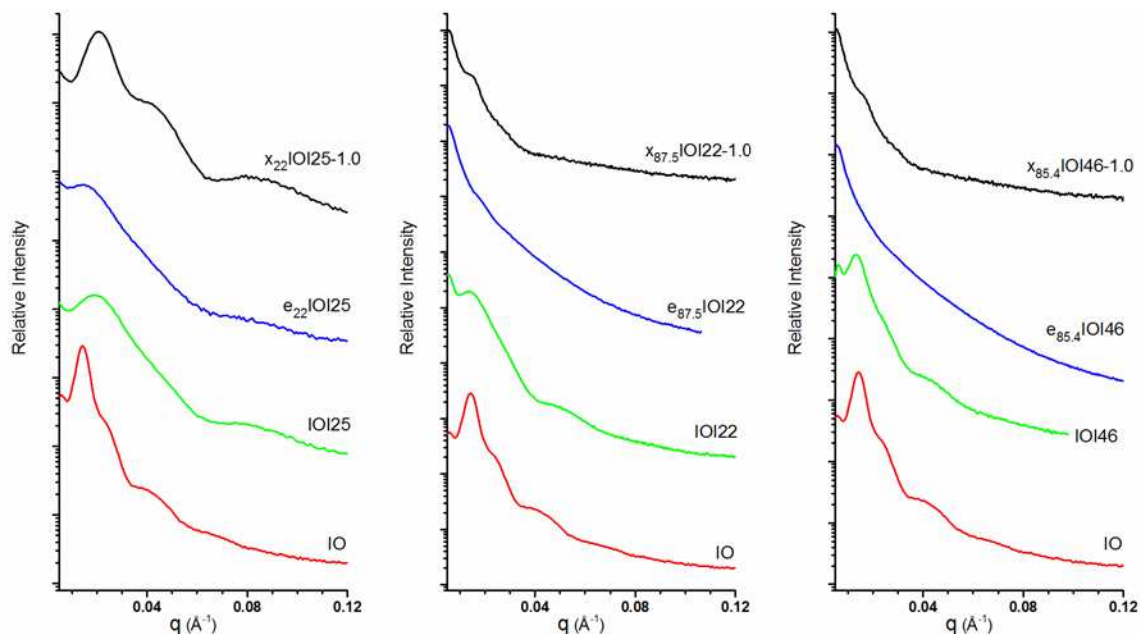


Figure 4.4 SAXS data for each of the three native coupling reaction products, their epoxidized state prior to crosslinking, and their final cross-linked form, each collected at 100°C. Data was collected on samples that were annealed at 100°C, 175°C, and 225°C for 1hr prior to analysis, however the results are shown only at 100°C here. All three blends show the same trends in phase separation behavior as they go through the process of epoxidation (loss of phase separation) and photo-initiated cross-linking (recovery of phase separated state) of the PI spherical domains.

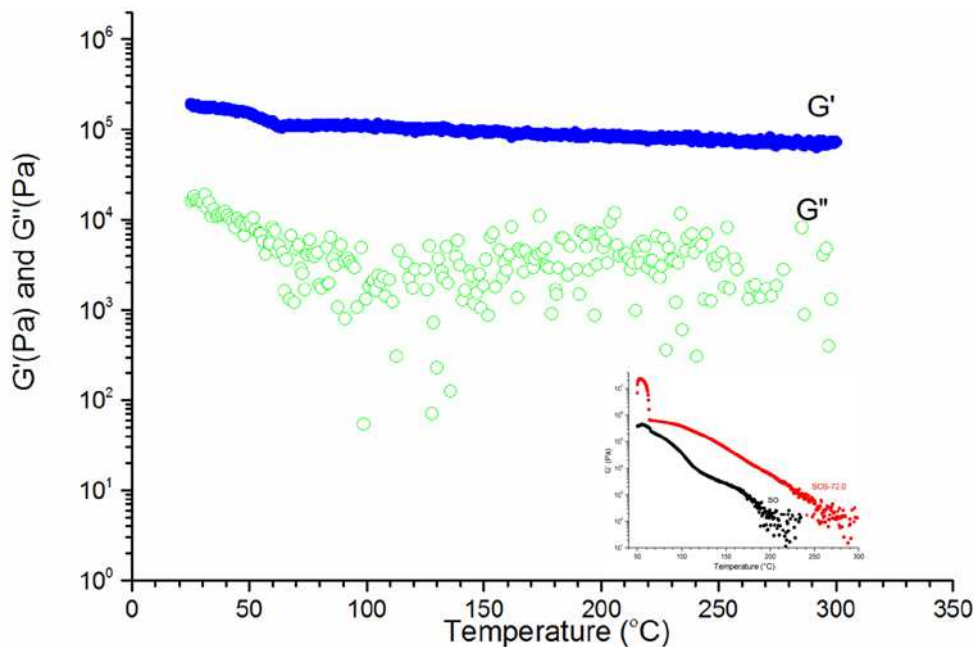


Figure 4.5 Dynamic temperature ramp test (DTRT) data for IOI25. Data were collected at $1^{\circ}\text{C min}^{-1}$ (while heating) at a frequency of 1 rad s^{-1} and a strain of 2%. The inset is DTRT data for an analogous SOS72 system (red) of similar block molecular weights and PEO volume fraction described in the publication by Guo et al^[17].

4.3.2 Epoxidation of block copolymer blends and characterization

Controlled partial epoxidation of the olefin units in the 1,4 repeat units of polyisoprene in the blends was attempted following procedures documented in a previous publication by our group^[4]. In order to explore the optimum cross-link density needed within the PI domains, incorporation of different concentrations of epoxy groups into the PI block was investigated.

The initial goal was to epoxidize 20% of the olefin units in the PI blocks of the IOI25 blend. Treatment with MCPBA, a common reagent used in the transformation of alkenes to epoxides, in methylene chloride resulted in the successful epoxidation of PI repeat units with a product yield of about 85%. ^1H NMR spectra of the product (Figure AII.2, Addendum II) confirmed a degree of epoxidation ($\sim 22\%$) consistent with the targeted value. The product of this

epoxidation is referred to as e₂₂IOI25, with the prefix denoting the percent epoxidation as 22%. This convention is used with all epoxidized blends discussed within this chapter.

In an attempt to epoxidize 100% of the olefin units in the PI chains, only 87.5% conversion was achieved (confirmed with the ¹H NMR in Figure 4.6). Likewise, a targeted epoxidation of 45% resulted in only 40% epoxidation of the chains. Resonances in the 1.90 - 2.25 ppm range, which correspond to the methyl and aliphatic protons in polyisoprene repeat unit show a change in the relative peak shapes and intensities. This is likely due to the increased oxygen incorporated within the polyisoprene backbone as a result of introducing the epoxide groups. As discussed in the caption of Figure 4.6, the percentage of epoxidation could be calculated by comparing the peak integral corresponding to the methyne proton in the oxirane ring in epoxidized PI repeat units (**e**, 2.6 – 2.8 ppm) with the residual vinyl protons left in the unmodified PI repeat units. (**I, x**, 4.6 – 5.2 ppm).

Isolation of the product was found to be very challenging at high levels of epoxidation, with the removal of benzoic acid formed during the epoxidation reaction being particularly difficult when the epoxidations were carried out in CHCl₂. To circumvent this issue, we changed the reaction solvent from CHCl₂ to t-BuOH to induce direct precipitation of the benzoic acid during formation, given its limited solubility in t-BuOH. This modification to the previously established protocol for epoxidation^[4] helped to separate the majority of the benzoic acid, but not removal was not quantitative. Residual benzoic acid was then neutralized by washing with Na₂CO₃ and finally DI water. This protocol was successful in removing the excess benzoic acid, however, product yield was increasingly compromised with each washing due to the increasing affinity of the epoxidized P blocks for the aqueous layer.

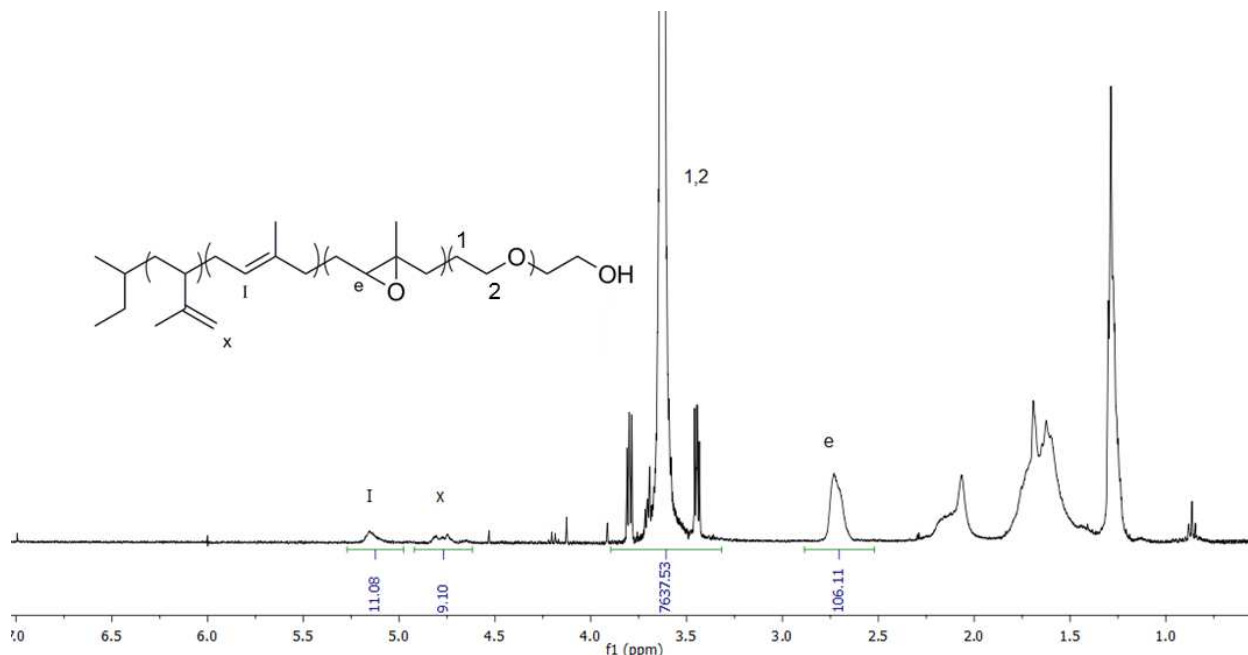


Figure 4.6 ^1H NMR of $e_{87.5}\text{IOI22}$. The percentage of epoxidation was calculated by comparing the peak integrals corresponding to methyne proton in the oxirane ring in epoxidized PI repeat units (**e**) with the residual vinyl protons left in the unmodified PI repeat units (**I**, **x**). ($= \text{Int}(\mathbf{e}) / [\text{Int}(\mathbf{e}) + \text{Int}(\mathbf{I}) + \text{Int}(\mathbf{x})/2]$)

As with epoxidation of the IOI25 blend, targeting 100% epoxidation of all olefin units in the PI blocks of the IOI46 blend resulted in an actual epoxidation of only 85.4%. This degree of epoxidation was calculated from the ^1H NMR of the product (Figure AII.3, Addendum II). Notably, it seems the conversion efficiency (efficiency of transforming the olefin units to epoxides) decreases as more epoxy units start to present on the PI block. When only 20% of the olefin units were targeted, 100% conversion efficiency was achieved simply adding stoichiometric amounts of MCPBA.

In contrast, the addition of stoichiometric amounts of MCPBA, when targeting higher epoxidation levels was not as efficient, with the reactions targeting epoxidation of 40% of the olefin units giving conversion efficiencies just shy of 90%, while reactions targeting 100% epoxidation resulted in conversion efficiencies consistently in the 85.4 - 87.5% range. While it is

feasible to increase the amount of MCPBA in these reactions, it is not clear that such an approach would improve conversion. It is likely that as the epoxidation levels increase along the polymer backbone, the steric hindrance to further epoxidation becomes significant and may slow the reaction kinetics severely.

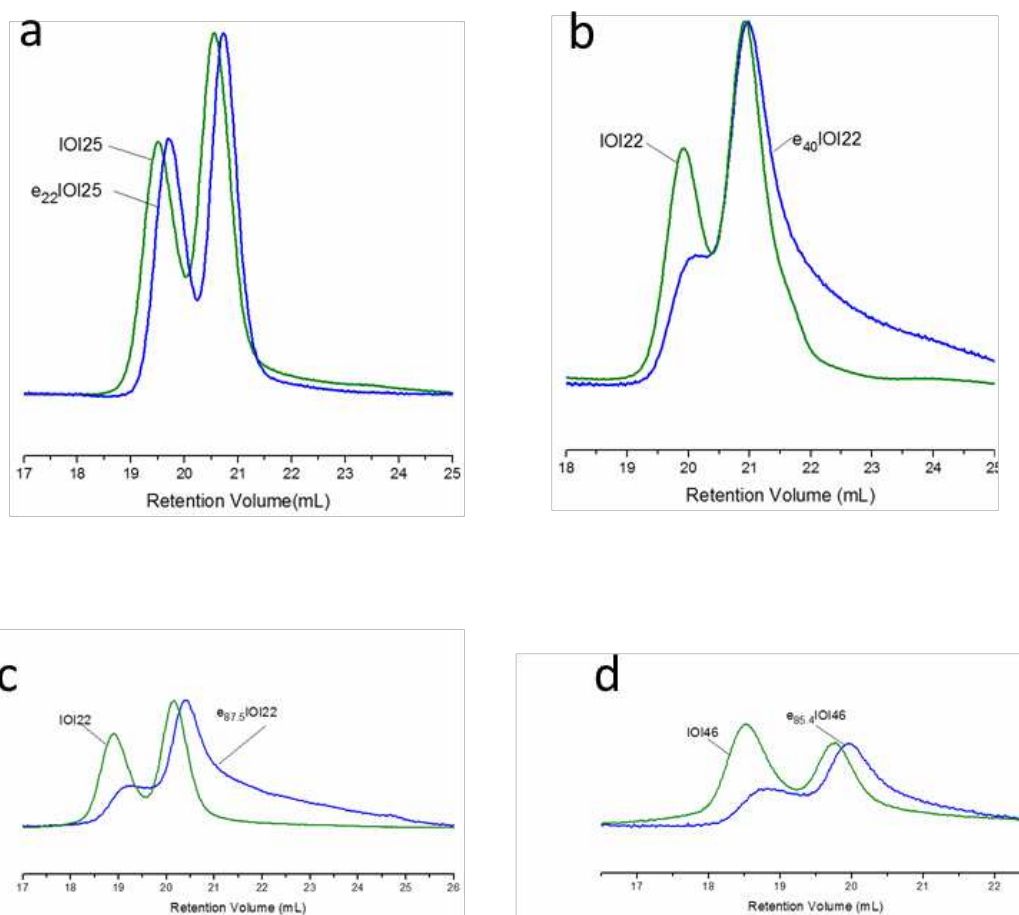


Figure 4.7 SEC analysis examining the effects of epoxidation modification on molecular weight distribution. a) Comparison of SEC chromatograms of the IOI25 system, run in THF as mobile phase at 40°C. IOI25 and e₂₂IOI25 share the same chain-size distribution that verifies no chain degradation after partial epoxidation step. b) Comparison of SEC chromatograms of IOI22 and e₄₀IOI22, run in THF at 40°C. A significant change in molecular distribution is present from IOI22 to e₄₀IOI22. c) Comparison of SEC chromatograms of IOI22 and e_{87.5}IOI22, run in DMF at 55°C. Poor solubility of e_{87.5}IOI22 in DMF required dilute samples, producing a lower signal to noise ratio. d) Comparison of SEC data for IOI46 and e_{85.4}IOI46, run in DMF at 55°C. Poor solubility of e_{85.4}IOI46 in DMF required very dilute samples, again limiting the signal to noise ratio in the data.

In total, four epoxidized blends were studied: e_{22} IOI25, e_{40} IOI22, $e_{87.5}$ IOI22, and $e_{85.4}$ IOI46. All epoxidized products were also characterized with SEC chromatography (Figure 4.7). As shown, the molecular weight distribution given by the SEC chromatogram of e_{22} IOI25 closely matched that of the unmodified IOI25, showing only a slight shift in the distribution to the right (Figure 4.7a). The shift to the right implies that the modified IOI25 (i.e., e_{22} IOI25) has a smaller hydrodynamic volume than the unmodified IOI25, despite the increase in molecular weight associated with the epoxidation of the olefin units. This further implies that as the oxygen content in the polydiene backbone is increased, the solubility of the chain in THF is decreasing causing some degree of collapse in the swollen chain conformation.

SEC data for $e_{87.5}$ IOI22 and $e_{85.4}$ IOI46 (Figure 4.7b, 4.7c and 4.7d) suggest the epoxidation modification with MCPBA has affected the molecular distributions of the starting material. In all cases of more than 22% epoxidation, two major changes to the original molecular distribution are visible. The first is the diminishing intensity of the peak corresponding to the triblock copolymer, and the second is increasing degree of tailing on the peak corresponding to the diblock copolymer chains. The first change may be due to the decoupling of triblock copolymer chains as an undesirable effect of the epoxidation conditions. The effective triblock copolymer mole percentages remaining after the modifications were calculated to be 4.6 mol% and 9.7 mol% for $e_{87.5}$ IOI22 and $e_{85.4}$ IOI46 respectively (compared with 22 mol% prior to modification). The loss of triblock copolymer following modification has a direct impact on the mechanical properties of the ultimate swollen network (using RTIL or water as a swelling solvent). As seen in Chapter 3 and the earlier publication from Guo, C. et al^[17], the mechanical strength of the swollen network is strongly correlated to the tether (triblock copolymer) concentration connecting the spherical domains in the molecular assembly of these BCP systems.

The tailing of the diblock copolymer peak is most probably caused by undesirable molecular interactions between oxygen (from epoxy groups) and the column packing, although this behavior may also be influenced by residual salts remaining following the acid neutralization and washing steps. We have experienced this effect on several other occasions with modified PEO chains.

The shift to the right of the whole molecular weight distribution after modification is also common to all three blends. As mentioned above, this common effect implies a lower hydrodynamic volume for the modified chain, as compared with unmodified chains. Since the addition of oxygen in increasing molecular weight, it appears the increase comes at the expense of reduced solubility in THF (and DMF), or a change in overall chain flexibility resulting in (perhaps counter-intuitively) a collapse in the swollen chain conformation.

The SAXS data of the epoxy-modified blends were previously included in Figure 4.4, together with the scattering observed for the unmodified systems. Notably, the SAXS data of the epoxy-modified systems shows a further decay in the scattering profile, with a partial to complete disappearance of the broad shoulder typical of the of S_{LLP} structure factor. A principal peak and broad hump persists in the case of lower epoxidation levels, as shown in the scattering of the e₂₂IOI25 blend, however, at very high epoxidation degrees (e_{87.5}IOI22 and e_{85.4}IOI46), the complete loss of any significant scattering signature occurs. It is believed that as more epoxy groups are incorporated into PI blocks, the chemical signature (increased oxygen in particular) of the ePI units becomes more like that of PEO. When the different blocks of a block copolymer become more alike in their chemical structure, the energy penalty of mixing often decreases and the material will be less likely to phase separate. Thus, it appears that the epoxidation is having the impact of compatibilizing the two blocks. In addition, the contrast (electron density

differences between the two blocks) may also be diminishing, reducing the ability of the system to scatter X-rays. Even though the modified blends were confirmed to lack a clear S_{LLP} morphology, we decided to continue the studies on feasibility of cross-linking these blends in melt state and in the presence of acid forming photo-initiator IPDPST. As is discussed below and can be seen in Figure 4.4, the cross-linking reaction appears to re-induce phase separation.

4.3.3 Photo cross-linking and swelling studies on each block copolymer blend

4.3.3.1 IOI25

As described in an earlier publication from our group, selective photo-crosslinking of PI domains to preserve the melt-state morphology was possible using onium salts^[4]. IPDPST is a thermally stable (up to 200°C) onium salt that has been used for initiation of cationic polymerization of epoxy groups on the PI block. The efficacy of this method in preserving the melt-state morphology of block copolymer systems with higher molecular weight blocks was examined using the epoxy-modified IOI blends.

The e_{22} IOI25 polymer blend, in which some degree of ordering (S_{LLP}) was present according to the SAXS data, was solution blended with the IPDPST photo initiator, freeze dried, and exposed to broad band UV light following a protocol established by our group previously^[4]. The amount of the IPDPST photo initiator added was 1.0 mol% of the total olefin units present in the unmodified IOI25 blend. Samples containing IPDPST hereafter are referred to using a suffix to denote the amount of photoinitiator in the blend. For example, the sample just described containing 1 mol% IPDPST is denoted e_{22} IOI25-1.0. Once exposed to UV to initiate the cross-

linking reaction, the “e” in the prefix is changed to “x” to denote the sample is now crosslinked. For the sample above, the designation following UV exposure is denoted $x_{22}\text{IOI25-1.0}$.

The $e_{22}\text{IOI25-1.0}$ samples were pressed into discs, photo cross-linked and then swollen in DI water and $[\text{EMIM}][\text{Tf}_2\text{N}]$. In both cases, the discs did not dissolve, which confirmed the chemical crosslinking. In contrast, non cross-linked $e_{22}\text{IOI25-1.0}$ was easily “dissolved” in water to form a heterogeneous, slightly cloudy solution.

Cross-linked $e_{22}\text{IOI25-1.0}$ samples ($x_{22}\text{IOI25-1.0}$) swollen in water to form hydrogels retained their shape but the mechanical properties were poor to an extent that did not allow any meaningful, quantitative mechanical testing to be performed on them. The swelling ratio in water (Q) for the $x_{22}\text{IOI25-1.0}$ sample was 11.9 g $\text{H}_2\text{O}/\text{g}$ polymer. The disk swollen with $[\text{EMIM}][\text{Tf}_2\text{N}]$ also retained its shape while submerged in the excess RTIL. However, once taken out of the RTIL, it could no longer retain its shape, and collapsed much like weakly cross-linked gelatin.

For purposes of comparison, two samples taken from the previously published studies from our group were examined. These samples consisted of sphere-forming blends of polybutadiene-*b*-poly(ethylene oxide) diblock copolymer and polybutadiene-*b*-poly(ethylene oxide)-*b*-polybutadiene triblock copolymer (BOB11.5) in which 20% PB olefin units were epoxidized. The samples, previously blended with 0.5mol% IPDPST ($e_{20}\text{BOB11.5-0.5}$), were exposed to UV under the same conditions we maintained for our previous experiments with the eIOI blends. Characterization data of this particular material ($e_{20}\text{BOB11.5-0.5}$) can be found in the publication by Scalfani et al^[2]. Cross-linked $x_{20}\text{BOB11.5-0.5}$ discs were then swollen in DI water and $[\text{EMIM}][\text{Tf}_2\text{N}]$. The resulting hydrogels showed better handling characteristics (qualitatively) compared to that made of $x_{22}\text{IOI25-1.0}$. The sample swollen in $[\text{EMIM}][\text{Tf}_2\text{N}]$

(ion gel), exhibited lower mechanical stability than the hydrogel made of the same material, however that difference in behavior is consistent with that found for SO/SOS based systems swollen in the two different solvents, as well. Additionally, the RTIL swollen x_{20} BOB11.5-0.5 sample was able to retain its shape during delicate handling, whereas the iongel based on x_{22} IOI25-1.0 was not able to do so.

The major differences between the two systems, e_{20} BOB11.5-0.5 and e_{22} IOI25-20-1.0 are 1) the block copolymer molecular weights, 2) the composition of triblock copolymer, and 3) the amount of photoacid used in the blend. The difference in molecular weight may be the most significant, as it gives rise to much different domain sizes within the spherical morphology formed. The diblock and lattice-matched triblock copolymers used in the e_{20} BOB11.5-0.5 blend are much lower in molecular weight (29.5kDa and 59 kDa, respectively) than that used in the e_{22} IOI25-1.0 blend (93kDa and 186kDa, respectively). Consequently, the derived (from the SAXS data) radii of the spherical PB and PI domains were 7.6 nm and 14.9 nm respectively^[2, 17]. In addition to producing smaller domain sizes, the degree of order achievable in lower molecular weight systems is significant with the e_{20} BOB11.5-0.5 blend able to form a very well-defined BCC packing of spheres (S_{BCC})^[2].

As we've discussed in an earlier chapter, the spherical domains are the anchoring points of the network and the integrity of the spherical domains is the key parameter that affects the mechanical properties of the hydrogels. Hence the degree of cross-linking of PI spherical domains should naturally influence their ability to withstand loading. In our SO/SOS systems, vitrification of the core, rather than cross-linking, was found to provide excellent core integrity at temperatures below the T_g and when water or [EMIM][Tf₂N] was the swelling medium. In those cases, with a solid core, we found that a large fraction (up to 90%) of the hydrogel modulus then

becomes attributed to the dynamic entanglements produced through overlap between the dense coronal PEO brushes emanating from adjacent spherical domains in the network. When the coronal chains are large, the population of dynamic entanglements is significantly greater than in low molecular weight systems, and gives rise to significantly enhanced mechanical performance. However, the mechanical properties of the hydrogels based on the x_{22} IOI25-1.0 blend, with much higher molecular weight PEO chains than those in x_{20} BOB11.5-0.5, were found to be *inferior* – directly contradicting this trend. This result implies degree of cross-linking in the cores was insufficient to completely solidify PI domains, such that the integrity of the core was the determining factor in the mechanical properties observed. However, the two blends do share identical concentrations of epoxide groups within the polydiene blocks. This effect is more likely due to the difference in sizes of the spherical domains of two samples. Since the degree of epoxidation on both samples were equivalent, it follows that not all of the epoxide sites within larger PI spheres are able to be cross-linked. Cross-linking is achieved using a cationic polymerization reaction (of the epoxides) initiated through light induced decomposition of IPDPST to form a protic acid. Hence efficient cross-linking requires that the protic species be generated in the vicinity of the ePI domains, such that access to the epoxide units is readily accomplished. At this juncture, it is not clear where the IPDPST resides within the sample, be it in the PEO domains, the PI domains, or distributed between the two. The protocol established by an earlier publication^[4] involving lower molecular weight PI blocks that were a larger fraction of the block volumes was to dissolve the block copolymer in benzene and the photoacid in CHCl_3 , mix the solutions, and freeze /vacuum dry the sample. However, after several experiments with this system, in which the PI block are higher in molecular weight but a smaller fraction of the sample composition, we found that the ratio of two solvents used has an effect on the efficacy of

photoacid. For this new system, the ratio of benzene to chloroform needed to be equal to or higher than 5:1 to achieve good cross-linking efficiency. We believe that transport (and retention) of IPDPST to the PI domains seems to be favored in benzene over chloroform. Anecdotally, we also concluded that traces of benzene present in the dry material also had the effect of diminishing the cross-linking efficiency. Obviously the drying step was critical to the successful crosslinking of ePI spherical domains. That being said, at 20% epoxidation, we were never able to achieve the mechanical stability exhibited by the much smaller x_{20} BOB11.5-0.5 system used as a comparison reference.

Finally, the x_{22} IOI25-1.0 sample was characterized with SAXS (Figure 4.4b). Characteristic S_{LLP} peaks are once again, present in the data. An interesting phenomenon discovered from the SAXS data was that cross-linking induced phase separation that had been previously lost with sample epoxidation (e_{22} IOI25-1.0). This trend has been observed previously in similar BCP systems^[19], and suggests that even the disordered systems retain some level of local organization. This retention of some degree of weak segregation is a hallmark of sphere forming block copolymers near or even beyond the order-disorder transition

As discussed earlier in this section, the amount of photo-initiator available to the ePI domains had direct impact on the degree of the cross-linking. In order to understand this further, a series of crosslinking studies was conducted on epoxy modified polyisoprene homo-polymer. These studies are discussed below.

4.3.3.2 PIOH

PIOH homopolymer (8450 g/mol) was modified such that 47.5% of the olefin units along the PI backbone were to be epoxidized. The product ($e_{47.5}$ PIOH) was characterized with ^1H NMR and SEC chromatography (Figure 4.9).

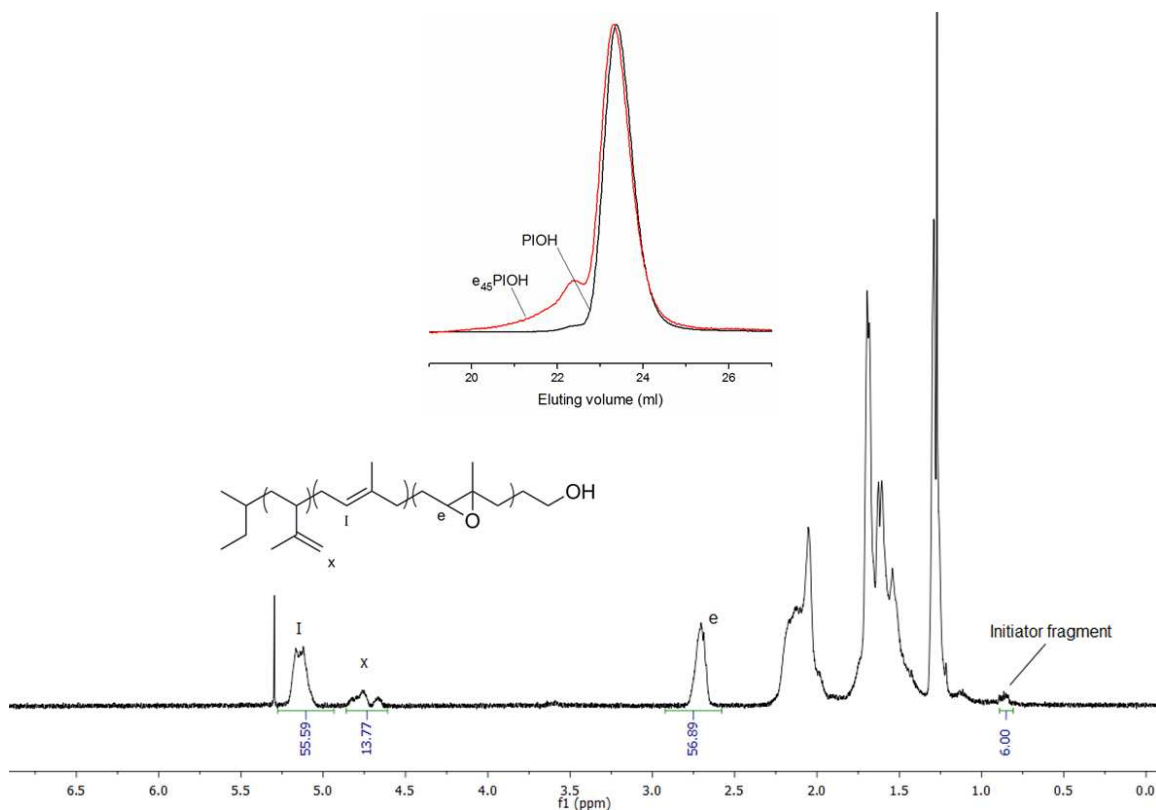


Figure 4.9 ^1H NMR and SEC data of $e_{47.5}$ PIOH. The percentage of epoxidation was calculated by comparing the peak integrals corresponding to methyne proton in the oxirane ring in epoxidized PI repeat units (**e**) with the residual vinyl protons left in the unmodified PI repeat units (**I**, **x**). ($= \text{Int}(\mathbf{e}) / [\text{Int}(\mathbf{e}) + \text{Int}(\mathbf{I}) + \text{Int}(\mathbf{x}) / 2]$)

As Figure 4.9 shows, the major fraction of the modified product closely follows the molecular distribution of the starting material (according to the SEC chromatogram). The small peak on the higher molecular weight side of the starting material is probably an indication of

some degree of cross-linking during the epoxidation. Interestingly, this phenomena seems to be predisposed to chain coupling, as indicated by the non-random higher molecular weight peak occurring at a location consistent with a molecular weight doubling event, and the lack of any lower molecular weight chain scission products eluting after the diblock copolymer. Such an undesirable side reaction may be the product of radical formation at high loadings of MCPBA or simply the nucleophilic attack of main epoxides by the terminal hydroxyls innate to each chain terminus.

Interestingly, the SOS22 membranes examined appear to exhibit a slightly higher average CO_2/N_2 selectivity when compared to the SOS46 composites when the behavior across all transmembrane pressures is considered. In contrast, the CO_2 permeability exhibits the inverse trend. While the inverse relationship itself, being consistent with the Robeson flux-selectivity tradeoff, is not entirely unexpected, that the membrane system containing the higher RTIL content (SOS22) should exhibit the lower permeability (but the higher selectivity) is not entirely obvious. As proposed earlier, it seems possible the role of RTIL mobility and liquid structure as a function of the PEO chain concentration throughout active layer may be playing an important role in the determination of ultimate gas separation performance. Different amounts of IPDPST photoacid (0.5, 1.0, 5.0 mole% of the olefins on PI) were added to e47.5PIOH by mixing solutions of the e47.5PIOH in benzene and the photoacid in CHCl_3 (5:1). Freeze drying of the combined mixture of polymer and photoacid on a Schlenk line was extremely slow and took about 10 days for 0.5g of polymer. This was primarily the consequence of requiring full removal of benzene from the viscous polymer liquid. Once dry, the three e47.5PIOH samples with differing amounts of photoacid (e47.5PIOH-0.5, e47.5PIOH-1.0 and e_{47.5}PIOH-5.0) were exposed to UV (mercury-xenon lamp) under the same experimental conditions described

previously. While curing these samples, their mechanical response under a small, constant-rate oscillatory shear was recorded in the form of a storage modulus (G') and a loss modulus (G'') with respect to time. Prior to the curing experiment, a dynamic strain sweep was performed on each sample in order to determine the linear viscoelastic region of each sample (prior to cure). All three samples showed a similar linear viscoelastic regime, where the moduli were independent of the strain and where the strain varied linearly with stress^[20, 21]. Actual measurements on all polymer samples were then initiated in their linear viscoelastic regime.

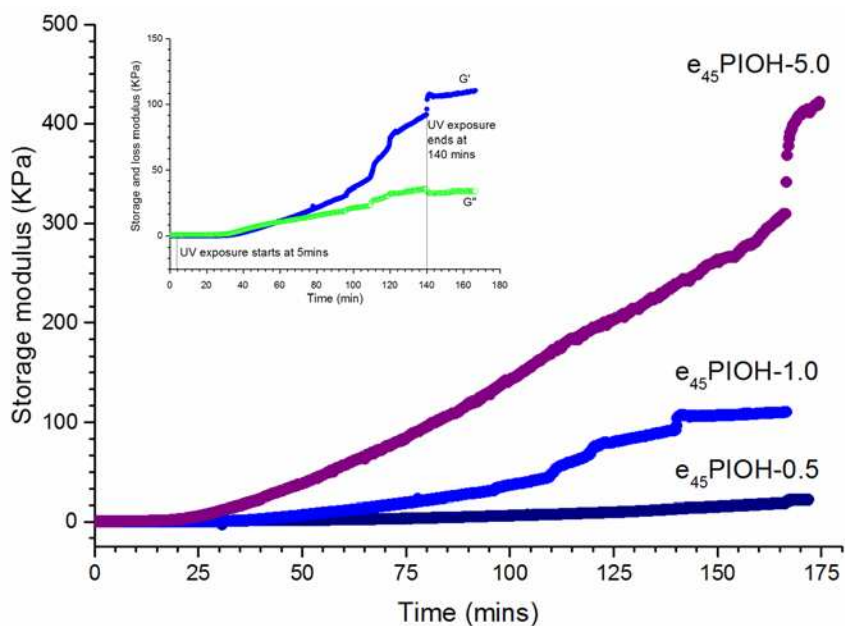


Figure 4.10 The storage modulus for e_{47.5}PIOH with 0.5 mol%, 1 mol% and 5.0 mol% IPDPST exposed to broadband UV (mercury-xenon lamp) under argon while under oscillatory shear (strain = 0.5%, frequency = 1 rad s⁻¹). Exposure to UV was started at 5 min and continued until 140 min. UV intensity was ~ 60 mW cm⁻² (measured in the range of 230-410 nm with a Con-Trol-Cure Silver Line UV-Radiometer. Inset shows the behavior of loss modulus with the increase of storage modulus for the e_{47.5}PIOH with 1.0 mol% sample.

Figure 4.10 shows variation of G' for the three samples as a function of time (dynamic time sweep test at a constant frequency of 1 rads⁻¹ and a constant strain rate of 0.5%). Upon exposure to UV, the photoacid degradation was expected to initiate the cationic

polymerization of the oxirane rings instantaneously with the propagation to additional oxiranes resulting in the crosslinking of the ePI chains. Cationic polymerizations are known for their extremely fast rates of reaction[4], which can favor rapid crosslinking. However, even at 15 mins of sample exposure to broadband UV (intensity at the curing site $\sim 60 \text{ mWcm}^{-2}$) we found the insufficient crosslinking to transform physical state of ePIOH from a viscous liquid to a solid. This delay may be explained by the limited solubility of the IPDTST causing it to phase separate into macroscopic aggregates during the drying process. Importantly, the mobility of the ePI chains at room temperature does not restrict the phase separation process. Ultimately, slow diffusion of the acid within highly viscous e47.5PIOH may be the culprit for the slow crosslinking kinetics. It is clear from the experiments that having more photoacid promote more rapid cross-linking.

Notably, e47.5PIOH-5.0 shows an increase in storage modulus at a nearly a constant rate of 240 Pa min^{-1} for a period of 140 min with a sudden gain of 106kPa in the 10 mins following the removal of UV light. In fact, all three samples experienced a sudden increase in moduli after the UV was removed. The cause of this sudden increase has not been determined, but may point to the possibility of “overexposure” that should be investigated further. It is known that the acid dissociation equilibrium can dramatically influence the kinetics of cationic polymerizations, and may be a factor here. After an exposure of 170 min to broadband UV, all three samples changed color from milky white to light yellow and changed texture from a viscous liquid to a more solid like paste. The photocured materials made suspensions in CHCl_3 whereas the pre-cured material dissolved easily in CHCl_3 . The inset of the Figure 4.10 shows both the storage and loss modulus changes of e47.5PIOH-1.0 with time. A decrease in loss modulus with a concurrent increase in storage modulus is consistent with what is classically expected for polymers undergoing a

crosslinking reaction. Based on the findings from this experiment (1.0% IPDPST), we decided to incorporate the same ratio of photoinitiator into the e87.5IOI22 and e85.4IOI46 samples and investigate mechanical property changes during cure.

4.3.3.3 IOI22

The e_{87.5}IOI22 was further characterized with SAXS prior to addition of photoinitiator (Figure 4.4b). SAXS data confirmed that the targeted periodic spherical morphology was disrupted by the epoxidation modification, which appeared to induce compatibilization of the two blocks. Despite this, investigating the photocrosslinking behavior of e_{87.5}IOI22-1.0 and e_{87.5}IOI22-5.0 was carried out.

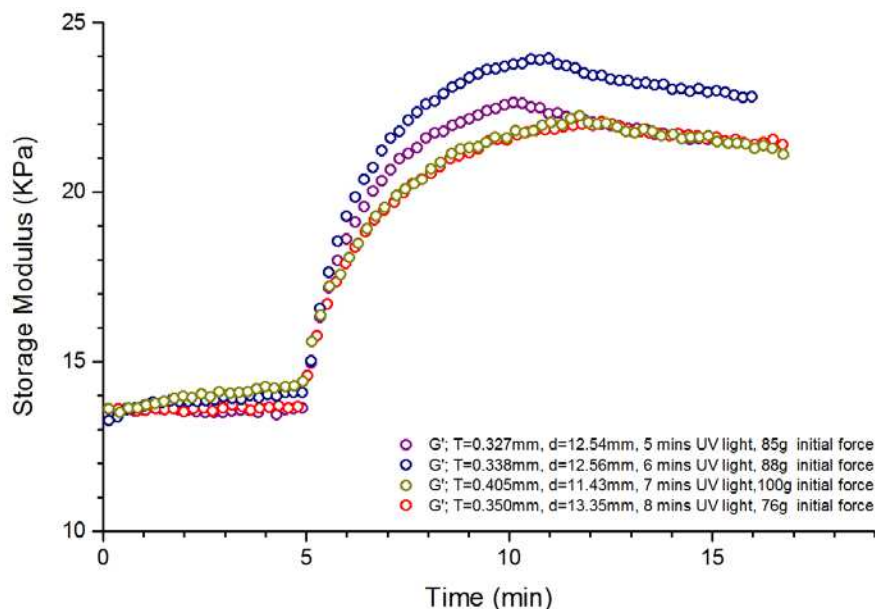


Figure 4.11 The effect of UV exposure time on modulus gain for e_{87.5}IOI22-1.0. Samples were heated to 95°C and maintained at 95°C for the whole duration of the experiment. UV exposure was started at 5 min and maintained for the duration indicated in the legend.

Figure 4.11 shows the data from this UV exposure time study performed on e_{87.5}IOI22-1.0 samples, in which UV exposure was varied between 5 and 8 minutes. As mentioned earlier, initiation of cationic polymerization epoxy groups by the IPDPST was expected to be instantaneous in the presence of broadband UV, if uniform distribution of the photoacid is possible. As the previous experiments indicated however, the solubility of the IPDPST in epoxidized PI appeared limited. In the case of IOI22, we hoped the added solubility of the IPDPST in the PEO block would help distribute the photoacid such that it was in close proximity with the homogeneously distributed ePI spherical domains. As Figure 11 shows, the sudden increase of storage modulus at 5 mins (at the beginning of the UV exposure) for all samples tested agrees with this theory. There was no observable (significant) difference (in modulus) between samples exposed to times over the range of 5 to 8 minutes and thus we believe there was likely no effect on the degree of crosslinking (which is reflected in the modulus) in this experiment. The starting moduli of all four samples are consistent (~13.5kPa) and the gain in modulus (~7-10kPa) with UV exposure varies in only over 2 kPa range. This variation may be due to the sample-to-sample difference in photoacid distribution and slight differences in the uniformity of the sample thicknesses (impacted by UV penetration depth).

The next step was to subject e_{87.5}IOI22-1.0 to longer exposure periods of UV light. Figure 4.12 shows the change in storage and loss moduli G' and G'' with time. An increase in G' within the first five minutes of UV exposure was about 6kPa and for the rest of the time it was just 3kPa. If we assume the change in modulus is roughly linearly dependent on the degree of crosslinking in the PI domains, the majority fraction of the crosslinking reaction (~67%) take place within the first 5 min.

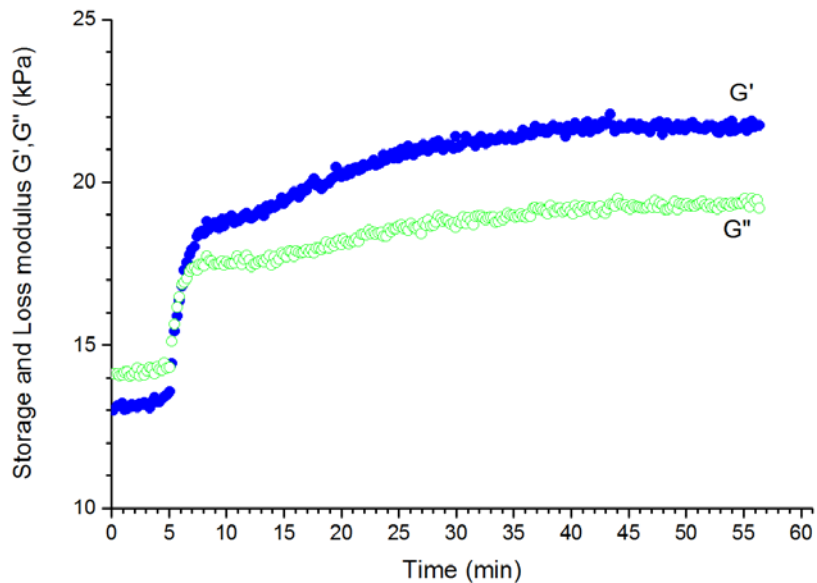


Figure 4.12 The $e_{87.5}$ IOI22-1.0 blend was heated to 95°C and maintained at 95°C for the whole duration of the experiment. UV exposure was started at 5 min and continued until 55 min.

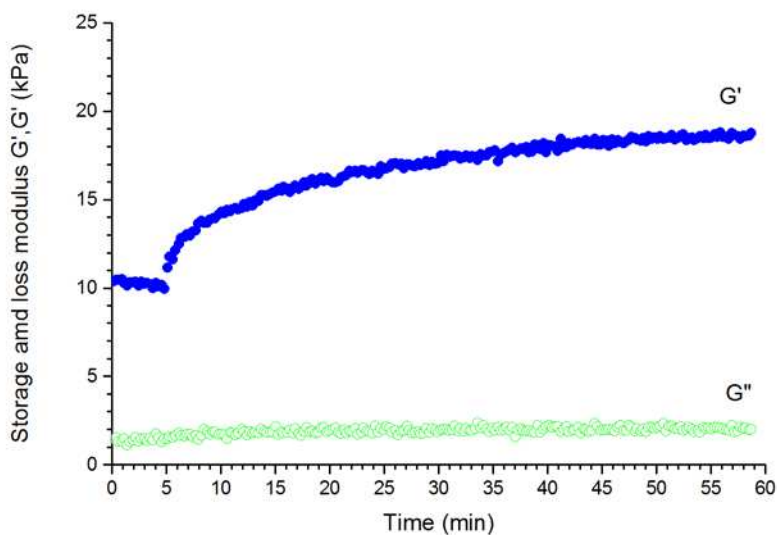


Figure 4.13 The e_{20} BOB11.5-0.5 blend was heated to 95°C and maintained at 95°C for the whole duration of the experiment. UV exposure was started at 5 min and continued until 55 min.

Another interesting observation is that there was no loss of storage modulus even at longer UV exposure times. Typically, longer UV exposure times (on the scale of hours) are associated with diene polymer degradation (usually associated with radical formation and chain scission). However, for our sample, polymer degradation, (if any present) due to longer UV exposure was not significant enough affect the moduli of the sample. Not unexpectedly, a greater starting G'' than G' was measured for uncured $e_{87.5}$ IOI22-1.0 melts, which was consistent with the lack of structure detected in the SAXS. As the cross-linking of the PI domains progressed, the rheology confirmed the decrease of liquid-like behavior (decreasing G'') and increase in solid-like behavior (increasing G') as expected for a material-undergoing cure.

Finally, the morphology of the $x_{87.5}$ IOI22-1.0 was characterized with SAXS (Figure 4.7b). Recovery of S_{LLP} ordering is evident from the appearance of the primary scattering peak at 0.015 \AA^{-1} , indicating the onset of cross-linking successfully induced phase separation between the ePI and PEO domains in the system.

For the purpose of comparison, a curing experiment on e_{20} BOB11.5-0.5 was performed (Figure 4.13), maintaining the same conditions that were used for the curing experiment carried out on $e_{87.5}$ IOI22-1.0. Similar to $e_{87.5}$ IOI22-1.0, the total G' gain with UV exposure by the e_{20} BOB11.5-0.5 sample was 7 kPa, with 50% of the modulus gain in first 5 min of UV exposure, and the rest occurring during the remaining 50 min). Interestingly, the loss modulus of this sample stays significantly lower than the PI-containing sample ($e_{87.5}$ IOI22-1.0). This may be due to the presence of a well developed ordered morphology (S_{BCC}) in e_{20} BOB11.5-0.5 in the melt prior to cure. In contrast, the PI-containing sample was essentially disordered prior to cure.

Photocross-linked $x_{87.5}$ IOI22-1.0 samples were then swollen in DI water to evaluate the swelling and mechanical behavior of the resulting hydrogels. All samples that were exposed to

UV (from 5 to 8 min), retained their shape when swollen in water. However, the mechanical properties of these hydrogels were so poor that they effectively disintegrated when handled out of the water. In contrast, the $x_{87.5}$ IOI22-1.0 sample exposed to UV for 55min showed better mechanical properties (qualitative conclusion) when swollen with DI water, than samples that had the much shorter curing times, although they remained quite fragile when handled. Overall, the poor mechanical stability of the hydrogels formed might be a consequence of a combination of factors: the lack of triblock in the blends post epoxidation (only 4.6% of triblock copolymer was present following the epoxidation modification of IOI22), and the lack of a well-developed S_{LLP} (verified with SAXS data-Figure 4.7b) morphology due to the compatibilization of blocks at high epoxidation levels.

4.3.3.3 IOI46

Just as in $e_{87.5}$ IOI22 samples, SAXS data for $e_{85.4}$ IOI46 (Figure 4.7c) showed the disappearance of all scattering peaks corresponding to the S_{LLP} morphology. Despite the fact that $e_{85.4}$ IOI46 samples lacked the ordered phase separation, the studies on curability of these materials were also continued. The $e_{85.4}$ IOI46-1.0 samples were exposed for approximately 120 min, then swollen with DI water. The resulting hydrogels (Figure 4.14) had improved mechanical properties over the ones based on $x_{87.5}$ IOI22 and x_{22} IOI25 (discussed in greater detail below). Isotropic swelling behavior was observed. Samples with a higher amount of IPDPST photoacid were then examined ($e_{85.4}$ IOI46-5.0) during cure while monitoring their moduli response to a fixed oscillatory shear. In this experiment, a sample sandwiched between quartz coverslips was first exposed to broadband UV for 125 min and then cooled to room temperature.

Subsequently, it was flipped and reheated to 100°C without UV for 30 min. The molten sample was then exposed to UV for another 85 min. Flipping of the sample was done to ensure the crosslinking throughout the sample thickness of 0.65mm, and examine whether UV depth penetration was playing a significant role in the modulus exhibited by the sample.

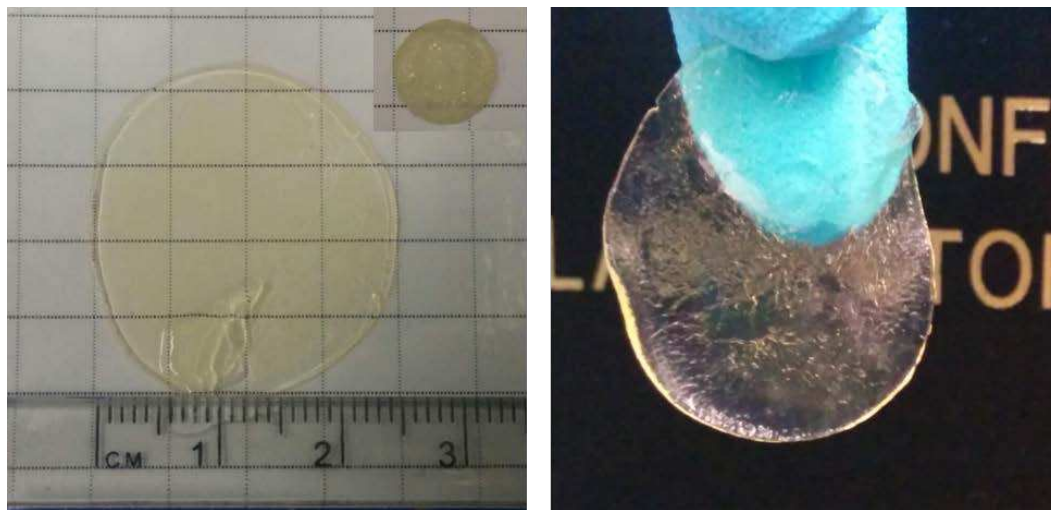


Figure 4.14 Hydrogels based on $x_{85.4}$ IOI46-1.0. Inset is a photograph of the dry polymer disk.

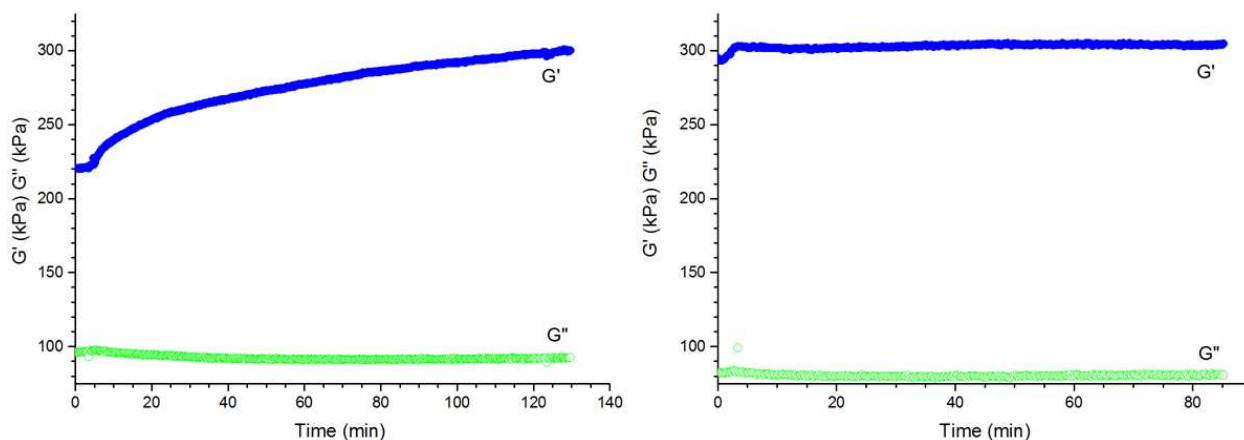


Figure 4.15 The change in G' and G'' of $e_{85.4}$ IOI46-5.0 with UV exposure time at 100°C. Sample exposure to broadband UV was started at 5 min and continued for another 125 min (first graph). The sample was then cooled to room temperature and flipped, reheated to 100°C without UV for 30 min, then exposed to UV for another 85 min (second graph). Flipping of the sample was done to examine the depth of penetration of the UV light throughout the sample thickness of 0.65mm.

The first plot in Figure 4.15 shows the gradual increase in G' of 100 kPa during the first curing step, and the second graph depicts the effect on modulus during exposure after flipping the sample. The second plot reveals only a slight increase in G' within the first 5 min and plateau behavior for the rest of the UV exposure time. This $x_{85.4}\text{IOI46-5.0}$ sample showed the highest G' gain with crosslinking when compared to all other samples examined. Also, the $x_{85.4}\text{IOI46-5.0}$ sample was characterized with SAXS and revealed the reemergence of the S_{LLP} morphology. In this case, incorporation of the additional onium salts may have aided in the curing induced phase separation of this sample. Salt-induced phase separations in BCP systems are not uncommon, and can be found occasionally documented in the literature^[22].

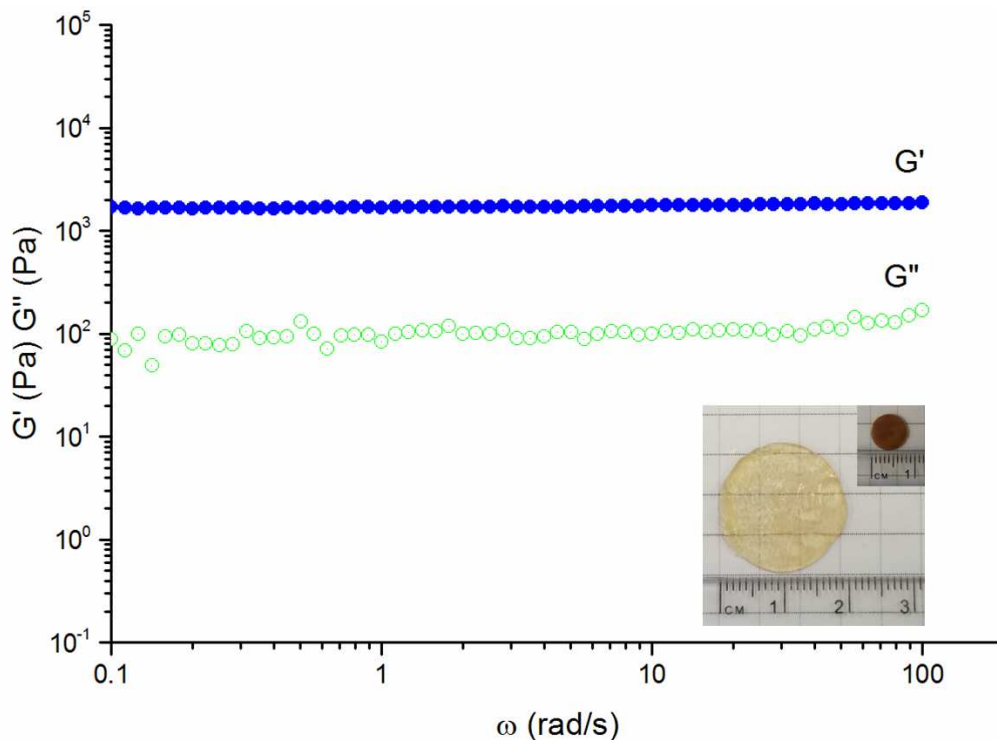


Figure 4.16 Frequency dependent moduli for a hydrogel based on $x_{85.4}\text{IOI46-1.0}$ under oscillatory shear (1% strain) at room temperature. The photograph in the inset shows the relative size of the pre-swollen and post swollen hydrogel formed from $x_{85.4}\text{IOI46-5.0}$.

Photographs of hydrogels formed from $x_{85.4}\text{IOI46-1.0}$ and $x_{85.4}\text{IOI46-5.0}$ are shown in Figure 4.14 and 4.16 (inset). Both hydrogels showed improved mechanical stability relative to the hydrogels based on $x_{87.5}\text{IOI22-1.0}$. This is clear evidence that the amount of triblock present in a blend is a key parameter in determining the mechanical stability of the resulting hydro/ion gels formed. In general, the storage and loss moduli exhibited during dynamic frequency sweeps of the hydrogels based on $x_{85.4}\text{IOI46-5.0}$ were in the same range as the hydrogels based on $\text{SOS7.5}^{[17]}$ and $x_{20}\text{BOB11.5-0.5}^{[2]}$. However, these small strain experiments rarely predict the response of a material under typical handling conditions, where strains placed on the sample can easily exceed those performed in a typical frequency sweep experiment.

4.4 CONCLUSIONS

A sound conclusion on the feasibility of replacing PS with cross-linked PI was unable to be drawn at this stage of the project, with further studies necessary. However the key findings from this study should permit future approaches to be significantly more streamlined, and allow for focused planning of new experiments going forward.

Three major issues were identified that need to be addressed in order to achieve the level of mechanical strength expected from these targeted membrane materials. At the forefront was the degree of epoxidation of olefin units in the PI domains. This conclusion was derived by comparing the qualitative mechanical properties of hydrogels based on $x_{20}\text{IOI25}$ and $x_{85.4}\text{IOI46}$. That is, $x_{20}\text{IOI25}$, which has approximately 25 mol% triblock present in the blend after the epoxy modification, showed significantly lower mechanical stability and strength than the $x_{85.4}\text{IOI46}$

sample, which retained only about 10% triblock in the blend. Inevitably, more epoxy sites in a sample enhance the higher degree of cross-linking within the PI domains, resulting in more solid-like spherical junction points that improve the toughness of the whole material. One of the challenges recognized in this study was the loss of triblock copolymer during the oxidation of the PI units. It was found that when the degree of epoxidation of the olefins on PI exceeds 25%, the molecular weight distribution of the whole BCP blend is negatively impacted. Alternative synthetic routes to incorporate epoxy groups into PI domains, that impose no or a minimal disturbance (triblock copolymer content) to the BCP molecular weight distribution will ultimately be necessary if replacement of the PS domains with cross-linked PI is to become feasible. Methyltrioxorhenium catalyzed epoxidation of olefins with hydrogen peroxide^[23] is one of the many alternative routes worth pursuing. In addition to the reaction conditions that force the decoupling of the triblocks in the blends, the presence of higher percentages of oxiranes on PI itself seems to hinder the self-ordering of the BCP blends (evidenced with the SAXS data). Hence, looking for a cross-linking strategy that does not require such extensive modification of PI, such as the use of 1-hydroxycyclohexyl-phenyl-ketone (HCPK) with free radical photo initiation^[24] may prove more appropriate. Ultimately, if the PEO blocks are successfully derivatized to include significant RTIL character, compatibilization through epoxidation may no longer be a considerable problem.

The second most influential factor on the overall mechanical properties of the hydrogels is the amount of the triblock copolymer present in the BCP blend. This conclusion was drawn from a comparison of the mechanical stability (handling properties) of hydrogels produced from the $x_{85.4}$ IOI46 and $x_{87.5}$ IOI22 samples. Both samples had approximately the same degree of epoxidation, but after the epoxidation modification only 9.4 and 4.6 mole percent triblock

copolymer were present in $e_{85.4}46$ and $e_{87.5}IOI22$ blends, respectively. Complex modulus response to dynamic frequency sweeps on a hydrogel made of $x_{85.4}IOI46-0.5$ (with 9.4 mole percent triblock copolymer) was in the same range of magnitude as a quite robust hydrogel with 7.5 mole percent triblock copolymer made from $SOS7.5$ ^[17]. However, the complex modulus of a hydrogel formed from the $x_{87.5}IOI22$ could not be measured due to the fragility of the swollen sample outside of water. Again, these results suggest that the adopting an epoxidation strategy that would preserve the amount of triblock in a blend will be required to reach the mechanical stability that is ultimately on par with (or exceeds that of) PS based hydrogels.

The third factor that should be addressed to improve the mechanical stability/strength of the hydrogels is careful selection of the molecular weight of the BCP system. When $e_{20}BOB11.5$ and $e_{22}IOI25$ systems are compared, the low molecular weight $e_{20}BOB11.5$ system possessed well-defined periodic S_{BCC} lattice with PB spherical domains (~7 nm radius), where as the higher molecular weight $e_{22}IOI25$ system lacked such periodic ordering (with spherical domains ~14 nm in radius). Cross-linking within the smaller PB domains seems to produce hydrogels of higher mechanical strength compared to cross-linking with the larger PI domains. This may be due to increased accessibility of the reactive groups to the protic acid initiator, and/or a higher degree of ordering possible due to a increased chain mobility during phase separation.

REFERENCES

- [1] J.E. Bara, T.K. Carlisle, C.J. Gabriel, D. Camper, A. Finotello, D.L. Gin, R.D. Noble, Guide to CO₂ Separations in Imidazolium-Based Room-Temperature Ionic Liquids, *Industrial & Engineering Chemistry Research*, 48 (2009) 2739-2751.
- [2] V.F. Scalfani, T.S. Bailey, Access to Nanostructured Hydrogel Networks through Photocured Body-Centered Cubic Block Copolymer Melts, *Macromolecules*, 44 (2011) 6557-6567.
- [3] C. Guo, T.S. Bailey, Tailoring mechanical response through coronal layer overlap in tethered micelle hydrogel networks, *Soft Matter*, 11 (2015) 7345-7355.
- [4] V.F. Scalfani, T.S. Bailey, Thermally Stable Photocuring Chemistry for Selective Morphological Trapping in Block Copolymer Melt Systems, *Chemistry of Materials*, 22 (2010) 5992-6000.
- [5] I.W. Cheong, C.M. Fellows, R.G. Gilbert, Synthesis and cross-linking of polyisoprene latexes, *Polymer*, 45 (2004) 769-781.
- [6] Y. Xu, H. Siswono, F. Yoshii, K. Makuuchi, Crosslinking of cis-1,4-polyisoprene rubber by electron beam irradiation, *Journal of Applied Polymer Science*, 66 (1997) 113-116.
- [7] Y. Apolinar, L.F. Ramos, H. Saade, L. az de, R. n, R.G. pez, Polyisoprene Nanoparticles Prepared by Polymerization in Microemulsion, *Journal of Nanomaterials*, 2010 (2010).
- [8] K.A. Cavicchi, A.S. Zalusky, M.A. Hillmyer, T.P. Lodge, An Ordered Nanoporous Monolith from an Elastomeric Crosslinked Block Copolymer Precursor, *Macromolecular Rapid Communications*, 25 (2004) 704-709.
- [9] M. Morton, J.A. Cala, I. Piirma, Crosslinking in isoprene polymerization, *Journal of Polymer Science*, 15 (1955) 167-182.
- [10] N.P. Balsara, B.A. Garetz, M.Y. Chang, H.J. Dai, M.C. Newstein, J.L. Goveas, R. Krishnamoorti, S. Rai, Identification of the Molecular Parameters that Govern Ordering Kinetics in a Block Copolymer Melt, *Macromolecules*, 31 (1998) 5309-5315.
- [11] M. Sugimoto, K. Sakai, Y. Aoki, T. Taniguchi, K. Koyama, T. Ueda, Rheology and morphology change with temperature of SEBS/hydrocarbon oil blends, *Journal of Polymer Science Part B: Polymer Physics*, 47 (2009) 955-965.
- [12] C.R. Harkless, M.A. Singh, S.E. Nagler, G.B. Stephenson, J.L. Jordan-Sweet, Small-angle x-ray-scattering study of ordering kinetics in a block copolymer, *Physical Review Letters*, 64 (1990) 2285-2288.

- [13] T.H. Epps, F.S. Bates, Effect of Molecular Weight on Network Formation in Linear ABC Triblock Copolymers, *Macromolecules*, 39 (2006) 2676-2682.
- [14] K.A. Cavicchi, T.P. Lodge, Self-Diffusion and Tracer Diffusion in Sphere-Forming Block Copolymers, *Macromolecules*, 36 (2003) 7158-7164.
- [15] K.A. Cavicchi, T.P. Lodge, Domain size equilibration in sphere-forming block copolymers, *Journal of Polymer Science Part B: Polymer Physics*, 41 (2003) 715-724.
- [16] X. Wang, E.E. Dormidontova, T.P. Lodge, The Order–Disorder Transition and the Disordered Micelle Regime for Poly(ethylenepropylene-*b*-dimethylsiloxane) Spheres, *Macromolecules*, 35 (2002) 9687-9697.
- [17] C. Guo, T.S. Bailey, Highly distensible nanostructured elastic hydrogels from AB diblock and ABA triblock copolymer melt blends, *Soft Matter*, 6 (2010) 4807-4818.
- [18] J.K.P.a.G.J. Yevick, *Phys Rev*, (1958) 1-13.
- [19] M. Okada, H. Masunaga, H. Furukawa, Concentric Pattern Formation during Phase Separation Induced by a Cross-Linking Reaction, *Macromolecules*, 33 (2000) 7238-7240.
- [20] P.C.L. Hiemenz, T. P., *Polymer chemistry*, (2007).
- [21] L.J. Fetters, D.J. Lohse, D. Richter, T.A. Witten, A. Zirkel, Connection between Polymer Molecular Weight, Density, Chain Dimensions, and Melt Viscoelastic Properties, *Macromolecules*, 27 (1994) 4639-4647.
- [22] T.H. Epps, T.S. Bailey, R. Waletzko, F.S. Bates, Phase Behavior and Block Sequence Effects in Lithium Perchlorate-Doped Poly(isoprene-*b*-styrene-*b*-ethylene oxide) and Poly(styrene-*b*-isoprene-*b*-ethylene oxide) Triblock Copolymers, *Macromolecules*, 36 (2003) 2873-2881.
- [23] H. Adolfsson, C. Copéret, J.P. Chiang, A.K. Yudin, Efficient Epoxidation of Alkenes with Aqueous Hydrogen Peroxide Catalyzed by Methyltrioxorhenium and 3-Cyanopyridine, *The Journal of Organic Chemistry*, 65 (2000) 8651-8658.
- [24] H.-L.C. Wenchuan Lee, Tsang Lang Lin, Correlation between crystallization kinetics and microdomain morphology in block copolymer blends exhibiting confined crystallization, *Journal of Polymer Science Part B: Polymer Physics*, 40 (2002) 519-529.

CHAPTER 5

INVESTIGATION OF ALTERNATIVE MATERIALS FOR CO₂/N₂ SEPARATION MEMBRANES⁵

5.1 INTRODUCTION

The CO₂/N₂ separation membranes discussed in chapter 3 have potential for further improvement. Crosslinking of the spherical cores in the membrane structure as a means of improving thermal and chemical tolerance was introduced in Chapter 4, although the approach involving the epoxidation of PI showed limited success. Productivity (CO₂ permeability) and enhanced transmembrane operating pressures represent two additional areas in which these membranes can be further improved. Strategies explored addressing the latter are the primary subject of this chapter. Because much of the work described in chapter 4 was carried out concurrently with the work described here, some of the themes regarding the use of epoxidized PI as an alternate core material arise here as well.

For improving the productivity of the membrane, the CO₂ permeability and permselectivity need to be increased. Increasing the mole percentage of RTIL in a membrane has shown to improve the CO₂ permeability of similar type membranes^[1, 2]. Also RTIL enriched

⁵ The content of this chapter was written by Dilanji Wijayasekara. This chapter is intended to serve as an educational chapter, documenting a range of findings pertinent to further development of these novel block copolymer materials.

matrix materials are expected to increase matrix solubility in the neat RTIL while simultaneously strengthening matrix-RTIL interactions aimed at preventing potential RTIL leaching under higher operating pressure differentials.

To capture each of these improvements, including increased chemical and thermal tolerance of the membranes, we proposed two additional novel block copolymer (BCP) systems aimed at enhancing RTIL content in the system.

The chemical structure of the first of these (system 1), P(NBe)-P(NBC₆mim)/ P(NBe)-P(NBC₆mim)-P(NBe) is given in Figure 5.2a. A BCP system very close to this proposed system has been previously synthesized by the Gin group at University of Colorado, Boulder and studied extensively in our lab for its unique morphological behavior^[3]. The highly tunable phase behavior of this BCP system (Figure 5.1^[3]) and the feasibility of polymerizing norbornene monomers derivatized with imidazolium based RTIL pendent groups provided the inspiration for the analogous BCP system 1 proposed here. The difference between the previously studied system and the proposed system is in the attached **R** group shown in the Figure 5.2. The epoxy ring in the proposed substituent (**R**) has been included to enable photoinduced crosslinking within the A block domains following self-assembly. As with the PI system studied in chapter 4, the very low glass transition temperature associated with polynorbornene and its derivatives require crosslinking to achieve the necessary mechanical strength required for use in these membranes. Importantly, the previously reported^[3] BCP system (without the epoxy functionality) does not possess an intrinsic chemical functionality in the non-ionic block amenable to chemical crosslinking.

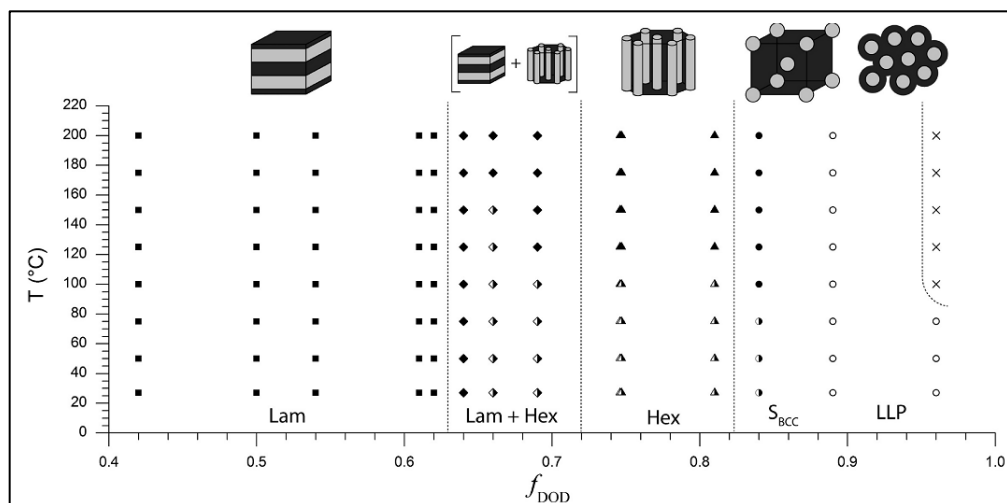


Figure 5.1 Phase diagram of morphologies observed in the imidazolium-based alkyl-ionic copolymer melt system including lamellae(L), hexagonally packed cylinders(Hex), coexisting L and Hex, spheres on a body centered cubic lattice (BCC) , and a liquid like packing (LLP) of spheres. Solid symbols represent regions of well-defined ordered structures, semi-filled and open circles represent regions of poorly ordered structures and cross symbols depict the disordered region^[3]

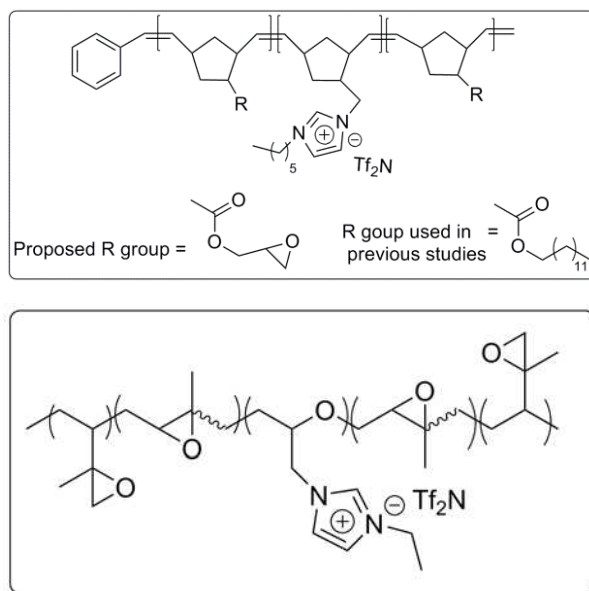


Figure 5.2 ABA BCP studied previously having an alkyl substituent on the 5 carbon ring vs. the proposed system of ABA BCP would have an oxirane substituent on the same location

Notably, a study investigating the CO₂/N₂ gas separation performance of this non-crosslinkable BCP system was also recently conducted.^[4] The results from these materials are reproduced here in the form of a Robeson plot (figure 5.3).

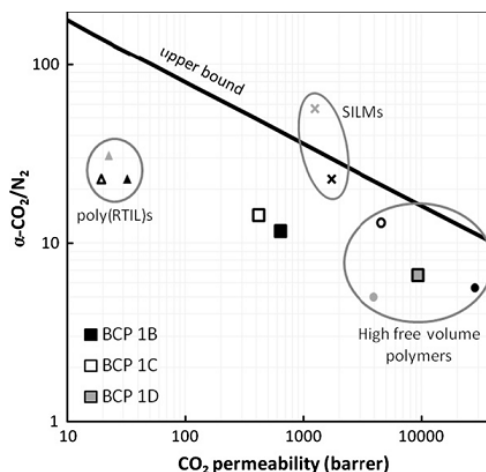


Figure 5.3 Robeson plot comparing CO₂ and N₂ transport properties of three BCP samples of alkyl-imidazolium system with other existing membrane materials.¹⁹

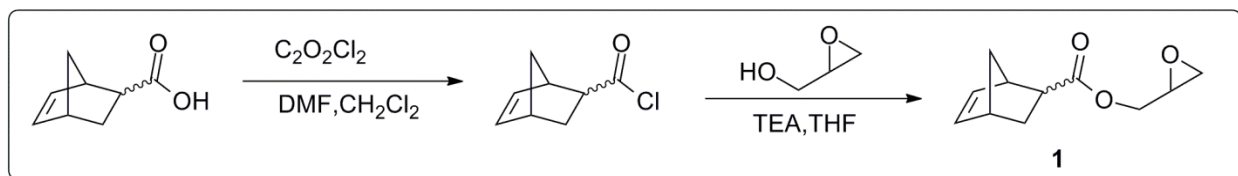
Unlike the sphere-based morphology proposed for the current membrane systems, the self-assembled nanoscale structures of the BCP samples in Figure 5.3 were lamella for 1B, and liquid-like packing of spheres for 1C and 1D^[4]. Further, samples 1C and 1D have a higher volume fraction of non-ionic blocks (according to the phase diagram Figure 5.1) whereas in our proposed system, non-ionic blocks (spheres) are designed to be the minority component. Importantly, without the ability to crosslink the non-ionic component, the mechanical performance of these materials was severely limited, and additional swelling with free RTIL led to complete loss of membrane integrity. These observations further justified our strategy to introduce the crosslinkable epoxy group to the non-ionic block.

The second BCP system proposed (system 2), (ePI)-P(EOemim) / (ePI)-P(EOemim)-(ePI), is more closely related to those studied in Chapters 3 and 4. The chemical structure can be found in Figure 5.2b. As we've discussed in the chapter 3, when neat RTIL is combined with PEO, a dramatic increase in permi-selectivity (CO_2/N_2) with only a slight loss of permeability was observed when compared to neat RTIL alone. The second BCP system proposed was thus designed to include an RTIL functionalized PEO block instead of just PEO alone as the matrix block. It was anticipated that adding a RTIL functionality to the PEO blocks would further aid in improving the permi-selectivity. Also the solubility of RTIL functionalized PEO in neat RTIL would likely be higher than PEO alone. Improved solubility of the solid matrix in neat RTIL would theoretically increase the membrane's liquid-like character, enhancing the solubility and diffusion of CO_2 in the matrix, and ultimately improving CO_2 permeability. The synthetic route proposed is based on using a polyglycidol starting block, such that a variety of imidazole based RTILs can be easily incorporated. The second BCP system was designed to have cross-linked PI spherical domains, since the concurrent research on this aspect was already in progress (see chapter 4). Extensive studies on synthetic feasibility of the proposed **BCP system 2** were carried out, with the findings reported in detail in Section 5.3.

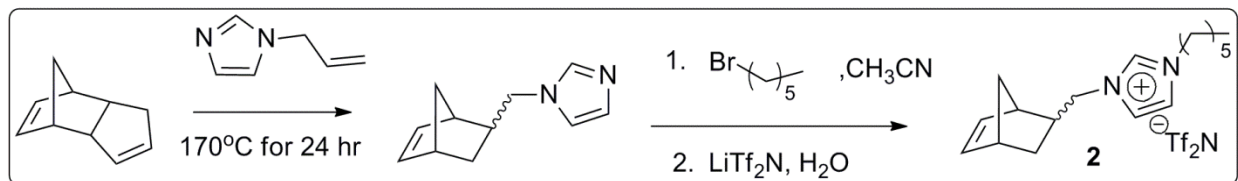
5.2 BCP SYSTEM 1 – P(NBE)-P(NBC₆MIM)/ P(NBE)-P(NBC₆MIM)-P(NBE)

The ring opening metathesis polymerization (ROMP) of epoxy and imidazolium functionalized norbornene monomers were proposed for the synthesis of BCP system 1. Polymerized (1*R*, 4*R*)-oxiran-2-ylmethyl bicyclo [2,2,1]hept-5-ene-2-carboxylate (NBe,

monomer **1**) was selected for the A blocks. As mentioned earlier, A blocks were to be designed to phase separate into spheres and the pendant epoxy functionality would allow these spheres to be internally cross-linked following self-assembly. The choice of the epoxy-derivatized norbornene monomer as the A block repeat unit was predicated on the ability of the epoxy unit to be cationically cured using thermally stable onium photoacids, in combination with the compatibility of the norbornene functionality with the ROMP polymerization mechanism used for the ionic B monomer, 3-Bicyclo[2.2.1]hept-5-en-2-ylmethyl-1-hexyl-3*H*-imidazolium bis(trifluoromethylsulfonyl)amide ([NBC₆mim][Tf₂N], monomer **2**) previously polymerized by our group. Synthetic schemes for monomer **1** and monomer **2** are shown below. The reaction conditions for Scheme **1** are adopted from previous collaborative work with the Gin group at University of Colorado, Boulder,^[3] involving the block copolymerization of bicyclo[2.2.1]hept-5-ene-2-carboxylic acid decylester^[3] with monomer **2**.

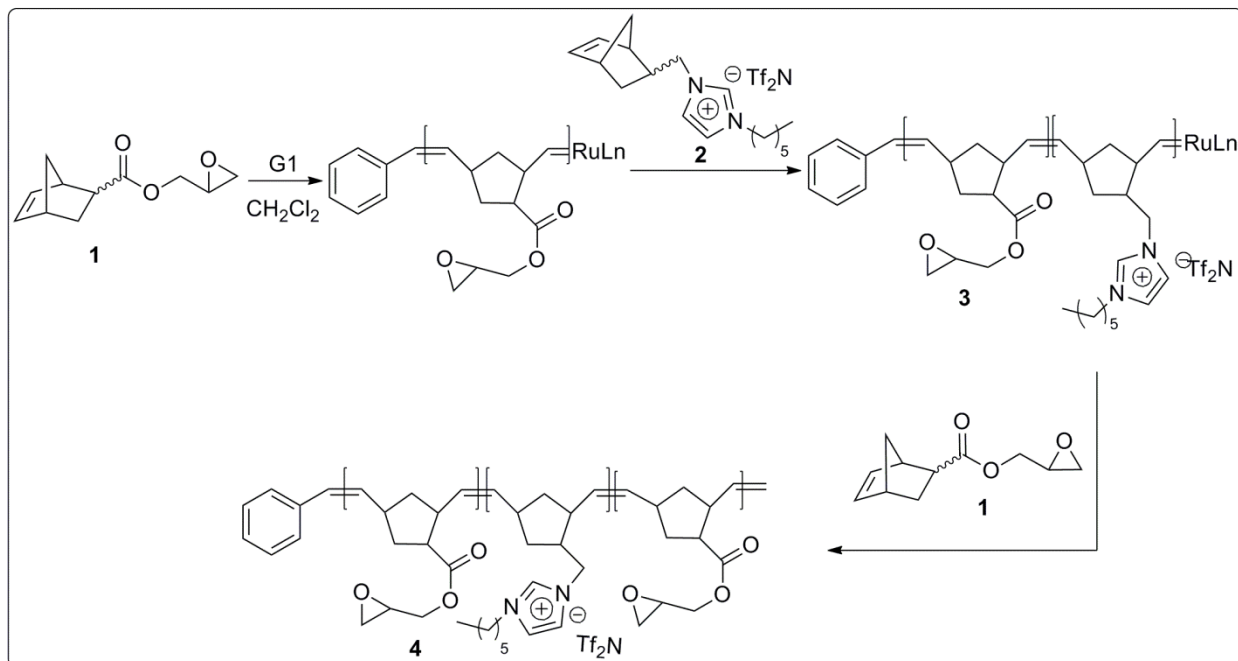


Scheme 1 (1*R*, 4*R*)-oxiran-2-ylmethyl bicyclo[2,2,1]hept-5-ene-2-carboxylate monomer; Monomer for 'A' blocks



Scheme 2 3-Bicyclo[2.2.1]hept-5-en-2-ylmethyl-1-hexyl-3*H*-imidazolium bis(trifluoromethylsulfonyl)amide monomer **2**

In this BCP system, AB diblock and ABA triblock copolymers were to be obtained via sequential ROMP of monomer **1** and monomer **2** as shown in Scheme 3. Grubb's 1st generation catalyst (**G1** C₄₃H₇₂Cl₂P₂Ru) was to be used to catalyze the polymerization. Ethyl vinyl ether was to be used as the terminating agent.



Scheme 3 Synthesis of AB diblock (**3**) and ABA triblock (**4**) via sequential ROMP

The previously reported that homopolymerization of monomer **2** via ROMP reported by Gin and coworkers resulted in a narrow molecular distribution^[3]. In addition, ROMP is recognized as a desirable polymerization technique for alkyl-imidazolium BCPs^[5] due to its living and linear character, precise molecular weight control, low poly dispersity (PDI) and tolerance of a diverse range of functional groups including epoxides^[6-8]. The independent polymerizations of monomers **1** and **2** via the readily available **G1** catalyst suggest the formation of diblock copolymer **3** and triblock copolymer **4** via Scheme 3 was likely reasonable and straightforward.

5.2.1 Experimental Procedures

5.2.1.1 Materials and General Procedures

5-norbornene-2-carboxylic acid, ethyl vinyl ether, and oxalyl dichloride were purchased from the Sigma Aldrich Co., and used as received. CH_2Cl_2 was purified by distilling prior to degassing. Glycidol was distilled under reduced pressure prior to use. All chemical syntheses were carried out in a dry argon atmosphere using standard Schlenk line techniques. Silica gel purification was performed using 230 - 400 mesh, normal-phase silica gel purchased from Sorbent Technologies.

5.2.1.2 Synthesis of (1R, 4R)-oxiran-2-ylmethyl bicyclo[2,2,1]hept-5-ene-2-carboxylate (monomer **1**)

5-Norbornene-2-carboxylic acid (3.5 g, 0.025 mol) and DMF (1.5 ml) were stirred in distilled methylene chloride (CH_2Cl_2 , 100 ml). Oxalyl dichloride (0.038 mol) was then added drop-wise to the mixture at 0°C , and the reaction mixture was stirred at room temperature for 18 hrs. The reaction mixture was then concentrated in vacuo (rm, 70 mTorr) before the addition of THF (70 mL), triethylamine (4.5 mL) and distilled oxiran-2-ylmethanol (glycidol, 1.7 mL) at room temperature. After stirring for 24 hrs, the reaction mixture was filtered and concentrated at room temperature using rotoevaporation. After stirring for 24 hrs, the reaction mixture was filtered and concentrated at room temperature using rotoevaporation. The crude product was purified by silica gel column chromatography using 80/20 hexanes/ethyl acetate (v/v) solution as

the eluent. The final product was concentrated from the elute in the rotovap and vacuum dried to yield a light brown oil.(1.5 g, 41%).

5.2.1.3 Polymerization of (1R, 4R)-oxiran-2-ylmethyl bicyclo[2,2,1]hept-5-ene-2-carboxylate (monomer **1**)

Under argon atmosphere, monomer **1** (0.69g, 3.55 mmol) was diluted to a total volume of 50 mL with dry, gas-free CH₂Cl₂. Under argon atmosphere, Grubb's 1st-generation catalyst (G1) stock solution was made (0.114M). From this stock solution, 0.8 mL was added to the monomer solution, and the reaction mixture was stirred at room temperature until the polymerization of monomer **1** was complete (~15 min). The ROMP copolymerization mixture was then quenched by addition of excess ethyl vinyl ether (0.5 mL). The resulting polymer was isolated by removal of the solvent in vacuo at ambient temperature for 24 hrs (0.5g, 72%).

5.2.1.4 Molecular characterization of synthesized products

¹H NMR was used for chemical characterization of the products and performed on a Varian Inova 400MHz spectrometer with a pulse delay of 25s to ensure complete relaxation of the end groups. The spectra were referenced to the residual protio solvent (CHCl₃). A Viscotek GPC-Max chromatography system outfitted with three 7.5 mm x 340 mm Polypore (Polymer Laboratories) columns in series was used to perform gel permeation chromatography (GPC) on polymers to determine the equivalent PS molecular weight and polydispersity index (PDI) of polymer. The columns were maintained at 40°C in an Alltech column oven. The GPC system

was attached to a Viscotek differential refractive index (RI) detector. All polymer samples were run in THF (mobile phase, 1 mL min⁻¹) and the molecular weights were measured against the polystyrene calibration standards. Term GPC and SEC (size exclusion chromatography) are inter-changeably used in this document as both referred to the same analysis.

5.2.2 Material Characterization and discussion

Monomer **1** was synthesized by mixing acid chloride of norbonene carboxylic acid with glycidyl alcohol in the presence of an acid scavenger to produce the glycidyl ester. The crude product isolated by solvent evaporation via rotoevapoartion was further purified by passing the product through a silica gel purification column. Adequate purification of monomer **1** was a constant challenge throughout almost all of the synthesis attempts of monomer **1**.

The ¹H NMR spectrum of monomer **1** is given in Figure 5.4. The presence of stereoisomers in both of the starting materials creates considerable complexity in the ¹H NMR spectrum of the product. For example, bicyclo[2.2.1]hept-5-ene-2-carboxylic acid is present in both endo and exo forms. The glycidol starting material contains a racemic mixture of R and S stereo isomers, as well. As a result the product produced can contain four possible stereoisomers of monomer **1**. The distinct resonances in the 5.75 - 6.25 ppm region correspond to the vinyl protons (20 and 21) on carbons 1 and 5^[3]. The distinction in these resonances is due to the two product isomers with both vinyl protons in the minority exo product (20' and 21') forming a single multiplet at 6.1 ppm. Further, the integral ratio under these peaks agrees with the endo to exo ratio reported for the norbonene carboxylic acid starting material. The signals which correspond to the different chiral configurations of the product (S and R) have not yet been

assigned due to the complexity of the spectra. The resonances in the 5.0 ppm -5.5 ppm range are not expected based on the chemical structure of the monomer. They may be due to the unidentified impurities in the product.

The multiplet at 3.2 ppm, adjacent to the peak 19, corresponds to either proton 26 or 27^[9]. Signals from 2.84 ppm- 2.5 ppm correspond to protons numbered 25 and either proton 26 or 27^[9]. Unfortunately, the signals in the range of 3.5 - 3.85 ppm are an indication of ring opening of the epoxy group^[9]. However, a fraction of the product seems to have retained the unopened epoxy functionality. That is evidenced by the two prominent multiplets at 3.9 ppm and 4.4 ppm, which correspond to the protons 23 and 24^[9]. Because of the considerable overlap of these peaks with other proton sources, the extent to which the epoxide is retained in the product has yet to be verified with reliable accuracy.

The ring opening of epoxides evidenced in ¹H NMR spectra, may be due to their high sensitivity to acidic environments and may demand a more efficient removal of the HCl byproduct during reaction **1** of scheme **1**. However, all attempts in this work resulted in considerable fractions of opened epoxide units. Opened epoxides can have significant impact on the ability to cationically cure epoxide systems using photoacids, and their presence was a major concern during the synthesis of this monomer. Some consideration was given to separating the opened and closed epoxide monomer species but this approach was never investigated due to the complex mixtures of isomers in the product complicating the separation. Regardless of this dilemma, some preliminary work was done investigating the polymerization of these new norbornene monomers regardless of the opened or closed state of the epoxide ring.

Figure 5.5 shows the ¹H NMR spectra of homopolymerized monomer **1**. Broadened signal peaks are an indication of polymerization. Calculation of the degree of polymerization and

the purity of the polymer was unsuccessful due to the level of complexity of the ^1H NMR spectrum. Impurities in the monomer and the four stereo-isomerized products result in a very intricate ^1H NMR spectrum, and more advance NMR experiments are likely required to extricate meaningful information regarding molecular weight and polymer composition.

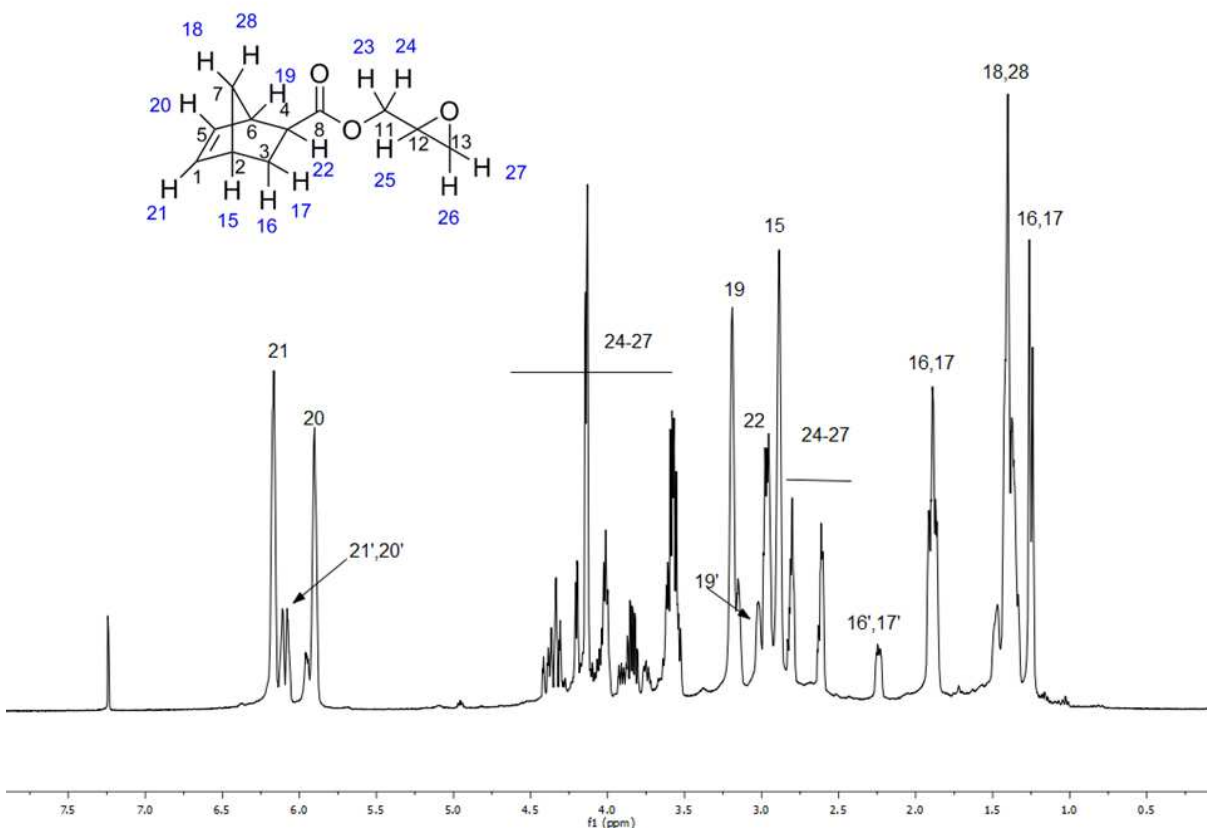


Figure 5.4 ^1H NMR spectra of (1*R*, 4*R*)-oxiran-2-ylmethyl bicyclo[2,2,1]hept-5-ene-2-carboxylate monomer

Despite some success, the purification of unreacted epoxy functional monomer coupled with the complexity of the product mixture for *BCP system 1* proved to be beyond the desired scope of the project, and alternate proposed solutions were ultimately pursued. However, a return to this system is likely warranted in future studies. In particular, selection of starting materials to

reduce the number of isomers in the monomer synthesis product mixture would facilitate accurate characterization. Identification of reaction conditions which minimize epoxide ring opening, or identification of a suitable purification process to eliminate ring-opened contaminants would also move this approach forward. However, as it stands, without progress in these areas of monomer synthesis, accurate polymerization and design of sphere-forming compositions of BCP with monomer **2** will continue to prove extremely difficult.

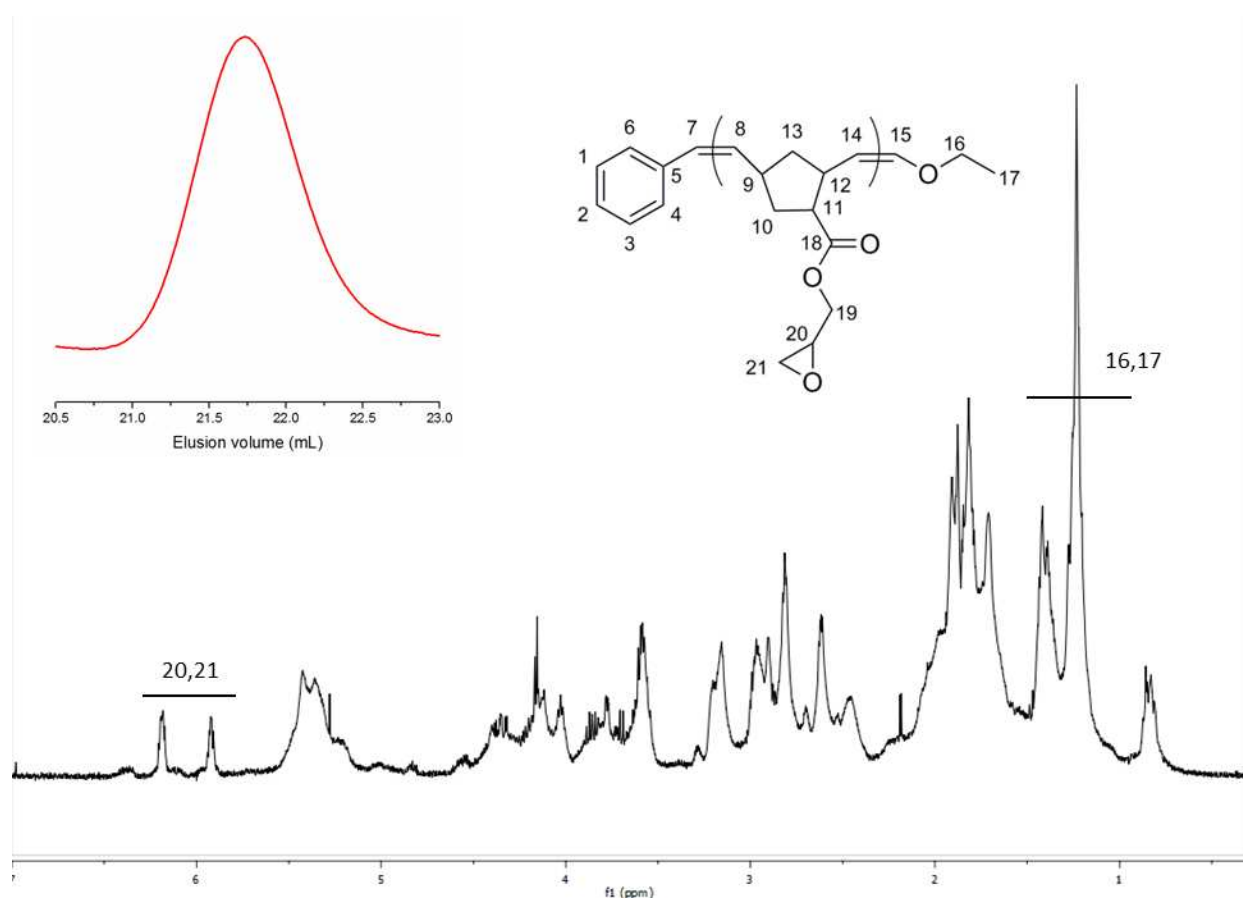


Figure 5.5 ¹H NMR spectra and the SEC chromatogram of homopolymerized monomer **1**.

5.2.3. Summary of progress on the investigation of BCP system 1

- 1) Scheme 1 was investigated as a viable route for monomer 1. Ultimately, a reproducible protocol was developed capable of achieving a product yield of 40%. Reaction products, however, always included monomer containing ring-opened epoxide units, and adequate purification protocols remain unidentified.
- 2) Homopolymerization of monomer 1 via ROMP was investigated. Polymerization was confirmed with crude product yield with 72%. Characterization of product using proton NMR remained incomplete due to the complexity of the spectra, although the presence of the epoxide unit (opened or closed) did not appear to inhibit polymerization.

5.3 BCP SYSTEM 2 – (EPI)-P(EOEMIM) / (EPI)-P(EOEMIM)- (EPI)

(epoxidized PI)-P(charged imidazolium functionalized EO) / (epoxidized PI)-P(charged imidazolium functionalized EO)-(epoxidized PI)

In the second BCP system proposed, the A and B blocks were to be substituted with epoxidized polyisoprene (ePI) and [emim][Tf₂N] derivatized poly(ethoxyethyl glycidyl ether) (PEEGE), respectively. Synthesis of AB diblocks was to be accomplished in three steps using a combination of anionic polymerization of isoprene and EEGE followed by [Emim][Tf₂N] functionalization of the EEGE block through post polymerization modification and partial epoxidation of the olefin repeat units in the PI backbone. The coupling of AB diblocks using dibromoxylene(DBX) was proposed to obtain the requisite ABA triblock copolymers.

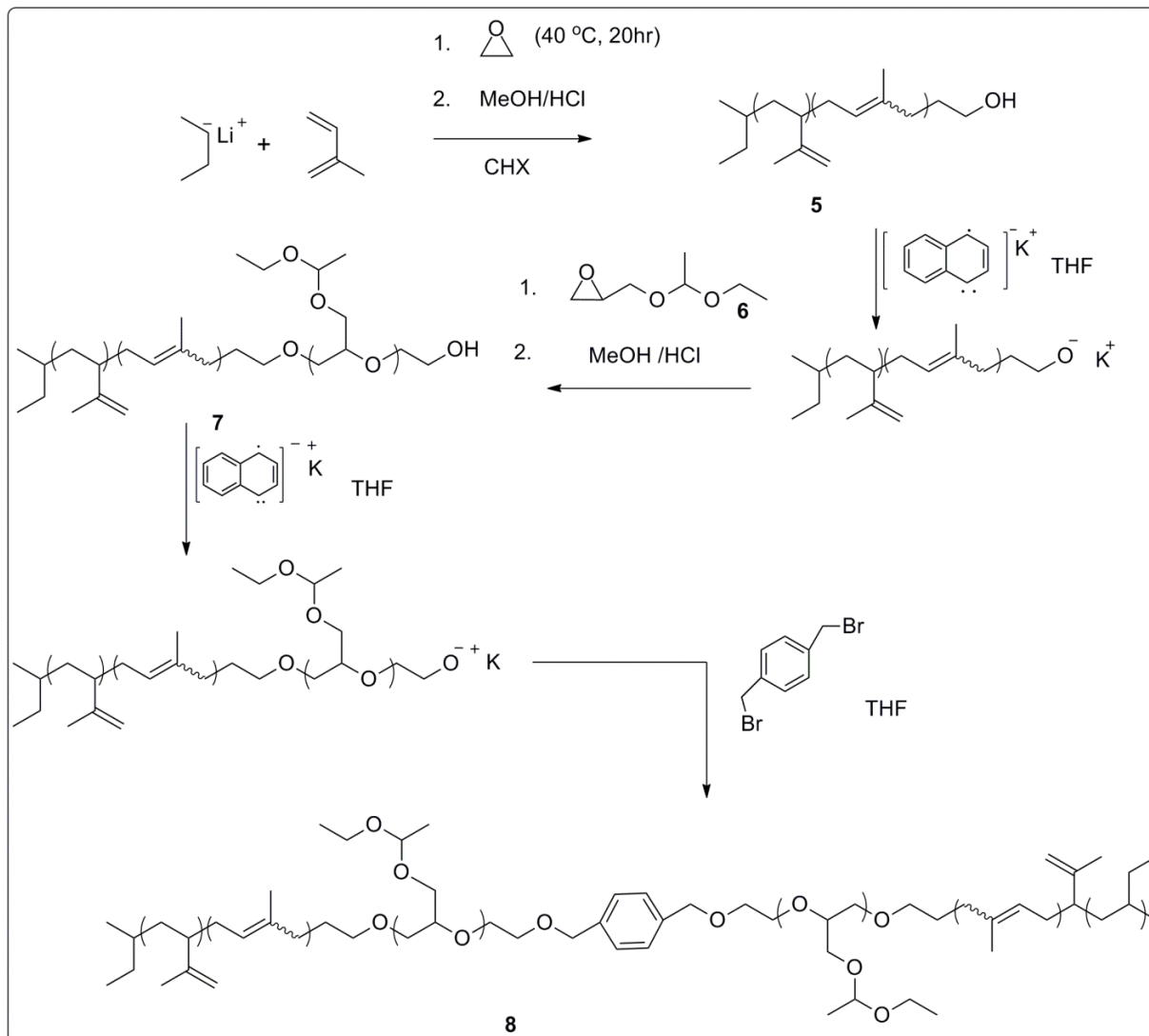
EEGE, which is an acetal protected glycidyl alcohol (monomer **6**) was to be synthesized following the procedures reported by Fitton et al.^[46]. By protecting the alcohol and removing the acidic proton source, the EEGE monomer can be made compatible with the anionic ring opening polymerization technique, which is not true for the unprotected glycidyl alcohols. The protected acetal group of EEGE, which is stable under the strongly basic polymerization conditions typical of anionic polymerizations is easily deprotected when the polymer is placed in an acidic environment^[27] (Scheme 5). Deprotection of the alcohol once polymerized would allow for facile post polymerization modification of the ethylene oxide main chain repeat unit.

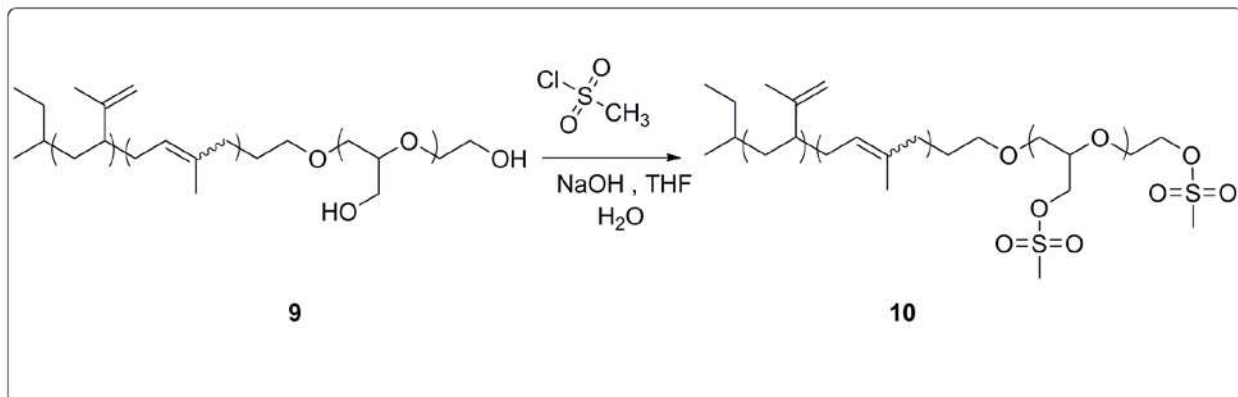
While the direct initiation of EEGE from a living polyisoprenyl lithium chain end is possible, the subsequent propagation of the EEGE polymerization with lithium as the counterion has proven to be extremely slow (~months). To facilitate quantitative exchange of the lithium cation with a much softer, larger potassium cation, the sequential anionic polymerization of isoprene and EEGE was to be broken into two distinct steps. In the first step, the sec-butyl lithium initiated polymerization of PI was to be followed by the addition of a single EO unit providing quantitative functionalization of the PI chain with a terminal alcohol. This terminal alcohol could be reinitiated to form a potassium alkoxide, from which EEGE polymerization proceeds at a much greater rate (although still relatively slow with typical reactions times in days). The resulting macro-initiator **5**, ω -Hydroxy polyisoprene (PI-OH), is shown in Scheme 4. The proposed construction of PI-PEEGE diblock copolymers and PI-PEEGE-PI triblock copolymers is also outlined Scheme 4. The synthetic route for making PI-PEEGE diblocks (Scheme 4) is analogous to that reported by Guo et al. for the synthesis of PS-PEO^[10], differing only in the monomers used.

Post-polymerization modification of the PEEGE block to generate the [emim][Tf₂N] RTIL pendant side chains was to be achieved through a series of synthetic steps; the initial step was the deprotection of the acetal group from each PEEGE repeat unit to liberate the polyglycidol (PG) (Scheme 5). The removal of the acetal group from EEGE is quick and quantitative using an aqueous solution of THF and hydrochloric acid^[11]. Transformation of the liberated hydroxyl groups to mesylates comprised the second step and is shown in Scheme 6. Reaction conditions outlined in Scheme 6 have been adopted from an analogous reaction reported by Bara et al.^[12]. The reaction between NaH and a solution of imidazole in THF is a well-established protocol for yielding an imidazolium anion^[12] to react with an electrophile, in this case the pendent mesylate groups along the polymer backbone (Scheme 7).

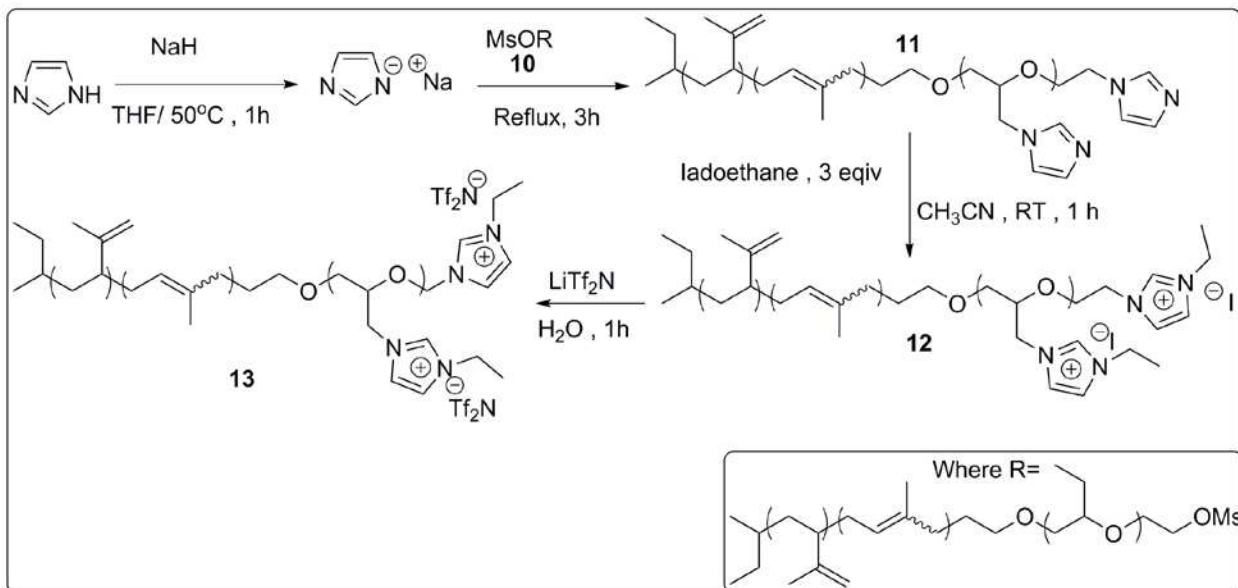
The final step of the proposed synthetic scheme was the partial epoxidization of olefin repeat units in the PI backbone of diblock **11** via a mild oxidation with metachloroperoxybenzoic acid (mCPBA). Scheme 8 demonstrates the epoxidation of AB diblock. The same reaction conditions should be compatible with the modification of the analogous ABA triblock copolymer, as well. Once the proposed AB and ABA block copolymers were synthesized, it was planned incorporate photoacid to the A domains and allow the AB/ABA blends to melt assemble in to the targeted tethered sphere nanostructure. Finally, it was planned to photo-crosslink the spherical domains as discussed in chapter 4.

Work presented in Chapter 4 and Chapter 5 was conducted simultaneously. Hence the conclusions derived from Chapter 4 could not be constructively applied to these BCP systems. For example, the polymerizations of EEGE may have been more appropriately initiated from hydroxyl-functional PS, not PI, given the challenges uncovered with achieving reasonable mechanical properties in the PI systems.

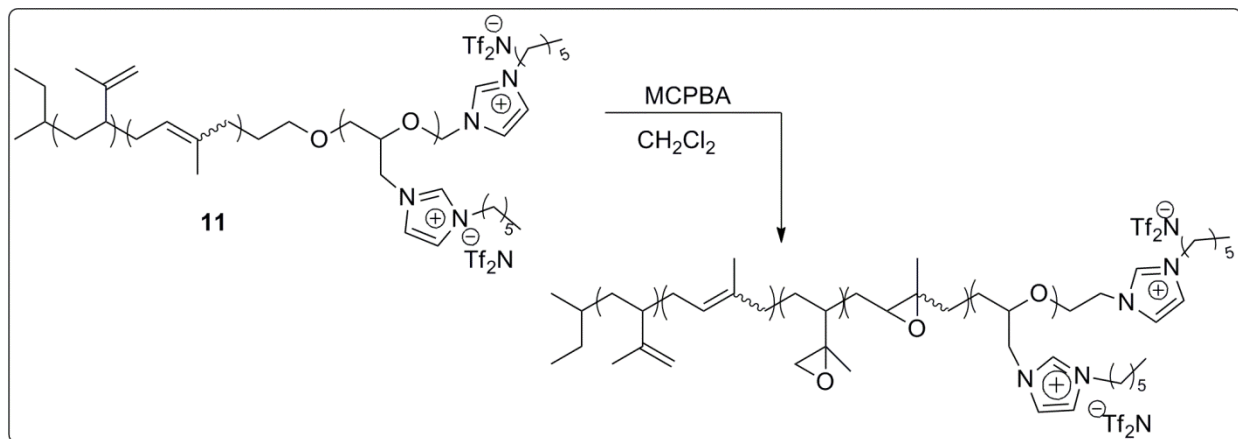




Scheme 6 Mesylation of Polyisoprene-*b*-poly-(ethoxyethyl glycidyl ether)



Scheme 7 $[\text{Emim}][\text{Tf}_2\text{N}]$ functionalization of Polyisoprene-*b*-poly-(ethoxyethyl glycidyl ether)



Scheme 8. Partial epoxidation of PI-P(EEGEemim)

At any rate, controlled polymerization of protected glycidol monomer (EEGE **6**) to yield high molecular weight PEEGE chains (at least 80,000 Da) initiated by the PIOH macro-initiator (product **7**) was found to be extremely challenging. Such high molecular weights are critical for achieving the asymmetry in block copolymer composition necessary to form the sphere morphology. With this newly imposed synthetic challenge, our goals for the proposed **BCP system 2** were primarily focused on exploring alternate strategies for the synthesis of linear high molecular weight polyglycidols initiated with a macro-initiator like PIOH. Despite the potential versatility of such systems, the reported synthetic routes have rarely (if ever) been applied to the formation of high molecular weight polyglycidols^[13] and no reports exist involving high molecular weight linear polyglycidol blocks initiated from macro-initiators (about 8000 g/mol) like PSOH or PIOH. Reports on anionic ring opening co-polymerizations of protected glycidol monomers like allyl glycidyl ether (AGE)^[14-17], ethoxy ethyl glycidyl ether (EEGE)^[18], isopropylidene glyceryl glycidyl ether (IGG)^[19], *tert*-butyl glycidyl ether (t-BuGE)^[20], ethylene glycol vinyl glycidyl ether (EGVGE) with (non-functional) ethylene oxide (EO) can be found in literature and were considered as a potential means of achieving higher molecular weight targets,

although with considerably smaller concentrations of polyglycidol repeat units available for modification. For example, there now exist several publications reporting high molecular weight PS-*b*-P(EO-*stat*-AGE)^[15, 21] BCP systems, however, the AGE mole percent of those high molecular weight systems is less than 3% of the total molecular weight. The most recent record found on anionic copolymerization of EO and AGE, initiating from macro-initiator PSOH, reports maximum number of AGE repeat units per P(EO-*stat*-AGE) chain of 58^[21]. This level of protected glycidol incorporation, while insufficient for our current objective, provided the motivation to explore many of the alternate strategies documented in this chapter. The text that follows documents these efforts.

5.3.1 Experimental Section.

5.3.1.1 Materials and Methods

Isoprene (99%, 100 ppm *p*-tert-butylcatechol inhibitor, Aldrich) was purified by successive static vacuum (15-30 mTorr) distillations from *n*-butyllithium (1.6M in hexanes, Aldrich). Ethylene oxide (99.5+%, compressed gas, Aldrich) was purified by successive distillations from di-*n*-butylmagnesium (1.0M in heptane, Aldrich). *sec*-butyllithium (1.3M in cyclohexane/hexane, Fisher) was used as received. Naphthalene (Fisher) was recrystallized once from diethyl ether. Potassium metal (98%, Fisher) was cut into pieces under light mineral oil and fresh non-oxidized metal surfaces were obtained by washing in pentane for 30s. Potassium naphthalenide solution was prepared by dissolving excess (1.1 x) recrystallized naphthalene and freshly cut potassium in tetrahydrofuran (THF) under argon. The dark green solution was allowed

to stir overnight with a glass spinbar before use. Lithium metal wires (99.9%, Aldrich) were used to make lithium naphthalenide, following the exact procedure for potassium naphthalenide. PIOH (8450 g/mol) and PSOH (8000 g/mol) used were synthesized in our lab and the synthesis and characterization were given in Chapter 4 and Addendum 3, respectively. All other common chemicals were used as received unless otherwise stated. THF was degassed by sparging with argon (10 psi) for a period of 45 minutes and then purified over two molecular sieve columns of neutral alumina (Glass Contour, Inc.). Cyclohexane (CHX) was degassed with argon and purified through a column of neutral alumina followed by a column of Q5 copper (II) oxide catalyst (Glass Contour, Inc.). Ultra high purity argon (99.998% Airgas) was passed through a column of 5 Å molecular sieves with drierite (Agilent) and an oxygen absorbing purifier column (Matheson Tri-gas). All glassware and polymerization reactors were flamed under vacuum and backfilled with argon (3x).

5.3.1.2 Physical and Analytical Measurements

¹H NMR spectra were recorded on a Varian Inova 400 MHz spectrometer with a pulse delay of 25s to ensure complete relaxation of end groups. The spectra were referenced to the residual protio solvent (CHCl₃). Gel permeation chromatography (GPC) was performed on a Viscotek GPC-Max chromatography system outfitted with three 7.5 x 340 mm Polypore (Polymer Laboratories) columns in series. The columns were maintained at 40°C in an Alltech column oven. The GPC system was attached to a Viscotek differential refractive index (RI) detector. All polymer samples were run in THF (mobile phase, 1 mL min⁻¹).

5.3.1.3 EEGE monomer synthesis and purification

EEGE monomer was synthesized following methods established by Fitton et al.^[22]. 40g of glycidol and 200ml of ethyl vinyl ether were stirred with a magnetic stir bar in a 500ml round bottom flask immersed in an ice bath. 1g of p-toluenesulfonic acid was added to the mixture in very small portions, keeping the reaction mixture temperature to below 40°C. The reaction was run for 3 hrs. After three hours, the reaction mixture was washed with saturated aqueous Na₂CO₃ and with DI water (3x). The washed product was then dried with anhydrous MgSO₄ and filtered twice with a Büchner funnel. Excess solvent in the filtrate was then removed by rotoevaporation at room temperature yielding a yellow, viscous clear liquid. The product was then vacuum distilled using T-arm set up and the colorless product EEGE was collected in the receiving side. Minimum of three (or more) freeze, pump and thaw (FPT) cycles were required for efficient static distillation. The distillation rate was slow, about 1g/hr. The final yield was 85-90%.

Due to the extreme monomer purity(>99.7)^[21] required for anionic polymerization, further distillation of the product was performed using short path distillation set up. Distillation was performed at 60°C with no vacuum with the distillation head covered in glass wool and foil. The middle fraction was collected and characterized with ¹H NMR.

5.3.1.4 Standard anionic polymerization procedure for EEGE with PIOH as macro-initiator

Dry PIOH (0.5g, 8450 g/mol) was dissolved in 250 mL dry THF. The solution was titrated with potassium naphthalenide until a light green color remained for at least 5 min at 45°C. EEGE monomer (4.5g), distilled from di-*n*-butylmagnesium, was added to the reactor

under a positive pressure of argon (1 psi). The solution immediately went from light green to clear. The reaction was run for 11 days. The terminal alkoxide was quenched with methanol (10 mL). The resulting polymer solution was transparent yet brownish-yellow in color. The solution was reduced to about 25 mL on a roto-evaporator. The product was then freeze-dried in vacuo (25°C, 72 hrs). The final product was a brown viscous oil. Table 1 summarizes the series of polymerizations attempted, the specific experimental/reaction conditions applied, and the product details.

5.3.1.5 De-protection of poly(EEGE) to yield Polyglycidol (PG)

PI-*b*-PEEGE (0.1g) was dissolved in 20 mL of THF. HCl (0.8 ml of 37%, 12.1M) was added to the polymer solution and stirred for 15 minutes at room temperature. Saturated NaOH was added to the mixture to neutralize the pH. Salts were removed by filtration and the filtrate was dried under vacuum for 12hrs.

5.3.1.6 De-protection of poly(EEGE) on PI-*b*-P(EO-*stat*-EEGE) to yield PI-*b*-P(EO-*stat*-G)

PI-*b*-P(EO-*stat*-EEGE) (0.8g, clear orange viscous liquid) was dissolved in 300 mL of THF. HCL (10 mL of 37%, 12.1M) was added to the polymer solution and stirred for 2 hrs at room temperature. Upon addition of the acid, the color of the mixture turned from clear orange to cloudy, and then with time turned to peach. After 2hrs, the reaction mixture was neutralized with saturated Na₂CO₃ (salt formation was visible but separation of salt by filtration using Büchner funnel was unsuccessful). The reaction mixture was then transferred to a separatory funnel and

left to settle. Ultimately, three distinct layers were visible: a clear brownish-yellow top layer, a cloudy light yellow mid-layer and a white, solid-like bottom layer (salt). The top and middle layers were collected separately, and each dried with anhydrous Na_2SO_4 , filtered with 0.22 micron filter and freeze dried in vacuo. The product was found in the top layer. The product was characterized with ^1H NMR (Figure 5.18)

5.3.1.7. Summary of polymerizations attempted to yield the high molecular weight linear polyglycidols block copolymers

Table 5.1 Experimental conditions, observations and result

Targeted product	Monomer	Initiator	T/°C	Solvent	time	Modifications to the standard procedure	Product Yielded
(1) PI- <i>b</i> -P(EEGE) ₇₁₀	EEGE	PIOH 8450 g/mol	45	THF	11 days		PI- <i>b</i> -PEEGE ₆ Product was a viscous oil of yellow/brown color. Figure 5.6
(2) PI- <i>b</i> -P(EEGE) ₅₇₀	EEGE	PIOH 8450 g/mol	120	Diglyme	24 hr	Reaction mixture terminated with methanol, was cooled down to room temperature and diglyme was distilled off using T arm set up and the remainder (the product) is vacuum dried	Mixture of PEEGE ₃₇ and PI- <i>b</i> -PEEGE ₃₇ Figure 5.7
(3) PI- <i>b</i> -P(t-BuGE) ₁₃₀₀	t-BuGE	PIOH 8450 g/mol	120	Diglyme	24 hr	Reaction mixture terminated with methanol, was cooled down to room temperature and diglyme was distilled off using T arm set up and the remainder (the product) is vacuum dried.	PI- <i>b</i> -P(t-BuGE) Product was a viscous yellow oil. Figure 5.8
(4) PS- <i>b</i> -P(EEGE) ₆₇	EEGE	PSOH 8000 g/mol	45	THF	7 days		PS- <i>b</i> -PEEGE ₂₆ Product was a off-white solid- more like PSOH Figure 5.9
(5) PS- <i>b</i> -P(EEGE) ₂₀₀	EEGE	Sec-butyl lithium	40	Benzene	4 days	Catalyst: Phosphazene base (P ₄ -t-Bu)	PS- <i>b</i> -PEEGE ₂₄ LiNap is dark green

						EEGE dried with CaH ₂ overnight before distilling. Catalyst to chain ends ratio= 2.4:1 PSOH was titrated with LiNap, then added EEGE followed by the catalyst	Li alkoxide was deep purple, with EEGE addition immediately turns to yellow/brown Final product is off white solid Figure 5.10
(6) PI- <i>b</i> -P(EEGE) ₆₀	EEGE	PIOH 8450 g/mol	40	Benzene	4 days	Catalyst: Phosphazene base (P ₄ -t-Bu) 0.8M in hexane Catalyst to chain ends ratio = 2:1 EEGE distilled over n-BuMgCl.	PI- <i>b</i> -P(EEGE) ₁ Li alkoxide was deep purple, and turned to yellow within 15min. With EEGE addition, reaction mixture instantly became colorless. Final product was viscous liquid with a clear brown color. Figure 5.12
(7) PI ₁₃₀ - <i>b</i> -P(EEGE) ₁₅₀	Isoprene, EEGE	Sec-butyl lithium	40	Benzene	3 days	Catalyst to chain ends ratio = 2:1 EEGE dried with CaH ₂ overnight before distilling. Sequence of reactant addition to the reactor: 1) Benzene 2) sec-BuLi 3) Isoprene (24 hrs) 4) EEGE 5) P ₄ -t-Bu (48 hrs) Methanol	PI ₁₃₉ - <i>b</i> -P(EEGE) ₃ and oligomers of EEGE Li alkoxide was deep purple, with EEGE addition immediately turns to yellow /brown. Final product was viscous liquid with a caramel color Figure 5.11
(8) PS- <i>b</i> -PEEGE ₁₅₀	EEGE	PSOH 8000 g/mol	30 mm	Toluene	24 hr	Titrate with Knap then THF was vacuumed off Initiator to catalyst ratio 1:5	Targeted product: PS ₇₇ - <i>b</i> -P(EEGE) ₁₅₀ Figure 5.13
(9) P(t-BuGE) ₂₀₀	t-BuGE (1M)	Sec-butyl lithium	30	Toluene	24 hr	(NOct ₄ Br):iBu ₃ Al 1:3	Oligomers

			rm				Figure 5.14
(10) PI- <i>b</i> -P(EO- <i>stat</i> -EEGE) EO units -1850 EEGE units - 280	EEGE EO	PIOH 8450 g/mol	40	THF	4 days		PI- <i>b</i> -P(EO- <i>stat</i> -EEGE) DP of EEGE = 74 DP of EO = 289 Figure 5.15

5.3.1.8 Modification of terminal hydroxyl group on PIOH with imidazolium

5.3.1.8.1 Mesylation of PIOH

Dry PIOH (2.7g, 8450 g/mol) was dissolved in 200 mL of dry methylene chloride. Methanesulfonyl chloride (0.5 mL, 20 equivalents of PIOH chains) and triethylamine (0.5 mL, 20 equivalents of PIOH chains) were added sequentially via gas tight syringes to the reaction flask placed in 35°C oil bath. The colorless reaction mixture turned to orange after 24 hrs. The reaction mixture was filtered with a Büchner funnel and neutralized with saturated Na₂CO₃. Finally, the product was washed with DI water (3x) and dried in vacuo overnight (25°C) to yield a brown, transparent and viscous oil. Product characterization was performed using ¹H NMR (Figure 5.19).

5.3.1.8.2 Imidazole modifications of mesylated PI

NaH (4 mg, 25 equivalent of polymer chains) was added to a two-neck round bottom flask equipped with a reflux condenser and argon bubbler, followed by 8 mg of imidazole dissolved in dry THF. The reaction was stirred for 1 hr at 50°C. After 1 hr, 0.5g of mesylated PI dissolved in THF was added to the vessel under argon. The reaction was continued for another 3 hrs at reflux. After 3 hrs, the reaction mixture was cooled to room temperature and filtered with a 0.45 micrometer filter. Excess solvent was removed via rotoevaporation and the sample dried in vacuo overnight. The product was characterized with ¹H NMR (Figure 5.19).

5.3.2 Results and Discussion

5.3.2.1 Investigation of synthetic strategies for integrating pendant hydroxyl functionality to SOS and IOI polymer systems.

Out of a range of possible protected glycidol monomers that are compatible for anionic ring opening polymerization, EEGE monomer was selected for a feasibility study aimed at producing controlled, high molecular weight linear polymer initiated from a PIOH macroinitiator. According to Erberich, M. et al. EEGE has shown the fastest polymerization rate when compared to other protected glycidol monomers like AGE or t-BuGE^[11].

To our knowledge, there is no literature on the polymerization of EEGE using the PIOH as a macroinitiator to yield controlled linear high molecular weight block copolymers. Our first attempts were based on simply applying the same reaction conditions typically applied to the polymerization of ethylene oxide from a PI₁₂₅-OH macroinitiator (Table 1, entry (1), THF, 45 °C), a reaction routinely performed by our group with quantitative conversion of monomer. Here, the 125 designates the PI DP associated with a molecular weight of 8450 g/mol. The intended target BCP product was PI₁₂₅-*b*-PEEGE₇₁₀, where the PEEGE block DP of 710 was selected to produce a spherical BCP morphology with PI comprising the spherical domains and PEEGE comprising the surrounding matrix. Our attempt at initiating a polymerization of EEGE from the PI₁₂₅-OH macro-initiator was successful, but propagation was limited to a very low degree of polymerization (DP) of EEGE even after 11 hours of reaction time. The number of repeat units of EEGE obtained on the attempted synthesis of PI₁₂₅-*b*-PEEGE₇₁₀ using this reaction methodology was a mere 6 units (calculations follow). The SEC chromatogram of the product

given in the inset to Figure 5.6 shows a monomodal distribution of polymer chains corresponding to the actual PI-*b*-PEEGE₆ product produced from the 11 day reaction, confirming chain degradation, for example, is not an issue during the long reaction time.

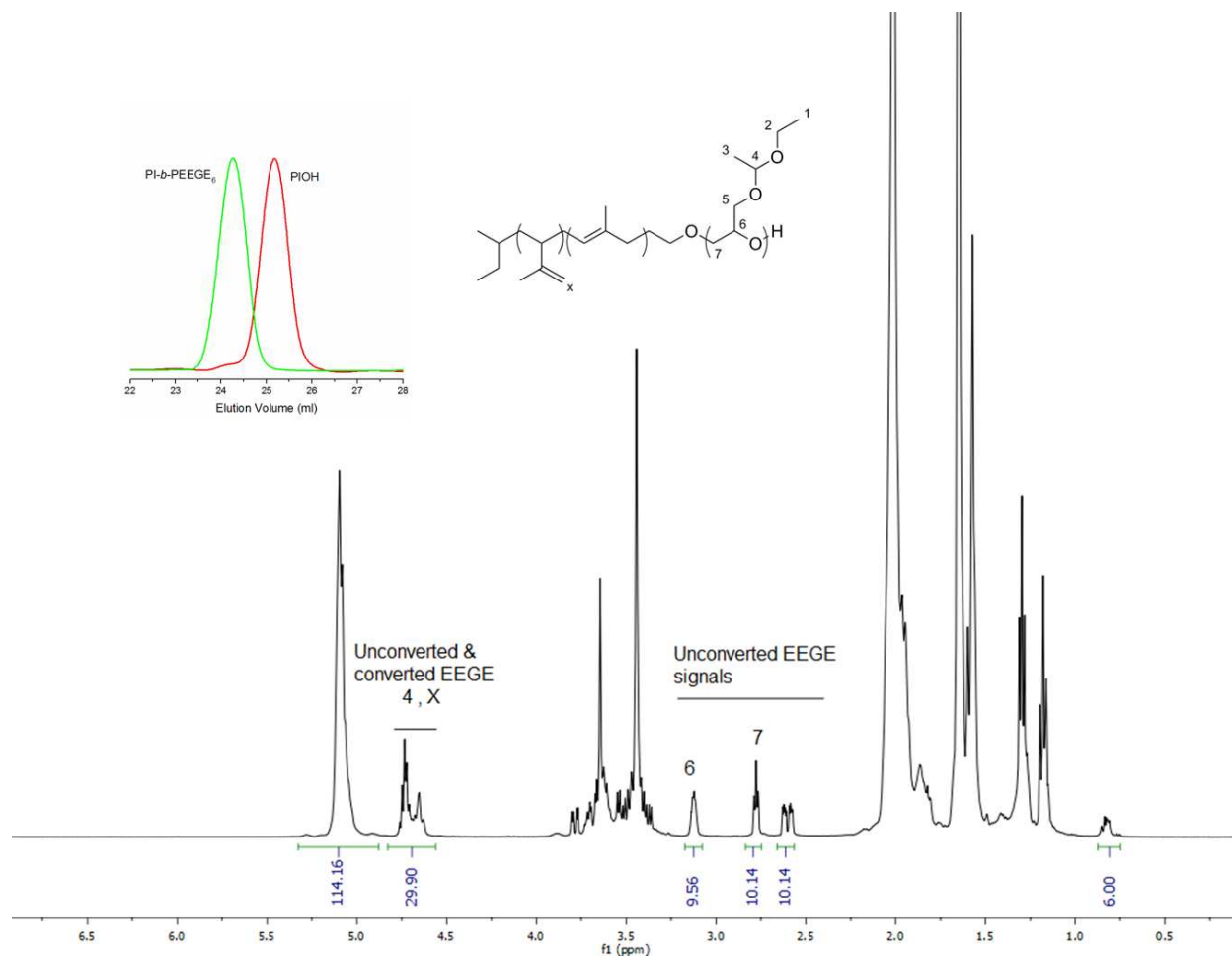


Figure 5.6 ¹H NMR and SEC data (day 10) from the anionic polymerization of EEGE using PI₁₂₅-OH as the macro-initiator, in THF at 45 °C (Table 1, entry (1)). No changes in EEGE conversion were detectable after the 10th day.

The calculation of the EEGE DP can be done efficiently using ¹H NMR (Figure 5.6), and is described here using the data from the resultant PI₁₂₅-*b*-PEEGE₆ product associated with this initial attempt. Proton signals in 2.5 - 3.25 ppm range correspond to protons in the epoxide ring of unconverted EEGE monomer left in the partially purified (vacuum dried) product. The

broadened signal at 4.5 - 4.75 ppm is a collection of three resonances corresponding to (1) the single proton on carbon **4**, (2) the analogous proton on un-polymerized EEGE monomer, and (3) the vinyl proton in the 1,2 units of the polyisoprene. The integrals of the spectra have been normalized to the initiator fragment, such that values shown in the spectrum are representative of a single average chain. The logic of a typical calculation of DP from the ^1H NMR is as follows. According to the spectra, the unique monomer proton signal at 2.6 ppm indicates approximately 10.14 unreacted monomer molecules are present for each polymer chain. The number of vinyl protons belonging to 1,2 units of the PIOH macro-initiator used was previously calculated to be approximately 14 per chain (Chapter 4, Figure 5.1). The difference between the integral of the multiplet at 4.5 - 4.75 ppm and the total number of protons from these two sources, gives the number of EEGE molecules on a PI chain. In this particular sample, that calculation gave 5.76 EEGE repeat units per chain ($= 29.90 - 10.14 - 14$).

By taking the ratio of the monomer present in the product to the total monomer fed in to the reaction, percentage of monomer conversion can be calculated. Monomer conversion was less than 1% for the reaction period of 11 days. The major fraction of unconverted monomer was evaporated off during the product isolation process (the vacuum drying step). Thus the EEGE present in the product's ^1H NMR spectrum is a minor fraction of the unconverted monomer. Such a low monomer conversion for the reaction time of 11 days implies either the propagation rate of EEGE is incredibly slow or that early termination of chain growth takes place. However, early chain termination has not typically been a problem in such reactions, and slow propagation is the likely culprit. As a result, it was concluded that typical anionic polymerization conditions used for EO are unable to yield high molecular weight EEGE in a practical experimental time frame.

Hence our next goal was to research different chemistries and polymerization conditions that might lead to higher monomer conversion and a higher molecular weight PEEGE blocks. Erberich, M. et al. has reported the homo-polymerization and copolymerization of glycidol monomers at 120°C using dry diglyme as the reaction solvent in order to achieve higher monomer conversions^[11]. Based on these reports, a second series of polymerization reactions were conducted with EEGE using the same PI₁₂₅-OH (8450 g/mol) macro-initiator (Table 1, entry (2), diglyme, 120 °C). In this attempt, the targeted product was PI₁₂₅-*b*-PEEGE₅₇₀. Changing the solvent from THF to diglyme and increasing the temperature from 45°C to 120°C resulted in 100% EEGE monomer conversion (verified with ¹H NMR, Figure 5.7), however the bimodal SEC chromatogram (Figure 5.7, inset) of the reaction mixture confirmed the existence of two predominant polymer products, one of higher (expected) and one of lower (unexpected) molecular weight than the original the PI₁₂₅-OH macroinitiator. The higher molecular weight product was expected based on the extension of the PI₁₂₅-OH but the lower molecular weight product appeared to be the result of simultaneous homopolymerization of EEGE. More exhaustive exploration of the literature revealed the proposed existence of an undesirable side reaction involving extensive chain transfer to the monomer^[23]. Hans et al. proposed that due to the basicity of the alkoxide at the propagating chain end, proton abstraction from the methylene group adjacent to the oxirane ring competes with chain propagation, forming an inactive hydroxyl terminated primary chain and a new active allyl alkoxide which can readily initiate a new, homopolymer chain. Similar chain transfer reactions have already been described in the literature in the polymerization of propylene oxide and phenyl glycidyl ether^[24, 25]. Characterization data of the product is presented in Figure 5.7.

In order to determine the molecular weights of the product by ^1H NMR end group analysis (Figure 5.7), the additional initiating groups have to be taken into account. By comparing the vinyl proton signal in the undesired initiating monomer (**a** in 6.25 - 6.6 ppm) and the methyl proton signals of the sec-butyl initiator fragment (**p**, 0.6 - 0.8 ppm) present in each PI₁₂₅-OH macroinitiator, the percentage of chains initiated by chain transfer (CT%) can be determined using equation **1**^[23].

$$\text{CT}\% = \frac{\text{int}(\mathbf{a})}{\text{int}(\mathbf{p})/6 + \text{int}(\mathbf{a})} \times 100\% \quad \mathbf{1}$$

Substituting the relevant integral values (int x) into equation **1**, the percentage of chains initiated by chain transfer was determined to be 93.4%. If the propagation rate of all the chains, initiated directly or by chain transfer, is assumed to be the same, we can calculate the DP of PEEGE homopolymer using the equation **2**.

$$\text{DP}_{\text{PEEGE}} = \frac{(\text{int}(4.5-4.75 \text{ ppm}) - 14)}{\text{int}(\mathbf{a})} \times 93.4\% \quad \mathbf{2}$$

As mentioned earlier, the broad multiplet at 4.5 - 4.75 ppm is a collection of signals from the vinyl protons of 1,2 units of PI₁₂₅-OH and the single proton on carbon **4** of EEGE monomer. The difference between the integral of multiplet at 4.5 - 4.75 ppm and the known number of vinyl protons on 1,2 unit of a PI chain (=14) gives the number of EEGE repeat units present (not necessarily attached) per PI chain (576.98). Since 93.4% of chains are initiated with chain transfer, equation **2** allows the DP of PEEGE homopolymer to be determined. Here, that calculation confirmed the DP of PEEGE homopolymer to be approximately 37 repeat units. Assuming the propagation rates remain identical, the DP of PEEGE in the block copolymer should also be approximately 37. Given that a DP of 37 on PI₁₂₅-*b*-PEEGE₃₇ was still not sufficient to produce the targeted spherical nanostructure, the separation of block copolymer from homopolymer via fractionation was not attempted. The dramatic increase in propagation

rate leading to total monomer conversion is consistent with the large increase in temperature applied to the systems, however, it concurrently produces extremely high rates of undesirable chain transfer incompatible with BCP formation.

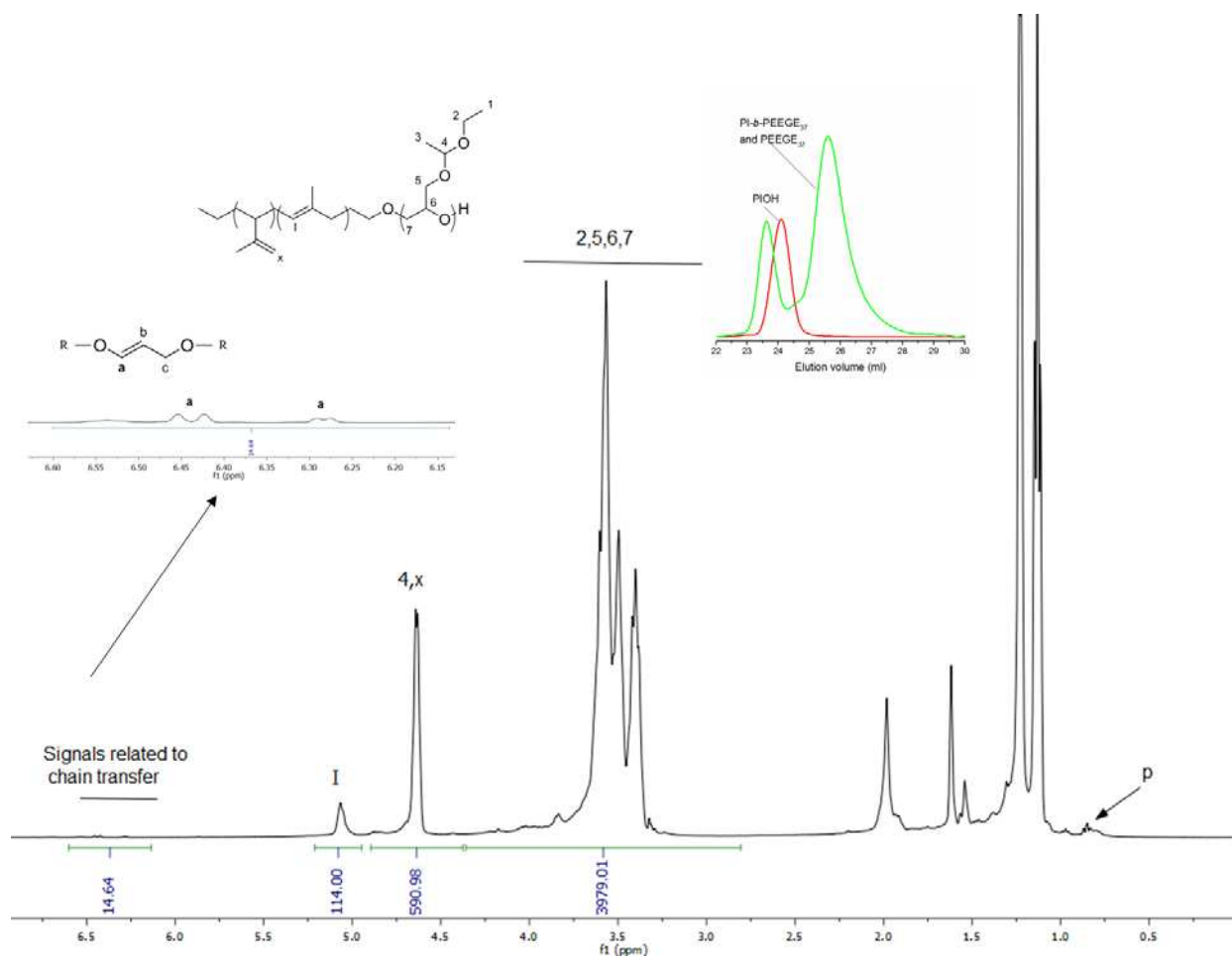


Figure 5.7 ^1H NMR and SEC data from the anionic polymerization of EEGE using $\text{PI}_{125}\text{-OH}$ as the macro-initiator, in diglyme at 120°C (Table 1, entry (2)).

Interestingly, it is not entirely clear if the increase in chain transfer is entirely a result of the temperature increase, or is enhanced by the switch in solvent from THF to diglyme. Both solvents are non-protio ethers, although the increased complexing ability of diglyme with alkali metal cations may be a factor in the increased chain transfer. Ultimately, the change in solvents

was necessary to accommodate high temperature reaction conditions selected, with diglyme possessing a much higher boiling point than THF (168 °C vs 66 °C). Regardless, increasing the temperature and changing the solvent seemed to have increased the reactivity of the propagating chain end such that it can attack not only the oxirane ring, but also the adjacent methylene protons resulting in chain transfer. At this point, it appeared that increasing polymerization temperature may provide a promising approach for achieving high molecular weight in practical reaction time periods, but the chain transfer tendency of the monomer would have to be eliminated.

Thus we attempted another polymerization under same reaction conditions, but with a different protected glycidol monomer, tert-butyl glycidyl ether (t-BuGE), in hopes that a bulkier substituent opposite the oxirane ring would hinder proton abstraction and thus chain transfer (Table 1, entry (3), diglyme, 120 °C). Importantly, t-BuGE was also compatible with highly basic anionic polymerization conditions and facile deprotection of an alcohol post-polymerization by simple exposure to a mild acidic environment.

In this experiment, the targeted product was $PI_{125-b-P(t-BUGE)_{1300}}$. Product characterization data is presented in Figure 5.8. Broadened signal peaks at 3.20 - 3.75 ppm in 1H NMR spectrum corresponding to main chain protons are an indication of polymerization of the monomer. The integral of the collection of signals from 3.20 - 3.75 ppm matches the expected value from the monomer feed (5 protons on carbon **1**, **2** and **3** x 1300), confirming quantitative conversion (polymerization) of monomer. However, similar to the 1H NMR for the polymerization of EEGE at these conditions (Figure 5.7), signals indicative of chain transfer are present in the 6.25 -6.6 ppm range. The percentage of chains initiated by chain transfer (CT%) can still be determined using equation **1**. According to the calculations 88.5% of chains were

initiated by chain transfer. This result is supported by the SEC chromatogram of the product which shows a very broad distribution with a majority of chains being lower molecular weight than the macroinitiator (PI₁₂₅-OH). By changing the monomer from EEGE to t-BuGE, it appears there may be a slight lowering of the overall percent of chains initiated from chain transfer (by about 5%), but this change is largely insignificant relative to the overall goals for the polymerization. It appears the steric hinderance by the bulky tert-butyl substituent is insufficient to alleviate significant chain transfer.

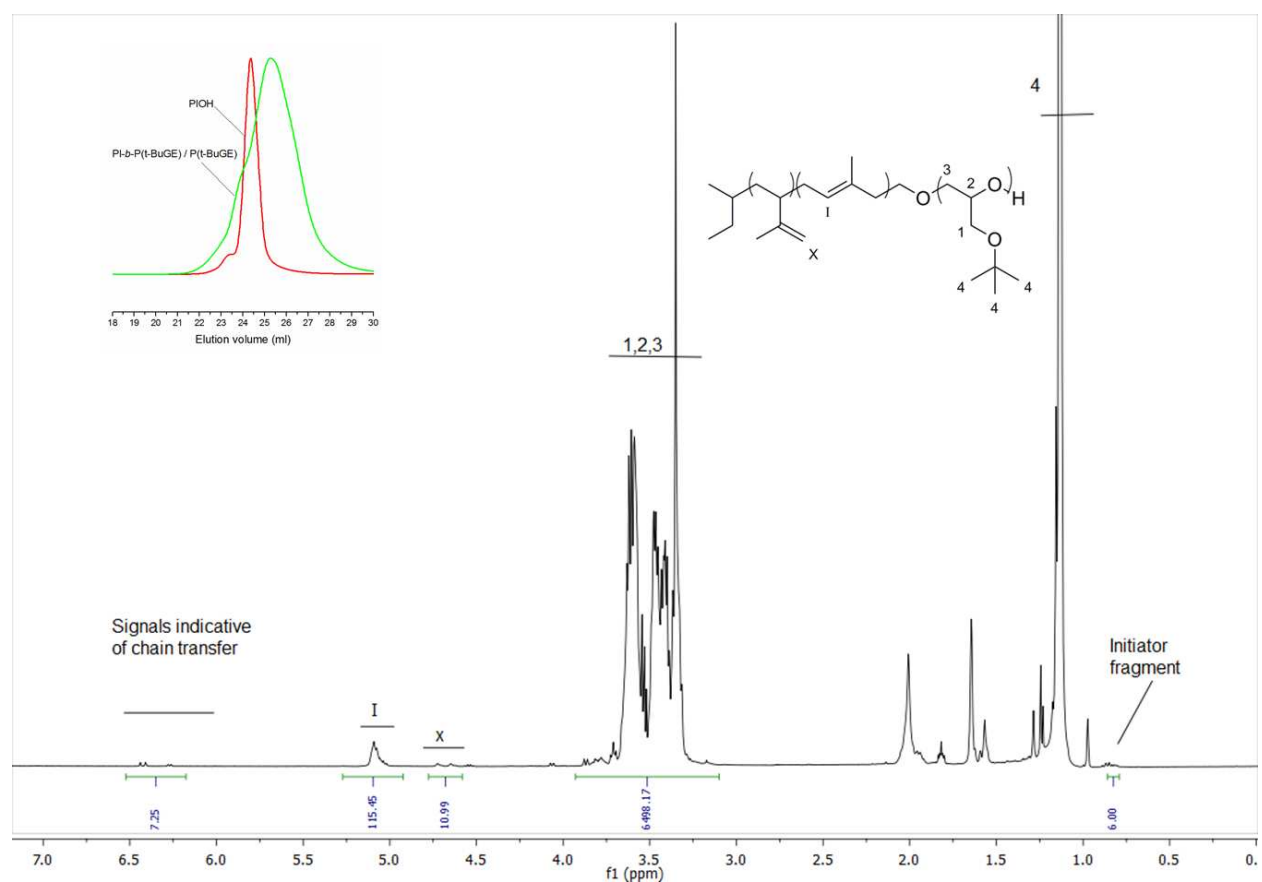


Figure 5.8 ¹H NMR and SEC data from the anionic polymerization of t-BuGE using PI₁₂₅-OH as the macro-initiator, in dyglyme at 120 °C (Table 1, entry (3)).

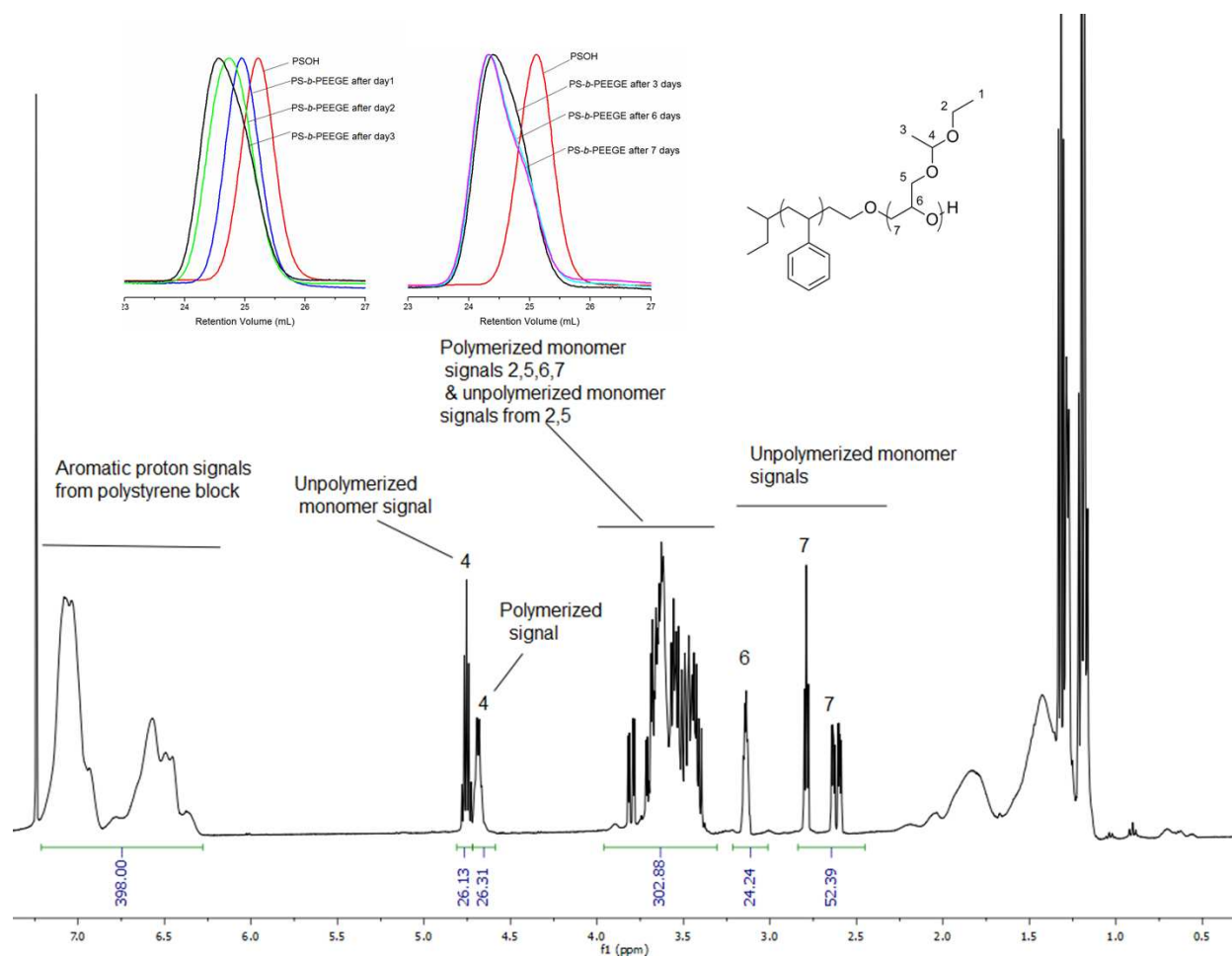


Figure 5.9 ^1H NMR and SEC data from the anionic polymerization of EEGE using PS₇₇-OH as the macro-initiator, in THF at 45 °C (Table 1, entry (4)).

Subsequent examination of the PI₁₂₅-OH macro-initiator revealed a bimodal distribution which was not anticipated from analysis prior to the polymerization. While the potential role of this bimodal distribution was unclear (if it existed at the time of initiation) the confirmed presence of chain transfer at levels rivaling the EEGE monomer suggested further experimentation was likely to be unfruitful. It was concluded that both monomers EEGE and t-BuGE share the same chain transfer propensity at higher temperatures that inhibits propagation of the primary chain to molecular weights required for sphere formation. Hence a decision was made to continue exploration of the different reaction conditions and chemistries aimed at

increasing the DP of EEGE itself, and abandoning investigation of t-BuGE as an EEGE alternative.

Hans et. al reported the apparent reduction of chain transfer in EEGE polymerizations initiated with 3-phenylpropanol/potassium 3-phenylpropanolate by lowering temperatures to 60 °C, yet the maximum DP of EEGE reported at 100% monomer conversion (claiming no chain transfer) was 24 repeat units^[23]. The initiator used and the initiator to monomer ratio were two factors, other than the temperature, identified by that study to affect the degree of chain transfer and the extent of monomer conversion^[23]. To evaluate the potential effect of the initiator to monomer ratio on chain transfer and monomer conversion using our macroinitiator system, another EEGE polymerization was conducted changing the macro-initiator from PI₁₂₅-OH to PS₇₇-OH (8000 g/mol) and increasing the initiator to monomer ratio from 1:710 to 1:67. Thus, the targeted product was PS₇₇-*b*-PEEGE₆₇. The reaction was run for one week and SEC samples were drawn once a day for three days, and then once again on day 6 and day 7. SEC chromatograms (Figure 5.9) of a monomodal distribution of molecular weights and the leftward shift of the peak maximum (to earlier elution volumes) with time indicate the chain extension of macroinitiator with EEGE. However, after day 3, no more shift of the peak maximum was observed. Interestingly, the chromatogram of day 6 shows a slight narrowing of the chain distribution and formation of a low molecular weight shoulder, which implies the existence of a group of early terminated chains and a fraction of chains continuing to propagate through day 6. From the ¹H NMR (Figure 5.9), the degree of polymerization was calculated to be 26. The two multiplets in 4.5 - 5.0 ppm correspond to the proton on carbon **4** of the polymerized and unpolymerized EEGE monomer. Resonances at 4.7 ppm are from polymerized EEGE repeat units and those at 4.8 ppm are from the analogous proton on unreacted EEGE monomer. Since

the integrals are normalized to the initiator fragment such that they represent a single average chain, the integral at 4.7 ppm (26.31) directly corresponds to the DP of PEEGE generated during the polymerization, presumably all initiated from the PS₇₇-OH macroinitiator, given the positioning of the product distributions to the left of the macroinitiator in the SEC chromatogram, and the absence of a low molecular weight homopolymer peak seen in previous reaction attempts. The integration of multiplet at 4.8 ppm (26.13) corresponds to the number unconverted EEGE monomers per chain that remain in the product after the vacuum isolation step. Also the monomer conversion calculated for this polymerization, by taking the ratio of converted EEGE present in product to the EEGE in the feed, was 34%. The improvement in DP of EEGE initiated with PS₇₇-OH compared to that of the PI₁₂₅-OH is about 20, which is still not high enough to achieve the targeted spherical morphology.

Ultimately, while the increase in initiator to monomer ratio appears to have suppress the chain transfer reaction for this attempt, such a change is contrary to our goal to achieve high molecular weight linear PEEGE. That is, such molecular weights by necessity require very low initiator to monomer ratios, and so increasing this value, while beneficial to the reduction of chain transfer, will not enable the high molecular weight chains needed for formation of the sphere morphology.

Siebert et al.^[26] has reported a sequential anionic polymerization of styrene and EEGE initiated with *sec*-BuLi in the presence of phosphazene base (P₄t-Bu) to achieve high molecular weights for the PEEGE block with partially controlled chain transfer. The reported polymerization resulted in a mixture of block copolymer (PS-*b*-PEEEGE) and homopolymer (PEEGE) with the BCP being the 80% of the total product. Siebert et al. explain the need for phosphazene base in order to grow higher molecular weight EEGE blocks from PSOH as follows

(paraphrasing): “Once all the styrene monomer is consumed, the reaction mixture is left with live carbanion chain ends. Addition of EEGE monomer transforms the live carbanion ends to alcoholates. This site transformation from a carbanion to an alcoholate forms a contact ion pair which is not active in further polymerization of EEGE^[27, 28]. The added phosphazene base acts as complexing agent for the Li⁺ ions forming solvent separated ion pairs. As soon as complexation of Li⁺ occurs the alcoholate initiates EEGE polymerization”. Interestingly, they do not actively address the potential chain transfer issues in this system, even though they did see homopolymer formation. Regardless, the amount of homopolymer appeared to be favorably reduced relative to that found in our previous polymerization attempts. The highest DP of PEEGE reported by Siebert et al was 210, in a PS₁₀₀-*b*-PEEGE₂₁₀ block copolymer. In an attempt to reproduce their results, we targeted the block copolymer product, PS₇₇-*b*-PEEGE₂₀₀. The reported protocol was adapted to our PS₇₇-OH macro-initiator (Table 1, entry (5)) using similar conditions, but starting the reaction from the lithium alcoholate (alkoxide) step. That is, PS₇₇-OH (8000 g/mol) was dissolved in dry benzene and titrated with *lithium* naphthalenide (LiNap) to form the oxanion and the Li⁺ contact ion pair. EEGE monomer was then added, followed by phosphazene base. The reaction was allowed to proceed for four days as reported. Fundamentally, these reaction steps recreate the sequential anionic polymerization reaction reported by Siebert et al. Analysis of the SEC chromatogram and the ¹H NMR spectra of the product (Figure 5.10) confirmed the existence of a mixture of block copolymer and homopolymer.

As in previous ¹H NMR analyses, the integrals of the spectra have been normalized to the initiator fragment, such that values shown are representative of a single average chain. Since the two multiplets at 4.8 ppm and 4.7 ppm correspond to resonances of the single proton on carbon **4** of unreacted EEGE monomer and PEEGE, respectively, the average DP of the PEEGE formed

(found in either BCP or homopolymer) equals the integral of the multiplet at 4.7 ppm (=23.61). Hence, the ratio of polymerized EEGE units present in the product (integral of the peak at 4.7 ppm) to the EEGE monomer in the feed gives the fraction of total monomer converted. For the attempted reaction, the total monomer conversion was 11.8%. Resonances characteristic to chain transfer typically show up in the 6.25 - 6.6 ppm range. However, quantification of those signals could not be determined since they overlap with the resonances from the aromatic protons of PS, which dominate in terms of overall concentration in the polymer chain. Given the limited monomer conversion, and SEC confirmation of homopolymer in the final product, the BCP produced has a PEEGE DP less than 24 (the maximum value if no chain transfer occurred). Thus, reproducibility of the Siebert et al.'s results was not particularly successful in this polymerization attempt.

In an attempt to eliminate the overlap in ^1H NMR resonances between the macroinitiator main chain (PS) and the chain transfer homopolymer product, the above mentioned polymerization was re-run changing the macroinitiator from PS₇₇-OH to PI₁₂₅-OH. In this attempt (Table 1, entry (6), we targeted a low DP of the EEGE of only 60 for two reasons: First, the previous polymerization showed slow propagation kinetics (only about 11.8% monomer conversion for reaction time of 4 days) even in the presence of the phosphazene base, a well known accelerator for anionic polymerizations. Second, we decided to avoid the chain transfer issues associated with high initiator to monomer ratios even though such an approach was still contrary to achieving a high molecular weight PEEGE block. At this point, we hoped to gain some understanding about the ability to chain extend the PI₁₂₅-OH macroinitiator using phosphazene bases, leaving the high molecular weight challenge for future studies.

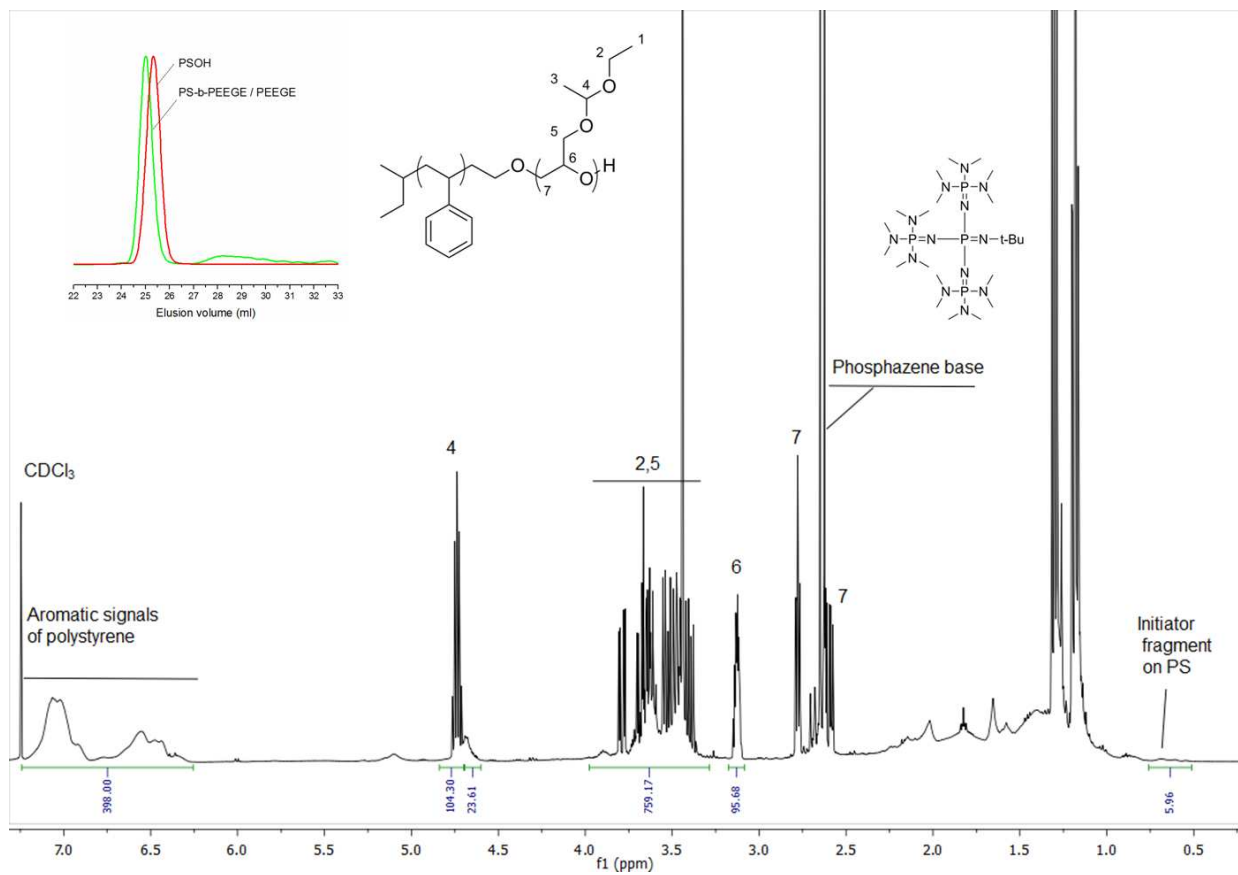


Figure 10. ^1H NMR and SEC data from the anionic polymerization of EEEG using $\text{PS}_{77}\text{-OH}$ as the macro-initiator, in benzene at 40°C , in the presence of phosphazene base (Table 1, entry (5)).

Figure 5.11 depicts the SEC chromatogram and the ^1H NMR of the product of this second attempt using the phosphazene base. The narrow monomodal SEC chromatogram shows a slight shift towards high molecular weight, and did not show any indication of homopolymer formation. Likewise, no evidence for chain transfer was found in the ^1H NMR. Using the same arguments made in the analysis of the Figure 5.6, the DP of PEEGE and the percent of monomer conversion were calculated for this product. The DP of the PEEGE on a PI chain was calculated to be a mere 3.51 ($=21.27-14-3.76$), confirming a very slow propagation rate using the $\text{PI}_{125}\text{-OH}$ macroinitiator.

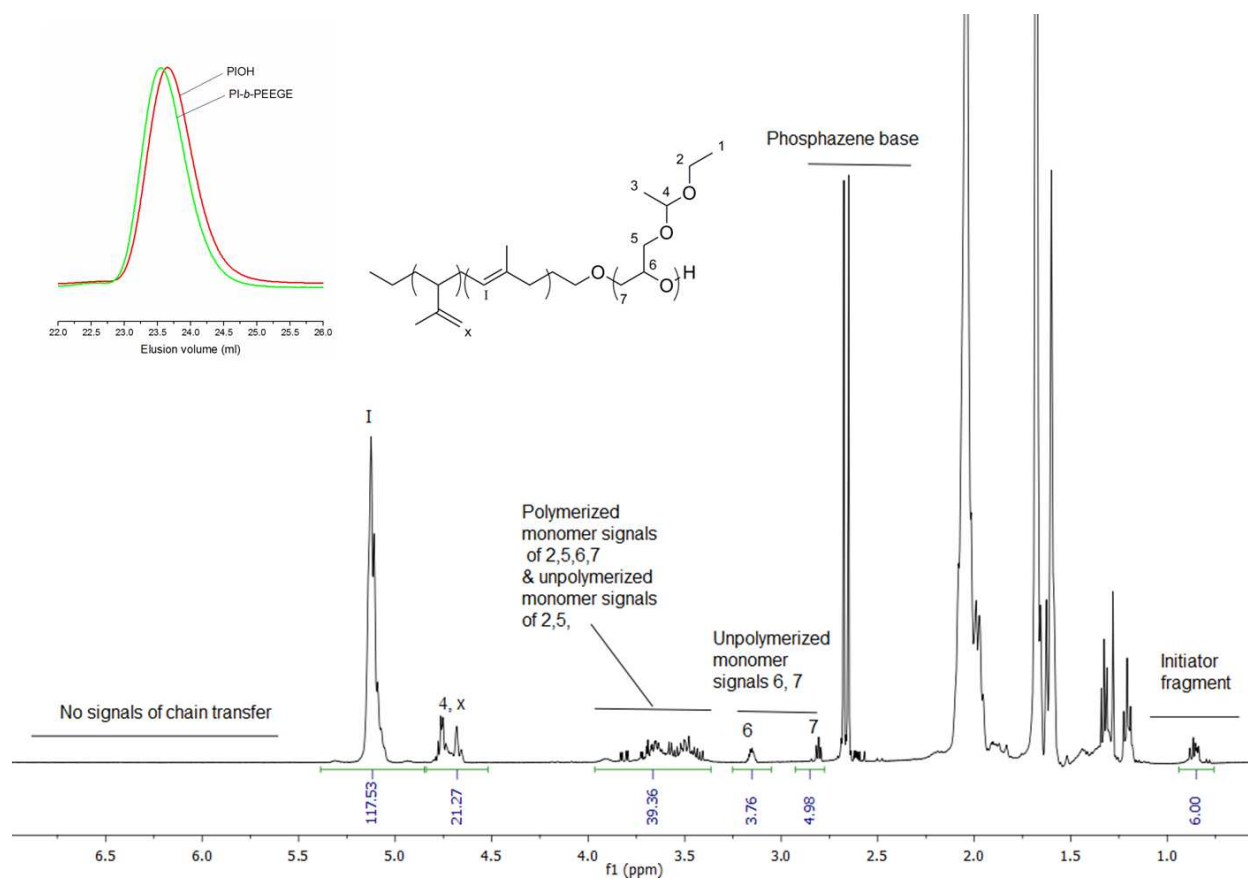


Figure 5.11 ^1H NMR and SEC data from the anionic polymerization of EEGE using $\text{PI}_{125}\text{-OH}$ as the macro-initiator, in benzene at 40°C , in the presence of phosphazene base (table 1, entry (6)).

When the monomer conversion rate is considered, PS-OH seems to be a better macroinitiator than PI-OH for growing PEEGE. In the last two polymerizations, a reduction in chain transfer was evident. But significant improvement of DP of PEEGE or in monomer conversions is not obvious with the use of phosphazene base as claimed by Siebert et al. The only difference between these two polymerizations and the protocol established by Siebert et al. was the use of a macroinitiator instead of growing the first polymer block in the same reactor. Theoretically, as long as a living oxyanion is present, propagation of the chain end should continue until all the monomer is consumed, but the influence of residual contaminants in the system, such as KOH base formed by reaction of lithium naphthalenide with adventitious water

during the titration step is unknown. In general, making a monomer moisture-free is more efficient than water removal from polymer, given the ability to use reactive distillation or distillation from drying agents with the former but not the latter. For example, drying isoprene monomer by distillation from n-butyllithium is much more efficient and effective than drying poly(isoprene). Drying 1g of isoprene via distillation takes about 15 mins whereas drying 1g of polyisoprene using vacuum takes roughly 18-24 hrs depending on the temperature used and the molecular weight of the polyisoprene. However, our lab has extensive expertise initiating polymerizations from macroinitiators and anionically polymerizing epoxy monomers like EO to achieve high molecular weights up to 100,000 g/mol with very narrow PDIs. In addition, drying polymer powders (polystyrene) is more efficient than viscous liquids (polyisoprene), and may be correlated to the improved DP obtained with the PS₇₇-OH initiator.

One additional caveat associated with our approach of starting the phosphazene polymerizations with macroinitiators instead of low molecular weight alcoholates, is the introduction of naphthalene and dihydro-naphthalene into the reaction at the titration step. It is possible that the phosphazene base can extract protons from either naphthalene or dihydro-naphthalene, making itself inactive.

Given these considerations, one last polymerization was conducted in the presence of the phosphazene base. The sequential anionic polymerization of isoprene and EEGE initiated with *sec*-BuLi in the presence of phosphazene base was attempted (table 1, entry (7)), closely following the conditions and the procedure established by Siebert et al. The SEC chromatogram of the product (Figure 5.12) shows a bimodal distribution indicative of the existence of both BCP and PEEGE homopolymer. For comparison, a small aliquot of the reaction mixture was taken following the isoprene polymerization, but prior to the addition of EEGE monomer.

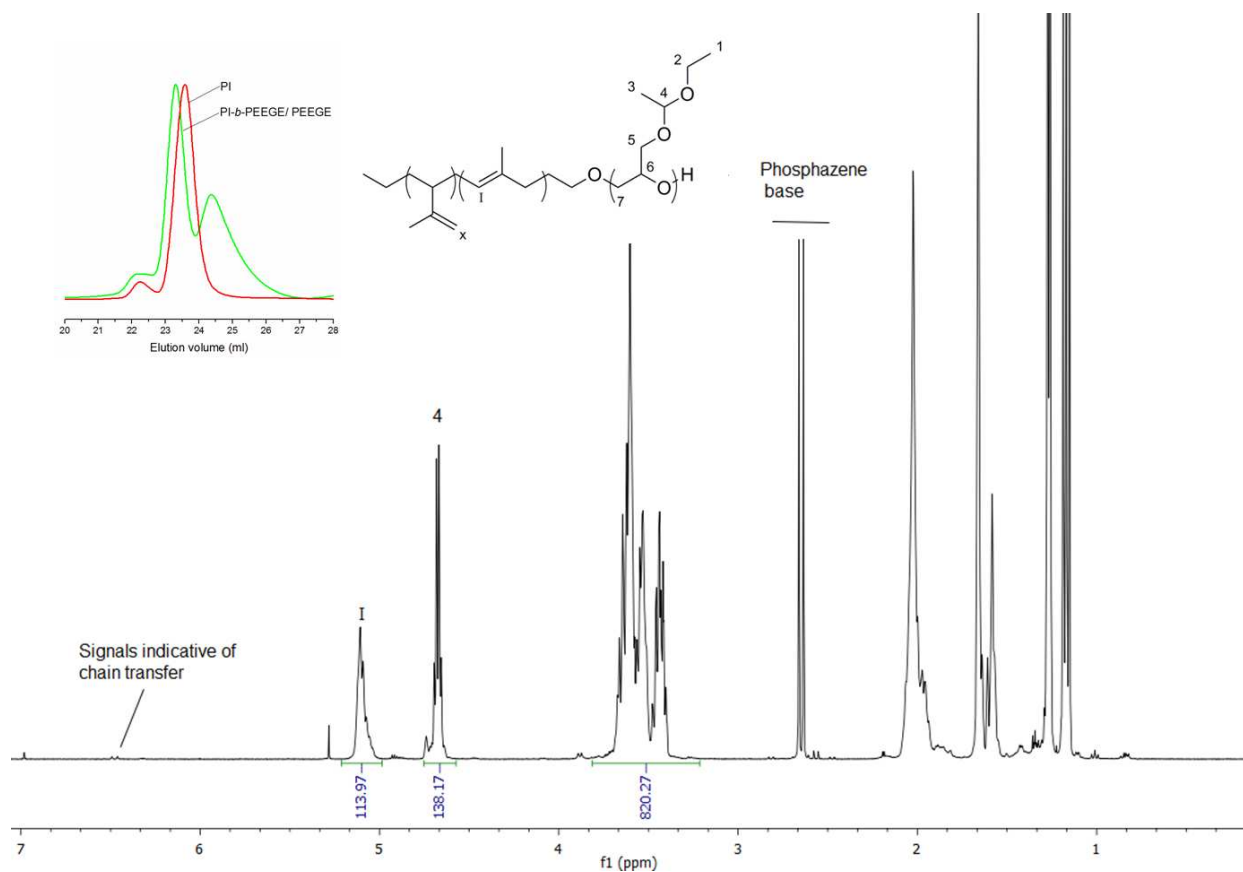


Figure 5.12 ^1H NMR and SEC data from the sequential anionic polymerization of isoprene and EEGE using *sec*-BuLi as the initiator, in benzene at 40°C , in the presence of phosphazene base (Table 1, entry (7)).

The SEC data for this PI intermediate is also included in Figure 5.12. In this particular SEC trace, the high molecular weight peak to the left is a byproduct of the sampling protocol, which involved cannulation of a small amount of the reaction mixture directly into methanol. The presence of dissolved oxygen in the methanol leads to a small percentage of coupled PI chains, which present in the SEC chromatogram. In contrast, termination of the BCP product, if all carbanions were converted to oxanions during EEGE addition to the reactor, should not be subject to such coupling. However, a high molecular weight shoulder suggestive of chain coupling exists in the SEC data for the BCP regardless. That is, the slight leftward shift in the primary elution peak suggests a small degree of chain extension, while the shoulder is likely due

to coupling of the extended chains (speculation). This result was not expected, and further investigation (^1H NMR of the distilled and undistilled isoprene monomer) revealed, that it was likely associated with the presence of degradation byproducts later found to be present in the isoprene monomer added to the reactor. While not identified, the presence of the contaminants appears to have affected the EEGE polymerization, while allowing the PI polymerization to proceed. It is likely that once the active PI chains were reacted with their first unit of EEGE, they became susceptible to chain coupling or chain transfer in the presence of the isoprene degradation byproducts. The bimodal SEC chromatogram suggests the tendency to undergo chain transfer to form homopolymer PEEGE was significant. Ultimately, the percentage of monomer conversion, the percentage of chains initiated by chain transfer and the DP of each monomer could have been derived from the ^1H NMR of the product using the same arguments and the equations used for analyzing Figure 5.6. Unfortunately, this unexpected contamination issue precludes drawing conclusions on the calculated values which have no physical relevance to the system. While a new batch of isoprene monomer was procured in time, we did not return to this particular approach, and the effectiveness of phosphazene base in maintaining the reactivity of the propagating chain end and suppression of chain transfer in the absence of the naphthalenide titration was never re-evaluated.

An interesting observation between previous two polymerizations (using PI and phosphazene base) is the significant difference in the degree of chain transfer. The latter of the two polymerizations (with degraded isoprene monomer) resulted in higher monomer conversion (likely a product of a higher degree of chain transfer) than the former polymerization initiated from the pre-formed $\text{PI}_{125}\text{-OH}$ macroinitiator. A fundamental conclusion that can be drawn from

these two polymerization attempts is that the purity of monomer (and by inference the reaction media) is a factor that controls the chain transfer.

Ultimately, the polymerization experiments with phosphazene base to achieve high DP of PEEGE did not show any advantage over other polymerization protocols performed. In addition, the presence of phosphazene base in the product in very high ratios is also an undesirable outcome not typically considered by previous reports. However, we found it could eventually be removed from the product by addition of acid followed by subsequent filtration of the formed salts. Given these results, a return to the phosphazene base approach may be warranted, if particular attention is given to assessing the importance of monomer purity on the ability to suppress chain transfer.

Virgini et al. reported a binary initiator system for accelerating the propagation rate of controlled polymerizations of epoxy monomers like propylene oxide and EO^[29, 30]. Gervais et al. reported using the same co-initiator system for the homopolymerization of EEGE and t-BuGE monomers. Inspired by their work, an attempt was made to polymerize EEGE initiated from the PS₇₇-OH macroinitiator applying the aforementioned chemistry (Table 1, entry (8)). In this reaction, the targeted product was PS₇₇-*b*-PEEGE₂₀₀. PS₇₇-OH was first titrated with potassium naphthalenide in THF to yield the alkoxide, after which the THF was removed via vacuum distillation and replaced with dry toluene. EEGE was then added to the reactor followed by the co-initiator triisobutylaluminum, (*i*-Bu)₃Al. According to Virgini. et al., (*i*-Bu)₃Al makes a complex with the oxygen in the monomer's oxirane ring, which makes the un-substituted carbon on the oxirane ring more reactive towards nucleophilic attack (by the oxanion chain end, presumably). The mole ratio of macroinitiator to (*i*-Bu)₃Al used was 1:5, identical to that used by Gervais et al. The only other significant deviation from previously established protocols for this

polymerization was the reaction temperature. This reaction was started at -30°C (during EEGE and $(i\text{-Bu})_3\text{Al}$ addition) and allowed to warm to room temperature.

Figure 5.13 shows the ^1H NMR and the SEC chromatograms of the product. The DP of PEEGE and the monomer conversion can be calculated following the arguments used in the analysis of the spectrum in Figure 5.9. The difference in the peak integrals corresponding to multiplets **4** and **6** gives a DP of PEEGE of 19.2 ($=42.83-23.63$). The SEC chromatogram of the product is narrow and monomodal and is shifted to left of the $\text{PS}_{77}\text{-OH}$ macroinitiator, which implies chain extension with EEGE. Also no formation of EEGE homopolymer or short chain oligomers through chain transfer is evident in this chromatogram. However, the DP of approximately 20 and monomer conversion of 9.5% over the four day reaction period implies that the propagation kinetics of this system have not improved from the use of $(i\text{-Bu})_3\text{Al}$ as suggested by Virgini, et al. In fact it was quite comparable (smaller only by 1.8%) to the kinetics observed in the previous polymerization attempt without $(i\text{-Bu})_3\text{Al}$ (Figure 5.9, Table 1, entry (4)). However, the controlled nature of the polymerization is evident by the narrow distribution of chains. This could be due to either monomer activation by $(i\text{-Bu})_3\text{Al}$ and/or the low reaction temperature.

Gervais, et al. have also reported homopolymerization of glycidyl monomers ($t\text{-BuGE}$ and EEGE) in the presence of ammonium salts, tetraoctyl ammonium bromide (NOct_4Br) and triisobutylaluminum ($(i\text{-Bu})_3\text{Al}$), both with high degrees of polymerization. The maximum DP of PEEGE and $\text{P}(t\text{-BuGE})$ that have been reported are 400 and 583, respectively. However, the related polydispersity indices (PDI) were slightly broad at 1.27 and 1.37, respectively^[13]. Even with slightly broad distributions, the reported results seem ground breaking. Hence, we made one

last attempt aimed at reproducing their results, with the intention of developing (or confirming) a protocol that would be applicable for co-polymerizations in our future work.

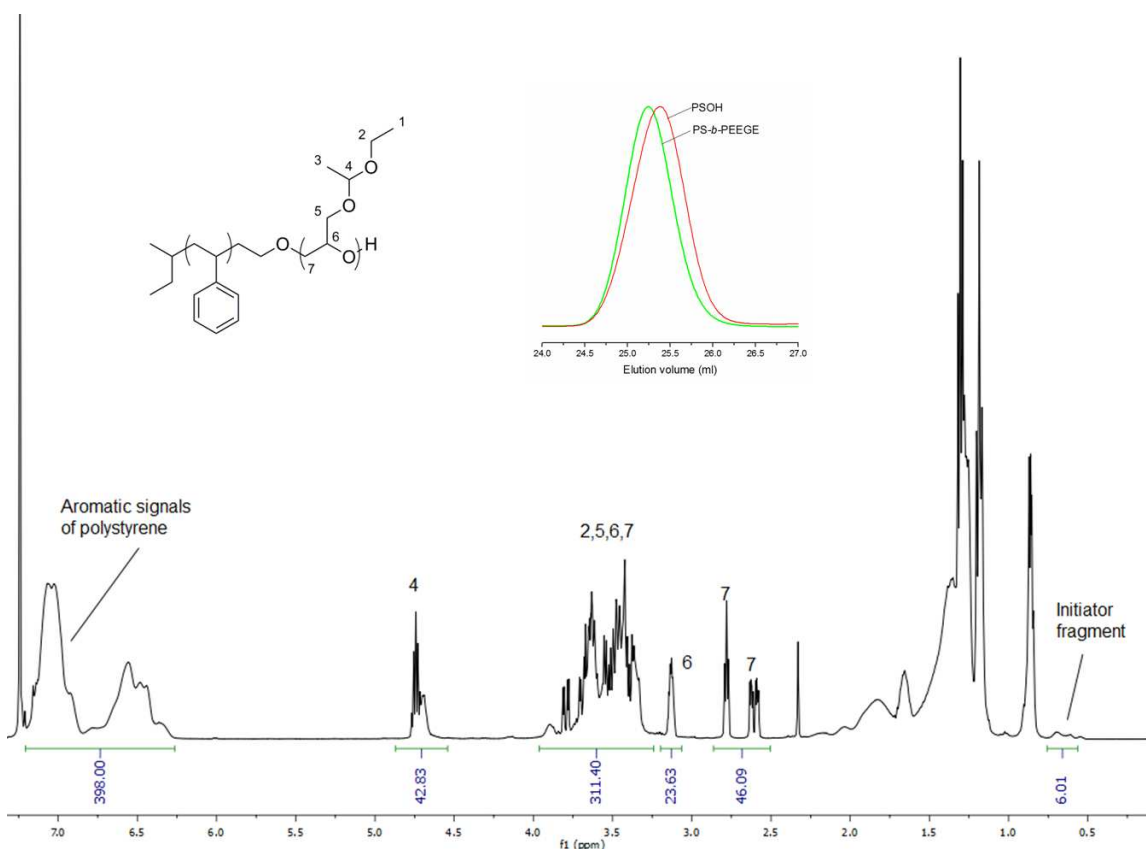


Figure 5.13 ¹H NMR and SEC data from the anionic polymerization of EEGE using PS₇₇-OH as the macro-initiator, in toluene at -30 °C, warming to room temperature, in the presence of (i-Bu)₃Al (Table 1, entry (8)).

In this polymerization attempt we followed the synthetic protocol reported by Gervais et al. very closely. The targeted product was P(t-BuGE)₂₀₀. However, this reaction attempt was not successful. The ¹H NMR and the SEC chromatograms of the product are given in Figure 5.14. The multi-peak SEC chromatogram with peaks in the range of the solvent flow markers indicates the presence of oligomers. The multiplet spanning 3.2 - 3.9 ppm in the ¹H NMR of the product corresponds to the protons on carbons **1**, **2** and **3**. However, the signals in the range of 1.2 - 1.8

ppm were not anticipated and most probably related to an undesirable product. A second attempt at reproducing the results from this publication (same experiment mentioned above) resulted in no polymerization at all.

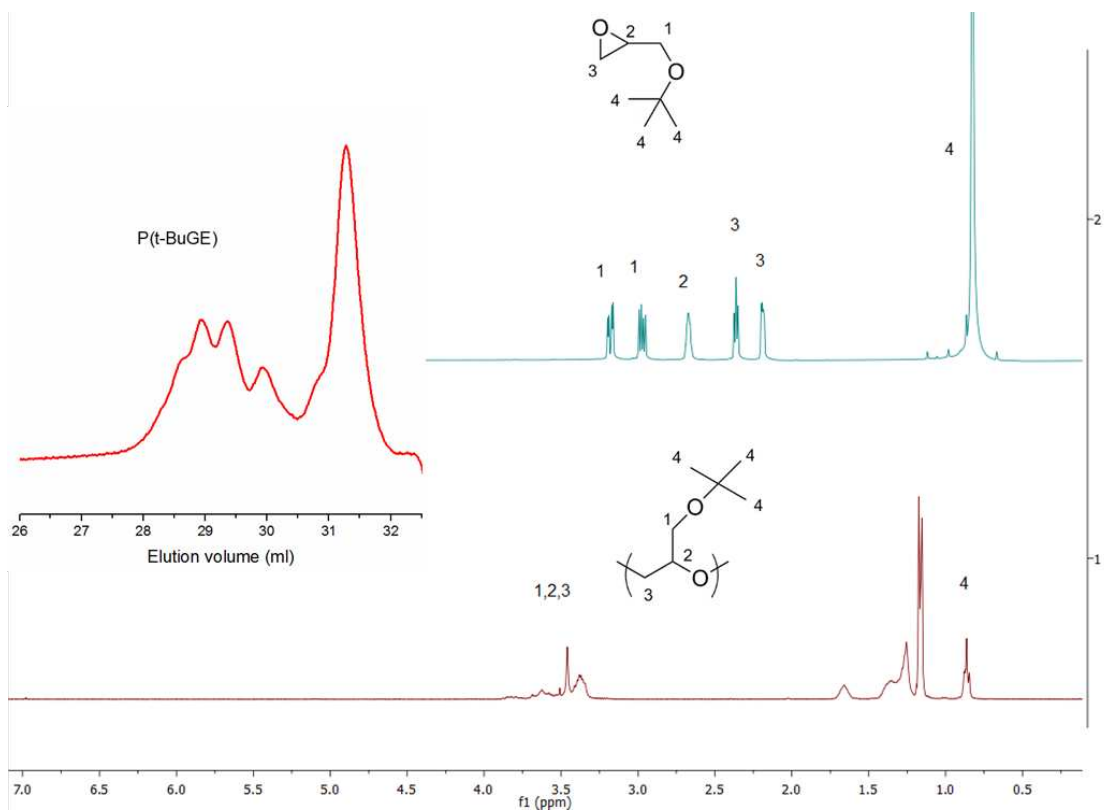


Figure 5.14 ¹H NMR and SEC data from the anionic polymerization of t-BuGE using NOct₄Br initiator and (i-Bu)₃Al as the monomer activator, in toluene at -30 °C, warming to room temperature (Table 1, entry (9)). ¹H NMR spectra on top right (blue) is of the t-BuGE monomer and the lower spectra from the product of the polymerization attempt.

Despite Gervais et al.'s claim of producing high molecular weight linear polyglycidol, a controlled polymerization of EEGE to yield a DP higher than 30 still remains an apparent challenge, with slow propagation rates and/or the undesirable chain transfer reaction that is particularly sensitive to the presence of very small concentrations of contaminants. If we were to run a polymerization reaction for a longer time scale (i.e. months), a more advanced reactor set

up may be required to maintain a long-term air-free/moisture-free environment (due to seal degradation with time).

A recent publication from Killops et al. has reported a controlled anionic copolymerization of AGE with EO initiated from a PSOH macro-initiator (11000 g/mol) achieving a total DP of the AGE monomer to be 58^[21]. An earlier publication from the same group of researchers, including Hawker and Lynd, showed that the addition of glycidyl monomers (AGE or EGVGE) to the initiator and growing chain end is favored over EO addition^[14], due to preferential coordination of the chain end to the AGE monomer. They also suggested that copolymerizations of EO with glycidyl monomers (AGE or EEGE) result in gradient-type copolymers where the functional glycidal ether is consumed early in the polymerization such that the chain produced is enriched near the initiator^[14]. Inspired by the work from these renowned researchers, and at the same time compelled with the existing challenges in synthesizing controlled high molecular weight PEEGE, we revised the 'B' blocks of the proposed *BCP system 2* from PEEGE to P(EO-*stat*-EEGE).

Anionic co-polymerization of EO and EEGE initiated from the PI₁₂₅-OH macroinitiator by forming the potassium alkoxide, was carried out in dry THF at 40°C (Table 1, entry (10)). In this reaction, the targeted DP for PEEGE and PEO was 280 and 1835, respectively. ¹H NMR and SEC chromatography were used to characterize the product and the results are shown in Figure 5.15. As in previous ¹H NMR spectra analyses, peak integrals across the spectrum have been normalized to the initiator fragment, such that values indicated are representative of a single average chain. According to the ¹H NMR spectrum, there are no shifts present at 4.4 ppm that would correspond to the unique proton on carbon **6** of EEGE monomer. This indicates that all of the unconverted monomer was removed during the product isolation process. The broadened

signal over 4.6 - 4.8 ppm is a collection of two resonances corresponding to the single proton on carbon **4** of PEEGE, and the vinyl protons in 1,2 units of the PI₁₂₅ block. The number of vinyl protons belonging to the 1,2 units of the PI₁₂₅-OH macroinitiator was previously calculated to be approximately 14 per chain (Chapter 4, Figure 4.1). The difference between the integral of the multiplet at 4.6 - 4.8 ppm and the protons belonging to PI block gives the number of EEGE molecules present per PI chain, which was calculated to be 74.07 (= 88.07-14). The EEGE conversion can be calculated by taking the ratio of this number to the targeted DP of PEEGE, which was 280 for this reaction. Hence the calculated EEGE conversion is 26% (=74.07/280). The broadened collection of shifts from 3.3 - 3.9 ppm can be assigned to the protons on carbons **2, 5, 6, and 7** of PEEGE and **8 and 9** of PEO. The fraction of the peak integral that corresponds to the contribution by PEEGE can be calculated from the DP of PEEGE (74.07 x 5 protons from **2,5,6,7** = 370.35). Subtraction of the peak integral from 3.3 - 3.9 ppm from the previously calculated value (370.35) corresponds to the total number of protons deriving from PEO (1528.99-370.35 = 1158.64). Since each EO unit possesses 4 protons, the calculated DP of PEO is 289 (=1158.64/4). The ratio of the DP of PEO in the product to the targeted DP of PEO gives the monomer conversion, calculated to be 15.8%. EO monomer conversion of 15.8% over four days suggests a drastic drop in rate of propagation of EO monomer in the presence of EEGE monomer. As Lee et al. suggests, if the glycidyl monomer is preferentially coordinated to the propoagating chain end relative to the EO monomer, the higher conversion of EEGE over EO observed here is consistent with their hypothesis.

The peak at 22.5ml on the SEC chromatogram of PI₁₂₅-OH macroinitiator, however was not expected; further investigation revealed that the PI₁₂₅-OH used had been spontaneously

partially modified/coupled disrupting the molecular distribution. Data specific to this latter investigation is included in the appendix (Figure AII.2).

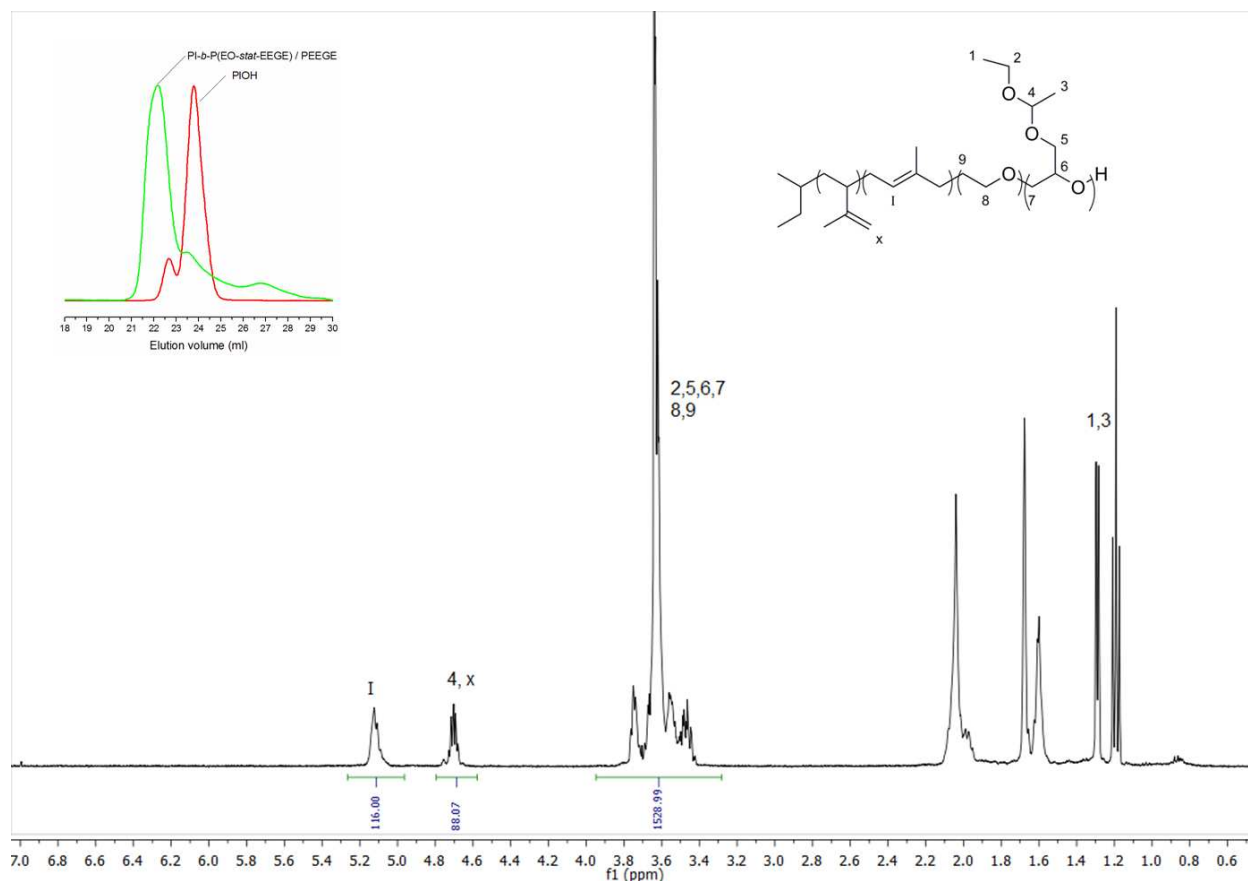


Figure 5.15 ¹H NMR and SEC data from the anionic co-polymerization of EEGE and EO using PI₁₂₅-OH macro-initiator, in THF at 40°C (Table 1, entry (10)).

The SEC chromatogram of the product has three distinguishable peaks implying the existence of three prominent products. The left most peak can be attributed to the majority product consisting of higher molecular weight chains than the starting macroinitiator (PI₁₂₅-OH). Since no signals characteristic of chain transfer to monomer (in the 6.25 - 6.5 ppm range) are present in ¹H NMR, the other high molecular weight product could probably be due to an early termination associated with byproducts in reaction mixture present in the degraded PI₁₂₅-OH

macroinitiator used. Further, the combination of an early-terminated population of chains with the third, low molecular weight peak in the oligomer range suggests chain transfer, albeit not to monomer, is a major contributor to the observed molecular weight distribution.

Sound conclusions cannot be drawn from this experiment, unfortunately, due to the use of partially degraded PIOH. However, even in the presence of some contamination, the chain extension with EO and EEGE observed was inspiring. Another trial of the same experiment using un-degraded PIOH and higher purity EEGE, is definitely worth investigating. In the scope of this thesis, however, this obvious next step remained uninvestigated and has been left for future researchers to explore.

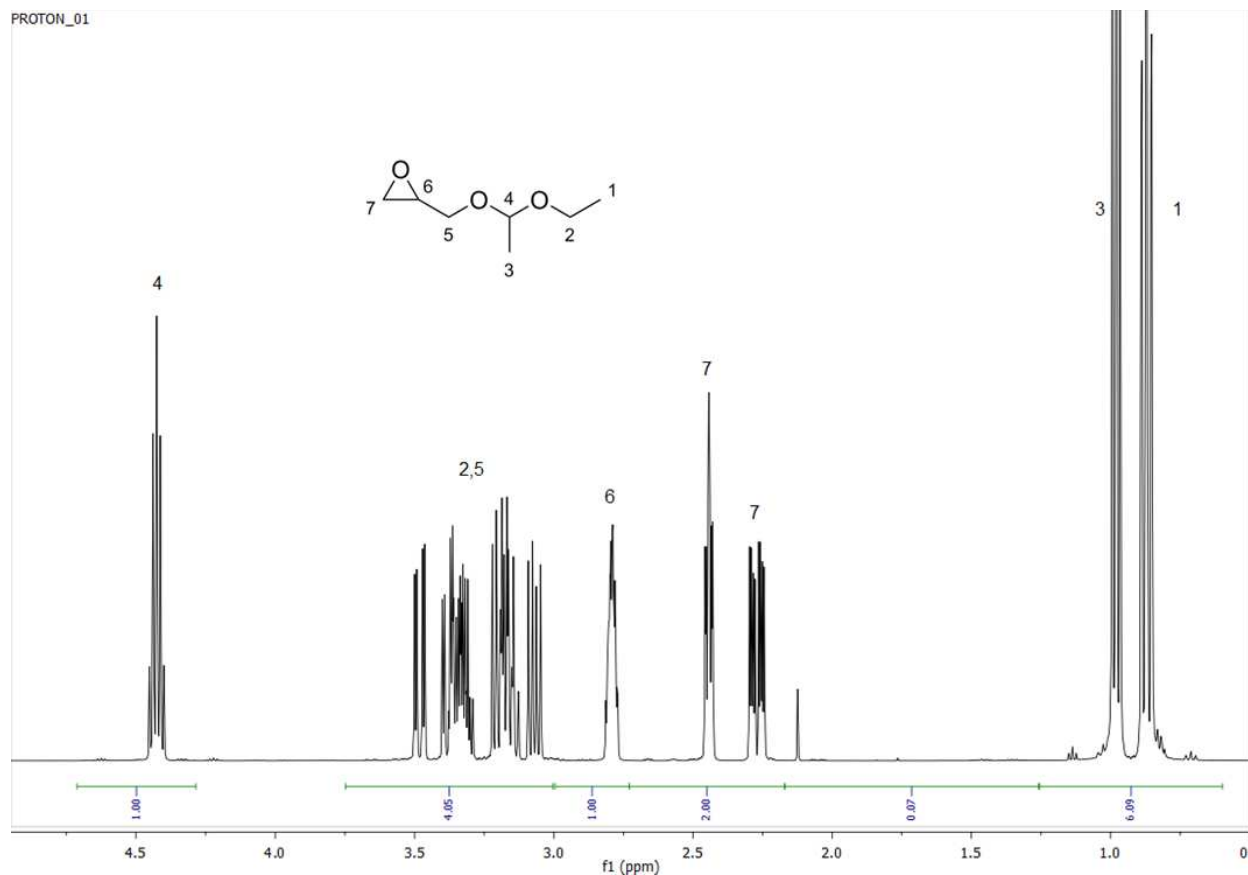


Figure 5.16 ¹H NMR of EEGE monomer distilled with short-path distillation set up.

Key learning from all these polymerization attempts is the importance of the level of monomer purity required in order to control the chain transfer. A protocol developed to achieve higher levels of purification is described in experimental section of this chapter, with the optimal conditions found. Glycidyl ether monomer purified with this new protocol was not used in any of the described polymerizations, since the development of this purification protocol was done at the last stages of this investigative work.

^1H NMR spectra of purified EEGE monomer based on this protocol is shown in Figure 16. Peak integrations are normalized to the resonance for the proton on carbon 4 such that the spectrum describes the relative number of protons detected per EEGE molecule. Resonances at 0.25 -1.25 ppm correspond to the six methyl protons on carbons 3 and 1. The integral of these two triplets should be 6.00, but the peaks integrated to 6.30 using the previous purification procedure (^1H NMR, Figure AII.1) suggesting additional contributions from another proton source. With the new purification procedures developed, the integral of those two triplets could be reduced from 6.30 to 6.09. The consistency in this relationship suggests a significant increase in purity of the monomer. However, the removal of the proton resonance at 2.18 ppm, which is not an expected resonance for an EEGE molecule remains even after the additional purification. Currently, its significance in the reaction is unknown. Regardless, a more sensitive characterization technique like gas chromatography (GC) may be needed for the validation of monomer purity in the future.

5.3.2.2 Deprotection of the PEEGE to yield PG

As a proof of concept experiment focused on validating the methodologies proposed to synthesize product **9** (scheme **5**), some additional investigative reactions were carried out on some of the polymeric species prepared. The acetal groups in the PEEGE block of PI-PEEGE block copolymer were cleaved to the resulting hydroxyl using simple contact of the chains with an acidic environment. Specifically, the product was first dissolved in THF and HCl was then added to the polymer solution and stirred for 15 minutes at room temperature. Next, saturated NaOH was added to the mixture to neutralize the pH. Salts were removed by filtration and the filtrate was dried under vacuum for 12hrs. and then extracted to DI water, dried in vacuo, and the characterized with ^1H NMR (Figure 5.17).

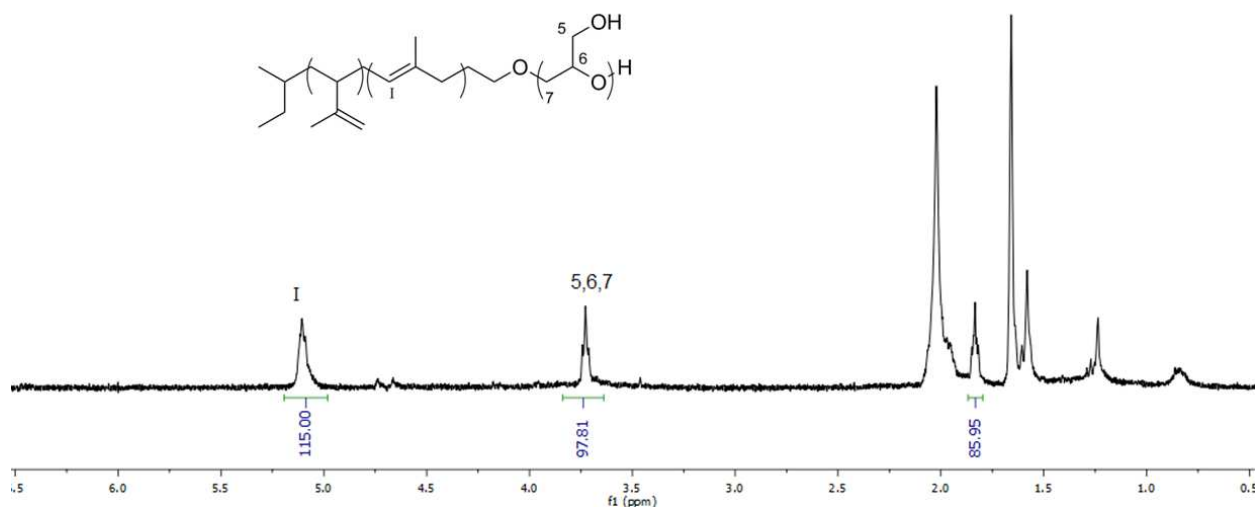


Figure 5.17 ^1H NMR of PI-*b*-PG₁₉

The integrals of the ^1H NMR are normalized such that the spectrum represents a single average chain. The integral of the triplet at 3.75 ppm should reflect the five protons on carbons **5**,

6 and **7**. Hence the DP of the resulting polyglycidol (PG), which is 19, was calculated by dividing this peak integral by the number of relevant protons ($97.81/5$). The triplet at 1.8 ppm is not characteristic to the unmodified PIOH macroinitiator and thus appears uniquely to the PG block.

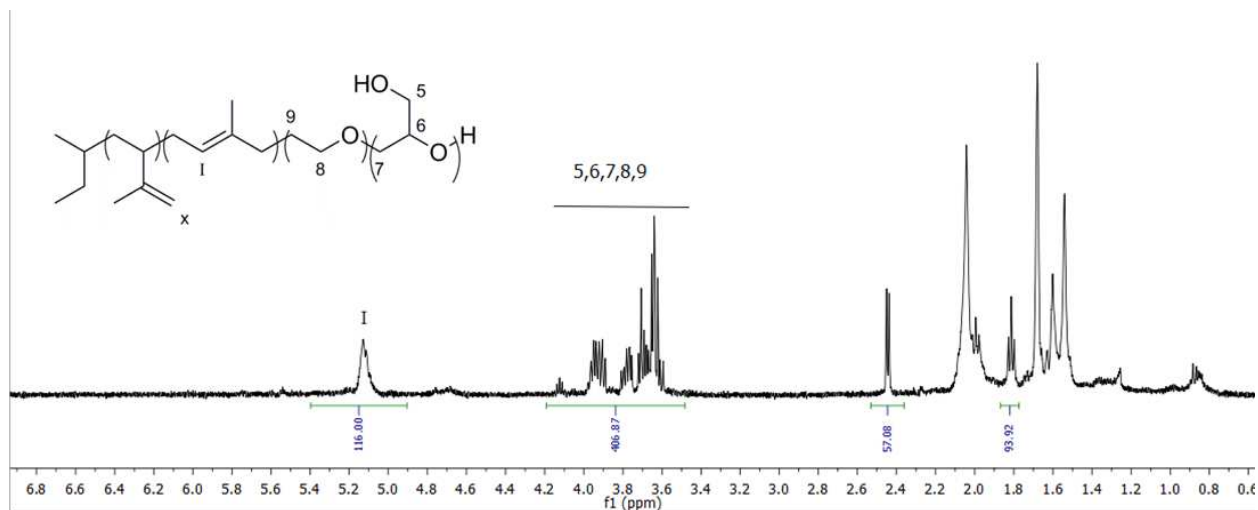


Figure 5.18 ^1H NMR of PI-*b*-P(EO-*stat*-G); The acetal group of EEGE was cleaved using simple exposure to a weakly acidic environment.

Additionally, the transformation of PI-*b*-P(EO-*stat*-EEGE) to PI-*b*-P(EO-*stat*-G) was performed in THF and HCL media as discussed earlier. However the product recovery was slightly different for the two starting products (sections 5.3.1.5 & 5.3.1.6). Extraction of the product (PI-*b*-P(EO-*stat*-G)) to an aqueous layer was possible in the case of the copolymer, perhaps due to the inclusion of water soluble EO repeat units. This product was also characterized with ^1H NMR for which the data is given in Figure 5.18. The triplet at 1.81 ppm and the doublet at 2.45 ppm are not characteristic to the PIOH or PI-*b*-PEO. Assignments of these two new signals have yet to be definitively made. Since the product contains a block of random copolymer of EO and EEGE, it is likely the chemical shifts of the protons on carbons **8**

and **9** on polymerized EO units are strongly influenced by the chemical identity of the repeat unit sequences along the backbone.

5.3.2.3 Functionalization of PIOH with imidazolium

To explore the feasibility of the chemistry proposed to synthesize product **11** (Scheme 7), conversion of the terminal hydroxyl on our PIOH macro-initiator to a terminal imidazolium was attempted. Mesylation of the hydroxyl on PIOH was followed by imidazolium functionalization through nucleophilic substitution. The product or intermediate at each step was characterized with ^1H NMR spectroscopy as presented in Figure 5.19. Peak integrals in both spectra are normalized such that each represents a single average chain. The resonance at 2.9 ppm in the lower spectra corresponds to the methyl protons in the mesylate group. The remainder of the spectra is characteristic to the PI, consistent with the mesylation of terminal hydroxyl on PI. The peak integral of the proton resonance at 2.9 ppm is expected to be 3 if quantitative functionalization was achieved. The actual integrated value near 2 implies that the functionalization efficiency achieved was only 66.6% ($\sim 2/3$). In upper ^1H NMR spectrum is the data corresponding imidazole functionalized PI (Figure 5.19 top).

Disappearance of resonances corresponding to mesyl protons and the appearance of aromatic resonances related to imidazole, verify the transformation. Excessive amounts of NaH and imidazole used in the reaction caused the product to be contaminated with these species. Further isolation of product was not attempted since that issue was preventable in future attempts.

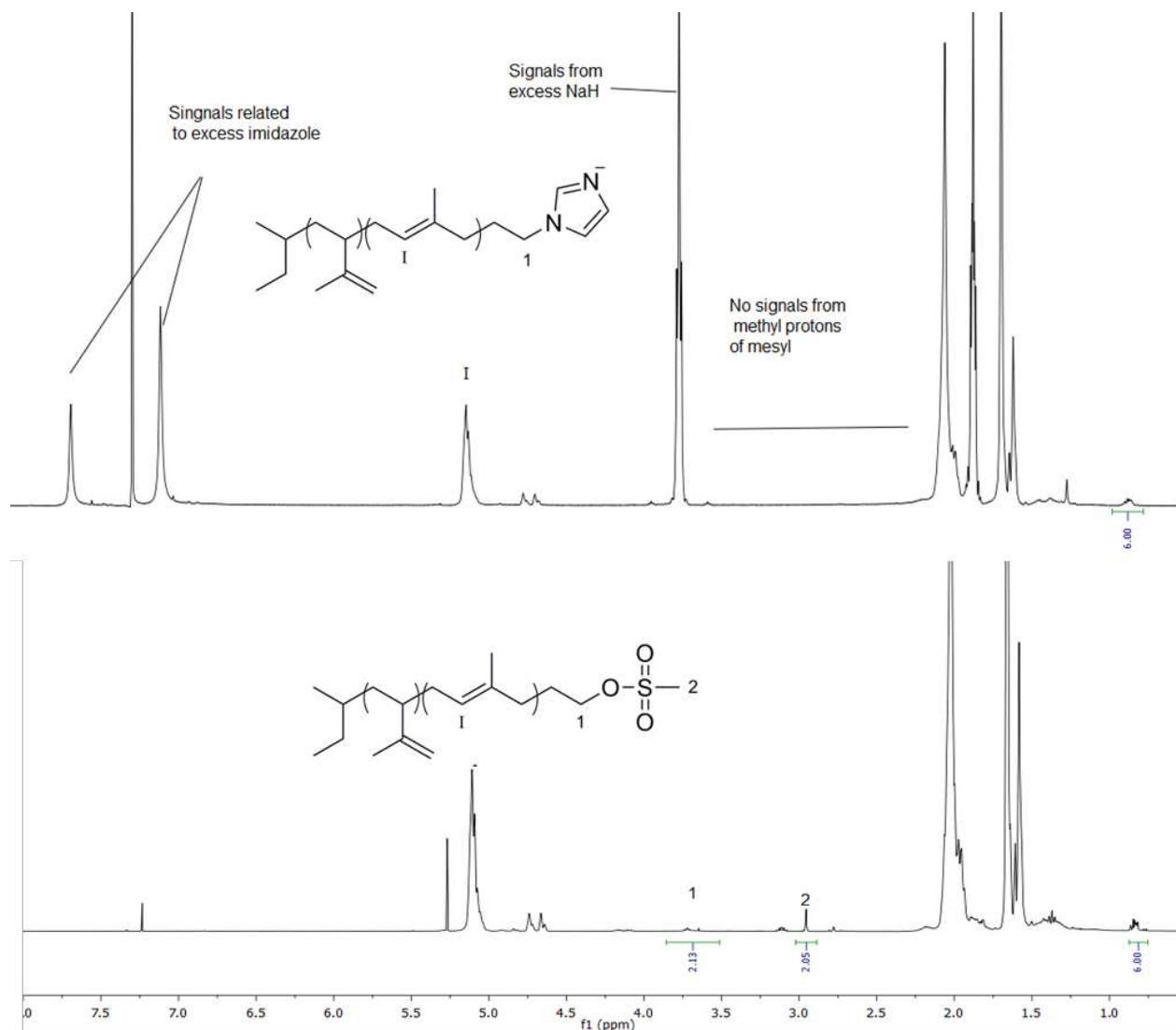


Figure 5.19 ¹H NMR of Imidazole functionalized PI (top) and Mesylated PI (bottom). Disappearance of signal of methyl protons at 2.9 ppm in top ¹H NMR signifies the successful substitution of imidazole to the mesylate

5.4 CONCLUSIONS AND RECOMMENDATIONS FOR RELEVANT FUTURE WORK

A key finding from this series of experiments is that undesirable chain transfer is controllable by lowering the temperature and increasing the purity of the reaction media and

monomer. Also, lowering the basicity of the propagating chain end without decreasing its nucleophilicity would be another option to control the chain transfer. Experimenting with different solvent combinations for the reaction media may be a route to further improve conditions (above mentioned) for the propagating chain end. The PSOH macro-initiator seems to be preferred over PIOH for direct extension with EEGE. Further, EEGE is preferred over t-BuGE as the functional glycidyl monomer for anionic polymerizations initiated with PSOH or PIOH macro-initiator. Since the purity of monomer is recognized as a dominant factor for controlling undesirable chain transfer, more sensitive characterization methods such as GC to validate the purity of the monomer are recommended. Overall, synthesis of controlled linear *high molecular weight* polyglycidol still remains a challenge, hence, the best route to achieve the targeted spherical morphology from PI-*b*-PG diblock and PI-*b*-PG-*b*-PI triblock blends likely remains a copolymerization of protected glycidol (EEGE) with ethylene oxide, as more suitable molecular weights appear to be obtainable.

REFERENCES

- [1] Y. Gu, T.P. Lodge, Synthesis and Gas Separation Performance of Triblock Copolymer Ion Gels with a Polymerized Ionic Liquid Mid-Block, *Macromolecules*, 44 (2011) 1732-1736.
- [2] Y. Gu, E.L. Cussler, T.P. Lodge, ABA-triblock copolymer ion gels for CO₂ separation applications, *Journal of Membrane Science*, 423–424 (2012) 20-26.
- [3] V.F. Scalfani, E.F. Wiesenauer, J.R. Ekblad, J.P. Edwards, D.L. Gin, T.S. Bailey, Morphological Phase Behavior of Poly(RTIL)-Containing Diblock Copolymer Melts, *Macromolecules*, 45 (2012) 4262-4276.
- [4] P.T. Nguyen, E.F. Wiesenauer, D.L. Gin, R.D. Noble, Effect of composition and nanostructure on CO₂/N₂ transport properties of supported alkyl-imidazolium block copolymer membranes, *Journal of Membrane Science*, 430 (2013) 312-320.
- [5] E.F. Wiesenauer, J.P. Edwards, V.F. Scalfani, T.S. Bailey, D.L. Gin, Synthesis and Ordered Phase Separation of Imidazolium-Based Alkyl–Ionic Diblock Copolymers Made via ROMP, *Macromolecules*, 44 (2011) 5075-5078.
- [6] C.W. Wiesenauer, R.H. Grubbs, *Progress in Polymer Science*, 32 (2007) 1.
- [7] E.B. Arstad, A.; Tedeschi, L. , *Tetrahedron Letters*, 44 (2003) 2703.
- [8] Y.S. Vygodskii, A.S. Shaplov, E.I. Lozinskaya, O.A. Filippov, E.S. Shubina, R. Bandari, M.R. Buchmeiser, Ring-Opening Metathesis Polymerization (ROMP) in Ionic Liquids: Scope and Limitations, *Macromolecules*, 39 (2006) 7821-7830.
- [9] J.W. Zhou, W.; Villarroja, S.; Thurecht, K. J.; Howdle, S. M., *The Royal Society of Chemistry*, (2008).
- [10] C. Guo, T.S. Bailey, Highly distensible nanostructured elastic hydrogels from AB diblock and ABA triblock copolymer melt blends, *Soft Matter*, 6 (2010) 4807-4818.
- [11] M. Erberich, H. Keul, M. Möller, Polyglycidols with Two Orthogonal Protective Groups: Preparation, Selective Deprotection, and Functionalization, *Macromolecules*, 40 (2007) 3070-3079.
- [12] J.E. Bara, C.J. Gabriel, S. Lessmann, T.K. Carlisle, A. Finotello, D.L. Gin, R.D. Noble, Enhanced CO₂ Separation Selectivity in Oligo(ethylene glycol) Functionalized Room-Temperature Ionic Liquids, *Industrial & Engineering Chemistry Research*, 46 (2007) 5380-5386.
- [13] M. Gervais, A.-L. Brocas, G. Cendejas, A. Deffieux, S. Carlotti, Linear High Molar Mass Polyglycidol and its Direct α -Azido Functionalization, *Macromolecular Symposia*, 308 (2011) 101-111.

- [14] B.F. Lee, M. Wolffs, K.T. Delaney, J.K. Sprafke, F.A. Leibfarth, C.J. Hawker, N.A. Lynd, Reactivity Ratios and Mechanistic Insight for Anionic Ring-Opening Copolymerization of Epoxides, *Macromolecules*, 45 (2012) 3722-3731.
- [15] M.D. Dimitriou, Z. Zhou, H.-S. Yoo, K.L. Killops, J.A. Finlay, G. Cone, H.S. Sundaram, N.A. Lynd, K.P. Barteau, L.M. Campos, D.A. Fischer, M.E. Callow, J.A. Callow, C.K. Ober, C.J. Hawker, E.J. Kramer, A General Approach to Controlling the Surface Composition of Poly(ethylene oxide)-Based Block Copolymers for Antifouling Coatings, *Langmuir*, 27 (2011) 13762-13772.
- [16] B. Obermeier, H. Frey, Poly(ethylene glycol-co-allyl glycidyl ether)s: A PEG-Based Modular Synthetic Platform for Multiple Bioconjugation, *Bioconjugate Chemistry*, 22 (2011) 436-444.
- [17] Y. Koyama, M. Umehara, A. Mizuno, M. Itaba, T. Yasukouchi, K. Natsume, A. Suginaka, K. Watanabe, Synthesis of Novel Poly(ethylene glycol) Derivatives Having Pendant Amino Groups and Aggregating Behavior of Its Mixture with Fatty Acid in Water, *Bioconjugate Chemistry*, 7 (1996) 298-301.
- [18] C. Mangold, F. Wurm, B. Obermeier, H. Frey, Hetero-Multifunctional Poly(ethylene glycol) Copolymers with Multiple Hydroxyl Groups and a Single Terminal Functionality, *Macromolecular Rapid Communications*, 31 (2010) 258-264.
- [19] C. Mangold, F. Wurm, B. Obermeier, H. Frey, Functional Poly(ethylene glycol)s: PEG-Based Random Copolymers with 1,2-Diol Side Chains and Terminal Amino Functionality, *Macromolecules*, 43 (2010) 8511-8518.
- [20] M. Gervais, A.-L. Brocas, G. Cendejas, A. Deffieux, S. Carlotti, Synthesis of Linear High Molar Mass Glycidol-Based Polymers by Monomer-Activated Anionic Polymerization, *Macromolecules*, 43 (2010) 1778-1784.
- [21] K.L. Killops, C.G. Rodriguez, P. Lundberg, C.J. Hawker, N.A. Lynd, A synthetic strategy for the preparation of sub-100 nm functional polymer particles of uniform diameter, *Polymer Chemistry*, 6 (2015) 1431-1435.
- [22] A.O.H. Fitton, J.; Jane, D.E.; Millar, R., *Synthesis*, (1987) 1140-1142.
- [23] M. Hans, H. Keul, M. Moeller, Chain transfer reactions limit the molecular weight of polyglycidol prepared via alkali metal based initiating systems, *Polymer*, 50 (2009) 1103-1108.
- [24] C.C. Price, Y. Atarashi, R. Yamamoto, Polymerization and copolymerization of some epoxides by potassium tert-butoxide in DMSO, *Journal of Polymer Science Part A-1: Polymer Chemistry*, 7 (1969) 569-574.
- [25] M. Osgan, C.C. Price, Polyethers. V. New catalysts for the preparation of isotactic polypropylene oxide, *Journal of Polymer Science*, 34 (1959) 153-156.

- [26] M. Siebert, H. Keul, M. Möller, Synthesis of Well-Defined Polystyrene-Block-Polyglycidol (PS-*b*-PG) Block Co-polymers by Anionic Polymerization, *Designed Monomers and Polymers*, 13 (2010) 547-563.
- [27] B. Esswein, M. Möller, Polymerization of Ethylene Oxide with Alkylolithium Compounds and the Phosphazene Base "tBuP₄", *Angewandte Chemie International Edition in English*, 35 (1996) 623-625.
- [28] A.A. Toy, S. Reinicke, A.H.E. Müller, H. Schmalz, One-Pot Synthesis of Polyglycidol-Containing Block Copolymers with Alkylolithium Initiators Using the Phosphazene Base t-BuP₄, *Macromolecules*, 40 (2007) 5241-5244.
- [29] A. Labbé, S. Carlotti, C. Billouard, P. Desbois, A. Deffieux, Controlled High-Speed Anionic Polymerization of Propylene Oxide Initiated by Onium Salts in the Presence of Triisobutylaluminum, *Macromolecules*, 40 (2007) 7842-7847.
- [30] V. Rejsek, D. Sauvanier, C. Billouard, P. Desbois, A. Deffieux, S. Carlotti, Controlled Anionic Homo- and Copolymerization of Ethylene Oxide and Propylene Oxide by Monomer Activation, *Macromolecules*, 40 (2007) 6510-6514.

CHAPTER 6

SUMMARY OF THE DISSERTATION AND FUTURE DIRECTIONS

6.1 MAJOR RESULTS AND RECOMMENDATIONS FOR FUTURE STUDIES

Development of novel free-standing robust membranes (for separating CO₂ from gas mixtures of CO₂ and N₂) that consistently challenge (and in some cases exceed) the Robeson 2008 upper bound was a major achievement of this work. Solvent-free melt-state self-assembly of sphere-forming SO/SOS diblock and triblock copolymer blends has been used to produce free-standing room temperature ionic liquid (RTIL) composite membranes with exceptional mechanical properties and CO₂/N₂ separation performance. By employing melt-state self-assembly with tailored diblock and triblock copolymer compositions, resulting membrane films could be swollen to greater than 94 wt% 1-ethyl-3-methylimidazolium bis(trifluoromethylsulfonyl)imide ([EMIM][TFSI]) RTIL.

Even with such high loadings of neat [EMIM][TFSI], these membranes exhibit the mechanical properties of solid elastomers, evident by the ultimate tensile strength of 250 kPa and the compressive modulus at 40% strain of 150 kPa for the membranes with 46% triblock copolymer content (SOS46). The CO₂ permeability performance was stable for 28 days of testing with no detectable RTIL leakage. Transmembrane pressures as high as 400 kPa could be accommodated and repetitive loadings at 230 kPa produced neither plastic deformation nor

diminished performance in gas separations over the 28 day period. These promising results are a product of the highly distensible and elastic nature of these membranes.

With the ultimate goal of further improving these membranes, two feasibility studies were conducted to address foreseeable performance limitations of the developed materials. Operating feed gas temperatures for the SO/SOS membranes are limited by the glass transition temperature (T_g) of PS domains (~ 80 °C). To address this limitation, replacement of thermoplastic PS spheres of these membranes with chemically cross-linked PI was proposed and a feasibility study was conducted. The ultimate result of the feasibility study was inconclusive due to an inability to effectively cross-link the PI system, however, the findings (listed below) from the study provide additional insight for the pursuit of promising replacement materials.

1. To achieve a degree of cross-linking that produces the level of mechanical stability required for the membranes, it is more suitable to keep the radius of spherical PI domains smaller, perhaps in the range of 7 nm.
2. The degree of epoxidation of PI directly improves the mechanical properties of the membranes through a presumed increase in the degree of cross-linking within the PI domains.
3. The current chemistry used for epoxidation modification (treatment with MCPBA) disrupts the compositional distribution of the block copolymer blends at high epoxidation degrees by decoupling the triblock copolymer. Hence adopting a milder olefin oxidation method for PI and/or robust coupling method in the synthesis of the triblock copolymer is recommended for future studies.
4. Even if high epoxidation levels can ultimately be achieved without a loss of triblock copolymer in a blend, compatibilization of highly epoxidized blocks with PEO (leading

to a diminished ability to phase separate) may limit practical implementation of this cross-linking approach. Hence, adopting a different cross-linking chemistry that does not require epoxidation of PI might also be a better option for future projects.

The second feasibility study concerned the development of an alternative BCP systems including new matrix materials (PEO alternatives) enriched with ionic groups aimed at improving CO₂ permeability and maximizing the transmembrane pressure differentials possible during operation (improved resistance to RTIL leakage). Synthesis of this alternative BCP system involved a sequential polymerization of isoprene and ethoxyethyl glycidyl ether (EEGE) monomers. Polymerization of EEGE to yield high molecular weight linear blocks proved to be extremely challenging, however. The key findings of this study do provide additional insight (listed below) for addressing the challenges facing high molecular weight polymerization of glycidol monomers and subsequent post polymerization modifications for introducing the RTIL substituents.

1. The undesirable chain transfer present in anionic polymerization of protected glycidol monomers (EEGE, t-BuGE) is best controlled by lowering the temperature and increasing the purity of the reaction media and monomer.
2. The PSOH macro-initiator seems to be preferable to PIOH for extension with EEGE. Further, EEGE is preferred over t-BuGE as the protected glycidyl monomer for anionic polymerizations initiated with the PSOH or PIOH macro-initiators.
3. The direct synthesis of controlled linear high molecular weight polyglycidol still remains a challenge; hence, the best route to achieve the targeted spherical morphology from PI-*b*-PG diblock and PI-*b*-PG-*b*-PI triblock blends would be the copolymerization of a protected glycidol (EEGE) with ethylene oxide as a substitute for the PG block.

4. The proposed synthetic schemes for transforming the alcohols to the imidazolium based ionic groups are feasible as shown by the series of proof of concept experiments.

APPENDIX I

THE ROLE OF ARCHITECTURE IN THE MELT-STATE SELF ASSEMBLY OF (POLYSTYRENE)_{star}-*b*-P(ISOPRENE)_{linear}-*b*-(POLYSTYRENE)_{star} POM-POM TRIBLOCK COPOLYMERS⁶

A.1 INTRODUCTION

Polystyrene-*b*-polyisoprene-*b*-polystyrene (SIS) triblock copolymers represent one of the most extensively researched thermoplastic elastomers (TPEs). In particular, they are extremely well known for their excellent mechanical properties, a product of their phase separated morphology of organized (and mechanically correlated) hard and soft domains with dimensions in the nanoscale range. As a result, attempts to influence the mechanical properties of SIS materials and their analogs through the introduction of processing^[1], morphology control^[2-6] and synthesis^[7-12] strategies has received considerable attention.

Traditional linear SIS triblock copolymers, in elastomer form, are comprised of glassy domains of polystyrene (PS) embedded within a soft connective matrix of viscoelastic polyisoprene (PI) chains acting to mechanically correlate the two types of domains. In concert,

⁶ The content of this document was written by Dilanji Wijayasekara and edited by Travis Bailey. The project represents collaboration with Daniel M. Knauss at Colorado School of Mines. Material synthesis, chemical characterization and AFM imaging were performed at Colorado School of Mines while morphological characterization (SAXS and rheology) was performed at Colorado State University. This document was adapted from the publication published in journal *Macromolecules* in 2016.

these interconnected domains produce the excellent elasticity for which these TPEs are so well known^[13]. However, the specific morphology produced during melt-state self-assembly, in combination with the organization of the SIS chains within that morphology, can strongly influence the resultant mechanical properties of the elastomers produced. Differences in morphology and chain organization can be manipulated by using well-defined molecular architectures like stars^[9, 14], rings^[15] combs^[16] and their combinations^[17-21], inspiring the integration of such structures into block copolymer-based TPE architectures^[22-31]. As an example, branched SIS copolymers have been shown to have a different morphological structure when compared with the linear symmetric architecture, at the same volume fractions^[12]. Likewise, tensile strength and the strain-at-break has been shown to increase with the number of branch points in TPE systems comprised of such molecules^[32]. Furthermore, SCF calculations by Matsen suggest the potential ability to use branched architectures to open stable regions within the phase diagram, providing yet another route for accessing interesting TPE materials^[33].

Within the many possible architectures for block copolymer (BCP) TPEs, the pom-pom molecular architecture^[34-36], in which two n-arm stars composed of glassy polymer A are covalently connected by a linear block of flexible, viscoelastic polymer B (designated A_nBA_n), is particularly intriguing. In fact, it has been proposed as an idealized (homo)polymer architecture (A_nAA_n) in its ability to behave analogously to commercial polyolefins in strong shear and extensional flows^[14, 37]. However, synthetically accessing the pom-pom block copolymer architecture can be particularly difficult, and production of large quantity scales even more so. In 2002, Knauss and Huang first reported a one-pot convergent anionic polymerization strategy that has made access to the complex pom-pom architecture particularly simple and straightforward^[17]. Key to their one-pot approach is the controlled introduction of non-

stoichiometric amounts of an anionically polymerizable terminating agent (4-chlorodimethylsilyl)styrene (CDMSS) to a reaction mixture of living polymer chains. The mechanism is shown pictorially in Figure 1. The result of such controlled addition is the formation of star-shaped polymers with hyperbranched *living* cores. Subsequent monomer addition allows chain extension from the core, which upon introduction of a coupling agent, produces the pom-pom architecture.

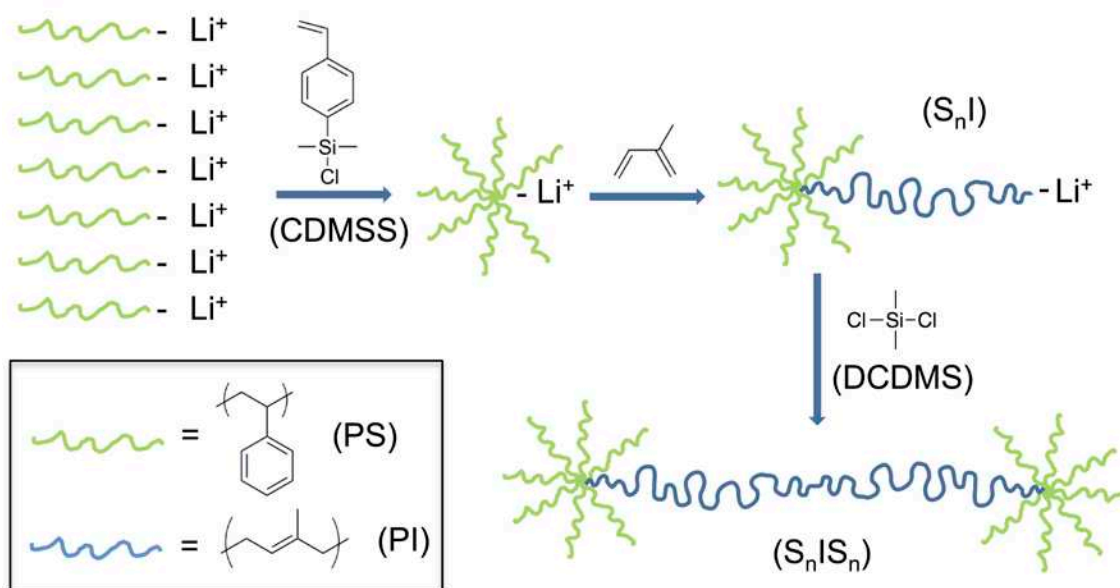


Figure A.1 Reaction sequence for the synthesis of S_nIS_n pom-pom triblock copolymers via ‘one-pot’ convergent anionic polymerization.

In that seminal work, they focused on the synthesis of all polystyrene containing systems $(S_nSS_n)^{[17]}$, and the subsequently extended the technique towards the successful formation of uniquely structured branched PS stars $((S_nS)_m)^{[18]}$. Most recently they were able to show the convergent anionic polymerization strategy could be applied to the direct one-pot formation of polyisoprene-containing pom-pom architectural triblock copolymers $(S_nIS_n)^{[23]}$ (Figure A.1) with interesting TPE implications. The objective of this report is to investigate the morphological and

rheological properties of these unique S_nIS_n pom-pom triblock copolymers, with a special focus on elucidating the effects of changing (1) arm number (n) within the PS stars (at a fixed total star molecular weight), and (2) the molecular weight of the linear PI midblock adjoining the PS stars. To this end, a series of S_nIS_n pom-pom triblock copolymers were synthesized using the convergent anionic polymerization approach and investigated using a combination of SAXS, rheology, and AFM.

A.2 EXPERIMENTAL

Materials: 1,2-Dibromoethane (99%, Aldrich), dichlorodimethylsilane (99%, Aldrich), p-chlorostyrene (97%, 500 ppm 4-tert-butylcatechol, Aldrich), styrene (99%, 10-15 ppm 4-tert-butylcatechol, Aldrich), and trichloromethylsilane (99%, Aldrich) were dried over calcium hydride and distilled under argon or under reduced pressure immediately prior to use. Isoprene (99%, 100 ppm 4-tert-butylcatechol, Aldrich) was distilled twice over calcium hydride and distilled once over a dibutylmagnesium solution (1.0 M in heptane, Aldrich) just prior to use. *sec*-Butyllithium (1.3 M in a mixture of cyclohexane and heptane) was kindly donated by FMC, Lithium Division and used as received. HPLC grade tetrahydrofuran (99.9+%, Fisher Scientific) was dried over sodium metal and distilled from sodium benzophenone ketyl under argon immediately prior to use. HPLC grade cyclohexane (99%, Fisher Scientific) was purified by repeated washings with H_2SO_4 and water and distilled from sodium metal. 4-(chlorodimethylsilyl)styrene (CDMSS) was synthesized as reported^[38], and was distilled from calcium hydride under reduced pressure immediately prior to use. All glassware, glass syringes,

and needles were oven dried at 150 °C for at least 24 hours, and cooled under argon. The glassware was further flame dried under an argon purge after assembly. Gastight syringes were prepared by washing with a dilute *sec*-butyllithium solution followed by washing with dry cyclohexane.

Synthesis of (polystyrene)_n-b-(polyisoprene)-b-(polystyrene)_n pom-pom triblock copolymers (S_nIS_n): In this work, a series of triblock copolymers was designed with control over the polystyrene to polyisoprene composition and variation in the number and molecular weight of polystyrene chains in the polystyrene star. The polymerization procedures were based on those previously reported by Huang and Knauss^[23]. A detailed procedure is described for producing a targeted (polystyrene)₅-b-(polyisoprene)-b-(polystyrene)₅ with 3 kDa PS arms and a 30/70 wt/wt PS/PI composition (TPE05, ESI).

Cyclohexane (900 mL) and styrene (20 mL, 0.17 mol) were added under an argon purge to a septum sealed, single-neck, round bottom flask containing a magnetic stir bar. *sec*-Butyllithium in cyclohexane (1.3 M) was added dropwise as a titrant for adventitious impurities until a pale yellow color (indicative of initiated polystyryllithium) was present. The calculated amount of *sec*-butyllithium required for the target molecular weight of the polystyrene chain (7.9 mL, 6.1 mmol for 3 kDa) was then added. After two hours of reaction time, approximately 1 mL of solution was removed and precipitated into argon-purged methanol for molecular weight analysis (as the PS star arm). The linear PS chains were then coupled into stars by reaction with CDMSS. CDMSS was added to the reaction solution with the amount calculated based on the target number of arms in the star according to the following equation.

$$\text{moles of CDMSS} = \text{moles of chains} * \left(1 - \frac{1}{\text{number of arms}}\right)$$

To the living polystyryllithium solution with targeted 3 kDa chains was added 9.8 mL (4.9 mmol) of CDMSS in cyclohexane (0.5 M). After one hour, the solution was partitioned via cannula under positive argon pressure into separate flame dried, septum-sealed round-bottom flasks and a 1.0 mL sample was removed for molecular weight analysis (as the star). A specific quantity of isoprene was introduced to each flask according to the target PS to PI composition. To one of the flasks containing approximately 300 mL of solution was added 20.5 mL (0.205 mol) of isoprene using a gastight syringe. The reaction proceeded for three hours and then a 5 mL sample was removed and precipitated in argon-purged methanol for molecular weight analysis (as the S_nI diblock). 10 mL of THF was added to the flask and a dichlorodimethylsilane solution in cyclohexane (0.20 M) was added slowly using a gastight syringe. The addition rate was controlled to a rate of 0.20 mL/hour by a syringe pump and the addition was continued until the reaction solution turned colorless. The reaction mixture was then precipitated into argon purged methanol, filtered, washed with more methanol, and dried to a constant weight at room temperature in a vacuum oven. 2,6-di-tert-butyl-4-methylphenol (0.02 wt %) was added to the methanol to prevent the oxidation of the polyisoprene block. The reaction yield was quantitative after considering the sampled aliquots and the partitioning of the reaction solution. Subsequent fractionation of the crude product was used to reduce uncoupled S_nI diblock copolymer contamination using toluene/methanol as a solvent/non-solvent pair. Example GPC data overlays showing the evolution of the S_nIS_n pom-pom triblock copolymers produced are included in the ESI. Generalized 1H NMR (ppm downfield from TMS): 6.20 - 7.26 (b, $-(C_6H_5)$), 4.90 - 5.30 (b, $-CH_2-CH=C(CH_3)-CH_2-$), 4.60 - 4.90 (b, $CH_2=C(CH_3)-$), 0.84 - 2.40 (b, $CH_2=C(CH_3)-C(R)H-CH_2-$, $-CH_2-CH=C(CH_3)-CH_2-$, and $C_6H_5-C(R)H-CH_2-$), 0.5 - 0.78 (m, $-CH_3$, initiator fragment).

Chemical Characterization: Initial molecular weights and molecular weight distributions were characterized by gel permeation chromatography (GPC) using a Hewlett-Packard model 1084B liquid chromatograph equipped with two HP Plgel 5 μ Mixed-D columns (linear molecular weight range: 200 – 400,000 g/mol), a calibrated RI (Waters R401) detector, and a Wyatt Technology miniDAWN multi-angle laser light scattering (MALLS) detector ($\lambda = 690$ nm, three detector angles: 45°, 90° and 135°), using Astra 1.5.0b2 molecular weight characterization software. Elutions were carried out at an ambient temperature with THF as the solvent and a flow rate of 0.70 mL min⁻¹. The refractive index increment (dn/dc) used for the polystyrene samples was 0.193 mL g⁻¹, which was obtained for the polystyrene stars and which also corresponds to linear polystyrene in THF.[39] The dn/dc of polyisoprene was determined to be 0.117 mL g⁻¹ in THF at room temperature by using an Abbe Refractometer (Bausch & Lomb). The refractive index increments of the SIS copolymers were calculated based on the summation of the products of the dn/dc of each block times its weight fraction. Subsequent verification of molecular weights and molecular weight distributions prior to SAXS and rheological analysis was performed on a Viscotek GPC-Max chromatography system outfitted with three 7.5mm 340mm Polypore (Polymer Laboratories) columns in series with a Viscotek differential refractive index (RI) detector. The columns were maintained at 40°C in an Alltech column oven. All polymer samples were run with THF as the mobile phase (1 mL min⁻¹). ¹H NMR spectroscopy was performed on samples dissolved in d-chloroform on a Chemagnetics CMX Infinity 400 instrument.

Small Angle X-ray Scattering (SAXS): Scattering data was collected on a Rigaku S-Max 3000 High Brilliance three pinhole SAXS system outfitted with a MicroMax-007HFM

rotating anode (CuK α), Confocal Max-Flux Optic, Gabriel multiwire area detector, and a Linkam thermal stage. Polymer samples were prepared as 8 mm diameter \square 0.9 mm thick disks, melt pressed (Carver Press) directly from powders using a stainless steel cutout sandwiched between teflon covered kapton sheets. Disks were held under a constant pressure of 500 psi at 150 °C for approximately 5 minutes, before being removed from the press and cooled (unassisted) to room temperature. The formed polymer was easily removed from the stainless steel cutout to give homogeneous, transparent disks. The disks were then sandwiched between kapton discs and mounted in the Linkam thermal stage. Each sample was then subjected to stepwise heating (in vacuo) from 80 to 225 °C (80 °C, 125 °C, 200 °C, 225 °C) with a 75 minute anneal at each temperature during which SAXS data was collected. Exposure times for data collection were typically 3600 s. A similar ramp was used to collect SAXS data while cooling back to 80 °C.

Rheological Analysis: Rheological experiments were run on a TA Instruments ARES rheometer. Samples disks prepared as described above (see SAXS, above) were placed between two parallel plates(8mm). The plates were then heated to 100 °C, and the gap was adjusted to ensure even distribution of the sample. Typical gaps were 0.3-0.5 mm. Dynamic temperature ramp tests were performed while heating and cooling at 1 °C min⁻¹ at an angular frequency of 1 rad s⁻¹ and a strains verified to be within the linear viscoelastic regime, typically between of 1.0 and 4.0%,.

Atomic Force Microscopy: Atomic Force Microscopy (AFM) was performed using a Digital Instruments Nanoscope III. Samples were prepared by spin coating a 5 wt. % solution of

polymer in THF on 1 cm² silicon wafers at 2000 rpm for 20s. Annealing was performed under argon purge at 110 °C for 24 hours.

A.3 RESULTS AND DISCUSSION

A series of S_nIS_n pom-pom block copolymers were synthesized following the convergent anionic polymerization approach described in Scheme 1^[22]. In total, eighteen unique S_nIS_n pom-pom block copolymers were synthesized, demonstrating the ability to control architectural parameters such as the number of arms in the PS star, the molecular weight of those arms, and the molecular weight of the adjoining PI block used to form the pom-pom architecture. The molecular weight of the PS arms could be directly tuned using the ratio of styrene monomer to *sec*-butyllithium initiator initially charged to the reactor. Subsequent adjustment of the amount of the coupling monomer (CDMSS) added could then be used to set the number of arms formed during star formation. Ultimately, the length of the PI midblock could then be quantitatively set by simply selecting the amount of isoprene monomer added prior to the final coupling step. Careful inspection of the characterization data for all 18 samples (ESI) shows that three and four member subsets of the series share identical PS star fragments. This was uniquely accomplished by partitioning the living polystyryllithium stars into several new reaction vessels prior to the addition of differing amounts of isoprene monomer to each. In this way, we were able to generate several S_nIS_n pom-pom triblock copolymers from a single initiation event, holding n as a true constant among the set.

Of the eighteen S_nIS_n pom-pom triblock copolymers produced (see ESI), five were selected for more careful morphological and rheological characterization (Table 1). The five selected formed a very specific set, affording an opportunity to evaluate the influence on morphology and rheological response of (1) the connective PI mid-block molecular weight, at constant star arm-number and molecular weight (**A4**, **B4**, **C4**), and (2) the arm number in the stars, at constant star and mid-block molecular weights (**B3**, **B4**, **B7**). In the labeling of these five samples, the first letter distinguishes the PI mid-block molecular weight and the numerical designation denotes the approximate number of arms in the stars. For example, samples **A4** and **B4** differ from each other by the lengths of their PI backbone, but they have same number of arms in their PS star. Additionally, the letter "d" (e.g. **A4d**) has been added when referring to the S_nI diblock copolymer precursor from which the corresponding pom-pom triblock copolymer (e.g., **A4**) was produced. Notably, the samples selected for this study were chosen such that the overall molecular weight of the star in the pom-pom architecture (Table A.1) remained roughly constant in the 14.3 – 16.5 kDa range.

A review of the characterization data in Table A.1 reveals a pair of molecular weights provided for each S_nIS_n pom-pom triblock copolymer sample, with an important difference distinguishing the two values. The first value calculated is based on an $M_{n,star}$ value determined using GPC-MALLS, relative compositions in the final S_nIS_n product given by 1H NMR, and an assumption of 100% coupling efficiency in the final synthetic step. As such, it is a largely a theoretical maximum expected for each pom-pom triblock copolymer sample. The second value is determined by direct analysis of the final, fractionated S_nIS_n product, using GPC-MALLS, and reflects a lower, but more accurate measurement in all cases. This latter measurement is sensitive to the presence of residual S_nI diblock copolymer remaining in the sample due to termination

during sampling as well as coupling and fractionation inefficiencies. As expected, diblock copolymer contamination in the final product is most prominent in the highest molecular weight **A4** sample, for which the chain end concentration (lowest) and molecular sterics (highest) during the coupling are most significant. Importantly, the relative PS and PI compositions for the sample are unaffected by the presence of uncoupled product, given the S_nI diblock and S_nIS_n triblock copolymer compositions are intrinsically self-consistent.

Table A.1 Chemical characterization data

Sample	$M_{n,star}^a$ [g mol ⁻¹]	n_{arms}^b ($M_{n,arms}^a$) [g mol ⁻¹]	PDI_{star}^a (PDI_{arm}^a)	w_{PI}^c (f_{PI}^d)	M_n^a (M_n) ^e [g mol ⁻¹]	PDI^a
A4 (TPE08)	14,300	4.1 (3,300)	1.08 (1.02)	0.87 (0.89)	158,000 (220,000)	1.06
B3 (TPE11)	15,500	2.9 (5,400)	1.30 (1.01)	0.80 (0.82)	132,000 (155,000)	1.02
B4 (TPE07)	14,300	4.1 (3,300)	1.08 (1.02)	0.80 (0.82)	107,000 (143,000)	1.04
B7 (TPE03)	16,500	7.1 (2,160)	1.20 (1.02)	0.81 (0.83)	105,000 (174,000)	1.07
C4 (TPE06)	14,300	4.1 (3,300)	1.08 (1.02)	0.75 (0.78)	92,000 (114,000)	1.06

^acalculated from GPC-MALLS; ^bcalculated from $M_{n,star} = nM_{n,arm} + (n-1)M_{DMSS}$; ^ccalculated from ¹H NMR of final fractionated product; ^d volume fraction of PI calculated using nominal densities at 140°C[40]; ^ecalculated from $M_{n,star}$ in combination with ¹H NMR of final product.

Small angle X-ray scattering (SAXS), atomic force microscopy (AFM) and dynamic rheology techniques were utilized in combination to characterize the morphology and the self-assembly behavior of each of these five samples (Figures A.2, A.4, A.5, A.7 and A.8). This systematic characterization of each pom-pom triblock copolymer was carried out by first measuring the storage (G') and loss (G'') modulus as a function of temperature with dynamic shear rheology over a complete constant rate (1°C min⁻¹) heating (to 200°C) and cooling (to 70°C) cycle. The cooling cycle was then immediately followed by a second constant rate heating ramp (1°C min⁻¹) purposefully extended through the order-disorder transition. As with rheology, SAXS data was also collected for each sample along a complete heating and cooling cycle

(spanning a temperature range of 80°C to 225°C) such that the effects of thermal annealing could be assessed in these uniquely architected systems. Importantly, four of the five S_nIS_n triblock copolymers investigated exhibited rheological behavior characteristic of disorder at 225°C, suggesting the temperature ramp applied during SAXS was likely sufficient for erasing latent thermal or solvent induced morphological memory in most of the samples. In addition, SAXS data was collected on the corresponding S_nI diblock copolymer samples collected as aliquots from the reactor prior to the final coupling reaction. Data was collected at the same temperature intervals indicated for the S_nIS_n triblock copolymers, although only a subset of the data is included in Figures A.2, A.4, A.5, A.7 and A.8. Finally, AFM was also performed on thin film samples of each S_nIS_n triblock copolymer species, both before and after annealing to visually capture the influence of sustained thermal soaking on self-assembly, approximating the thermal cycles imposed during rheological and SAXS data collection.

Figure A.2 contains a summary of the rheology, AFM and SAXS data collected for the **A4** triblock copolymer sample. SAXS data for the corresponding diblock copolymer (**A4d**) is also included. Sample **A4** was the most compositionally asymmetric pom-pom triblock copolymer investigated ($f_{PI} = 0.89$) with the two 14.3 kDa 4-arm stars adjoined by a linear PI block of 191 kDa in molecular weight. In a linear AB or ABA architecture, such a block copolymer would be expected to adopt a spherical morphology although the size of the molecule would produce very slow ordering kinetics^[41-43]. In fact, in similarly sized polystyrene-b-poly(ethylene oxide)-b-polystyrene linear triblock copolymers, the spherical morphology that developed never achieved more than a liquid-like packing despite theoretical predictions of a closed-packed lattice^[42, 44]. The melt-state rheological data of sample **A4** revealed that both storage and loss moduli during heating and cooling ramps closely tracked one another with only

slight hysteresis detected during reordering of the sample during cooling (rates were $1\text{ }^{\circ}\text{C min}^{-1}$). Notably, such reversibility in the rheological response was shared by all five samples investigated. For the **A4** sample specifically, the magnitude of the storage and loss moduli (G' and G'') in the $10^4 - 10^5$ Pa range was consistent with that typically produced in phase separated block copolymer melts^[45]. This behavior included a storage modulus that exceeded the loss modulus at temperatures below $100\text{ }^{\circ}\text{C}$, where the glassy behavior of the PS domains would be anticipated to provide some degree of elasticity to the system. However increasing the temperature beyond the PS T_g produced a gradual but systematic decay in both moduli typical of BCP melts in which the segregation degree is weak or system ordering is limited due to kinetic constraints^[41-44]. When the former is at play, disorder is typically imminent. In the latter, the system retains some structure as the thermodynamic forces driving phase separation remain. In this case, while the rheology clearly shows a loss modulus that overtakes the elastic modulus just beyond 100°C , the elastic modulus remains measurable and persistent until the system appears to finally give way to disorder near 225°C . As suggested above, this rheological signature is typical in high molecular systems with such large asymmetries in composition^[41, 42, 44].

The AFM images of Figure A.2 confirm the phase-separated state suggested by the rheological data. The bright and dark areas in AFM images, typical of glassy PS domains in a soft PI matrix, respectively^[46], reveal a distinct difference in the degree of order present in annealed and non-annealed systems. Phase separation is clearly present in both, however the random dispersion of small, irregularly shaped domains present just after casting gives way to order with extended thermal treatment suggestive of a weakly-developed lamellar or cylindrical morphology. It is significant, however, that the PS domains never achieve any sort of axial or longitudinal continuity despite what appears to be a layered structure correlated across multiple

domain periods. Our interpretation is that the aggregation of PS chains into a continuous domain structure is hampered by the inability of the PS arms to adequately fill space (through chain stretching) in a regular, periodic manner. The lack of a uniform domain structure seems to be a clear indication of the high level of packing frustration the chains are experiencing. More specifically, the system must balance a large driving force (from the extreme compositional asymmetry) to bend the domain interface towards the minority PS component, against an inability of the star architecture (due to chain crowding) comprising that minority component to actually do so. Figure A.3b captures the essence of these arguments pictorially. Consistent with this observation is that the assumed development of this layered lamellar or cylindrical morphology during rheological annealing does not appear to be reflected in any mechanical response improvement measured for the BCP. The implication is that the degree of order induced upon annealing remains insufficient to produce a major change in the viscoelasticity of the bulk melt.

Of course, the influence of the confining surfaces (substrate below and air above) on the degree of phase separation achieved and morphology indicated in the AFM samples cannot be completely disregarded^[47]. However, as we will see throughout this series of five samples, the morphologies indicated in the AFM images are all in qualitative agreement with the results of the SAXS measurements, performed on bulk samples where the influence of confining surfaces is largely eliminated. For the **A4** sample, SAXS confirms the limited ordering achievable even after thermal annealing. More specifically, the scattering data in Figure A.2 shows a well-developed principal scattering peak for all the temperatures measured between 25°C and 225°C, during both the heating and cooling cycles. The presence of this peak confirms the phase separation implied by the rheology and revealed in the AFM images. With such a significant asymmetry in

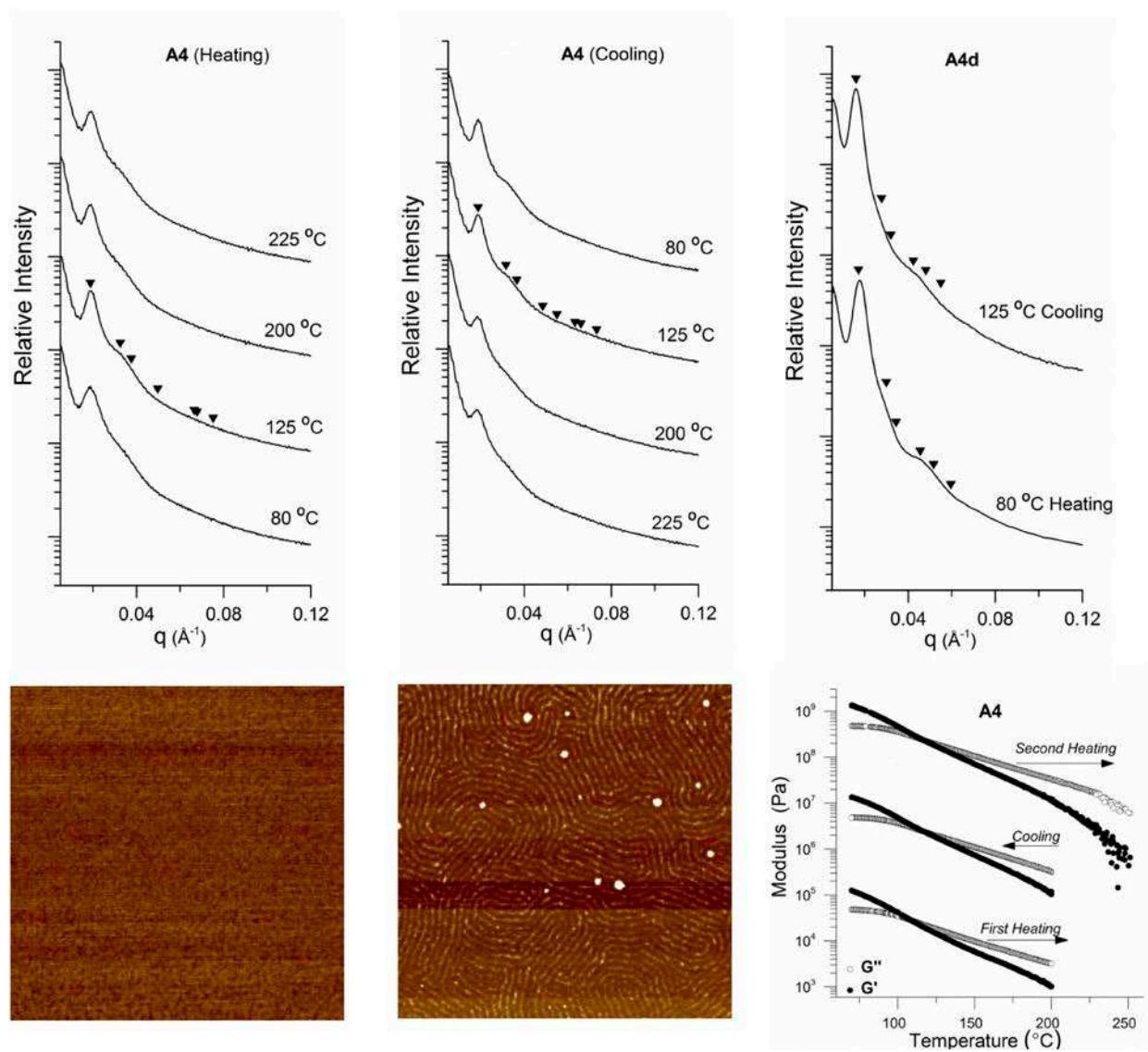


Figure A.2 SAXS data of sample **A4** along a complete heating (upper left) and cooling (upper center) thermal cycle. SAXS data of **A4d** diblock copolymer along a complete heating and cooling thermal cycle (upper right). Inverted triangles represent the locations of allowed reflections for HPC morphology, based on the position of the primary scattering wave vector $q^*=q_{100}$: q/q^* at $\sqrt{1}$, $\sqrt{3}$, $\sqrt{4}$, $\sqrt{7}$, $\sqrt{9}$, $\sqrt{12}$, $\sqrt{13}$, $\sqrt{16}$, etc. AFM images of pre (lower left) and post annealed **A4** (lower center) All images are $2 \mu\text{m} \times 2 \mu\text{m}$. Dynamic temperature ramp over both heating and cooling cycles of **A4** (lower right) at 1°C min^{-1} , 1 rad s^{-1} and 4% strain (within the linear viscoelastic regime). The cooling cycle has been shifted vertically two orders of magnitude for clarity. The second heating cycle has also been shifted vertically four orders of magnitude.

the composition, we believe the layered images in AFM are more consistent with a cylindrical domain structure than stacked lamellae, which are favored by more symmetric compositions.

Furthermore, adoption of a lamellar morphology would require unlikely degrees of chain stretching by the PS stars in order to achieve the minimal interfacial curvature intrinsic to a layered morphology.

However, the strict adoption of a highly correlated, hexagonal packing of cylinders observed and predicted for linear BCP melts does not appear possible for the **A4** sample. Inverted triangles representing the locations of allowed reflections for hexagonally packed cylinders (HPC), based on the position of the principal scattering wave vector $q^*=q_{100}$: q/q^* at $\sqrt{1}$, $\sqrt{3}$, $\sqrt{4}$, $\sqrt{7}$, $\sqrt{9}$, $\sqrt{12}$, $\sqrt{13}$, $\sqrt{16}$, etc. have been included with the scattering profiles at 125°C during both heating and cooling. There is a clear lack of any higher order diffraction beyond the principle peak corresponding to HPC at any of the temperatures probed. However, the clear shoulder at lower q values is consistent with the presence of structure factor scattering, likely associated with a poorly ordered, liquid-like packing (LLP) of cylindrical domains^[48]. Importantly, this interpretation is consistent with the AFM images and the system rheology. This includes a diminished scattering intensity at 225°C where the rheological response is highly viscous. It is interesting that even with the decay in rheological response, SAXS data does indicate some phase separation is still present. This is consistent with behavior often seen in highly asymmetric spheres where the phase separation can persist well beyond the expected disordering transition^[49, 50]. The origins of the limited degree of order in the system may be thermodynamic, kinetic or both. As previously discussed, the compression of the PS volume fraction into a dense star architecture reduces the conformational flexibility of the PS chains, which may preclude the uniform and periodic filling of space in a manner that provides a free energy advantage over the more loosely ordered structure (Figure A.3b). On the other hand, the pom-pom architecture, and particularly the long mid-block molecular weight present in **A4**,

would be expected to be highly susceptible to dynamic chain entanglements with long kinetic lifetimes. As described pictorially in Figure A.3a, relaxation of entanglements through reptation dynamics should be hindered by the steric bulk of the star architecture intrinsic to the pom-pom BCP chain ends.

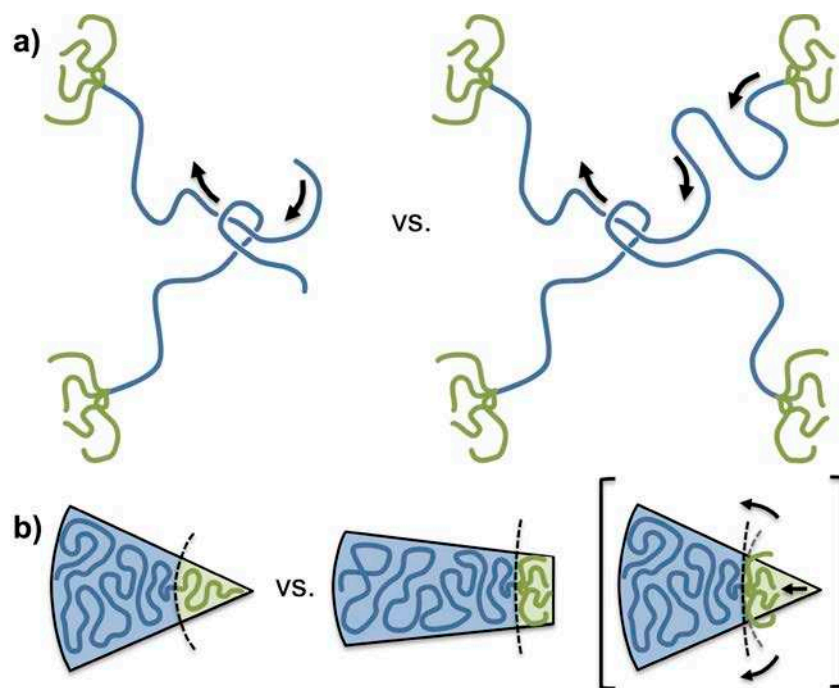


Figure A.3 a) Entanglement relaxation through chain reptation is intrinsically hindered by the pom-pom architecture of the S_nIS_n triblock copolymers, in contrast, for example, to their S_nI diblock copolymer precursors. b) Simple linear block copolymers, adopt spontaneous interfacial curvature to accommodate large compositional asymmetries. In pom-pom architecture, such curvature towards the minority component is inherently opposed by PS chain crowding at interface, and an inability of the PS chains to fill space, both a consequence of the compact star architecture. However, flattening of the interface to accommodate the dense star architecture increases interfacial contact between the PS and PI domains, and requires considerable chain stretching in the PI domain. The self-assembly behavior of the S_nIS_n systems investigated appears to reflect such architecturally produced packing frustration.

To gain additional insight into the degree to which chain kinetics was influencing the lack of order developing in the **A4** system, the diblock copolymer precursor of **A4**, referred to as **A4d** in Figure A.2, was also characterized with SAXS using the same heating and cooling thermal

cycle applied to **A4**. Importantly, the **A4d** diblock copolymer precursor is compositionally identical to the **A4** triblock copolymer species, because of the symmetry associated with the final coupling step. At both 80°C (heating) and 125°C (cooling), the **A4d** diblock copolymer also fails to produce a diffraction pattern indicating a highly correlated (e.g. hexagonally packed) cylindrical structure. However, the structure factor scattering consistent with a LLP of cylinders is still clearly present, with the increased intensity and sharpness of the principal scattering peak suggests a slightly more segregated morphology is achieved by the **A4d** diblock copolymer. This small degree of enhanced phase separation may be attributable to the increased relaxation dynamics expected for the diblock copolymer precursor (Figure A.3a), but the improvement does not appear sufficient to produce a level of order leading to Bragg-type diffraction. This suggests that, in the case of the **A4** sample, the inability to fill space uniformly is, to a large degree, the result of both compositional and architectural asymmetry acting to energetically frustrate the morphology selection process.

Figure A.4 contains a summary of the rheology, AFM and SAXS data collected for the **B4** triblock copolymer sample together with the SAXS data for the corresponding **B4d** diblock copolymer. Compared with sample **A4** just described, **B4** is much less compositionally asymmetric ($f_{PI} = 0.82$) due to a PI mid-block that is less than two-thirds (114 kDa) the molecular weight of that in found in the **A4** sample (ca. 191 kDa). Importantly, the two 14.3 kDa 4-arm stars used to generate the pom-pom architecture are identical to those used in **A4**, a result of the living polymerization partitioning strategy adopted. In a linear AB or ABA architecture, such a block copolymer would be expected to fall at the border of the sphere (BCC)-cylinder (HPC) phase boundary based on volume fraction alone.

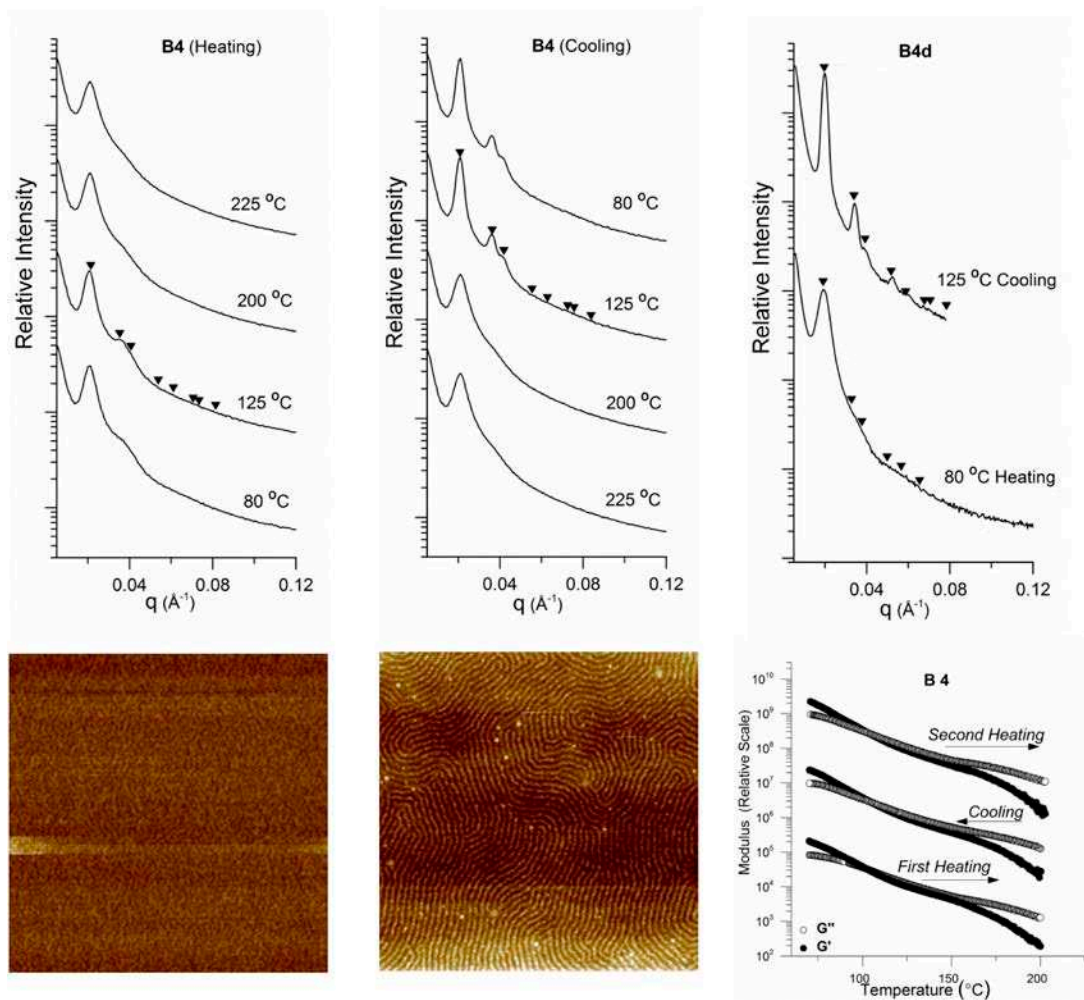


Figure A.4 SAXS data of sample **B4** along a complete heating (upper left) and cooling (upper center) thermal cycle. SAXS data of **B4d** diblock copolymer along a complete heating and cooling thermal cycle (upper right). Inverted triangles represent the locations of allowed reflections for HPC morphology, based on the position of the primary scattering wave vector $q^*=q_{100}$: q/q^* at $\sqrt{1}$, $\sqrt{3}$, $\sqrt{4}$, $\sqrt{7}$, $\sqrt{9}$, $\sqrt{12}$, $\sqrt{13}$, $\sqrt{16}$, etc. AFM images of pre (lower left) and post annealed **B4** (lower center) All images are $2 \mu\text{m} \times 2 \mu\text{m}$. Dynamic temperature ramp over both heating and cooling cycles of **B4** (lower right) at 1°C min^{-1} , 1 rad s^{-1} and 4% strain (within the linear viscoelastic regime). The cooling cycle has been shifted vertically two orders of magnitude for clarity. The second heating cycle has also been shifted vertically four orders of magnitude.

Like sample **A4**, the rheological data for sample **B4** showed minimal thermal hysteresis through reversal of the thermal ramp, and produced storage and loss moduli (G' and G'') in the $10^4 - 10^5 \text{ Pa}$ range. In general, the behavior of the dynamic moduli during the ramp of **B4** shares many of the basic features also found for the **A4** sample. For example, the elastic modulus of the sample is significantly greater than the loss modulus below the PS softening temperature, with

the convergence and ultimate crossing of the two moduli occurring near 100°C. A gradual decay in both moduli then follows, as also seen in sample **A4**. However, a direct comparison of the rheological data found in Figure 6 reveals a number of notable differences, including the dramatic impact of the shortened PI mid-block on the disordering temperature. A much earlier transition to disorder in the **B4** sample is evident, with a complete loss of elastic modulus by 190°C (ca. 225°C). Such a difference is consistent with the considerable decrease in overall system molecular weight, which favors an earlier disordering temperature. Moreover, one can now easily detect a subtle but significant change in the relationship between the storage and loss modulus just beyond the softening temperature. In comparison with **A4** (Figures A.2 and A.6), a subtle inflection in the storage modulus indicates a decay rate that is decreasing slightly with increasing temperature. This is eventually followed by a second inflection near 170°C, after which the decay rate accelerates as the sample approaches disorder. This behavior, while subtle, is in contrast to sample **A4** in which the rate of decay remains essentially constant throughout this region of the thermal ramp. As confirmed in the SAXS and AFM data described below, the emergence of these two inflections is a harbinger of increasing order in these block copolymer melts. In fact, highly ordered systems can often produce plateau like behavior in the storage modulus (with both inflections being very sharp) over significant temperature ranges when the degree of periodic order is particularly high in the sample^[51-53].

As expected from the evolving rheological signature, the AFM images pre and post annealing confirm the emergence of increasing order and periodicity in the phase separated morphology of the **B4** sample. Like the **A4** sample, the as cast thin film shows clear phase separation with a structure consistent with rapid solvent removal, featuring of a random arrangement of small, irregularly shaped domains. Upon annealing the **B4** sample is able to

develop a layered morphology (by appearance), with correlation between domains perpendicular to the axial direction reminiscent of the annealed morphology adopted by **A4**. However, a direct comparison of the AFM images for these two samples (shown together in Figure 6) suggests that the increased PS volume fraction and reduced overall system molecular weight appear to favor improved domain continuity. That is, the reduced compositional asymmetry relative to **A4** relieves some of the packing frustration, giving rise to improved uniformity in of the developed morphology. However, at $f_{PS} = 0.18$, the perforated appearance of the PS domains does linger, confirming considerable packing frustration remains in spite of the increased PS volume fraction. Ultimately, the system still retains an architectural design in which chain crowding in the minority component acts contrary to the compositionally preferred curvature of the system.

The SAXS data for sample **B4** (Figure A.4) confirms the emergence of enhanced local ordering upon annealing suggested by the rheology and AFM data. This ordering process is characterized by the gradual development of a diffraction pattern consistent with HPC, with multiple easily resolved reflections emerging as the sample is cooled from 200°C to 125°C. Inverted triangles in Figure A.4 represent the locations of allowed reflections for HPC morphology, based on the position of the primary scattering wave vector $q^* = q_{100}$: q/q^* at $\sqrt{1}$, $\sqrt{3}$, $\sqrt{4}$, $\sqrt{7}$, $\sqrt{9}$, $\sqrt{12}$, $\sqrt{13}$, $\sqrt{16}$, etc. Once the highly ordered structure is established at 125°C (heating), the order is preserved during subsequent cooling with no further evidence of any rheological transitions or decay in diffraction intensity which would accompany a return to the weakly ordered state. Notably, the initial scattering pattern prior to heating does indicate clear phase separation, but with broad, poorly defined reflections more consistent with a LLP of cylinders characteristic of the **A4** sample. This initial weakly ordered structure (at 80°C, for example) is presumably an artifact of slow ordering kinetics associated with chain dynamics,

surely influenced by the pom-pom architecture. Importantly, the sluggish evolution of the HPC extends even to the **B4d** diblock copolymer precursor, which shows identical LLP behavior at low temperatures, followed by the development of a highly resolvable HPC diffraction pattern upon thermal annealing. Consistent with the coupling method used to convert **B4d** to **B4**, the principal scattering peak for both systems falls at the same q value, confirming the two systems are effectively "lattice matched". This is notable, as it affirms that the presence of diblock copolymer as a contaminant in the S_nIS_n samples has no significant influence on the domain spacing adopted by the composite blend. This is also true for the A4 sample.

Finally a direct comparison between the post-annealing SAXS signatures of **A4** and **B4** is presented in Figure A.6, from which the true impact of decreasing the PI mid-block molecular weight can be seen. At the forefront is the clear contrast in the degree of periodic order present in the two samples, with the absence of higher order Bragg reflections in the higher molecular weight **A4** sample, and the unmistakable HPC reflection pattern in the smaller **B4** analog. Additionally, decreasing the mid-block molecular weight creates a concurrent shift in the position of the primary scattering peak to significantly smaller q values. In terms of nanoscale structure, the shift in q represents a reduction in the principal domain spacing from about 33.4 to 27.0 nm, which is consistent with the reduction in molecular weight of the PI mid-block.

Figure A.5 contains a summary of the rheology, AFM and SAX data collected for the **C4** triblock copolymer sample together with the SAXS data for the corresponding **C4d** diblock copolymer. Compared with samples **A4** and **B4** just described, **C4** is the least compositionally asymmetric ($f_{PI} = 0.78$) of this three member series containing 14.3 kDa 4-arm PS stars. In this case the PI mid-block (85.7 kDa) is significantly smaller than the midblock molecular weights

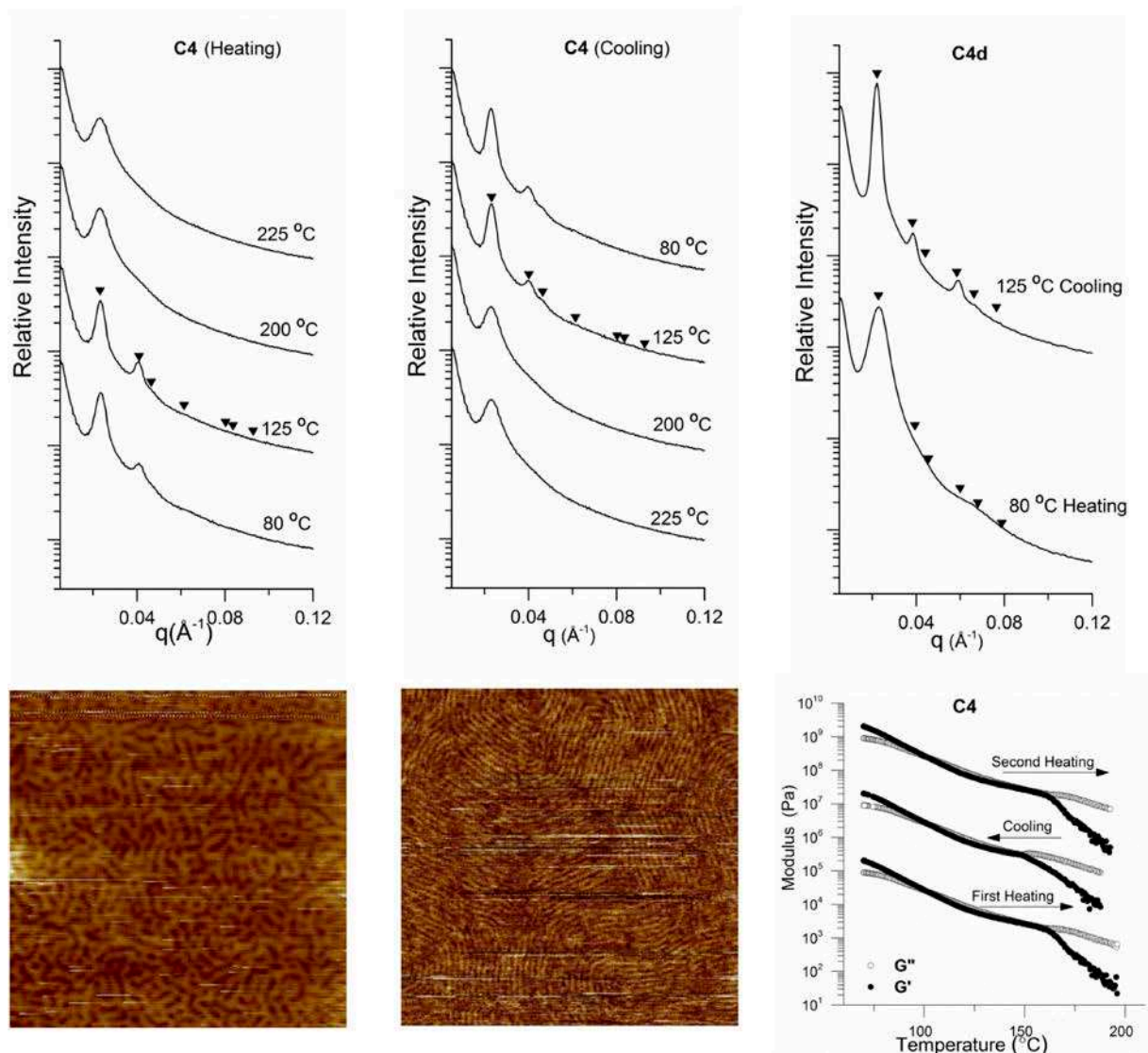


Figure A.5 SAXS data of sample **C4** along a complete heating (upper left) and cooling (upper center) thermal cycle. SAXS data of **C4d** diblock copolymer along a complete heating and cooling thermal cycle (upper right). Inverted triangles represent the locations of allowed reflections for HPC morphology, based on the position of the primary scattering wave vector $q^*=q_{100}$: q/q^* at $\sqrt{1}$, $\sqrt{3}$, $\sqrt{4}$, $\sqrt{7}$, $\sqrt{9}$, $\sqrt{12}$, $\sqrt{13}$, $\sqrt{16}$, etc. AFM images of pre (lower left, $1 \mu\text{m} \times 1 \mu\text{m}$) and post annealed **C4** (lower center, $2 \mu\text{m} \times 2 \mu\text{m}$). Dynamic temperature ramp over both heating and cooling cycles of **C4** (lower right) at 1°C min^{-1} , 1 rad s^{-1} and 4% strain (within the linear viscoelastic regime). The cooling cycle has been shifted vertically two orders of magnitude for clarity. The second heating cycle has also been shifted vertically four orders of magnitude.

found in the **A4** (191 kDa) and **B4** (114 kDa) samples, respectively. At this slightly reduced volume fraction, a linear analog of the block copolymer would still be expected fall within the cylinder (HPC) phase boundaries, despite the large change in PI molecular weight.

As expected, **C4** shares many of the same basic behavioral characteristics observed in the **A4** and **B4** samples. Minimal rheological hysteresis, G' and G'' in the $10^4 - 10^5$ Pa range, an elastic modulus that starts significantly greater than the loss modulus below the PS softening temperature, and the eventual convergence of the moduli near 100°C are all attributes of these three samples. However, the **C4** sample distinguishes itself in several ways. The shortest PI mid-block produces the earliest transition to disorder of the series, now easily detectable through a clearly defined drop in elastic modulus that begins near 160°C , and continues rapidly to disorder. The subtle inflections detected in the elastic modulus of **B4** (just after PS softening and just before disorder), are now clearly obvious in **C4** and suggestive of improved periodic order. In fact, the overlay of rheological data in Figure 6 really emphasizes the dramatic sharpening of the order to disorder transition as the midblock molecular weight and overall PI volume fraction are reduced for the system. This type of trend underscores the influence of mid-block molecular weight internal to the pom-pom architecture on the block copolymer's ability (kinetically speaking) to self-organize beyond the initial phase separation process. AFM imaging confirmed the improved ordering in the **C4** sample, with the as-cast sample even showing the beginnings of domain elongation order prior to substantial thermal annealing. Once annealed, the **C4** sample develops a very strongly correlated layered domain structure consistent with hexagonally packed cylinders aligned with their long axis parallel to the sample-air interface. Notably, the perforated appearance of the PS domains seems to still be apparent, again suggesting the packing frustration associated with the juxtaposition of the linear and star blocks remains in spite of the increased PS volume fraction. However, a direct comparison of the post-annealed AFM images for all three 4-arm samples shown in Figure A.6 highlights the strong progression in interfacial sharpness and domain continuity produced upon reduction of the linear bridging block.

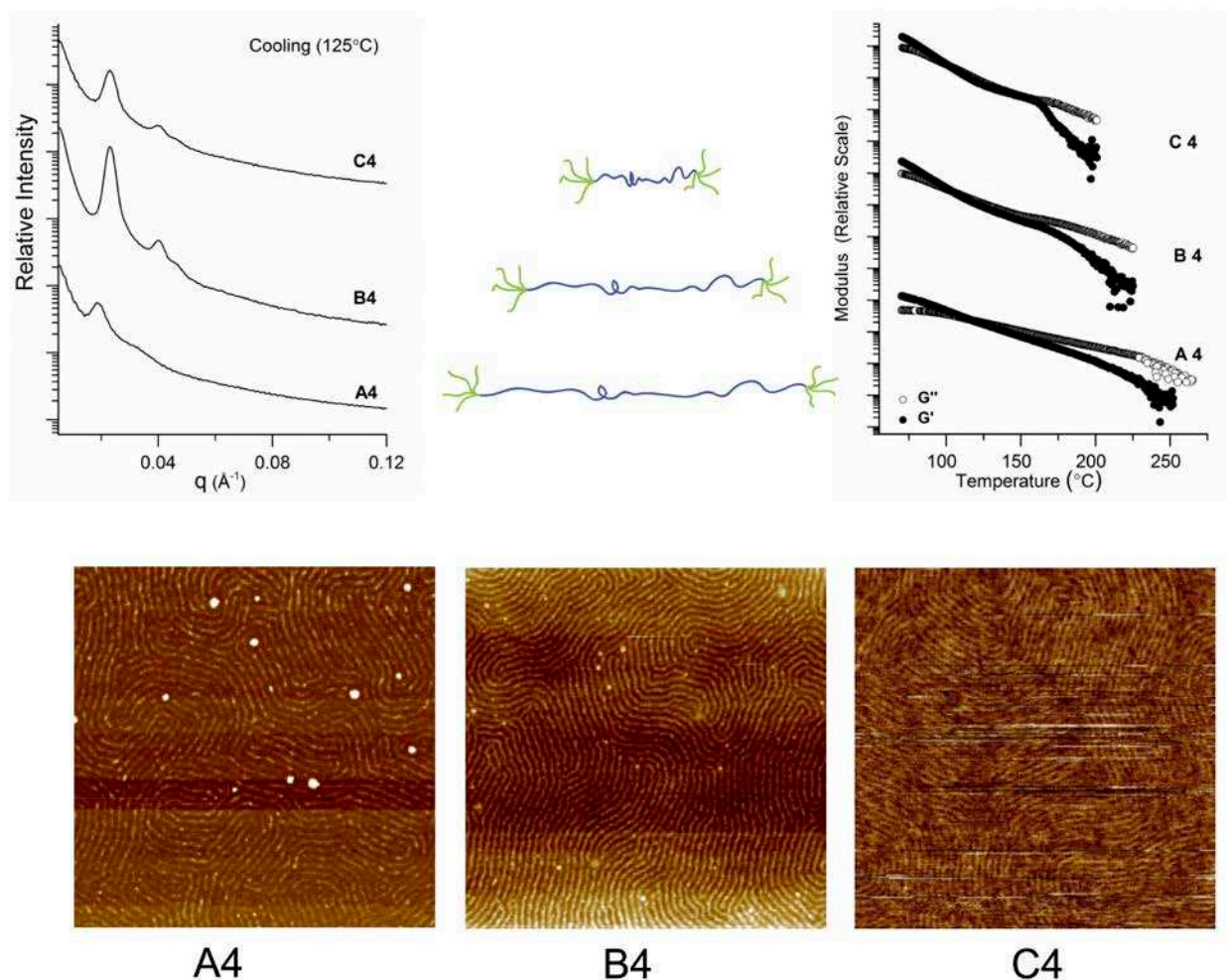


Figure A.6 SAXS data at 125°C (upon cooling) for samples having the equal number of arms but different lengths of the PI midblock (left). Dynamic temperature ramp heating and cooling cycles of same samples (right) at 1°C min⁻¹, 1 rad s⁻¹ and 4% strain (within the linear viscoelastic regime). Data for the **B4** and **C4** samples have been shifted two orders of magnitude and four orders of magnitudes up in the scale for clarity. AFM images of annealed samples **A4**, **B4**, and **C4** (bottom). All images are 2 μm x 2 μm.

Not surprisingly, the enhanced ordering suggested by the rheology and AFM of **C4** is confirmed by SAXS. Evidence of the HPC morphology is already present at 80 °C prior to annealing. Inverted triangles again represent the locations of allowed reflections for HPC morphology, based on the position of the primary scattering wave vector $q^* = q_{100}$: q/q^* at $\sqrt{1}$, $\sqrt{3}$, $\sqrt{4}$, $\sqrt{7}$, $\sqrt{9}$, $\sqrt{12}$, $\sqrt{13}$, $\sqrt{16}$, etc. The diffraction pattern remains at 125°C (heating), but reverts to LLP beyond the disorder transition (~ 160°C). Consistent with the reports of Wang et al.^[50] the

scattering remains consistent with phase separation and retention of LLP of micelles in particular as high as 225°C. Cooling the sample induces reordering, evident by recovery of the HPC diffraction pattern. Interestingly, the **C4d** diblock copolymer precursor exhibits behavior more like the **B4** and **B4d** samples, showing LLP behavior at low temperatures, followed by the development of a highly resolvable HPC diffraction pattern upon thermal annealing. As with **A4** and **B4**, the **C4** and **C4d** samples appear to be "lattice matched". A direct comparison between the post-annealing SAXS data for **A4** through **C4** (Figure A.6) summarizes the effects of changing mid-block molecular weight on cylinder forming pom-pom TPEs. Clearly shorter mid-block molecular weights, which produce higher minority component (PS) volume fractions, appear necessary for the formation of an ordered, hexagonal lattice. The higher volume fraction seems to help alleviate the packing frustration produced by the architecturally imposed chain crowding at the PS/PI interface, which intrinsically favors curvature that opposes cylinder formation.

The next series of samples examined, **B3**, **B4**, and **B7**, all share approximately identical (within experimental error) PI compositions ($f_{PI} \sim 0.82$) and similar overall star molecular masses (14.3 – 16.5 kDa), but differ in the average number of arms comprising the star architecture. Specifically, the three samples, **B3**, **B4**, and **B7**, contain on average 2.9, 4.1, and 7.1 arms, respectively. Of course, the morphological behavior of sample **B4** has already been discussed, being the central member of both series studied.

Figure A.7 contains a summary of the rheology, AFM and SAXS data collected for the **B3** triblock copolymer sample together with the SAXS data for the corresponding **B3d** diblock copolymer. Compared with the **B4** sample ($n_{arms} = 4.1$, $M_{n,arm} = 3.3$ kDa), **B3** has an average arm number and arm molecular weight of 2.9 and 5.4 kDa, respectively. While this change appears

slight, the impact on the morphological behavior is quite dramatic. For example, sample **B3** is the first sample to show rheological behavior in which the elastic modulus remains greater than the loss modulus throughout the ordered region, suggesting a high degree of fidelity in the self-assembled state. It also exhibits an ability to remain ordered to much higher temperatures than any of the other S_nIS_n pom-pom triblock copolymer samples examined, with the inflection in G' that denotes the onset of (a relatively long) disordering process, not appearing until near 275°C. A direct comparison with the 4.1-arm **B4** sample (Figure A.9), underscores the extent of this dramatic change, where the same inflection in G' occurs at nearly 100°C lower in temperature.

The AFM images of preannealed **B3** samples clearly show that phase separation is present even in the as-cast samples, with the early stages of domain elongation becoming visible. Annealing establishes a highly ordered hexagonal packing of cylinders, with large regions of sample showing alignment with the long axis perpendicular to the exposed surface, as is shown in the image included in Figure A.7. Of particular note for the annealed image is the reversal of contrast when compared with the pre-annealed sample. This reversal is simply a product of the instrument configuration at the time of measurement. PS remains the minority component comprising the cylindrical domains. Notably, examples of small regions of perpendicularly aligned domains can be clearly identified in the pre-annealed sample, in which the normal contrast is present.

Finally, the SAXS data for **B3** confirms the high degree of order achievable by the sample. Like the other pom-pom triblock copolymer samples examined in this paper, the **B3** sample shows LLP without annealing. Unlike the other samples, the **B3** sample actually shows ordering prior to reaching the disorder temperature, although not until surpassing 200°C. Order is seen even at temperatures as high as 225°C, although that was the highest temperature probed.

Access to the disorder temperature during SAXS was therefore not possible, which the rheological data suggests occurs above 275°C. Inverted triangles again represent the locations of allowed reflections for HPC morphology, based on the position of the primary scattering wave vector $q^* = q_{100}$: q/q^* at $\sqrt{1}$, $\sqrt{3}$, $\sqrt{4}$, $\sqrt{7}$, $\sqrt{9}$, $\sqrt{12}$, $\sqrt{13}$, $\sqrt{16}$, etc. The sample clearly establishes the HPC morphology and maintains it through the cooling process. The **B3d** diblock copolymer precursor exhibits similar behavior, showing LLP behavior at low temperatures, followed by the development of a highly resolvable HPC diffraction pattern upon thermal annealing. As expected, the lattice dimensions for **B3** and **B3d** are matched. It is remarkable that a redistribution of the molecular weight in the star from an average of four to an average of three arms produces such an improvement in the samples ability to order, and retain that order to such high temperatures.

A direct comparison between the post-annealing SAXS data of **B3** and **B4** may provide some insight. At 125°C, both **B3** and **B4** have adopted the HCP morphology. However the location of the principal scattering peak for each reveals a hexagonal unit cell dimensions that are significantly different. Using a combination of these scattering wave vector values and the volume fraction of the PI block (identical at $f_{PI} = 0.82$) one finds that the PS cylinder radii in **B3** and **B4** are 8.7 nm and 7.0 nm, respectively. This stresses the importance of the extra length and decreased crowding of the PS chains within in the cylindrical domains of the **B3** sample. The added length allows the domain to stretch out, reducing the curvature required at the interface. Meanwhile, the reduction from four arms to three alleviates additional packing frustration in the face of the opposing HCP curvature. That is, both changes, longer length and fewer arms work in concert to facilitate a much lower free energy state, in which packing frustration has been greatly reduced when compared with that in the **B4** sample. The consequence is that the morphology of

B3 is greatly stabilized relative to that in **B4**, and requires much greater temperatures before the entropy of the disordered phase becomes more favorable to the system.

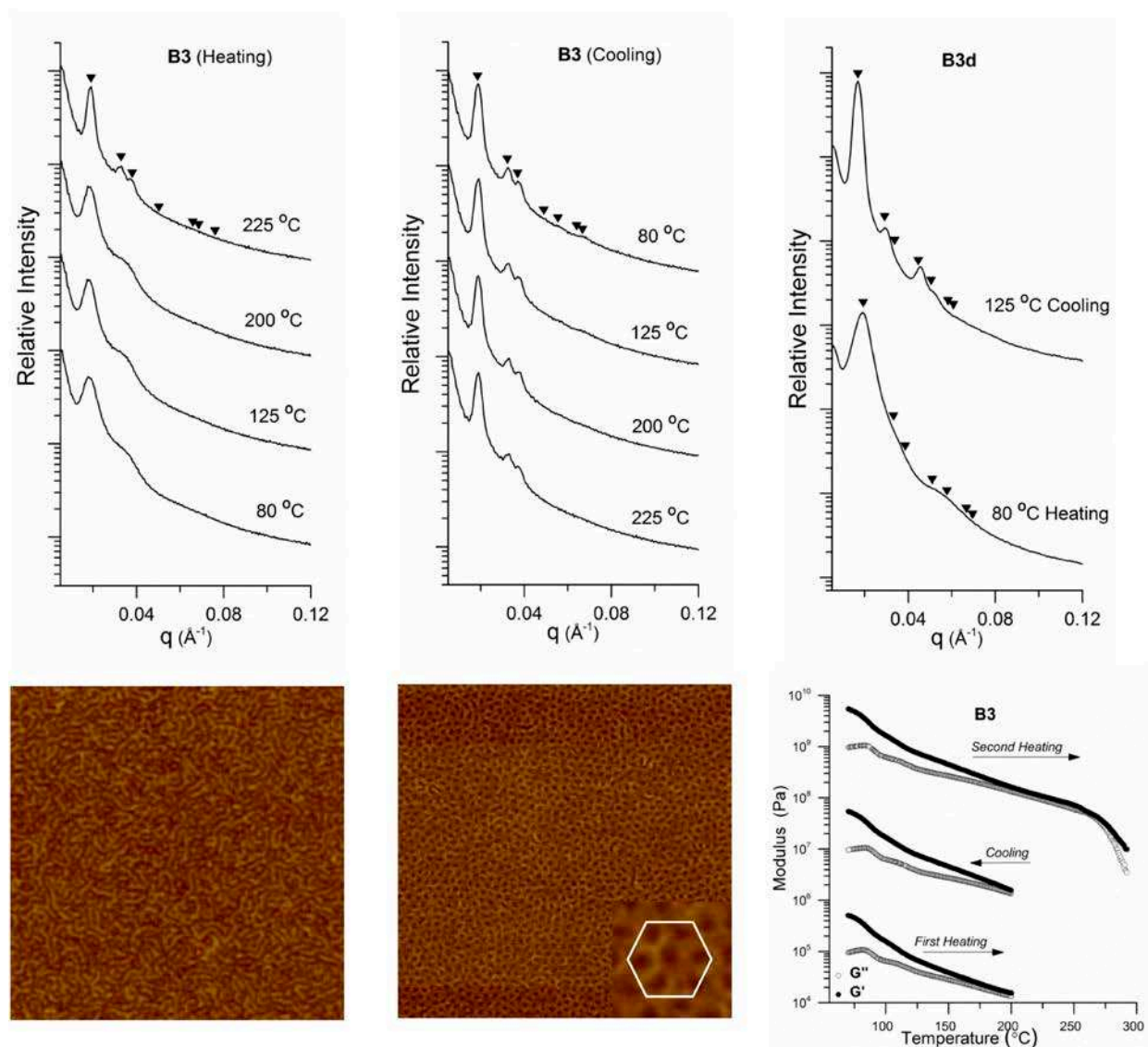


Figure A.7 SAXS data of sample **B3** along a complete heating (upper left) and cooling (upper center) thermal cycle. SAXS data of **B3d** diblock copolymer along a complete heating and cooling thermal cycle (upper right). Inverted triangles represent the locations of allowed reflections for HPC morphology, based on the position of the primary scattering wave vector $q^*=q_{100}$: q/q^* at $\sqrt{1}$, $\sqrt{3}$, $\sqrt{4}$, $\sqrt{7}$, $\sqrt{9}$, $\sqrt{12}$, $\sqrt{13}$, $\sqrt{16}$, etc. AFM images of pre (lower left) and post annealed **B3** (lower center), exhibiting features consistent with HPC morphology. All images are $2\ \mu\text{m} \times 2\ \mu\text{m}$. Dynamic temperature ramp over both heating and cooling cycles of **B3** (lower right) at $1^\circ\text{C}\ \text{min}^{-1}$, $1\ \text{rad}\ \text{s}^{-1}$ and 4% strain (within the linear viscoelastic regime). The cooling cycle has been shifted vertically two orders of magnitude for clarity. The second heating cycle has also been shifted vertically four orders of magnitude.

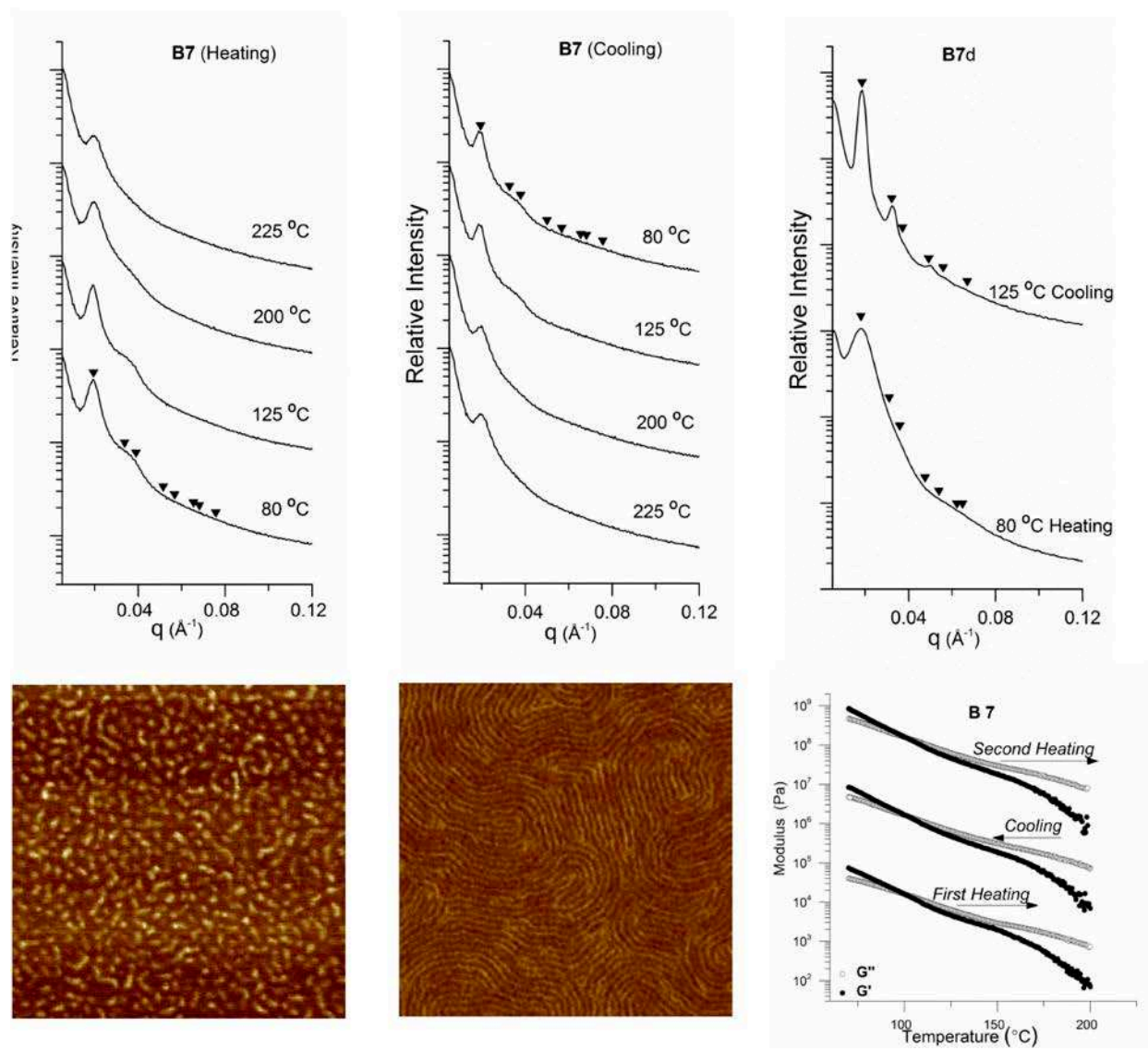


Figure A.8 SAXS data of sample **B7** along a complete heating (upper left) and cooling (upper center) thermal cycle. SAXS data of **B7d** diblock copolymer along a complete heating and cooling thermal cycle (upper right). Inverted triangles represent the locations of allowed reflections for HPC morphology, based on the position of the primary scattering wave vector $q^*=q_{100}$: q/q^* at $\sqrt{1}$, $\sqrt{3}$, $\sqrt{4}$, $\sqrt{7}$, $\sqrt{9}$, $\sqrt{12}$, $\sqrt{13}$, $\sqrt{16}$, etc. AFM images of pre (lower left, $1 \mu\text{m} \times 1 \mu\text{m}$) and post annealed **B7** (lower center, $2 \mu\text{m} \times 2 \mu\text{m}$). Dynamic temperature ramp over both heating and cooling cycles of **B7** (lower right) at 1°C min^{-1} , 1 rad s^{-1} and 4% strain (within the linear viscoelastic regime). The cooling cycle has been shifted vertically two orders of magnitude for clarity. The second heating cycle has also been shifted vertically four orders of magnitude.

In contrast, the final sample examined, **B7**, is architecturally designed to exacerbate the packing frustration in the system. That is, compared with the **B4** sample ($n_{\text{arms}} = 4.1$, $M_{n,\text{arm}} = 3.3$ kDa), **B7** has an average arm number and arm molecular weight of 7.1 and 2.2 kDa, respectively.

Figure A.8 contains a summary of the rheology, AFM and SAXS data collected for the **B7** triblock copolymer sample together with the SAXS data for the corresponding **B7d** diblock copolymer. As one might expect, the impact of the dense star architecture coupled with short arm lengths is to incite early disorder.

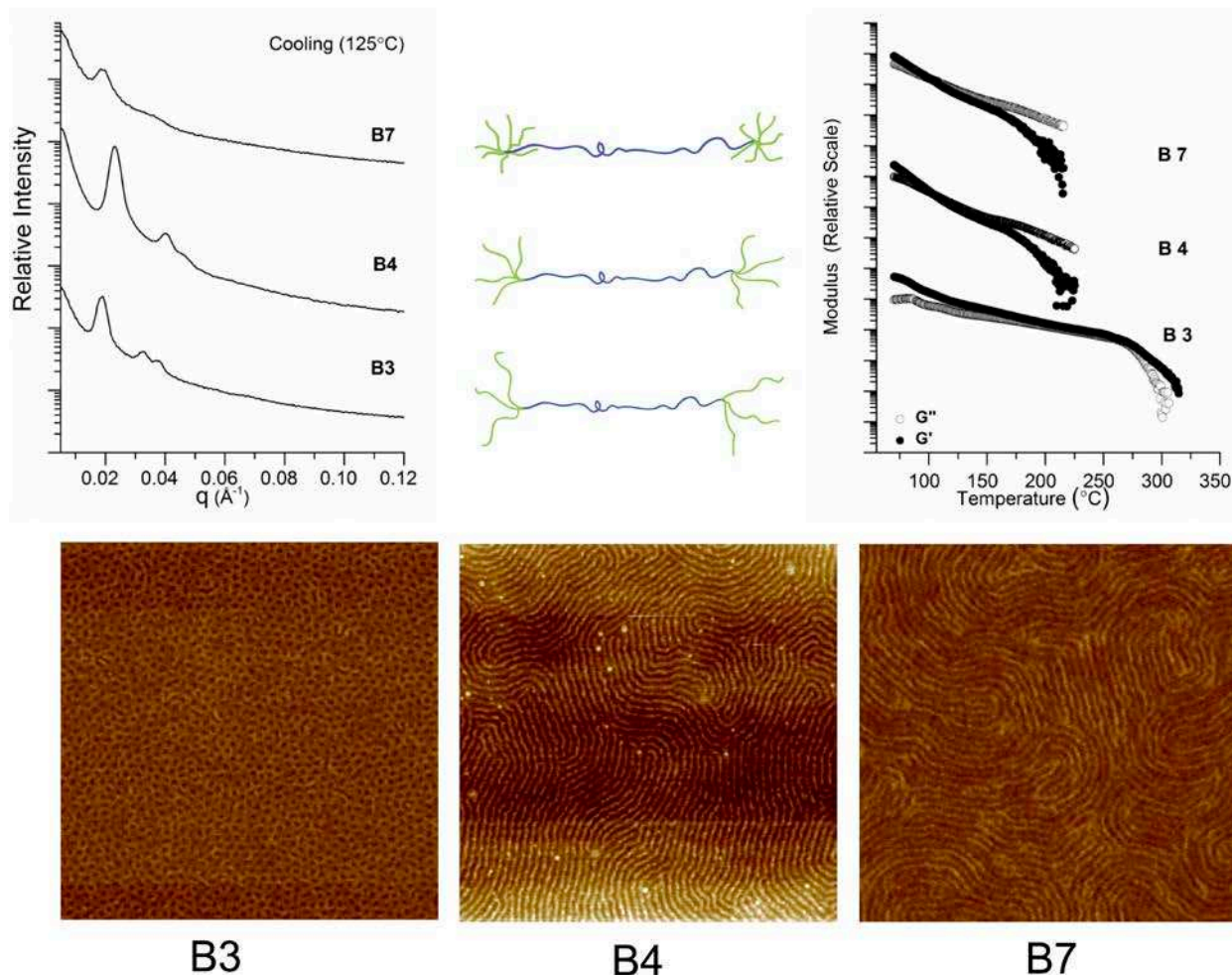


Figure A.9 SAXS data at 125°C (upon cooling) for samples having the equal molecular weight PI mid-blocks but different numbers of arms in the PS star (left) end caps. Dynamic temperature ramp heating and cooling cycles of same samples (right) at 1 C min^{-1} , 1 rad s^{-1} and 4% strain (within the linear viscoelastic regime). Data for the **B4** and **B7** samples have been shifted two orders of magnitude and four orders of magnitudes up in the scale for clarity. AFM images of post-annealed sample B3, B4, and B7. All images are $2\text{ }\mu\text{m} \times 2\text{ }\mu\text{m}$.

Figure A.8 shows that the inflection in elastic modulus denoting the onset of the disordering process occurs now at approximately 160°C, about 10°C lower than in **B4** (Figure A.9). This change appears small, especially when compared with the extensive difference generated upon changing four arms (**B4**) to three (**B3**). It suggests that the morphological structures between the two systems produce similar rheological responses, and may be closely related in terms of the free energy landscape in which they exist (with respect to the balance between the enthalpic and entropic contributions to the system free energy, in particular).

AFM images of the pre-annealed and post-annealed **B7** samples are also reminiscent of the type of order exhibited by **B4** (Figure A.9). As-cast thin films show clear phase separation featuring of a random arrangement of small, irregularly shaped domains. Upon annealing the **B7** sample is also able to develop a layered organization of PS and PI domains. However, a direct comparison of the AFM images for these two samples (shown together in Figure A.9) suggests that the additional interfacial chain crowding in the PS does reduce the domain continuity and the sharpness of the morphology produced, giving the perforated appearance of the PS domains prevalent in **A4**. The SAXS data for sample **B7** (Figure A.8) confirms this is likely the case. That is, like **A4**, the **B7** sample fails to achieve a hexagonal packing at a level that produced Bragg diffraction, even after cooling from above the disorder temperature. The SAXS clearly exhibits a principal scatter peak confirming phase separation consistent with a primary domain spacing for the system, but a LLP of these cylindrical domains prevails. It seems apparent that the extreme degree of packing frustration at the PS/PI interface, in combination with an architecture that kinetically hinders entanglement relaxation dynamics, impedes morphology development in the **B7** sample. Notably, the development (after annealing) of the HPC morphology in the **B7d** diblock copolymer precursor (Figure A.8) suggests that the hindered entanglement relaxation

because of the pom-pom architecture actually does play a significant role. A direct comparison between the post-annealing SAXS signatures of **B3**, **B4**, and **B7** presented in Figure A.9, nicely summarizes the impact of progressively redistributing the PS mass into a larger number of arms in the pom-pom triblock copolymer architecture.

A.4 CONCLUSIONS

A series of eighteen S_nIS_n pom-pom triblock copolymers were synthesized using a one-pot convergent anionic polymerization strategy demonstrating the ability to control architectural parameters such as PS arm molecular weight, the number of arms contained in the star, and the PI mid-block molecular weight. Of the 18, five were selected for detailed characterization using rheology, AFM, and SAXS, to better understand the influence of changes in these architectural parameters on the morphological behavior exhibited. The five selected all shared PS star blocks as the minority component, with overall star molecular weights that were held approximately constant in the 14.3 kDa to 16.5 kDa range. All samples showed clear phase separation, with two of the five limited to a LLP of cylindrical domains while the remaining three were able to adopt a highly ordered hexagonal packing confirmed through SAXS. Longer mid-block molecular weights and increased numbers of arms in the star both impeded formation of highly ordered cylinder phases. Increasing the number of arms in the stars also favored earlier transitions to a disordered phase. These results are consistent with the prominent role of interfacial packing frustration in determining the ability of the system to adopt high fidelity, continuous domain structures with the minority component (PS), cylinder-forming star blocks. The chain crowding

produced by the PS star architecture intrinsically favors interfacial curvature towards the PI mid-block, while the PI majority component volume fraction favors interfacial curvature towards the PS star. The results support the important interplay between these two thermodynamic driving forces, and systems in which the competition is most extreme (large numbers of arms, high PI mid-block molecular weights) have the most difficulty forming a highly ordered HPC phase. In addition, it is suspected that these same structural parameters significantly impacts entanglement relaxation dynamics, which slows the kinetic evolution of the morphologies developed in these systems.

REFERENCES

- [1] Y.S. Zhao, B. Su, L.C. Zhong, F. Chen, Q. Fu, Largely Improved Mechanical Properties of a Poly(styrene-*b*-isoprene-*b*-styrene) Thermoplastic Elastomer Prepared under Dynamic-Packing Injection Molding, *Industrial & Engineering Chemistry Research*, 53 (2014) 15287-15295.
- [2] Q. Chen, Y. Matsumiya, T. Iwamoto, K. Nishida, T. Kanaya, H. Watanabe, A. Takano, K. Matsuoka, Y. Matsushita, Dielectric Behavior of Guest *cis*-Polyisoprene Confined in Spherical Microdomain of Triblock Copolymer., *Macromolecules*, 45 (2012) 2809-2819.
- [3] S.H. Lee, K. Char, G. Kim, Order-disorder and order-order transitions in mixtures of highly asymmetric triblock copolymer and low molecular weight homopolymers, *Macromolecules*, 33 (2000) 7072-7083.
- [4] N. Sota, N. Sakamoto, K. Saijo, T. Hashimoto, Phase transition from disordered sphere to hex-cylinder via transient ordering into Bcc-sphere in SIS triblock copolymer, *Macromolecules*, 36 (2003) 4534-4543.
- [5] N.Y. Vaidya, C.D. Han, D. Kim, N. Sakamoto, T. Hashimoto, Microdomain Structures and Phase Transitions in Binary Blends Consisting of a Highly Asymmetric Block Copolymer and a Homopolymer, *Macromolecules*, 34 (2001) 222-234.
- [6] J.H. Laurer, D.A. Hajduk, J.C. Fung, J.W. Sedat, S.D. Smith, S.M. Gruner, D.A. Agard, R.J. Spontak, Microstructural analysis of a cubic bicontinuous morphology in a neat SIS triblock copolymer, *Macromolecules*, 30 (1997) 3938-3941.
- [7] H.T. Ban, T. Kase, M. Kawabe, A. Miyazawa, T. Ishihara, H. Hagihara, Y. Tsunogae, M. Murata, T. Shiono, A new approach to styrenic thermoplastic elastomers: Synthesis and characterization of crystalline styrene-butadiene-styrene triblock copolymers, *Macromolecules*, 39 (2006) 171-176.
- [8] X.Y. Cao, R. Faust, Polyisobutylene-based thermoplastic elastomers. 5. Poly(styrene-*b*-isobutylene-*b*-styrene) triblock copolymers by coupling of living poly(styrene-*b*-isobutylene) diblock copolymers, *Macromolecules*, 32 (1999) 5487-5494.
- [9] J. Feldthusen, B. Ivan, A.H.E. Muller, Synthesis of linear and star-shaped block copolymers of isobutylene and methacrylates by combination of living cationic and anionic polymerizations, *Macromolecules*, 31 (1998) 578-585.
- [10] H. Schmalz, V. Abetz, R. Lange, M. Soliman, New Thermoplastic Elastomers by Incorporation of Nonpolar Soft Segments in PBT-Based Copolyesters†, *Macromolecules*, 34 (2001) 795-800.
- [11] J.D. Tong, R. Jérôme, Synthesis of poly(methyl methacrylate)-*b*-poly(*n*-butyl acrylate)-*b*-poly(methyl methacrylate) triblocks and their potential as thermoplastic elastomers, *Polymer*, 41 (2000) 2499-2510.

- [12] Y.Q. Zhu, R. Weidisch, S.P. Gido, G. Velis, N. Hadjichristidis, Morphologies and mechanical properties of a series of block-double-graft copolymers and terpolymers, *Macromolecules*, 35 (2002) 5903-5909.
- [13] G. Holden, *Understanding thermoplastic elastomers*, Hanser Hanser Gardner Publications, Munich, 2000.
- [14] L.R. Hutchings, R.W. Richards, Influence of architecture on arm dimensions and interaction parameters in polybutadiene star polymers, *Macromolecules*, 32 (1999) 880-891.
- [15] I. Neubert, A.D. Schluter, Dendronized polystyrenes with hydroxy and amino groups in the periphery, *Macromolecules*, 31 (1998) 9372-9378.
- [16] G. Koutalas, H. Iatrou, D.J. Lohse, N. Hadjichristidis, Well-defined comb, star-comb, and comb-on-comb polybutadienes by anionic polymerization and the macromonomer strategy, *Macromolecules*, 38 (2005) 4996-5001.
- [17] D.M. Knauss, T.Z. Huang, Star-block-linear-block-star triblock (pom-pom) polystyrene by convergent living anionic polymerization, *Macromolecules*, 35 (2002) 2055-2062.
- [18] D.M. Knauss, T.Z. Huang, ((PS)(n)PS)(m) star-shaped polystyrene with star-shaped branches at the terminal chain ends by convergent living anionic polymerization, *Macromolecules*, 36 (2003) 6036-6042.
- [19] A. Hakiki, R.N. Young, T.C.B. Mcleish, Synthesis and characterization of H-shaped polyisoprene, *Macromolecules*, 29 (1996) 3639-3641.
- [20] J. Roovers, P.M. Toporowski, Preparation and Characterization of H-Shaped Polystyrenes, *Macromolecules*, 14 (1981) 1174-1178.
- [21] N. Hadjichristidis, M. Xenidou, H. Iatrou, M. Pitsikalis, Y. Poulos, A. Avgeropoulos, S. Sioula, S. Paraskeva, G. Velis, D.J. Lohse, D.N. Schulz, L.J. Fetters, P.J. Wright, R.A. Mendelson, C.A. Garcia-Franco, T. Sun, C.J. Ruff, Well-defined, model long chain branched polyethylene. 1. Synthesis and characterization, *Macromolecules*, 33 (2000) 2424-2436.
- [22] I. Gitsov, J.M.J. Frechet, Novel Nanoscopic Architectures - Linear-Globular ABA Copolymers with Polyether Dendrimers as a-Blocks and Polystyrene as B-Block, *Macromolecules*, 27 (1994) 7309-7315.
- [23] T.Z. Huang, D.M. Knauss, (Star PS)-block-(linear PI)-block-(star PS) triblock copolymers - Thermoplastic elastomers with complex branched architectures, *Macromolecular Symposia*, 215 (2004) 81-93.
- [24] T. Emrick, W. Hayes, J.M.J. Frechet, A TEMPO-mediated "living" free-radical approach to ABA triblock dendritic linear hybrid copolymers, *J Polym Sci Pol Chem*, 37 (1999) 3748-3755.

- [25] S.P. Gido, C. Lee, D.J. Pochan, S. Pispas, J.W. Mays, N. Hadjichristidis, Synthesis, characterization, and morphology of model graft copolymers with trifunctional branch points, *Macromolecules*, 29 (1996) 7022-7028.
- [26] H.R. Kricheldorf, T. Stukenbrock, New polymer syntheses. XC. A-B-A triblock copolymers with hyperbranched polyester A-blocks, *J Polym Sci Pol Chem*, 36 (1998) 31-38.
- [27] C. Lee, S.P. Gido, Y. Poulos, N. Hadjichristidis, N.B. Tan, S.F. Trevino, J.W. Mays, H-shaped double graft copolymers: Effect of molecular architecture on morphology, *J Chem Phys*, 107 (1997) 6460-6469.
- [28] A. Avgeropoulos, N. Hadjichristidis, Synthesis of model nonlinear block copolymers of A(BA)(2), A(BA)(3), and (AB)(3)A(BA)(3) type, *J Polym Sci Pol Chem*, 35 (1997) 813-816.
- [29] H. Iatrou, A. Avgeropoulos, N. Hadjichristidis, Synthesis of Model Super H-Shaped Block-Copolymers, *Macromolecules*, 27 (1994) 6232-6233.
- [30] H. Iatrou, L. Willner, N. Hadjichristidis, A. Halperin, D. Richter, Aggregation phenomena of model PS/PI super-H-shaped block copolymers. Influence of the architecture, *Macromolecules*, 29 (1996) 581-591.
- [31] G. Velis, N. Hadjichristidis, Synthesis of model PS(PI)(5) and (PI)(5)PS(PI)(5) nonlinear block copolymers of styrene (S) and isoprene (I), *Macromolecules*, 32 (1999) 534-536.
- [32] R. Weidisch, S.P. Gido, D. Uhrig, H. Iatrou, J. Mays, N. Hadjichristidis, Tetrafunctional Multigraft Copolymers as Novel Thermoplastic Elastomers, *Macromolecules*, 34 (2001) 6333-6337.
- [33] M.W. Matsen, Effect of Architecture on the Phase Behavior of AB-Type Block Copolymer Melts, *Macromolecules*, 45 (2012) 2161-2165.
- [34] G. Bishko, T.C.B. McLeish, O.G. Harlen, R.G. Larson, Theoretical molecular rheology of branched polymers in simple and complex flows: The pom-pom model, *Phys Rev Lett*, 79 (1997) 2352-2355.
- [35] G.B. Bishko, O.G. Harlen, T.C.B. McLeish, T.M. Nicholson, Numerical simulation of the transient flow of branched polymer melts through a planar contraction using the 'pom-pom' model, *J Non-Newton Fluid*, 82 (1999) 255-273.
- [36] T.C.B. McLeish, R.G. Larson, Molecular constitutive equations for a class of branched polymers: The pom-pom polymer, *J Rheol*, 42 (1998) 81-110.
- [37] E. van Ruymbeke, M. Kapnistos, D. Vlassopoulos, T. Huang, D.M. Knauss, Linear Melt Rheology of Pom-Pom Polystyrenes with Unentangled Branches, *Macromolecules*, 40 (2007) 1713-1719.
- [38] D.M. Knauss, H.A. Al-Muallem, T.Z. Huang, D.T. Wu, Polystyrene with dendritic branching by convergent living anionic polymerization, *Macromolecules*, 33 (2000) 3557-3568.

- [39] M.B. Huglin, in: J. Bandrup, E.H. Immergut (Eds.) *Polymer Handbook*, John Wiley & Sons, Inc., New York, 1989, pp. V445.
- [40] L.J. Fetters, D.J. Lohse, D. Richter, T.A. Witten, A. Zirkel, Connection between Polymer Molecular-Weight, Density, Chain Dimensions, and Melt Viscoelastic Properties, *Macromolecules*, 27 (1994) 4639-4647.
- [41] K.A. Cavicchi, T.P. Lodge, Domain size equilibration in sphere-forming block copolymers, *J Polym Sci Pol Phys*, 41 (2003) 715-724.
- [42] C. Guo, T.S. Bailey, Highly distensible nanostructured elastic hydrogels from AB diblock and ABA triblock copolymer melt blends, *Soft Matter*, 6 (2010) 4807-4818.
- [43] V.F. Scalfani, T.S. Bailey, Access to Nanostructured Hydrogel Networks through Photocured Body-Centered Cubic Block Copolymer Melts, *Macromolecules*, 44 (2011) 6557-6567.
- [44] C. Guo, T.S. Bailey, Tailoring mechanical response through coronal layer overlap in tethered micelle hydrogel networks, *Soft Matter*, 11 (2015) 7345-7355.
- [45] I.W. Hamley, *The physics of block copolymers*, Oxford University Press, Oxford ; New York, 1998.
- [46] T.A. Mykhaylyk, O.O. Mykhaylyk, S. Collins, I.W. Hamley, Ordered structures and phase transitions in mixtures of a polystyrene/polyisoprene block copolymer with the corresponding homopolymers in thin films and in bulk, *Macromolecules*, 37 (2004) 3369-3377.
- [47] A.P. Smith, A. Sehgal, J.F. Douglas, A. Karim, E.J. Amis, Combinatorial mapping of surface energy effects on diblock copolymer thin film ordering, *Macromolecular Rapid Communications*, 24 (2003) 131-135.
- [48] J.S. Higgins, H. Benoît, *Polymers and neutron scattering*, Clarendon Press, 1994.
- [49] E.E. Dormidontova, T.P. Lodge, The order-disorder transition and the disordered micelle regime in sphere-forming block copolymer melts, *Macromolecules*, 34 (2001) 9143-9155.
- [50] X.H. Wang, E.E. Dormidontova, T.P. Lodge, The order-disorder transition and the disordered micelle regime for poly(ethylenepropylene-b-dimethylsiloxane) spheres, *Macromolecules*, 35 (2002) 9687-9697.
- [51] T.S. Bailey, H.D. Pham, F.S. Bates, Morphological behavior bridging the symmetric AB and ABC states in the poly(styrene-b-isoprene-b-ethylene oxide) triblock copolymer system, *Macromolecules*, 34 (2001) 6994-7008.
- [52] M.B. Kossuth, D.C. Morse, F.S. Bates, Viscoelastic behavior of cubic phases in block copolymer melts, *J Rheol*, 43 (1999) 167-196.

[53] V.F. Scalfani, T.S. Bailey, Thermally Stable Photocuring Chemistry for Selective Morphological Trapping in Block Copolymer Melt Systems, *Chem Mater*, 22 (2010) 5992-6000.

SUPPORTING INFORMATION I

ELASTIC FREE-STANDING RTIL COMPOSITE MEMBRANES FOR CO₂/N₂ SEPARATION BASED ON SPHERE-FORMING TRIBLOCK/DIBLOCK COPOLYMER BLENDS

Permeability and selectivity data for the SO/SOS membranes are included in Tables S1.1–S1.7. ¹H NMR and size-exclusion chromatography (SEC) data for S-OH and SO precursor molecules are included in Figure S1.1 – S1.3. SEC data for SOS22 and SOS46 blends are given in Figure S1.4. Stress-strain data for the compressive cyclic loading on SOS46 are given in Figure S1.5. FTIR/ATR-IR of neat SOS46, SOS46 + [EMIM][TFSI], and neat [EMIM][TFSI] are given in Figure S1.6. Structural characterization data (SAXS) for SOS22 and SOS46 are given in Figure S1.7 and Table S1.8.

S1.1 EXPERIMENTAL DATA

S1.1.1 Gas permeation data

Note that the diffusivity and solubility measurements obtained for N₂ and CH₄ using our apparatus have a high degree of inaccuracy. Thus, the data is presented only for completeness and observation of general trends.

SOS22 MEMBRANES

Table S1.1. Permeability, diffusivity, and solubility coefficients of CO₂ for SOS22/[EMIM][TFSI] membranes.

Feed Pressure (kPa)	CO ₂ Permeability (barrers)	CO ₂ Diffusivity (10 ⁻⁶ cm ² /s)	CO ₂ Solubility (cm ³ of CO ₂ at STP)
37 ¹	847	1.7	3.7
52 ¹	826	1.6	3.8
84 ¹	774	1.4	4.1
112 ¹	716	1.6	3.2
345 ¹	575	1.1	3.8
413 ¹	589	1.2	3.6
27 ²	678	1.6	3.2
42 ²	705	1.6	3.4
61 ²	640	1.6	3.0
76 ²	618	1.6	2.9
26 ³	712	1.2	4.7
27 ³	659	1.2	4.3
52 ³	658	1.1	4.6
53 ³	624	1.2	4.0
54 ³	573	1.1	4.0
85 ³	591	1.0	4.3

¹ First membrane tested (280 μm). ² Second membrane tested (175 μm). ³ Third membrane tested (135 μm).

Table S1.2. Permeability of N₂ for SOS22/[EMIM][TFSI] membranes.

Feed Pressure (kPa)	N ₂ Permeability (barrers)
27 ¹	31
55 ¹	28
84 ¹	26
123 ¹	18
385 ¹	15
393 ¹	14
27 ²	20
42 ²	25
61 ²	16
76 ²	16

29 ³	15
53 ³	14
85 ³	11

¹ First membrane tested (280 μm). ² Second membrane tested (175 μm). ³ Third membrane tested (135 μm).

Table S1.3. Permeability, diffusivity, and solubility coefficients of CH₄ for SOS22/[EMIM][TFSI] membranes.*

Feed Pressure (kPa)	CH ₄ Permeability (barrers)	CO ₂ Diffusivity (10 ⁻⁶ cm ² /s)	CH ₄ Solubility (cm ³ of CO ₂ at STP)
108	41	0.9	0.3
398	33	0.4	0.6
391	34	0.4	0.5
398	32	0.5	0.5

*Membrane thickness (280 μm).

SOS46 MEMBRANES

Table S1.4. Permeability, diffusivity, and solubility coefficients of CO₂ for SOS46/[EMIM][TFSI] membranes.

Feed Pressure (kPa)	CO ₂ Permeability (barrers)	CO ₂ Diffusivity (10 ⁻⁶ cm ² /s)	CO ₂ Solubility (cm ³ of CO ₂ at STP)
28 ¹	845	2.0	3.2
56 ¹	807	1.9	3.3
86 ¹	770	1.7	3.4
118 ¹	796	1.8	3.3
132 ¹	800	1.7	3.7
26 ²	940	1.7	4.1
57 ²	936	1.6	4.4
89 ²	872	1.4	4.6
109 ²	853	1.7	3.9
154 ²	827	1.6	3.8
212 ²	844	1.5	4.1
58 ³	771	N/A	N/A
81 ³	754	N/A	N/A
401 ⁴	612	1.5	3.1

404 ⁴	639	1.7	2.8
409 ⁴	567	1.3	3.2

¹ First membrane tested (200 μm). ² Second membrane tested (185 μm). ³ Third membrane tested (185 μm). ⁴ Fourth membrane tested (430 μm).

Table S1.5. Permeability, diffusivity, and solubility coefficients of N₂ for SOS46/[EMIM][TFSI] membranes.

Feed Pressure (kPa)	N ₂ Permeability (barrers)
27 ¹	20
63 ¹	23
88 ¹	23
111 ¹	22
175 ¹	23
27 ²	27
52 ²	25
76 ²	24
104 ²	22
150 ²	22
182 ²	22
27 ³	32
53 ³	30
82 ³	30
112 ⁴	14
337 ⁴	23
387 ⁴	22

¹ First membrane tested (200 μm). ² Second membrane tested (185 μm). ³ Third membrane tested (185 μm). ⁴ Fourth membrane tested (430 μm).

Table S1.6. The measured permeability, diffusivity, and solubility coefficients of CH₄ for SOS46/[EMIM][TFSI] membranes.

Feed Pressure (kPa)	CH ₄ Permeability (barrers)	CH ₄ Diffusivity (10 ⁻⁶ cm ² /s)	CH ₄ Solubility (cm ³ of CH ₄ at STP)
85 [*]	32	1.5	0.0
96 [*]	38	1.0	2.7
405 [*]	52	2.2	0.2
480 [*]	50	1.2	0.0

^{*} Membrane thickness (430 μm).

Table S1.7. The measured permeability, diffusivity, and solubility coefficients of CO₂ for an SOS46/[EMIM][TFSI] membrane over 28 days at a feed pressure of approximately 230 kPa.*

Day	CO₂ Permeability (barrers)	CO₂ Diffusivity (10⁻⁶ cm²/s)	CO₂ Solubility (cm³ of CO₂ at STP)
1	889	1.6	4.3
3	854	2.5	2.6
3	845	2.5	2.6
4	942	2.8	2.6
6	938	2.9	2.5
8	989	3.1	2.4
8	980	1.6	3.0
8	970	2.7	2.7
21	957	3.0	2.5
21	975	2.9	2.6
22	977	2.9	2.5
23	972	2.9	2.5
24	955	3.1	2.4
25	955	2.4	3.0
26	996	3.2	2.4
28	971	2.8	2.6

*Membrane thickness (255 μm).

SI.1.2. Synthesis methods and characterization data for S-OH, SO, SOS22 and SOS46

Materials. Styrene (99%, 4-tert-butylcatechol inhibitor, Aldrich) and ethylene oxide (99.5+%, compressed gas, Aldrich) monomer were each purified by successive vacuum distillations (10–20 mTorr) from dried di-n-butylmagnesium (0.1 mmol g⁻¹ monomer, 1.0 M solution in heptane, Aldrich) before use. Both purified styrene and ethylene oxide monomer were stored in glass burettes in the dark, at room temperature (styrene) and 3 °C (ethylene oxide), respectively, before use (typically less than 24 h). Argon degassed cyclohexane (CHX) was purified by passing the solvent over activated alumina followed by Q-5-like supported copper catalyst (Glass Contour, proprietary). Argon degassed tetrahydrofuran (THF) was purified by passing the solvent over activated alumina. High-purity argon (99.998%, Airgas) was passed through additional oxygen and moisture traps prior to use. Glassware and polymerization reactors were flamed under vacuum and backfilled with argon (3x). Polymerizations and functionalization reactions were carried out using standard air-free techniques. All other materials were used as received.

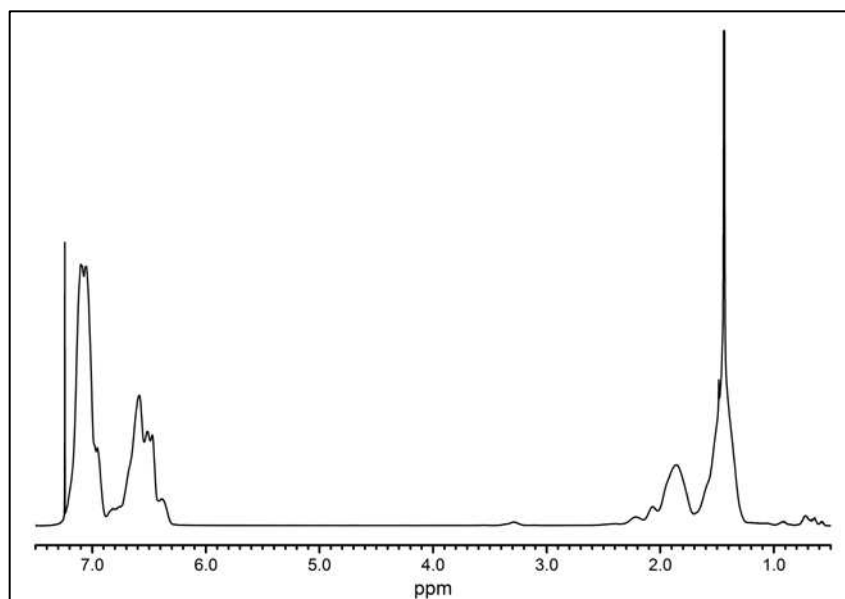


Figure S1.1 ^1H NMR of **S-OH** precursor. Peak assignments: δ_{H} (400 MHz; CDCl_3): 6.20-7.26 (b, $-\text{C}_6\text{H}_5$), 3.2-3.5 (m, $-\text{CH}_2\text{OH}$), 0.84-2.60 (b, $-\text{CH}(\text{C}_6\text{H}_5)\text{CH}_2-$, $\text{CH}_3\text{CH}(\text{CH}_2\text{CH}_3)-$, $-\text{CH}_2\text{CH}_2\text{OH}$), 0.5-0.78 (m, $\text{CH}_3\text{CH}(\text{CH}_2\text{CH}_3)-$).

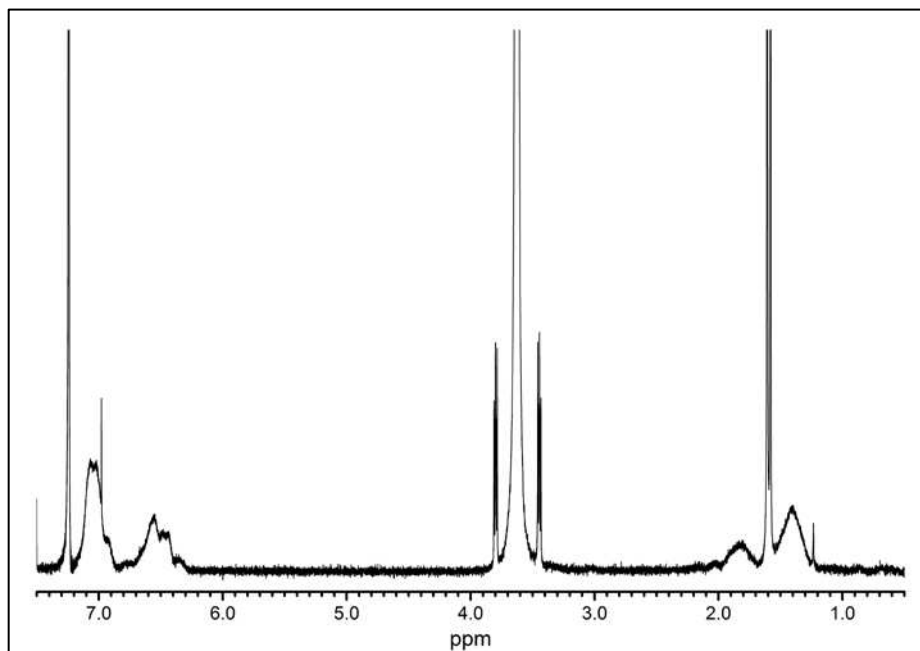


Figure S1.2 ^1H NMR of **SO-H** diblock copolymer. Peak assignments: (**SO**, **SOS**): δ_{H} (400 MHz; CDCl_3): 6.20-7.26 (b, $-\text{C}_6\text{H}_5$, $-\text{OCH}_2(\text{C}_6\text{H}_4)\text{CH}_2\text{O}-$), 4.55 (s, $-\text{OCH}_2(\text{C}_6\text{H}_4)\text{CH}_2\text{O}-$), 3.1-4.0 (b, $-\text{CH}_2\text{CH}_2\text{O}-$, $-\text{CH}(\text{C}_6\text{H}_5)\text{CH}_2\text{CH}_2\text{O}-$), 1.0-2.30 (b, $-\text{CH}_2\text{CH}(\text{C}_6\text{H}_5)-$, $\text{CH}_3\text{CH}(\text{CH}_2\text{CH}_3)-$, $-\text{CH}(\text{C}_6\text{H}_5)\text{CH}_2\text{CH}_2\text{O}-$), 0.5-0.78 (m, $\text{CH}_3\text{CH}(\text{CH}_2\text{CH}_3)-$).

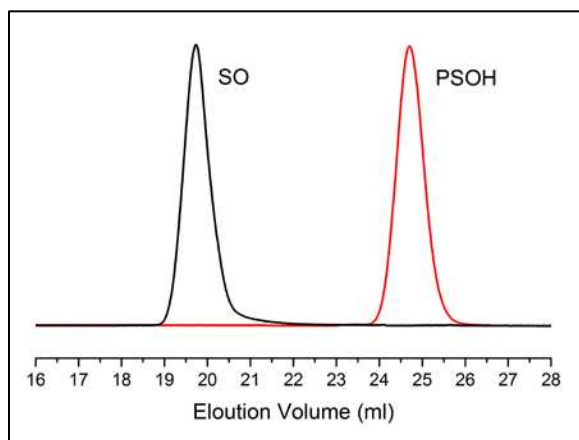


Figure S1.3 Size-exclusion chromatography chromatograms of S-OH (PS-OH) and SO.

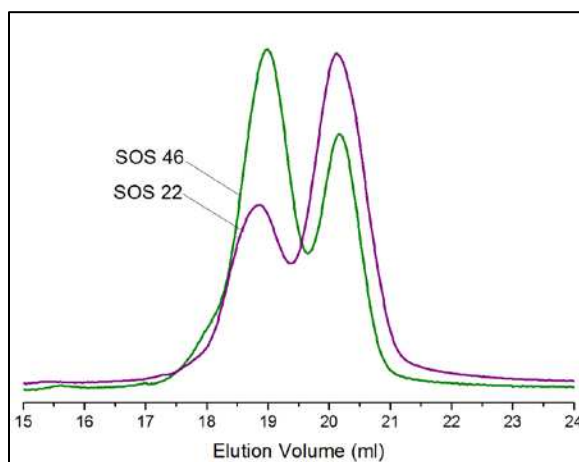


Figure S1.4 Size-exclusion chromatography chromatograms of dry polymer blends SOS22 and SOS46. Left and right peak positions correspond to the elution of SOS triblock and SO-H diblock copolymer in each blend, respectively.

S1.1.3 Stress-strain data under cyclic compressive loading

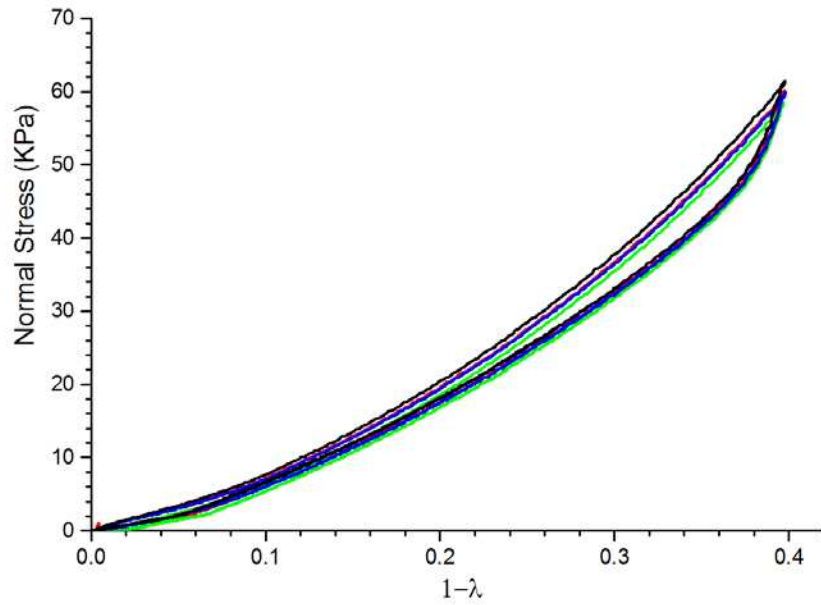


Figure S1.5 Cyclic compression loading on SOS46. Stress strain curves for the cycles 2- 9 are overlaid.

S1.1.4 ATR-IR of neat SOS46, SOS46 + [EMIM][TFSI], and neat [EMIM][TFSI]

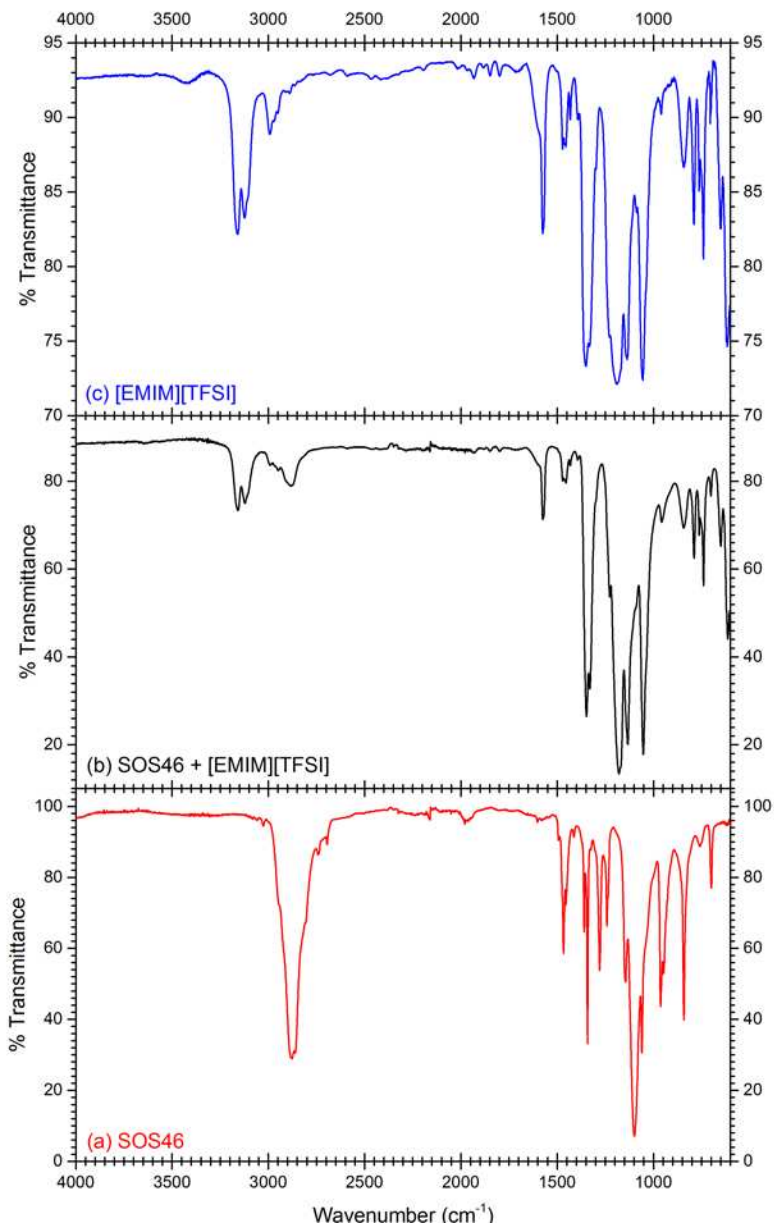


Figure S1.6 ATR-IR and FT-IR data comparing (a) dry SOS46 (ATR-IR), (b) SOS46 swollen with [EMIM][TFSI] (membrane form, ATR-IR), and (c) neat [EMIM][TFSI] (FT-IR). Compatibility of [EMIM][TFSI] with the PEO matrix may involve coordination of the polyether backbone with the cationic imidazolium, and potential hydrogen bonding of the oxygen species in the PEO backbone with the C(2)-H of the imidazolium heterocycle. The latter, in particular, would manifest as a shift in the C(2)-H stretch ($\nu_{\text{CH}} \sim 3425 \text{ cm}^{-1}$) to lower wavenumbers as described by Arduengo et al. [1] Its apparent absence in the membrane form (SOS46 + [EMIM][TFSI]) may be the consequence of hydrogen bonding with the PEO backbone, however, it is quite broad and difficult to discern a conclusive peak shift from the SOS absorption and surrounding baseline regions.

S1.1.5 Structural characterization of SOS22 and SOS46 nanoscale morphology via SAXS

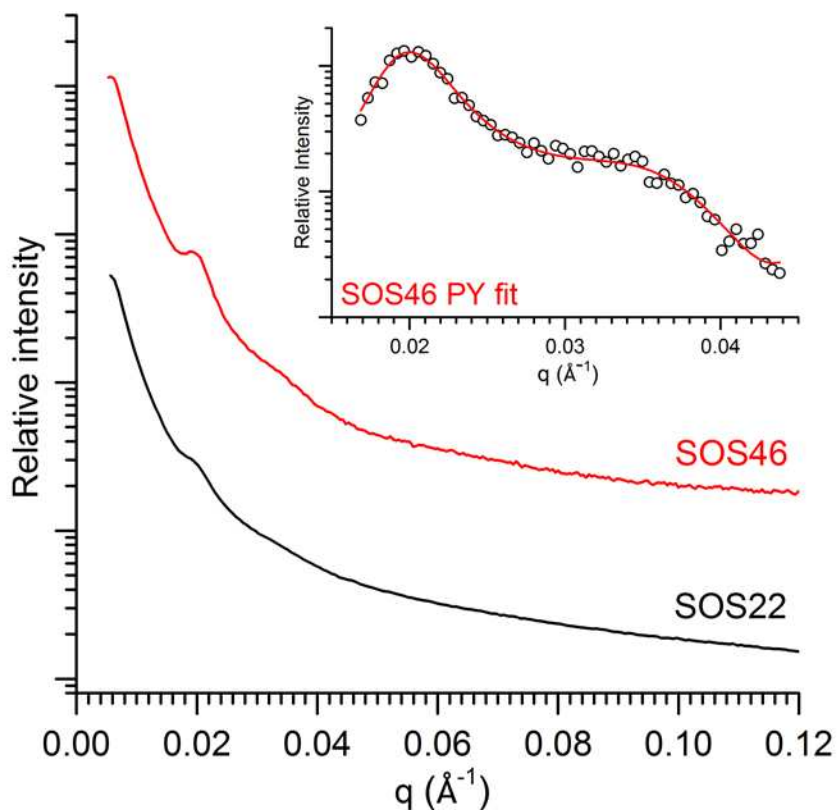


Figure S1.7 1D azimuthally integrated SAXS data for SOS22 and SOS46 in the melt at 120 °C just prior to vitrification. The primary peak and adjacent broad shoulder are typical scattering signatures for SOS blends exhibiting a liquid-like packing of spheres, as described previously by our group^[2, 3] and others^[4-8]. Fits of the SOS46 data (inset) to a Percus-Yevick hard sphere model [9] for polydisperse spheres confirms a polystyrene core radius of 10.5 nm, with an principal domain spacing of about 32 nm. While the signal contrast in the SOS22 scattering data was too weak to perform a reliable Percus-Yevick fit, the coincidence of the principal scattering peak position ($q^* = 0.020 \text{ \AA}^{-1}$) and similarity of the scattering profiles is a strong indication of the structural similarity in these two SOS blends. Such similarity is expected based on our previous experience with these types of blends (used in hydrogel applications), and is an intended byproduct of using "lattice matched" SO and SOS block copolymer compositions^[2, 3].

Table S1.8. Chemical and melt-state morphological characterization data of block copolymer blends

Sample	Tether added (mol%)	$q^*/\text{\AA}^{-1}$	d^*/nm	f_{PS}	Percus-Yevick hard sphere model				
					R_c^a/nm	ϕ_c^b	θ_{PS}^c	$R_{\text{hs}}^d/\text{nm}$	ϕ_{hs}^e
SOS22	22.0	0.0197	31.9	0.085	-	-	-	-	-
SOS46	46.0	0.0196	32.0	0.085	10.5	0.108	338	17.0	0.46

^a Micelle core radius, ^b Micelle core overall volume fraction, $\phi_c = (R_c/R_{\text{hs}})^3 \phi_{\text{hs}}$, based on the PY parameters, ^c Mean aggregation number (i.e., PS chains per sphere), based on the PY parameters, ^d apparent hard sphere radius, ^e hard sphere volume fraction.

REFERENCES

- [1] AEFERCarbene) Proton Complex - Structure of a C-H-C Hydrogen-Bond, *JACS*, 117 (1995) 572-573.
- [2] C. Guo, T.S. Bailey, Highly distensible nanostructured elastic hydrogels from AB diblock and ABA triblock copolymer melt blends, *Soft Matter*, 6 (2010) 4807-4818.
- [3] C. Guo, T.S. Bailey, Tailoring mechanical response through coronal layer overlap in tethered micelle hydrogel networks, *Soft Matter*, 11 (2015) 7345-7355.
- [4] E.E. Dormidontova, T.P. Lodge, The order-disorder transition and the disordered micelle regime in sphere-forming block copolymer melts, *Macromolecules*, 34 (2001) 9143-9155.
- [5] D.J. Kinning, E.L. Thomas, Hard-Sphere Interactions between Spherical Domains in Diblock Copolymers, *Macromolecules*, 17 (1984) 1712-1718.
- [6] M. Schwab, B. Stuhn, Thermotropic transition from a state of liquid order to a macrolattice in asymmetric diblock copolymers, *Phys. Rev. Lett.*, 76 (1996) 924-927.
- [7] M. Schwab, B. Stuhn, Asymmetric diblock copolymers - Phase behaviour and kinetics of structure formation, *Colloid. Polym. Sci.*, 275 (1997) 341-351.
- [8] X. Wang, E.E. Dormidontova, T.P. Lodge, The Order-Disorder Transition and the Disordered Micelle Regime for Poly(ethylenepropylene-b-dimethylsiloxane) Spheres, *Macromolecules*, 35 (2002) 9687-9697.
- [9] J.K. Percus, G.J. Yevick, Analysis of Classical Statistical Mechanics by Means of Collective Coordinates, *Phys. Rev.*, 110 (1958) 1-13.

ADDENDUM I

PROTOCOL FOR MEASURING AND CALCULATING THE GAS PERMEATION DATA FOR GAS SEPARATION MEMBRANES⁷

AI.1 EVALUATION OF THE GAS SEPARATION PERFORMANCE OF GAS PERMEABLE MEMBRANES

The instrumentation used for gas separation measurements included in this dissertation is a custom made apparatus fabricated by the laboratory of Rich Noble at the University of Colorado, Boulder. The key measurement made with this apparatus is the time dependent change of the transmembrane pressure as a function of time. Hence the testing device is commonly referred to as a *constant volume variable pressure (time-lag) apparatus*. Schematic diagram describing the major components of the apparatus can be found in Figure AI.1a. A photograph showing the experimental setup is also included in Figure AI.1b. The apparatus contains two cells (two volumes), one above the membrane (feed volume) and one below the membrane (permeate volume). The two volumes are physically separated by the membrane of interest (to be tested). The feed gas pressure is measured with a 0-100 psia pressure transducer and the permeate pressure with a 0-15 psia transducer. Only one gas is tested at a time.

⁷ The contents of this addendum document the procedures used to evaluate the gas separation performance of the membranes developed in Chapter 3. The evaluation was conducted using a 'time-lag apparatus' housed in Richard Noble's laboratory at University of Colorado, Boulder. The contents of this addendum are the product of a collaborative effort between Dr. Matthew Cowan (CU Boulder) and Dilanji Wijayasekara.

AI.2 DETAILED EXPERIMENTAL PROTOCOL FOR GAS PERMEABILITY MEASUREMENTS.

AI.2.1 Experiment Start Up

Prior to starting an experiment, the membrane is degassed for 3 or more hours, by exposing the membrane to vacuum via permeate side, until no pressure rise is observed when the permeate volume is closed. All valves on the time-lag apparatus are then closed. The feed volume is split in to two volumes with one valve just above the membrane cell. Then the top portion of the feed volume is backfilled 6 times with the experimental gas prior to starting the experiment. At this point, pressure and temperature data collection is started at time increments of one second with feed to the membrane still closed (perfect sealing of the membrane holder and full degassing of the membrane are indicated by no recorded pressure changes).

The top portion of the membrane is then exposed to the experimental gas by opening the secondary feed valve. Depending on whether the 0-100 psia pressure transducer is above or below the secondary dose valve, the start of the experiment is signaled by a pressure drop or rise, respectively. Data is collected every 1 to 10 seconds for the first 1-3 minutes, depending on how permeable the gas is (e.g., 1s for very permeable gases). After that point, data can be collected every 10 to 60 seconds, again depending on how permeable the gas is.

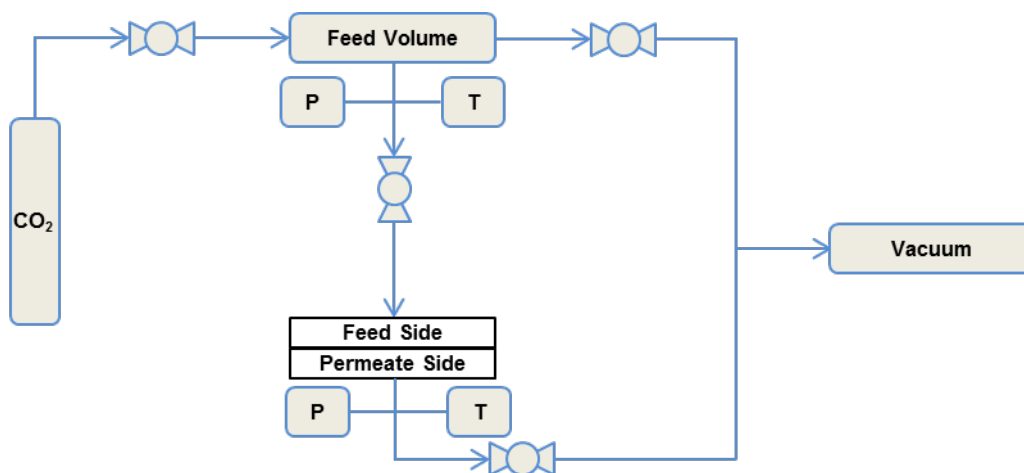


Figure AI.1a. Schematic of the ‘time-lag’ apparatus used for gas permeation measurements.

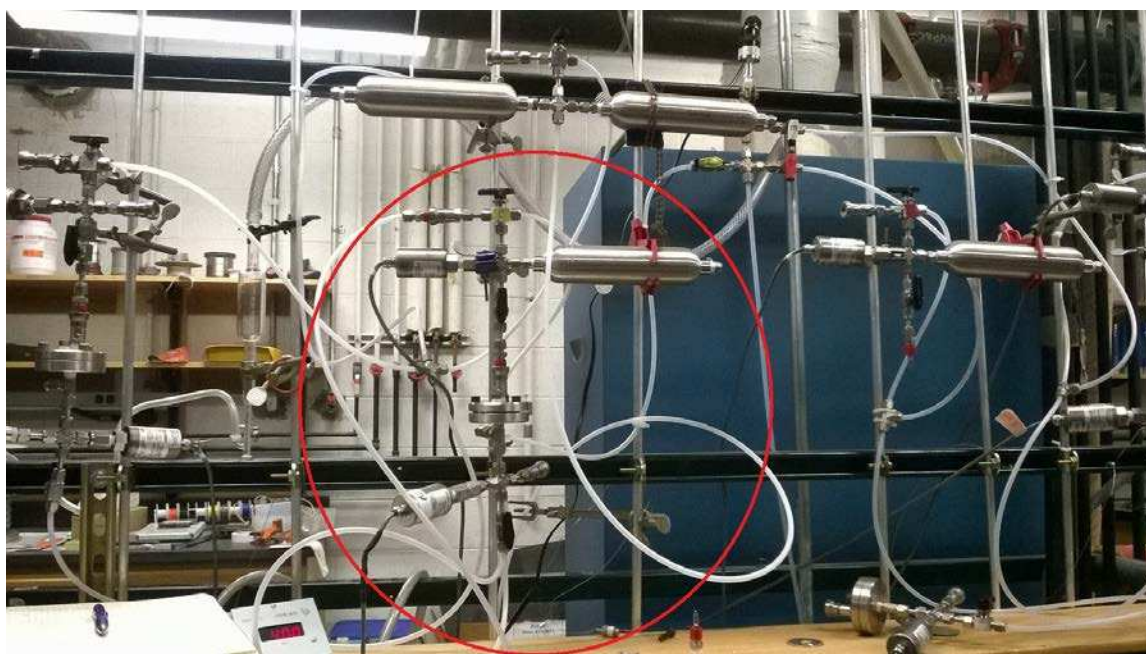


Figure AI.1b ‘time-lag’ apparatus used for gas permeation measurements.

AI.2.2 Experiment Shut down

The data collection time varies from membrane to membrane, depending on the permeability. For very permeable membranes, the end of the experiment is clearly indicated by a decay of the permeate pressure vs. time curve that we observe in the Labview window. In other words, it is clearly evident that the linear portion of the curve (i.e., steady-state flux) has already been obtained. The decay of flux occurs because of the reduced driving force across the membrane as the permeate pressure rises. When the end of an experiment is not clearly evident (often the case with N₂), we will run the very first experiment for a sufficient amount of time (3-4 h) to obtain steady-state data. After analysis of the data in Excel (see below), we can determine when the steady-state portion of the data occurs and how long to let the next experiment run. An experiment is terminated by opening the permeate volume to vacuum, followed by gradually opening the feed volume to vacuum. The membrane should be degassed for a sufficient amount of time prior to performing the next gas permeability testing.

AI.2.3 Calculation of permeability

Permeability of the test gas for a particular membrane is calculated using the ideal gas law, hence several parameters must first be known. These include the permeate volume (V_p), membrane thickness (l), membrane surface area (A), experimental gas temperature (T), and the transmembrane pressure drop (ΔP). The permeate volume is measured by calibrating the apparatus with a known volume. The membrane surface area is constant from experiment to experiment and was initially measured with micrometer. We base this area on the “active

portion” of the membrane, which is exposed to the feed gas and is encircled by an O-ring. The membrane thickness is measured with optical profilometer after experimentation is completed. The experimental temperature is measured with a temperature sensor that is plumbed into the feed volume and the transmembrane pressure drop is taken as the difference in pressure between the feed and permeate volumes.

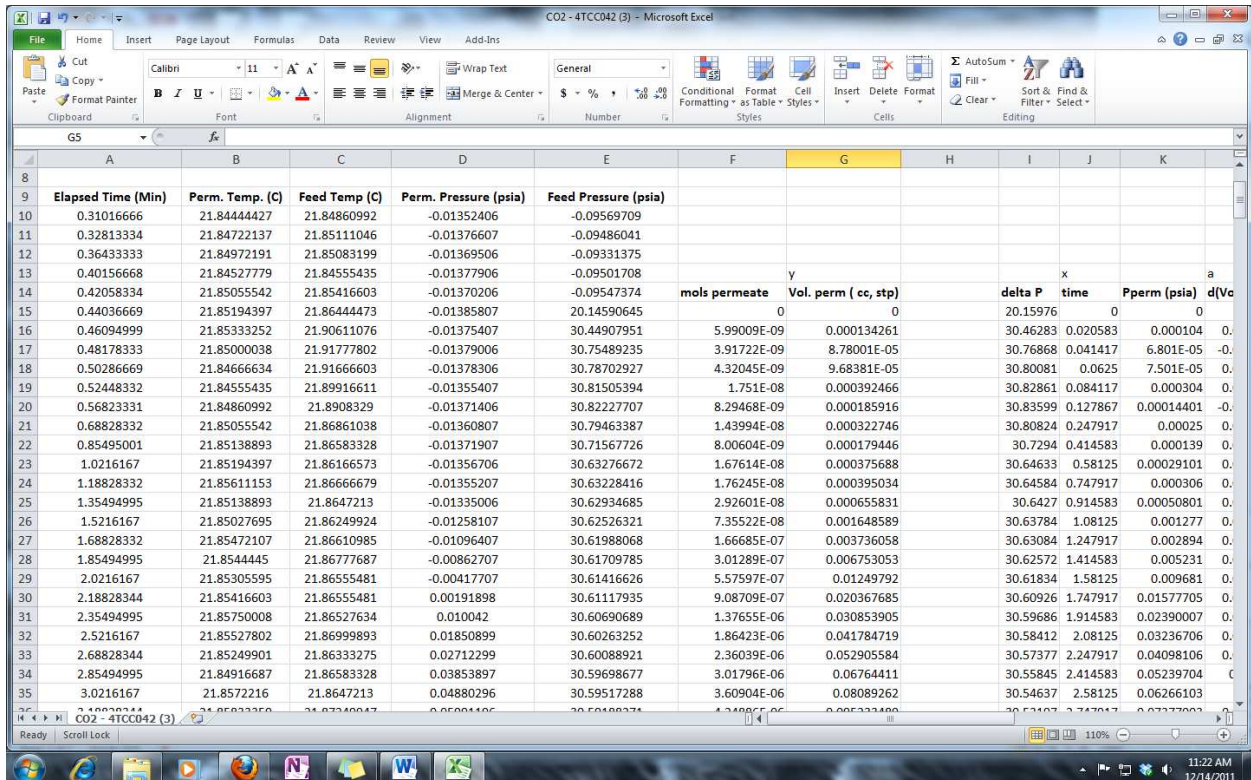


Figure AI.2 Example of Excel spreadsheet with raw data collected from the setup and calculated moles and gas volume (STP) in the permeate volume.

The following section explains systematic processing of raw data to derive the permeability. MS Excel is the software tool utilized for data analysis. The raw data from Labview is shown in columns A-E (Figure AI.2). As seen in column E, row 15, a sudden rise in feed pressure demarks the beginning of the experiment (when the secondary feed valve was

opened). From this point down in the spreadsheet we begin our calculations and set this time as time zero.

We first calculate the number of accumulated moles of gas in the permeate column using the ideal gas law with the measured temperature (column C), permeate pressure (column D) and the known permeate volume using the equation **1**.

$$\text{Moles} = \frac{(P_{p,t} - P_{p,0})V_{perm}}{RT_t} \quad \mathbf{1}$$

Where, $P_{p,t}$ is the permeate pressure at each time (t), $P_{p,0}$ is the initial permeate pressure, V_{perm} is the permeate volume, R is the ideal gas constant, and T_t is the temperature at each time(t). We then calculate the volume of permeate at standard temperature and pressure (STP) using equation **2**.

$$\text{Vol [cc,STP]} = 22400 \times \text{Moles} \quad \mathbf{2}$$

This is based on 1 mole of gas at STP being equal to 22400 cc. In columns I and J we have calculated the transmembrane pressure drop (feed pressure minus permeate pressure) and the experimental time in minutes, respectively. The transmembrane pressure drop will come into play later when we make our final permeability calculation. First we must determine the linear, or steady-state, region in the plot of permeate gas volume vs. time data.

There are two ways to determine the steady-state linear region of the data. The first is to plot the first derivative of the accumulated permeate volume (V_p) vs. time (i.e., $d(V_p)/dt$ vs. t), and determine the region of the curve where the flux ($d(V_p)/dt$) reaches a maximum value and the time frame over which the flux is constant. The first derivative is calculated by taking the average instantaneous slope at each point of the V_p vs. time curve. Three consecutive data points are used to calculate the average slope (i.e., tangent) of the middle data point (point 2) (e.g.,

slope between points 1 and 2, and the slope between points 2 and 3 are averaged for instantaneous slope of point 2). The first derivative is shown in Figure AI.3, column L of the spreadsheet. The first derivative is plotted vs. time in Figure AI.4. The points shown in red are the data determined to be steady-state data. The flux, marked by the red data points, represents a maximum and constant value for this experiment. Before the data shown red, the flux had not reached a maximum, steady value. After the data shown in red, the flux begins to decay due to a decrease in driving force.

	E	F	G	H	I	J	K	L	M	N	O
11	-0.09486041										
12	-0.09331375										
13	-0.09501708										
14	-0.09547374	mols permeate	Vol. perm (cc, stp)		delta P	time	Pperm (psia)	d(Vol)/dt	Inst. Intercept	time lag (s)	
15	20.14590645	0	0		20.15976	0	0	0.002146344	9.00823E-05	-2.518208028	
16	30.44907951	5.99009E-09	0.000134261		30.46283	0.020583	0.000104	0.002146344	9.00823E-05	-2.518208028	
17	30.75489235	3.91722E-09	8.78001E-05		30.76868	0.041417	6.801E-05	-0.000900727	0.000125105	8.333612678	
18	30.78702927	4.32045E-09	9.68381E-05		30.80081	0.0625	7.501E-05	0.007052317	-0.000343932	2.926117018	
19	30.81505394	1.751E-08	0.000392466		30.82861	0.084117	0.000304	0.004477403	1.5842E-05	-0.21229261	
20	30.82227707	8.29468E-09	0.000185916		30.83599	0.127867	0.00014401	-0.001790685	0.000414885	13.90143488	
21	30.79463387	1.43994E-08	0.000322746		30.80824	0.247917	0.00025	0.000139989	0.000288041	-123.4555196	
22	30.71567726	8.00604E-09	0.000179446		30.7294	0.414583	0.000139	0.000158825	0.0001136	-42.91542731	
23	30.63276672	1.67614E-08	0.000375688		30.64633	0.58125	0.00029101	0.000646763	-2.43002E-07	0.022543277	
24	30.63228416	1.76245E-08	0.000395034		30.64584	0.747917	0.000306	0.000840431	-0.000233538	16.67276179	
25	30.62934685	2.92601E-08	0.000655831		30.6427	0.914583	0.00050801	0.003760665	-0.00278361	44.41145087	
26	30.62526321	7.35522E-08	0.001648589		30.63784	1.08125	0.001277	0.009240679	-0.008342895	54.17066175	
27	30.61988068	1.66685E-07	0.003736058		30.63084	1.247917	0.002894	0.015313396	-0.015373783	60.23660739	
28	30.61709785	3.01289E-07	0.006753053		30.62572	1.414583	0.005231	0.026285579	-0.030430086	69.46033785	
29	30.61416626	5.57597E-07	0.01249792		30.61834	1.58125	0.009681	0.040843876	-0.05208646	76.515451	
30	30.61117935	9.08709E-07	0.020367685		30.60926	1.747917	0.01577705	0.055067975	-0.075886551	82.68313924	
31	30.60690689	1.37655E-06	0.030853905		30.59686	1.914583	0.02390007	0.064251115	-0.092160204	86.06251055	
32	30.60263252	1.86423E-06	0.041784719		30.58412	2.08125	0.03236706	0.066155006	-0.095900389	86.97789677	
33	30.60088921	2.36039E-06	0.052905584		30.57377	2.247917	0.04098106	0.077578198	-0.121483747	93.95712975	
34	30.59698677	3.01796E-06	0.06764411		30.55845	2.414583	0.05239704	0.08396113	-0.135087029	96.53540584	
35	30.59517288	3.60904E-06	0.08089262		30.54637	2.58125	0.06266103	0.0827681	-0.132752538	96.2345676	
36	30.59188271	4.24886E-06	0.095233489		30.53197	2.747917	0.07377003	0.094717973	-0.165043617	104.5484467	
37	30.58723259	5.01766E-06	0.112465268		30.51397	2.914583	0.08711701	0.099290411	-0.176924903	106.9135884	
38	30.58650589	5.72548E-06	0.128330285		30.50096	3.08125	0.099407	0.102712887	-0.188153801	109.9105315	

Figure AI.3 Calculation of the first derivative of the permeate volume vs. time data (d(Vp)/dt) and the instantaneous time lag.

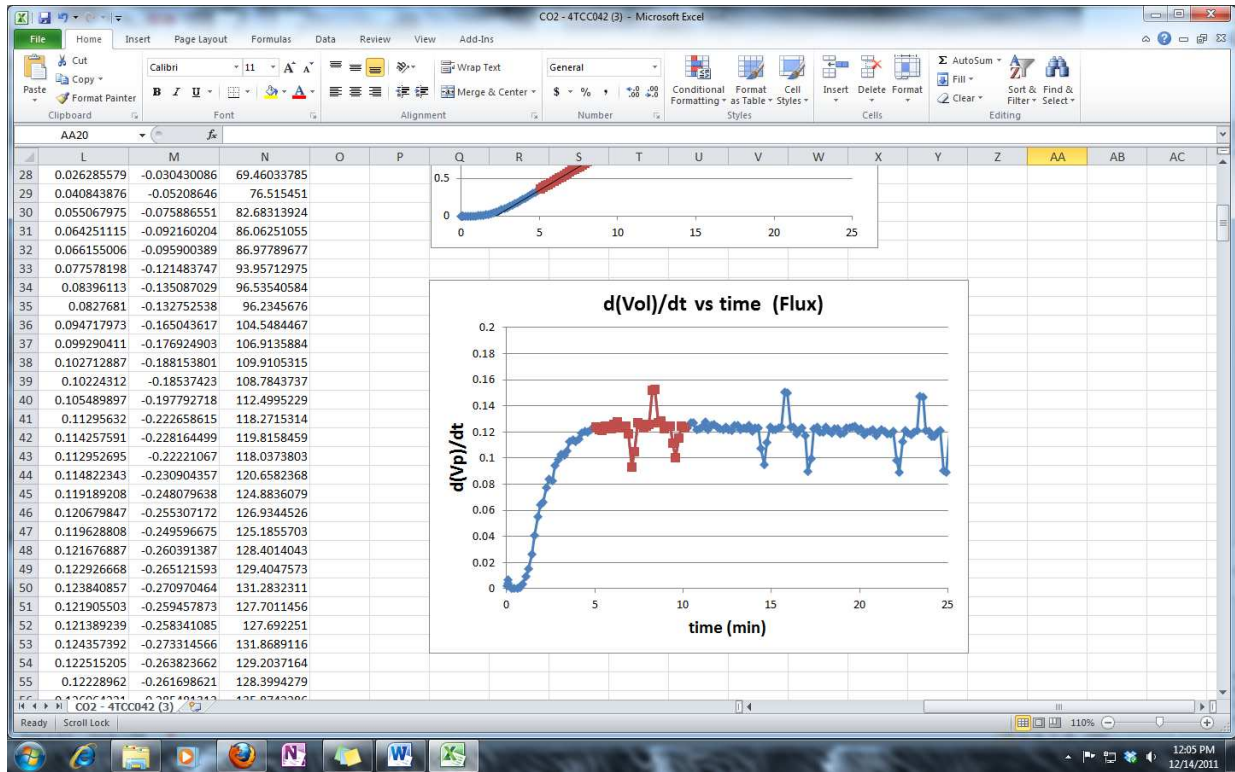


Figure AI.4 Plot of $d(V_p)/dt$ vs. t and the determination of “steady-state” flux, shown as red data points.

Now that we know the time frame over which steady-state flux occurs, we can calculate an average steady-state flux and time lag. In Figure AI.5, we have plotted the accumulated permeate volume vs. time. The steady-state portion of this data is shown in red. To calculate an average flux we fit a linear trend line to the steady-state data and obtain an expression for the steady-state volume change with time (Figure AI.5). For example, in Figure AI.5, the value of 0.1236 for the slope is the steady volume flow rate in cc(STP)/min. Notice that this value corresponds to the constant value of $d(V_p)/dt$ achieved in Figure AI.4 over the steady-state period. To obtain the flux, simply divide the slope by the known membrane “active” surface area. Calculation of membrane permeability is relatively simple at this point using equation 3.

$$\text{Permeability} = \frac{\text{Flux} \times l}{\Delta P} \quad 3$$

The membrane thickness (l) is known by measurement with optical profilometer. The average transmembrane pressure drop (ΔP) is determined by the pressure drop (Figure 3, column I) over the steady-state time period. To obtain the permeability in barrers, the units of time must be converted to seconds, pressure units must be converted to cmHg, and length units must be converted to cm.

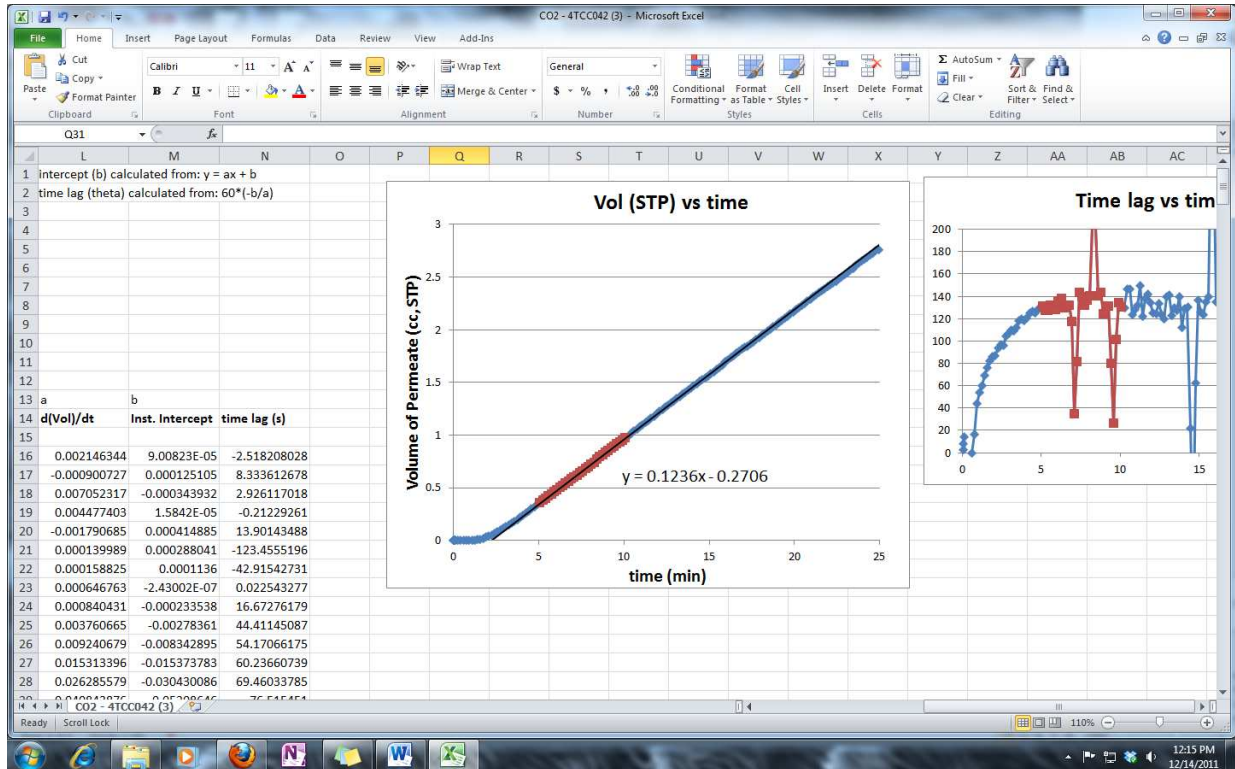


Figure AI.5 Permeate volume vs. time and determination of steady-state flux and time lag.

Knowing the equation of the trend line (Figure AI.5), we can also calculate the diffusivity of a particular gas by equation 4.

$$D = \frac{l^2}{6\theta} \quad 4$$

Here, l is membrane thickness and θ is the time-lag, which corresponds to the x-axis intercept of the trend line.

As mentioned above, there is a second method to determine the steady-state region of data. It is more of a secondary measure to confirm the first derivative method described above. As the flux, or slope of the data in Figure AI.5, increases with experimental time, so will the time lag (θ) at any instantaneous point of the data. In other words, if we were to fit a linear trend line for each data point as the experiment moves along, the slope of those trend lines would steadily increase and eventually reach a maximum, which means the time lag would also reach a maximum. Once the flux begins to decay after the steady-state region (Figure AI.4), the time lag calculated from the slope of an instantaneous point would steadily decrease with time. Just as we determined the time period where the flux reached a maximum in the first method, we must determine the time period over which the time-lag reaches a constant value in this second method. The time period for both should always be the same.

Calculating the instantaneous time lag at a given point is relatively simple since we already determined the instantaneous slope of each time point on the V_p vs. time curve. We can then use the point-slope formula to determine the intercept (i.e., instantaneous time lag) associated with each tangent (e.g., $b = y - mx$, with y (V_p), x (t) and m $d(V_p)/dt$ known). The instantaneous time lag calculated in this manner can be found in column N of the spreadsheet, as shown in Figure AI.3. The instantaneous time lag vs. time is plotted in Figure AI.6.

The time region when the instantaneous time lag reaches a maximum, constant value, corresponds to steady-state region. These data are shown in red in Figure AI.6. As mentioned above, this region should agree with the steady-state time region determined from the first derivative method.

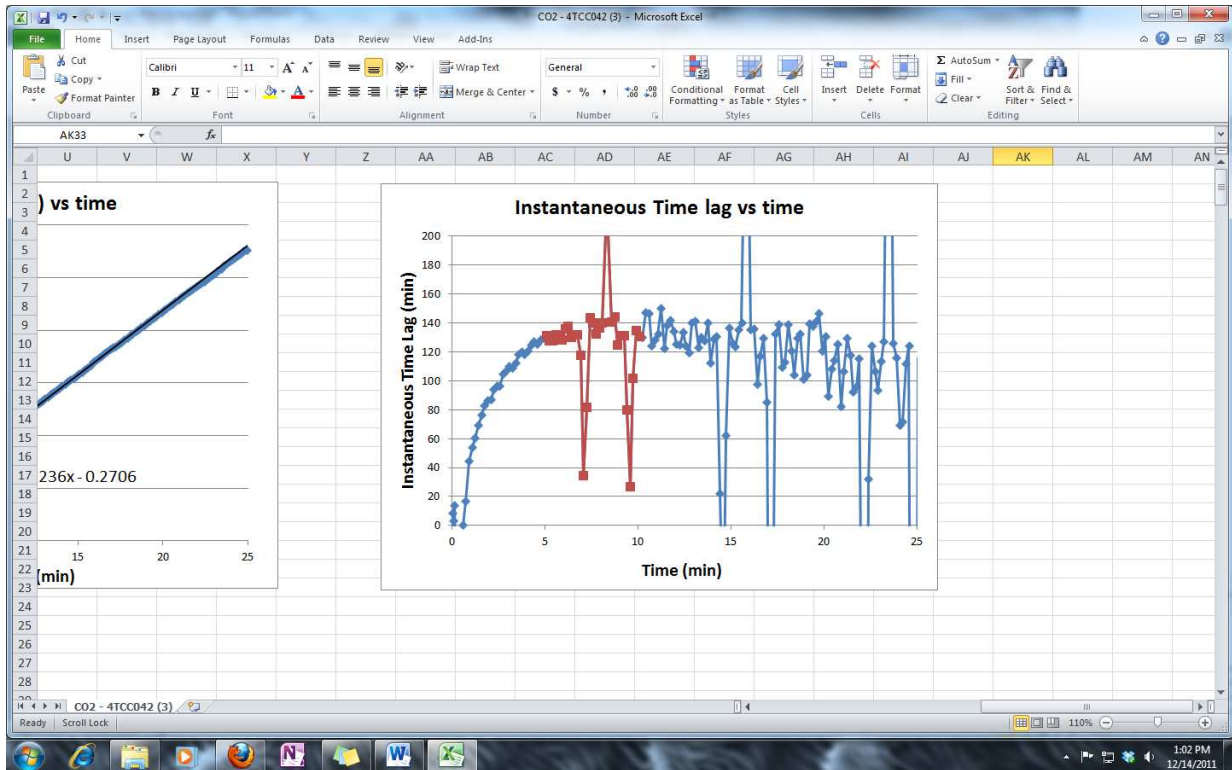


Figure A1.6 Instantaneous time lag vs. time and determination of the steady-state time region.

ADDENDUM II

TO

CHAPTER 4⁸

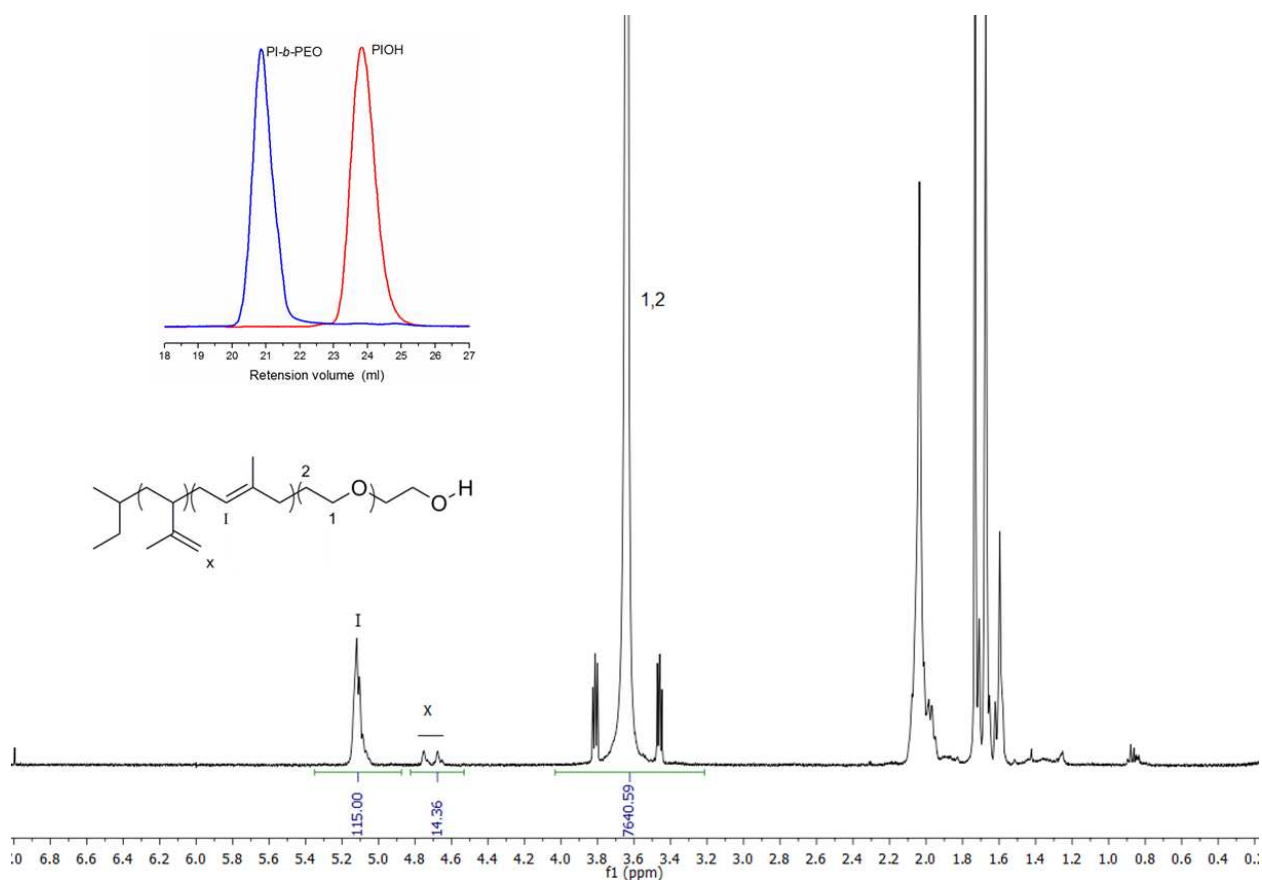


Figure AII.1 ¹H NMR and SEC data for the block copolymer IO initiated from I-OH. Molecular weight of the diblock copolymer was calculated by comparing the vinyl protons on isoprene units to the four-methyl protons on an EO unit. $Mw_{IO} = [\text{Int}(x)/2 + \text{Int}(I)] * 68.01 + \text{Int}(1,2) * 44.05 \text{ g/mol}$

⁸ This addendum contains ¹H NMRs of the base materials IOI, e₂₂IOI25, e_{85.4}IOI46 mentioned in Chapter 4. The ¹H NMRs were used to calculate the molecular weight of IOI and the degree of epoxidation of IOI25 and eIOI46.

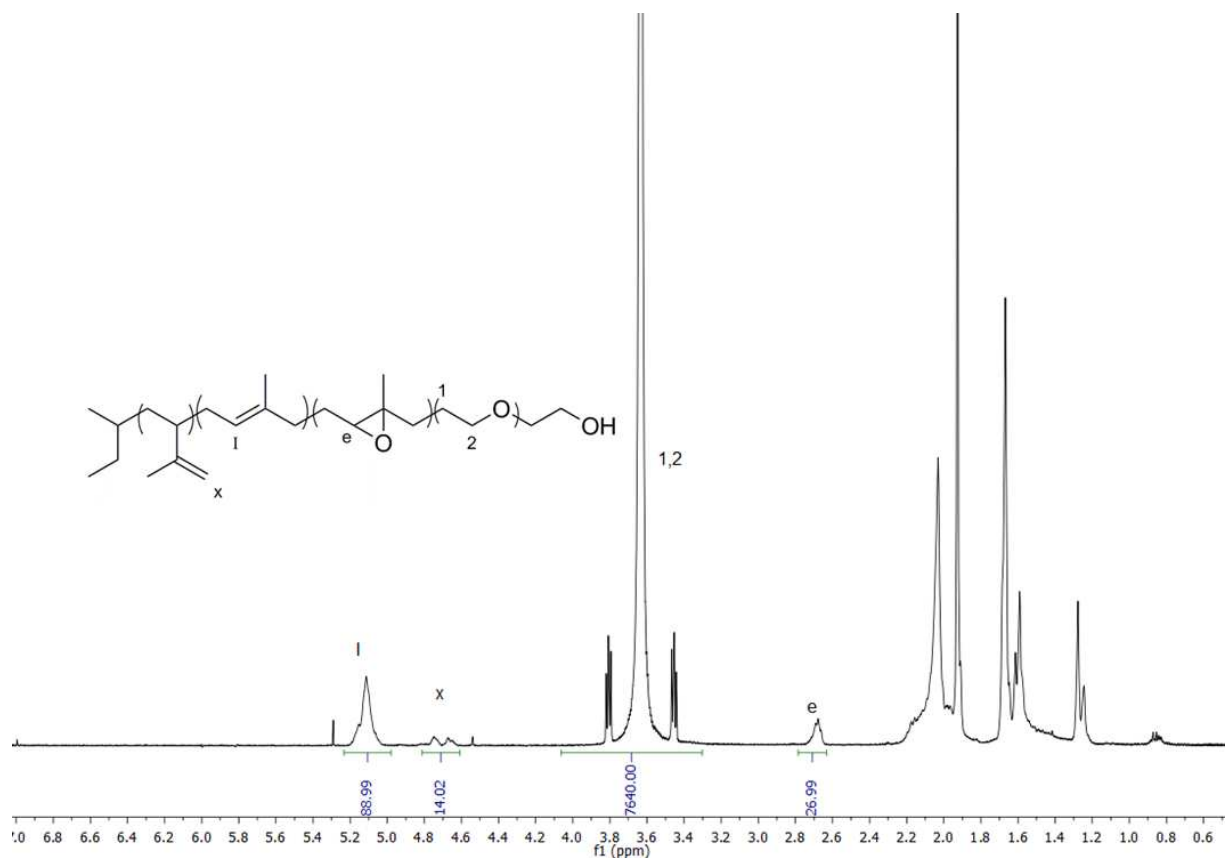


Figure AII.2 ¹H NMR of e₂₂IOI₂₅. The percentage of epoxidation was calculated by comparing the peak integrals corresponding to methyne proton in the oxirane ring in epoxidized PI repeat units (**e**) with the residual vinyl protons left in the unmodified PI repeat units (**I**, **x**). ($= \text{Int}(\mathbf{e}) / [\text{Int}(\mathbf{e}) + \text{Int}(\mathbf{I}) + \text{Int}(\mathbf{x})/2]$)

pat-ePI46_80_TB1_PROTON_01
pat-ePI46_80_TB1

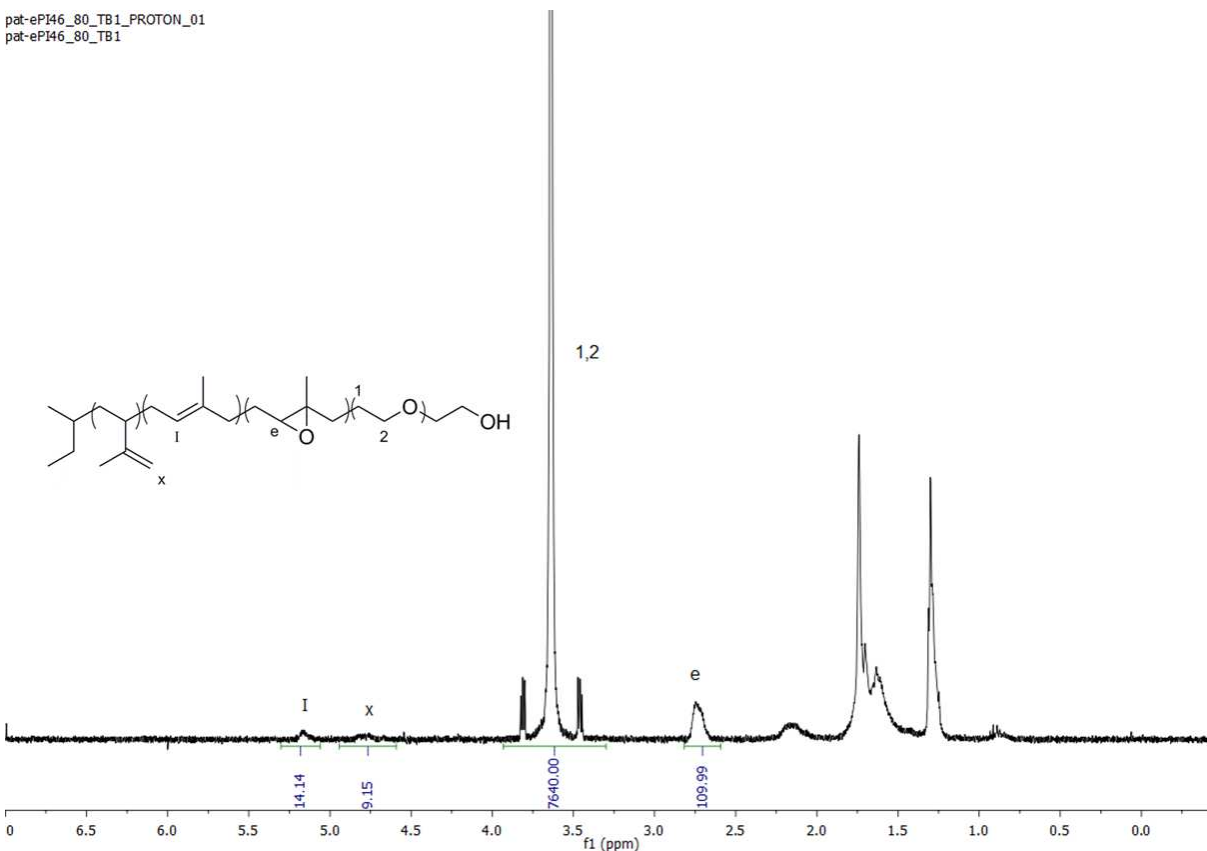


Figure AII.3. ¹H NMR of e_{85.4}IOI46. The percentage of epoxidation was calculated by comparing the peak integrals corresponding to methyne proton in the oxirane ring in epoxidized PI repeat units (**e**) with the residual vinyl protons left in the unmodified PI repeat units (**I**, **x**). ($= \text{Int}(\mathbf{e}) / [\text{Int}(\mathbf{e}) + \text{Int}(\mathbf{I}) + \text{Int}(\mathbf{x})/2]$)

ADDENDUM III

TO

CHAPTER 5⁹

ω-Hydroxy-polystyrene (PS-OH)

Styrene (99%, 4-tert-butylcatechol inhibitor, Aldrich) and ethylene oxide (99.5+%, compressed gas, Aldrich) monomer were each purified by successive distillations (10–20 mTorr) from dried dibutylmagnesium (1.0 M solution in heptane, Aldrich) before use. Both purified styrene and ethylene oxide monomer were stored in glass burettes wrapped in foil, at room temperature (styrene) and 0°C (ethylene oxide), respectively. Argon degassed cyclohexane (CHX) was purified by passing the solvent over activated alumina followed by Q-5-like supported copper catalyst (Glass Contour, proprietary). Argon degassed tetrahydrofuran (THF) was purified by passing the solvent over activated alumina.

Purified styrene monomer (120.0 g, 1.14 mol, 20°C) was added under argon (3 psig) to a stirring solution of sec-butyl lithium (10.23 mL, 1.3M in cyclohexane, Aldrich) and dry, air-free cyclohexane (1L, 20°C) in a 2 L reaction vessel. The temperature of the reaction mixture was raised to 40°C and stirred continuously for approximately 8 hrs. At this point the reactor pressure was reduced to approximately 1 psig and purified ethylene oxide (6.6g, 0.15 mol, 0°C, liquid)

⁹ This addendum contains the experimental procedure used for the synthesis of PSOH, which was used as a macroinitiator for many of the polymerizations mentioned in the main text.

In addition, ¹H NMR of EEGE (distilled using the typical vacuum distillation set up) is also included to allow for the comparison with the ¹H NMR of EEGE distilled with the short arm set up discussed in the main text.

¹H NMR of a contaminated PIOH also included for the information of future users. The resonance related to the contamination is identified in the ¹H NMR.

was added to the reaction vessel. The reaction was maintained at 40°C for an additional 24 hours, after which all excess ethylene oxide was purged from the reactor under a constant argon flow. The reaction was terminated by direct addition of methanol (50 mL). The polymer was precipitated in methanol (5 L total) to give a fluffy white solid. The polymer was dried under vacuum at room temperature over a 48 h period (yield 116 g, 97%).

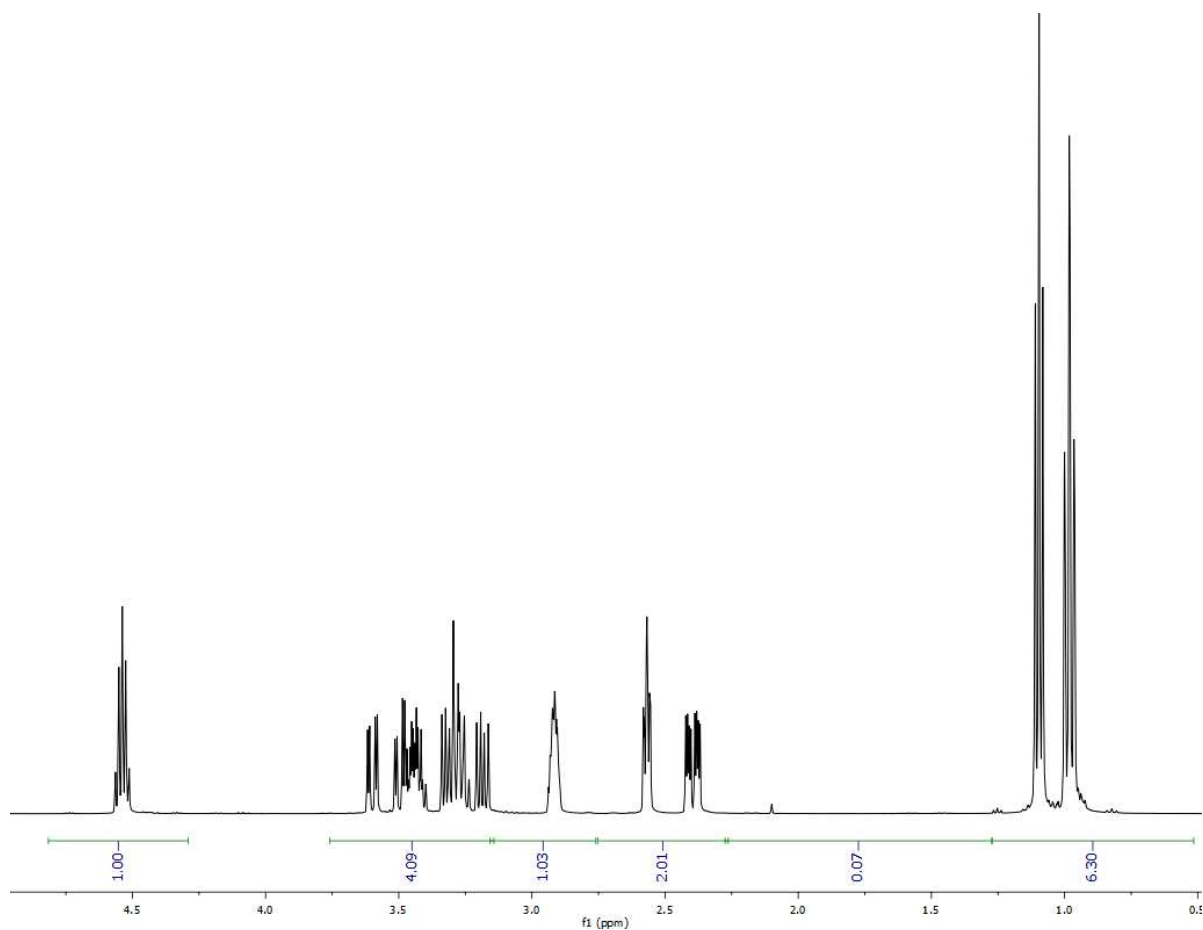


Figure A1. ^1H NMR of EEGE monomer without further purification (distilled without using short path distillation set up).

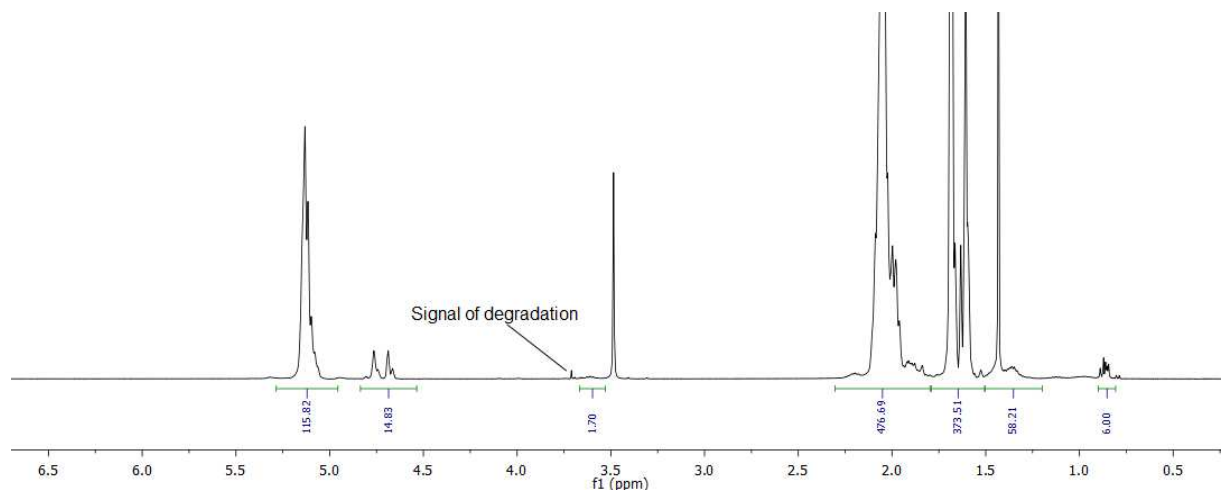


Figure A2: ^1H NMR of a partially degraded PIOH macro-initiator. The spectra differs from pristine PIOH by a the small resonance appearing at 3.7 ppm.

The signal at 3.7 ppm is not characteristic to the PIOH and may be associated with the change in molecular weight distribution observed in this system. The integral at 3.6 ppm corresponds to the two methyl protons adjacent to terminal hydroxyl. Since the spectra are normalized such that it represent an average single PIOH chain, the integral should reflect the number of protons on carbon **1**, which is two. In this case, the integral is only 1.7 , which implies a modification of nearly 15% of the terminal hydroxyl units (according to this ^1H NMR).

SUPPORTING INFORMATION II

THE ROLE OF ARCHITECTURE IN THE MELT-STATE SELF ASSEMBLY OF (POLYSTYRENE)_{star}-b-P(ISOPRENE)linear-b(POLYSTYRENE)_{star} POM-POM TRIBLOCK COPOLYMERS¹⁰

S2.1 CHEMICAL CHARACTERIZATION OF ALL 18 SNISN POM-POM TRIBLOCK COPOLYMERS

Table S2.1 Chemical characterization data

Sample	$M_{n,star}^a$ [g mol ⁻¹]	n_{arms}^b ($M_{n,arms}^a$) ^a [g mol ⁻¹]	PDI_{star}^a (PDI_{arm}^a) ^a	w_{PI}^c ($w_{PI,feed}$)	f_{PI}^d	dn/dc^e [mL g ⁻¹]	M_n^a (M_n) ^f [g mol ⁻¹]	PDI^g
TPE01	16,500	7.1 (2,160)	1.20 (1.02)	0.69 (0.70)	0.72	0.141	73,600 (106,000)	1.06
TPE02	16,500	7.1 (2,160)	1.20 (1.02)	0.77 (0.75)	0.80	0.133	89,800 (143,000)	1.07
TPE03 (B7)	16,500	7.1 (2,160)	1.20 (1.02)	0.81 (0.80)	0.83	0.131	105,000 (174,000)	1.07
TPE04	16,500	7.1 (2,160)	1.20 (1.02)	0.86 (0.85)	0.88	0.128	138,000 (236,000)	1.06
TPE05	14,300	4.1 (3,300)	1.08 (1.02)	0.69 (0.70)	0.72	0.141	73,500 (92,300)	1.07

¹⁰ Supporting information includes the chemical characterization of all 18 S_nIS_n pom-pom triblock copolymers (S2.1), GPC-MALLS of selected S_nIS_n pom-pom triblock copolymers and precursor molecules (S2.2), and additional AFM images for 17 of the 18 S_nIS_n pom-pom triblock copolymers synthesized (S2.3).

TPE06 (C4)	14,300	4.1 (3,300)	1.08 (1.02)	0.75 (0.75)	0.78	0.136	92,000 (114,000)	1.06
TPE07 (B4)	14,300	4.1 (3,300)	1.08 (1.02)	0.80 (0.80)	0.82	0.132	107,000 (143,000)	1.04
TPE08 (A4)	14,300	4.1 (3,300)	1.08 (1.02)	0.87 (0.85)	0.89	0.127	158,000 (220,000)	1.06
TPE09	15,500	2.9 (5,400)	¹ .30 (1.01)	0.71 (0.70)	0.74	0.139	102,000 (107,000)	1.03
TPE10	15,500	2.9 (5,400)	1.30 (1.01)	0.75 (0.75)	0.78	0.136	113,000 (124,000)	1.03
TPE11 (B3)	15,500	2.9 (5,400)	1.30 (1.01)	0.80 (0.80)	0.82	0.132	132,000 (155,000)	1.02
TPE12	15,500	2.9 (5,400)	1.30 (1.01)	0.84 (0.85)	0.86	0.129	160,000 (194,000)	1.04
TPE13	10,600	4.5 (2,200)	1.20 (1.05)	0.56 (0.60)	0.60	0.150	34,600 (48,200)	1.10
TPE14	10,600	4.5 (2,200)	1.20 (1.05)	0.69 (0.70)	0.72	0.141	50,000 (68,400)	1.03
TPE15	10,600	4.5 (2,200)	1.20 (1.05)	0.81 (0.80)	0.83	0.131	74,200 (112,000)	1.03
TPE16	15,600	3.9 (3,890)	1.23 (1.01)	0.57 (0.60)	0.61	0.150	59,500 (72,600)	1.04
TPE17	15,600	3.9 (3,890)	1.23 (1.01)	0.69 (0.70)	0.72	0.141	76,700 (101,000)	1.03
TPE18	15,600	3.9 (3,890)	1.23 (1.01)	0.81 (0.80)	0.83	0.131	115,000 (164,000)	1.03

^acalculated from GPC-MALLS; ^bcalculated from $M_{n,star} = nM_{n,arm} + (n-1)M_{DMSS}$; ^ccalculated from ¹H NMR of fractionated product; ^d volume fraction of PI calculated using nominal densities at 140°C¹; ^ecalculated based on the summation of the products of the dn/dc of each block times its weight fraction; ^fcalculated from $M_{n,star}$ in combination with ¹H NMR of final product.

S2.2 GPC-MALLS OF SELECTED SNISN POM-POM TRIBLOCK COPOLYMERS AND PRECURSOR MOLECULES

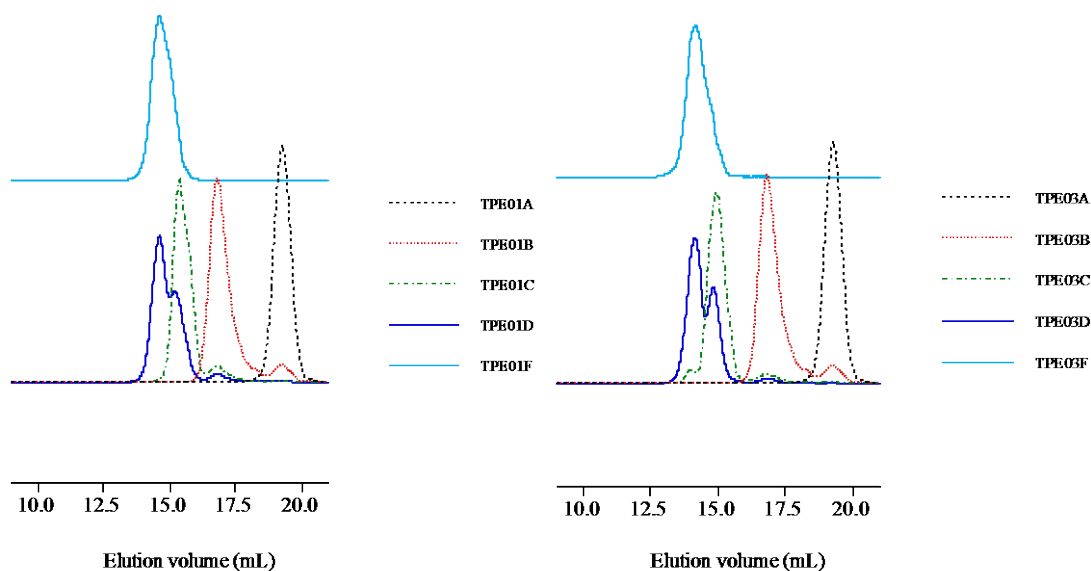
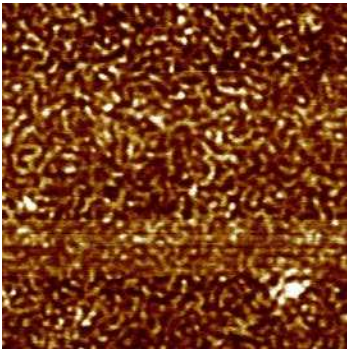
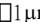
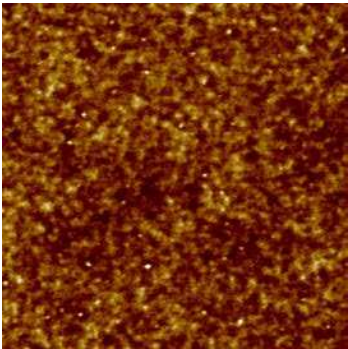
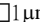
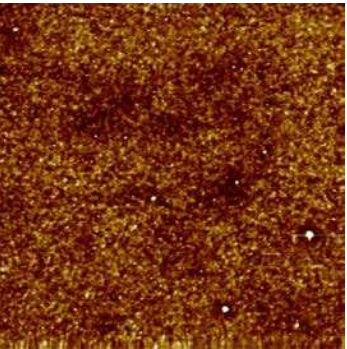
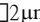
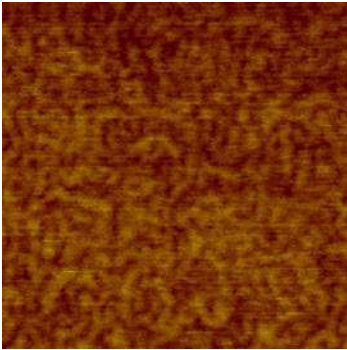
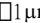
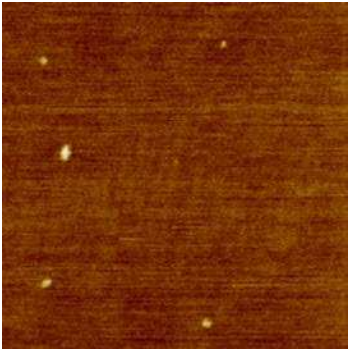
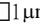
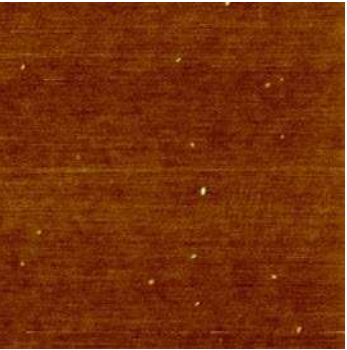
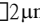
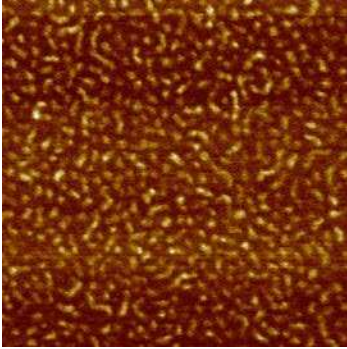
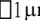
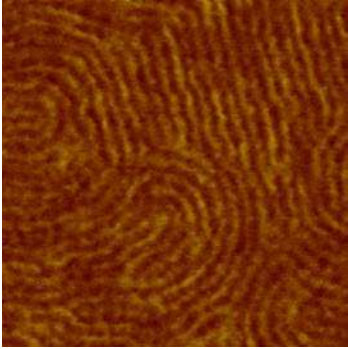
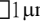
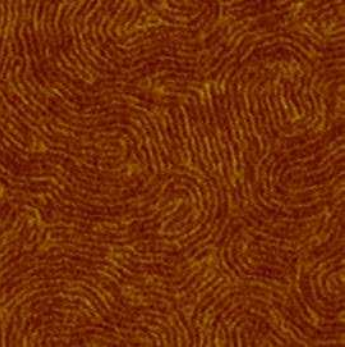
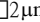
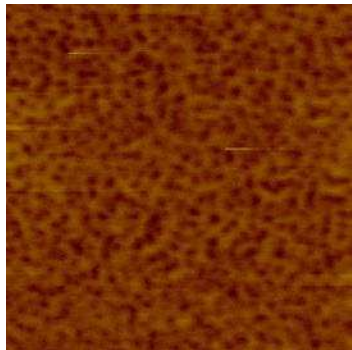
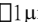
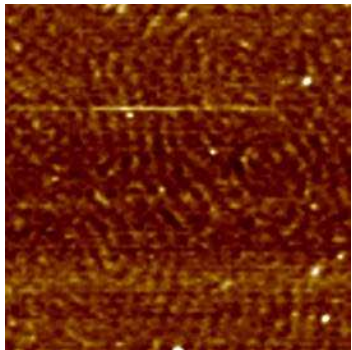
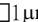
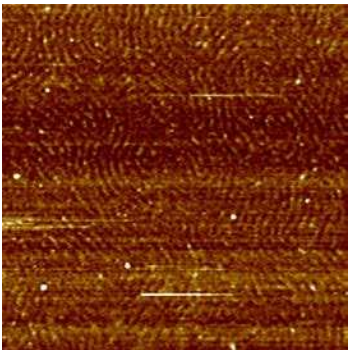
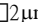
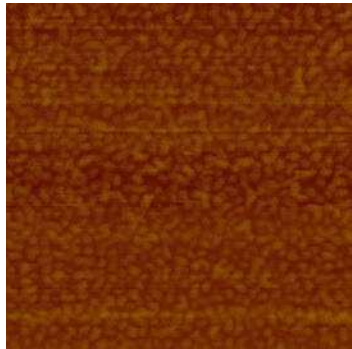
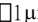
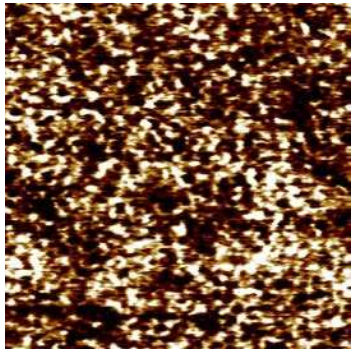
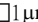
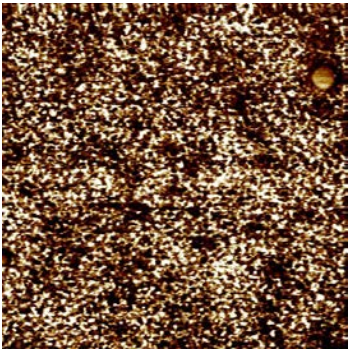
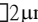
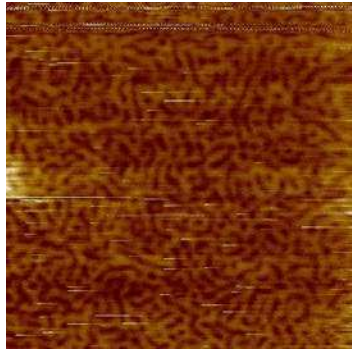
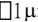
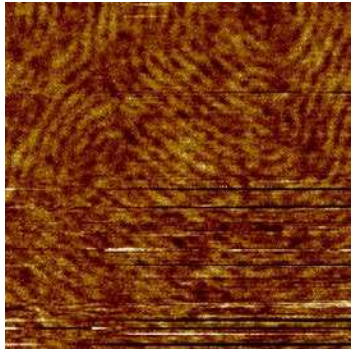
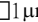
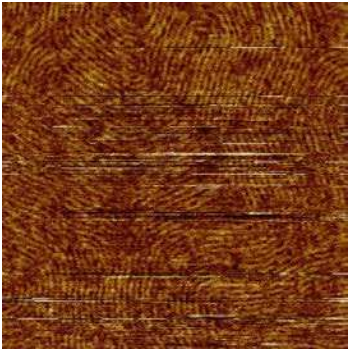
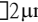
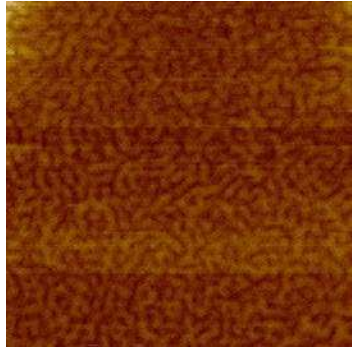
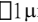
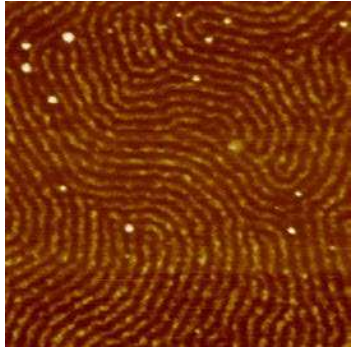
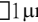
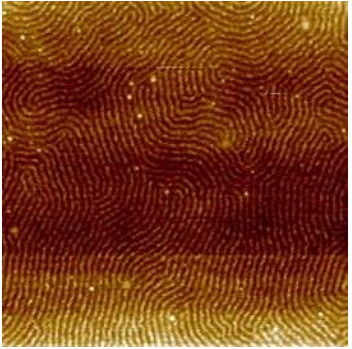
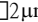


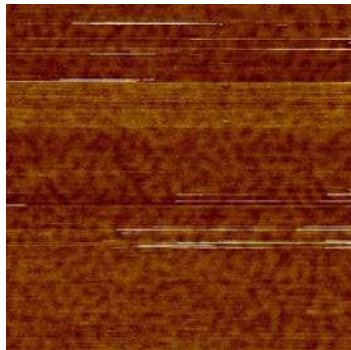
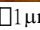
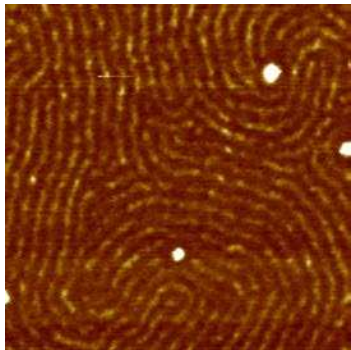
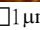
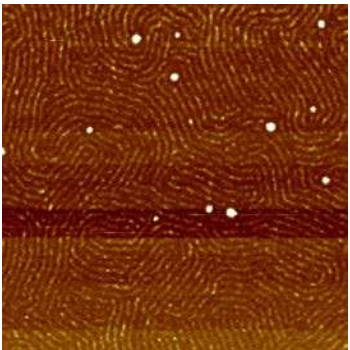
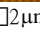
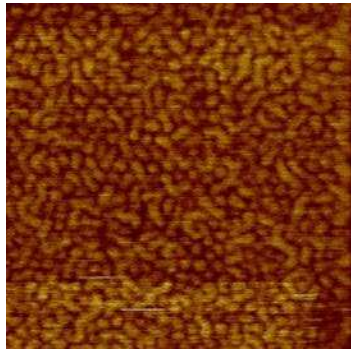
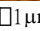
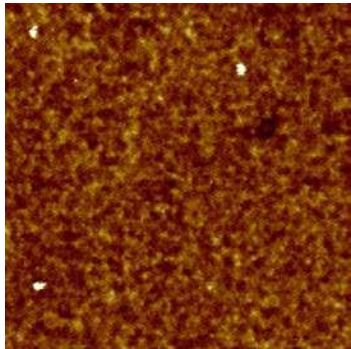
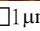
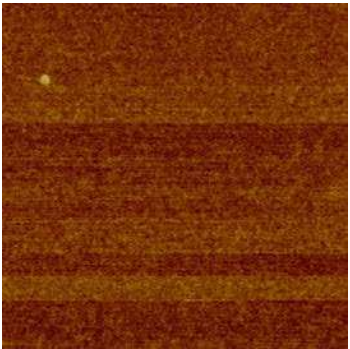
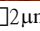
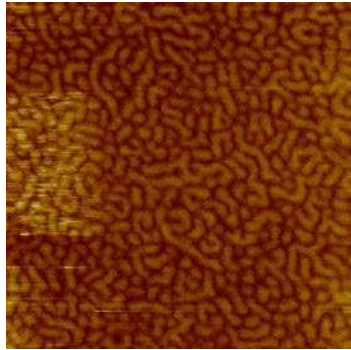
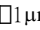
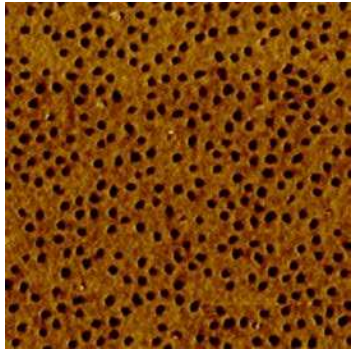
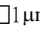

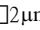
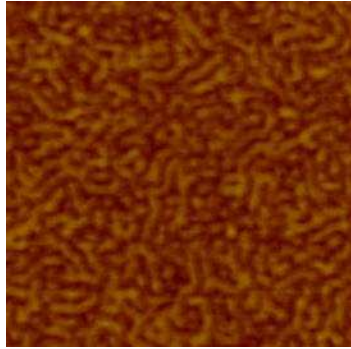
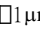
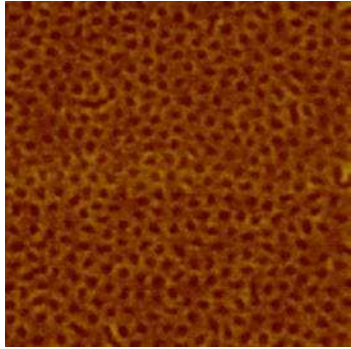
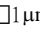
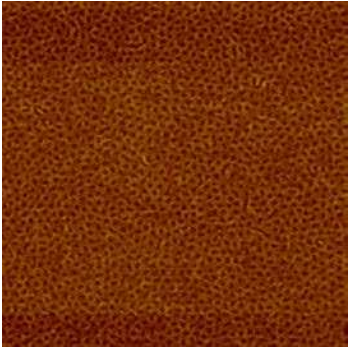
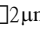
Figure S2.1 GPC Chromatograms showing the molecular weight distribution for samples TPE01 and TPE03 (**B7**) throughout the multi-step continuous polymerization process, including the final fractionated product. **A**: PS arm; **B**: PS star; **C**: S_nI diblock copolymer; **D**: Crude S_nIS_n triblock copolymer; **F**: Fractionated S_nIS_n triblock copolymer.

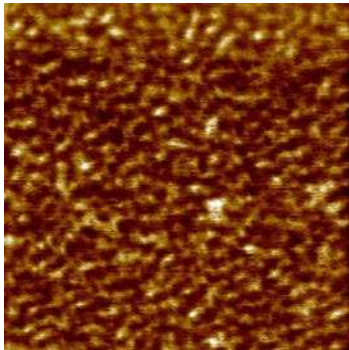
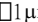
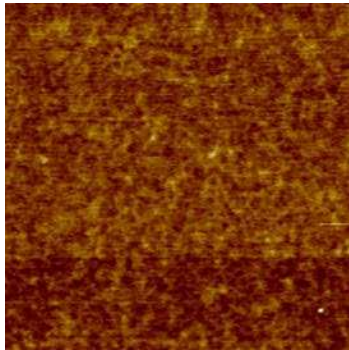
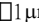
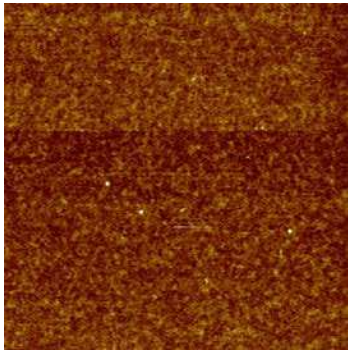
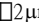
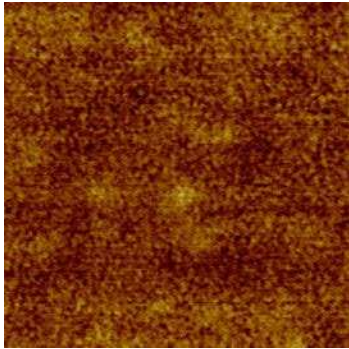
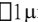
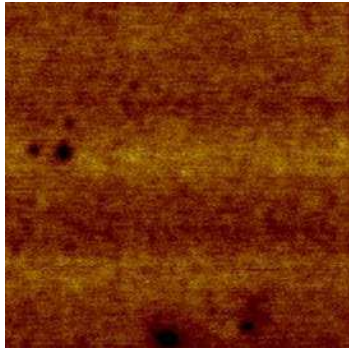
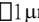
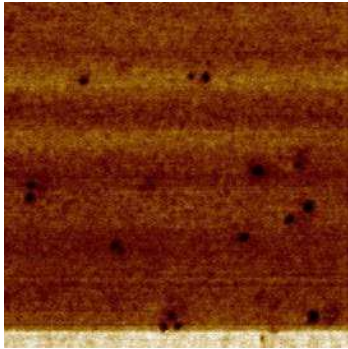
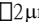
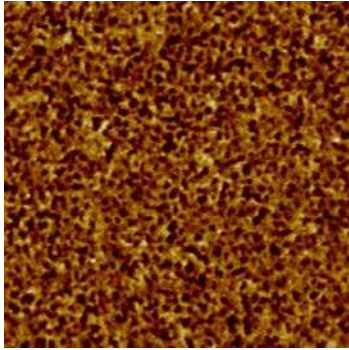
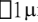
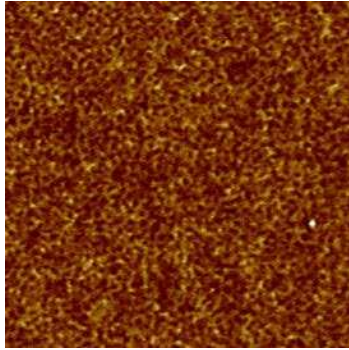
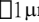
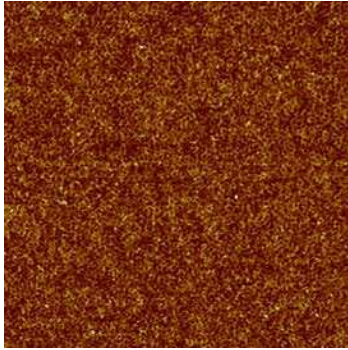
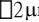
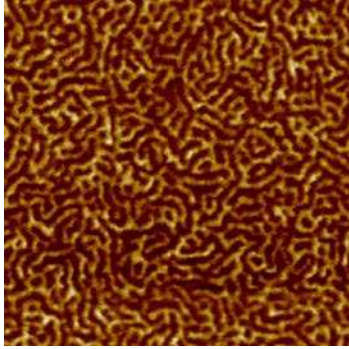
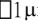
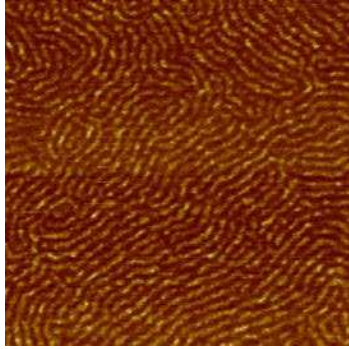
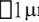
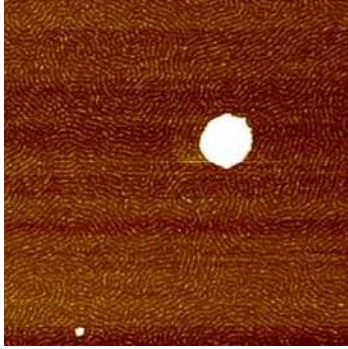
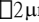
S2.3. AFM IMAGES OF SELECTED S_NIS_N POM-POM TRIBLOCK COPOLYMERS

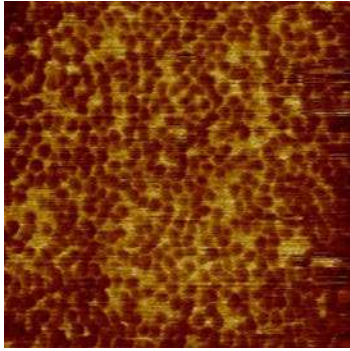
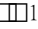
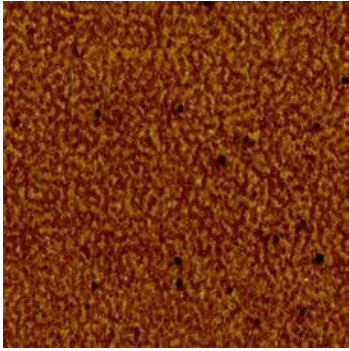
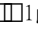
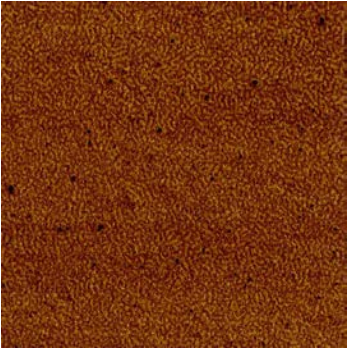
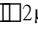
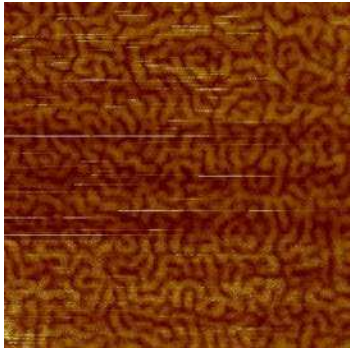
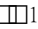
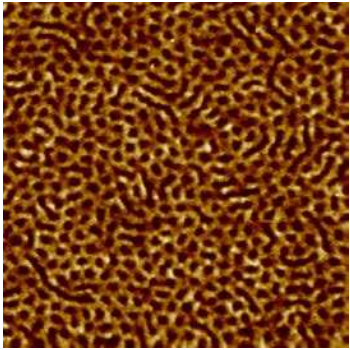
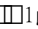

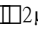
Table S2.2 Chemical characterization data

S_nIS_n	As Cast	Annealed	Annealed
TPE01	 1 μm  1 μm	 1 μm  1 μm	 2 μm  2 μm
TPE02	 1 μm  1 μm	 1 μm  1 μm	 2 μm  2 μm
TPE03 (B7)	 1 μm  1 μm	 1 μm  1 μm	 2 μm  2 μm

S_nIS_n	As Cast	Annealed	Annealed
TPE04	 1 μm  1 μm	 1 μm  1 μm	 2 μm  2 μm
TPE05	 1 μm  1 μm	 1 μm  1 μm	 2 μm  2 μm
TPE06 (C4)	 1 μm  1 μm	 1 μm  1 μm	 2 μm  2 μm
TPE07 (B4)	 1 μm  1 μm	 1 μm  1 μm	 2 μm  2 μm

S_nIS_n	As Cast	Annealed	Annealed
TPE08 (A4)	 1 μm  1 μm	 1 μm  1 μm	 2 μm  2 μm
TPE09	 1 μm  1 μm	 1 μm  1 μm	 2 μm  2 μm
TPE10	 1 μm  1 μm	 1 μm  1 μm	 2 μm  2 μm
TPE11 (B3)	 1 μm  1 μm	 1 μm  1 μm	 2 μm  2 μm


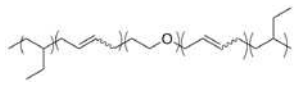
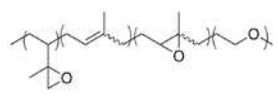
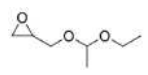
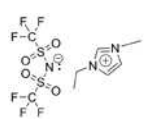
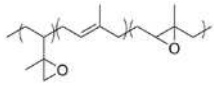

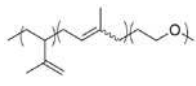
S_nIS_n	As Cast	Annealed	Annealed
TPE12	 1 μm  1 μm	 1 μm  1 μm	 2 μm  2 μm
TPE13	 1 μm  1 μm	 1 μm  1 μm	 2 μm  2 μm
TPE14	 1 μm  1 μm	 1 μm  1 μm	 2 μm  2 μm
TPE15	 1 μm  1 μm	 1 μm  1 μm	 2 μm  2 μm
TPE16	No image	No image	No image


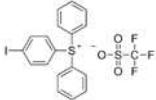
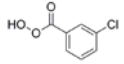
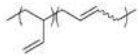
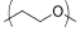
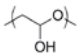
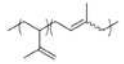
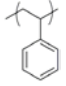
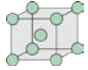

S_nIS_n	As Cast	Annealed	Annealed
TPE17	 <p data-bbox="313 594 440 621">1 μm  1 μm</p>	 <p data-bbox="690 594 816 621">1 μm  1 μm</p>	 <p data-bbox="1066 594 1193 621">2 μm  2 μm</p>
TPE18	 <p data-bbox="313 980 440 1008">1 μm  1 μm</p>	 <p data-bbox="690 980 816 1008">1 μm  1 μm</p>	 <p data-bbox="1066 980 1193 1008">2 μm  2 μm</p>

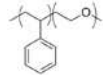
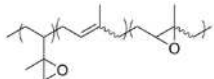
REFERENCES

- [1] Fetters, L. J.; Lohse, D. J.; Richter, D.; Witten, T. A.; Zirkel, A. *Macromolecules* **1994**, *27*, (17), 4639-4647.

COMMON ABBREVIATIONS AND CHEMICAL STRUCTURES USED WITHIN
DISSERATION

Abbreviation	Full Name	Chemical Structure/ Cartoon (Where applicable)
BCP	Block copolymer	
BO	Poly(butadiene)- <i>b</i> -poly(ethylene oxide)	
BOB	Poly(butadiene)- <i>b</i> -poly(ethylene oxide)- <i>b</i> -poly(butadiene)	
e _n IOI22	Partially epoxidized IOI22 blend (n mol% of olefins in polyisoprene is epoxidized)	
EEGE	Ethoxy ethyl glycidyl ether	
[emim][Tf ₂ N] [emim][TFSI]	1-ethy-3-methylimidazolium bis(trifluoromethyl-sulfonyl)imide	
ePI	Partially epoxidized poly isoprene	
G'	Storage (elastic) modulus	
G''	Loss (viscous) modulus	
GPC	Gel permeation chromatography	
HPC	Hexagonally packed cylinders	
¹ H NMR	Proton nuclear magnetic resonance	
IL	Ionic liquid	
IO	Poly(isoprene)- <i>b</i> -poly(ethylene oxide)	

Abbreviation	Full Name	Chemical Structure/ Cartoon (Where applicable)
IOI	Poly(isoprene)- <i>b</i> -poly(ethylene oxide)- <i>b</i> -poly(isoprene)	
IOI22	22 mol% IOI and 78% IO blend	
IOI46	46 mol% IOI and 54% IO blend	
IPDPST	(4-Iodophenyl)diphenylsulfonium triflate photoacid	
LLP	Liquid like packing	
MCPBA	meta Chloroperoxy benzoic acid	
PB	Poly(butadiene)	
PEO	Poly(ethylene oxide)	
PG	Polyglycidol	
PI	Polyisoprene	
PS	Polystyrene	
ROMP	Ring opening metathesis polymerization	
RTIL	Room temperature ionic liquid	
SAXS	Small angle X-ray scattering	
S _{BCC}	Body-centered cubic	
SEC	Size exclusion chromatography	
S _{LLP}	Liquid like packing of spheres	

Abbreviation	Full Name	Chemical Structure/ Cartoon (Where applicable)
SO	Polystyrene- <i>b</i> -poly(ethylene oxide)	
SOS	Polystyrene- <i>b</i> -poly(ethylene oxide)- <i>b</i> -polystyrene	
SOS22	22 mol% SO and 78% SOS blend	
SOS46	46 mol% SO and 54% SOS blend	
x_n IOI22-p	Cross-linked IOI22 blend (carried n mol% epoxy groups and p mol% photo acid)	
e_n PI	Partially epoxidized PI (n mol% of olefins in PI is epoxidized)	
x_n PI	Cross-linked polyisoprene (carried n mol% epoxy groups and p mol% photo acid)	
χ	Flory interaction parameter	